DISS. ETH NO. 30154

SYNTHESIS AND DYNAMICS OF CARBONACEOUS NANOPARTICLES DURING ENCLOSED SPRAY COMBUSTION

A thesis submitted to attain the degree of

DOCTOR OF SCIENCES

(Dr. sc. ETH Zurich)

presented by

UNA TRIVANOVIC

MASc, Mechanical Engineering, University of British Columbia

born on *17.06.1993*

accepted on the recommendation of

Prof. Dr. Sotiris E. Pratsinis, examiner
Prof. Dr. Steven N. Rogak, co-examiner
Prof. Dr. Jing Wang, co-examiner

2024

Acknowledgements

I would like to first and foremost express my gratitude to my supervisor, Prof. Dr. Sotiris E. Pratsinis for his invaluable mentorship, guidance, and scientific discussions throughout the last four years. I am incredibly lucky to have had such a dedicated supervisor. I would also like to thank Prof. Dr. Georgios A. Kelesidis for his mentorship and scientific exchanges both during his time at ETH and his continued support since starting his new position at Rutgers University. In addition, I would like to thank Prof. Dr. Inge Herrmann for serving as the co-advisor of my thesis and Prof. Dr. Jing Wang for serving on my committee and giving me the opportunity to present in his group. I am also grateful to Prof. Dr. Steven N. Rogak for his support getting to ETH, without which I may not have ended up where I am today and for serving on my committee.

My research would not have been possible without the technical support of René Plüss who was always able to find a solution for anything we wanted to build or fix in the lab, and it was always done as fast as possible. I would also like to thank Dr. Karsten Wegner for sharing his deep knowledge of the experimental systems and instruments in the lab, his mentorship and positive attitude. Dr. Frank Krumeich was also invaluable to my research, providing me with microscopy of thousands of soot particles over the course of my doctorate. I would also like to express my sincere gratitude to Agnes Güntner for her help with all the administrative issues and more, little would get done at PTL without her.

One of my favourite parts of my studies was getting to work with students and so, I would like to thank Michael Pereira Martins, Matteo D'Andria, Amogh Nagarkar, Simon Benz, Yannik Meisterhans, Giacomo Rizzo, and Alex Weber for choosing to do projects with me. I would also like to thank my colleagues and friends at the Particle Technology Laboratory (PTL) who made this a fun and meaningful time in my life including Dr. Ines Weber, Dr. Dina Oosthuizen, Sofía González Correra, Dr. Kasia Jabłczyńska, Christian Kubsch, Luca Dahle, Dr. Nicolay Pineau, Dr. Pascal Gschwend, Sebastian Abegg, Sebastian Keller, Florian Schenk and David Klein.

Outside of PTL, my friends and family were vital to my well-being over the last four years. Thank you to Natalia Smatsi, Davide Stucchi, Kate Lonergan, the groups of Prof. Herrmann and Prof. Güntner for many lunch and coffee breaks. Finally, a big thank you to my parents who are my biggest supporters no matter what I set out to do and my brother for moral support in the form of photos of his pets.

I would also like to acknowledge the Natural Science and Engineering Research Council of Canada (NSERC CGSD3-547016-2020) and the Swiss National Science Foundation (200020_182668, 250320_163243 and 206021_170729) for providing financial support for this research.

Table of Contents

Acknowledgements ..... **i**
Table of Contents ..... **iii**
Summary ..... **vii**
Zusamenfassung ..... **xi**
1. Eliminating aircraft soot emissions **1**
Abstract 1
1.1 Introduction 2
1.2 Formation and dynamics of aircraft soot 5
1.3 Means for the elimination of aircraft soot 9
1.3.1 Sustainable aviation fuels *9*
1.3.2 Aircraft Combustor Design & Operation *12*
1.4 Conclusions 17
1.5 References 19
2. High-throughput generation of aircraft-like soot **27**
Abstract 27
2.1 Introduction 28
2.2 Experimental 30
2.2.1 Particle production *30*
2.2.2 Particle sampling and on-line characterization *31*
2.2.3 Offline analysis *31*
2.3 Results and Discussion 32
2.3.1 Impact of EQR on soot d_m and d_p *32*
2.3.2 Soot morphology *35*
2.3.3 Organic carbon content of soot *37*
2.3.4 Soot mass concentrations *38*
2.3.5 Soot pore size distribution (PSD) and specific surface area (SSA) *40*
2.4 Conclusions 41
2.5 References 42
3. Dynamics of soot formation by enclosed spray combustion of jet fuel **47**
Abstract 47
3.1 Introduction 48
3.2 Experimental 49
3.3 Theory 51

3.4 Results and Discussion 52
3.4.1 Flame temperature 52
3.4.2 Soot dynamics along the burner axis 53
3.4.3 Impact of EQR on soot PP size distribution and nanostructure 57
3.5 Conclusions 60
3.6 References 61
4. Trade-off between soot and NO emissions during enclosed spray combustion of jet fuel 65
Abstract 65
4.1 Introduction 66
4.2 Experimental 67
4.2.1 Particle synthesis and sampling 67
4.2.2 Online measurements 68
4.2.3 Offline characterization of soot 68
4.3 Results and Discussion 69
4.3.1 Flame temperature 69
4.3.2 Soot concentration and size 69
4.3.3 Nitric oxide emissions 72
4.4 Summary & Conclusions 76
4.5 References 76
5. Outlook and Research Recommendations 79
5.1 References 81
A. Toward elimination of soot emissions from jet fuel combustion 83
Abstract 83
A1. Introduction 84
A2. Materials and Methods 85
A3. Results and Discussion 88
A4. Discussion and Outlook 93
A5. References 94
B. Impact of sustainable aviation fuels on soot from enclosed spray combustion 99
Abstract 99
B1. Introduction 100
B2. Experimental 102
B3. Results and Discussion 103
B4. Conclusions 110
B5. References 111

C. Supplementary Information for Chapter 2: High-throughput generation of aircraft-like soot 115

C1. Equivalence ratio calculation and range 115

C2. Thermal gravimetric analysis (TGA) 117

C3. Primary particle sizing 117

C4. Mass concentration correction 120

C5. Molar flow rate of spray combustion unit and miniCAST 121

C6. Nitrogen adsorption isotherms 121

C7. References 122

D. Supplementary Information for Chapter 3: Dynamics of soot surface growth and agglomeration by enclosed spray combustion of jet fuel 123

D1. References 133

E. Supplementary Information for Chapter 4: Trade-off between soot and NO emissions during enclosed spray combustion of jet fuel 135

E1. References 142

Curriculum Vitae 143

Publications and Presentations 146

Summary

Carbonaceous nanoparticles are both pollutants (soot) with negative effects on human health and the environment and valuable nanomaterials (carbon black). Understanding the processes which form such particles is therefore essential for designing combustion engines and reactors that minimize harmful emissions and enhance commercial profit. Aviation is a growing industry and an important source of soot. Soot from aviation tends to have a small size relative to other soot sources (e.g. diesel engines) which may result in greater health risks due to the higher toxicity of small particles. However, questions remain regarding the biological mechanisms tied to the negative health effects of soot. Similarly, aviation is unique in that it emits soot at high altitudes, where the particles may act as ice condensation nuclei forming contrails. These effects, however, are still poorly understood as experiments with real jet engines are costly and difficult to access. Low-cost and high-throughput methods for soot research are needed to better quantify the impact of soot on the climate, human health and to design improved engines. This way, trade-offs that minimize the impact of aviation on human health and the environment can be made. In this thesis, these challenges will be addressed through an overview of existing technologies, development of a laboratory soot generator and the application of this soot generator to better understand soot and NO emissions from jet fuel combustion.

Chapter 1 gives an overview of existing strategies to reduce soot emission while considering industry requirements to limit pollutants such as CO_2, carbon monoxide (CO), unburned hydrocarbons (UHC), oxides of nitrogen (NO_x), and meeting strict safety and performance standards. Computational models are used to aid in aircraft engine design. However, models struggle to accurately capture the soot mobility diameter, d_m, and volume fraction, f_v, observed experimentally. Part of this discrepancy could be due to models' oversimplification of the irregular morphology of soot and the current poor understanding of soot formation processes. Even so, aircraft combustors have been reducing soot emissions through extensive oxidation with the Rich-Quench-Lean (RQL) concept or by preventing soot formation with near-premixed, lean combustion such as in Lean Premixed Prevaporized (LPP) combustors. Near-premixed combustion prevents soot from forming in fuel-rich pockets while very lean combustion keeps temperatures low, thus preventing NO_x formation. The use of alternative fuels could also reduce soot emissions. Sustainable Aviation Fuels (SAF) tend to have lower aromatic content compared to conventional jet fuels, which reduces the formation of soot particularly at low engine thrusts. The use of SAF is attractive logistically, as it can be a drop-in fuel requiring no new infrastructure or engines; however, the short-term supply is

limited. In this regard, it is important that policies promote high blends of SAF which can reduce soot rather than adding a small amount of SAF to all flights, which has little to no impact on soot emissions.

Chapter 2 describes the development of a low-cost, laboratory burner to produce aircraft-like soot from real jet fuels with high throughput. Laboratory burners are essential for facilitating research on soot emissions in a lower-cost and more controlled environment compared to a real aircraft engine. However, existing commercial soot generators fail to produce soot similar to that produced by aircrafts at high thrust. High-thrust aircraft soot tends to have Organic Carbon to Total Carbon (OC/TC) ratios < 25 % and small median mobility diameters, d_m, in the range of 11 – 61 nm. Here, enclosed spray combustion (ESC) of jet A1 fuel is used to produce soot with similar OC/TC, d_m and primary particle diameter, d_p, to that observed in soot from real aircraft. Specifically, OC/TC ratios were consistently < 20% while the median d_m ranged from 15 – 150 nm depending on the Effective eQuivalence Ratio (EQR) employed. Soot particles produced at the low end of this range (d_m < 50 nm) can be considered 'aircraft-like'. The specific surface area (SSA) was quantified for the first time for aircraft-like particles (160 – 239 m^2/g) with mainly small pores (< 2 nm). ESC therefore provides a new, lab-based method to replicate soot produced by aircrafts at high thrust.

Chapter 3 explores the formation and growth dynamics of soot produced by the ESC burner developed in Chapter 2 at various EQR. This characterization and modeling of the formation and growth of soot during spray combustion of jet fuel can be used to improve the understanding and modeling of soot from aircraft engines. The centerline flame temperature peaked at Heights Above the Burner (HAB) = 5 – 10 cm then dropped continuously through to the end of the enclosure at HAB = 63 cm. The maximum temperature depended on the EQR with lower EQR (closer to stoichiometric) resulting in higher temperatures than the richer flames. Within a flame, the d_m of soot grew continuously from HAB = 5 to 63 cm while the d_p was approximately constant at all points along the enclosure. Discrete Element Modeling (DEM) revealed that this behavior is attributable to the leveling off of soot surface growth after short residence times, before HAB = 5 cm and agglomeration then took over as the primary mechanism for particle growth. At low EQR = 1.46, the d_p leveled off at approximately 14 nm. At higher EQR (e.g. 1.88) soot surface growth was enhanced leading to larger d_p, up to 23 nm. Across the same range, the Raman D/G ratio dropped from 0.9 to 0.8 at EQR = 1.46 and 1.88, respectively, while the crystallite length increased from 1.24 to 1.47 nm. These correlations suggests that high EQR produced larger d_p with more graphitic, crystalline particles compared to the smaller more disordered primary particles produced at low EQR.

Chapter 4 investigates the trade-off between soot and nitric oxide (NO) during ESC of jet fuel as combustion conditions that reduce soot emissions tend to increase NO_x, making it difficult to reduce both pollutants at the same time. Judicious swirl-injection of air downstream of ESC can drastically reduce soot emissions through oxidation. However, this swirl-injection strategy leads to higher temperatures that promote NO. Early injection of air results in the lowest soot emissions, but the highest NO, nearly triple that produced when air is injected far downstream of the burner. Conversely, late injection of air does not reduce soot emissions although NO remained low. Here, a quantitative correlation is found between injection location, temperature, soot and NO. Therefore, the combustion conditions which allowed for a balanced trade-off between NO and soot emissions was found and on par with or lower than the lowest NO_x emissions per unit mass of fuel from in-service aircraft engines.

Enclosed spray combustion of jet fuel provides a high-throughput method for producing soot with comparable morphology and composition to that from aircraft at high thrust for the first time. The understanding of soot formation and growth during ESC of jet fuel can help to improve modeling and design of aircraft engines through an improved fundamental understanding of the processes involved. Furthermore, quantifying the trade-off between soot and NO emissions is essential for developing engines which minimize both pollutants. In the future, ESC could be used for calibrating regulatory instrumentation, testing novel jet fuels or production of sufficiently large quantities for further research on the biological effects of soot.

Zusamenfassung

Kohlenstoffhaltige Nanopartikel sind sowohl Schadstoffe (Russ) mit negativen Auswirkungen auf die menschliche Gesundheit und die Umwelt als auch wertvolle Nanomaterialien (Carbon Black). Das Verständnis der Prozesse, die zur Bildung solcher Partikel führen, ist daher für die Entwicklung von Verbrennungsmotoren und Reaktoren, die schädliche Emissionen minimieren und den wirtschaftlichen Gewinn steigern, von entscheidender Bedeutung. Die Luftfahrt ist ein wachsender Wirtschaftszweig und eine wichtige Russquelle. Russ aus der Luftfahrt hat im Vergleich zu anderen Russquellen (z. B. Dieselmotoren) in der Regel eine geringe Grösse, was aufgrund der höheren Toxizität kleiner Partikel zu grösseren Gesundheitsrisiken führen kann. Es gibt jedoch noch Fragen zu den biologischen Mechanismen, die mit den negativen gesundheitlichen Auswirkungen von Russ verbunden sind. Auch die Luftfahrt ist insofern einzigartig, als sie Russ in grossen Höhen ausstösst, wo die Partikel als Eiskondensationskerne wirken und Kondensstreifen bilden können. Diese Auswirkungen sind jedoch noch wenig bekannt, da Experimente mit echten Düsentriebwerken kostspielig und schwer zugänglich sind. Kostengünstige und durchsatzstarke Methoden für die Russforschung werden benötigt, um die Auswirkungen von Russ auf das Klima und die menschliche Gesundheit besser quantifizieren und verbesserte Triebwerke entwickeln zu können. Auf diese Weise können Kompromisse gefunden werden, die die Auswirkungen des Luftverkehrs auf die menschliche Gesundheit und die Umwelt minimieren. In dieser Arbeit werden diese Herausforderungen durch einen Überblick über bestehende Technologien, die Entwicklung eines Labor-Russgenerators und die Anwendung dieses Russgenerators zum besseren Verständnis der Russ- und NO-Emissionen bei der Verbrennung von Flugzeugtreibstoff angegangen.

Kapitel 1 gibt einen Überblick über bestehende Strategien zur Verringerung der Russemissionen unter Berücksichtigung der Anforderungen der Industrie zur Begrenzung von Schadstoffen wie CO_2, Kohlenmonoxid (CO), unverbrannten Kohlenwasserstoffen (UHC) und Stickstoffoxiden (NO_x) sowie zur Einhaltung strenger Sicherheits- und Leistungsstandards. Computermodelle werden als Hilfsmittel bei der Konstruktion von Flugzeugtriebwerken eingesetzt. Die Modelle haben jedoch Schwierigkeiten, den experimentell beobachteten Durchmesser der Russmobilität dm und den Volumenanteil f_v genau zu erfassen. Diese Diskrepanz könnte zum Teil darauf zurückzuführen sein, dass die Modelle die unregelmässige Morphologie des Russes zu stark vereinfachen und die Russbildungsprozesse derzeit nur unzureichend verstanden werden. Dennoch haben Flugzeugbrennkammern die Russemissionen

durch eine umfassende Oxidation mit dem Rich-Quench-Lean-Konzept (RQL) oder durch die Verhinderung der Russbildung mit einer fast vorgemischten, mageren Verbrennung wie in LPP-Brennkammern (Lean Premixed Prevaporized) reduziert. Die Verbrennung mit annähernder Vormischung verhindert die Bildung von Russ in brennstoffreichen Taschen, während die sehr magere Verbrennung die Temperaturen niedrig hält und so die Bildung von NO_x verhindert. Auch der Einsatz alternativer Kraftstoffe könnte die Russemissionen verringern. Nachhaltige Flugkraftstoffe (Sustainable Aviation Fuels, SAF) haben im Vergleich zu herkömmlichen Düsenkraftstoffen einen geringeren Gehalt an Aromaten, was die Russbildung insbesondere bei niedrigem Triebwerksschub verringert. Die Verwendung von SAF ist logistisch attraktiv, da es sich um einen Drop-in-Kraftstoff handelt, der keine neue Infrastruktur oder Triebwerke erfordert; allerdings ist das kurzfristige Angebot begrenzt. In diesem Zusammenhang ist es wichtig, dass die Politik hohe SAF-Beimischungen fördert, die den Russausstoss verringern können, anstatt allen Flügen eine geringe Menge SAF beizumischen, die nur geringe oder gar keine Auswirkungen auf den Russausstoss hat.

Kapitel 2 beschreibt die Entwicklung eines kostengünstigen Laborbrenners zur Erzeugung von flugzeugähnlichem Russ aus echten Düsentreibstoffen mit hohem Durchsatz. Laborbrenner sind für die Erforschung von Russemissionen in einer im Vergleich zu einem echten Flugzeugtriebwerk kostengünstigeren und kontrollierteren Umgebung unerlässlich. Mit den vorhandenen kommerziellen Russgeneratoren kann jedoch kein Russ erzeugt werden, der dem von Flugzeugen bei hohem Schub erzeugt wird. Flugzeugruss mit hoher Schubkraft hat in der Regel ein Verhältnis von organischem Kohlenstoff zu Gesamtkohlenstoff (OC/TC) von < 25 % und einen kleinen mittleren Mobilitätsdurchmesser (dm) im Bereich von 11 bis 61 nm. Hier wird die geschlossene Sprühverbrennung (ESC) von Jet-A1-Kraftstoff verwendet, um Russ mit ähnlichen OC/TC-, dm- und Primärpartikeldurchmessern (dp) zu erzeugen, wie sie in Russ aus echten Flugzeugen beobachtet werden. Insbesondere waren die OC/TC-Verhältnisse durchweg < 20 %, während der mittlere dm-Wert zwischen 15 und 150 nm lag, je nach dem verwendeten effektiven equivalenzverhältnis (EQR). Russpartikel am unteren Ende dieses Bereichs (d_m < 50 nm) können als "flugzeugähnlich" angesehen werden. Die spezifische Oberfläche (SSA) wurde zum ersten Mal für flugzeugähnliche Partikel (160 – 239 m^2/g) mit überwiegend kleinen Poren (< 2 nm) quantifiziert. Die ESC bietet somit eine neue, laborgestützte Methode zur Nachbildung von Russ, der von Flugzeugen bei hohem Schub erzeugt wird.

In Kapitel 3 wird die Dynamik der Bildung und des Wachstums von Russ untersucht, der von dem in Kapitel 2 entwickelten ESC-Brenner bei verschiedenen EQR erzeugt wird.

Diese Charakterisierung und Modellierung der Russbildung und des Russwachstums bei der Sprühverbrennung von Düsentreibstoff kann dazu dienen, das Verständnis und die Modellierung von Russ aus Flugzeugtriebwerken zu verbessern. Die Flammentemperatur in der Mittellinie erreichte ihren Höhepunkt bei einer Höhe über dem Brenner (HAB) von 5 bis 10 cm und fiel dann kontinuierlich bis zum Ende des Gehäuses bei HAB = 63 cm. Die maximale Temperatur hing vom EQR ab, wobei ein niedriger EQR (näher an der Stöchiometrie) zu höheren Temperaturen führte als die reicheren Flammen. Innerhalb einer Flamme nahm der dm-Wert des Russes von HAB = 5 bis 63 cm kontinuierlich zu, während der d_p-Wert an allen Punkten entlang der Umhüllung annähernd konstant war. Die Modellierung mit diskreten Elementen (DEM) ergab, dass dieses Verhalten auf das Abflachen des Russoberflächenwachstums nach kurzen Verweilzeiten vor HAB = 5 cm zurückzuführen ist und dass dann die Agglomeration als primärer Mechanismus für das Partikelwachstum übernommen wurde. Bei einer niedrigen EQR = 1.46 pendelte sich der d_p bei etwa 14 nm ein. Bei höheren EQR (z. B. 1.88) wurde das Russoberflächenwachstum verstärkt, was zu grösseren dp von bis zu 23 nm führte. Im gleichen Bereich sank das Raman-D/G-Verhältnis bei EQR = 1.46 bzw. 1.88 von 0.9 auf 0.8, während die Kristallitlänge von 1.24 auf 1.47 nm anstieg. Diese Korrelationen deuten darauf hin, dass ein hoher EQR grössere dp mit mehr graphitischen, kristallinen Partikeln im Vergleich zu den kleineren, ungeordneteren Primärpartikeln bei niedrigem EQR erzeugt.

In Kapitel 4 wird der Zielkonflikt zwischen Russ und Stickoxid (NO) beim ESC von Düsenkraftstoff untersucht, da Verbrennungsbedingungen, die die Russemissionen verringern, die NO_x-Emissionen tendenziell erhöhen, so dass es schwierig ist, beide Schadstoffe gleichzeitig zu verringern. Eine gezielte Dralleinspritzung von Luft nach dem ESC kann die Russemissionen durch Oxidation drastisch reduzieren. Allerdings führt diese Dralleinblasstrategie zu höheren Temperaturen, die die NO-Emissionen fördern. Eine frühe Lufteinspritzung führt zu den geringsten Russemissionen, aber zu den höchsten NO-Werten, die fast dreimal so hoch sind wie bei einer Lufteinspritzung weit hinter dem Brenner. Umgekehrt führt eine späte Lufteinspritzung nicht zu einer Verringerung der Russemissionen, während die NO-Emissionen niedrig bleiben. Hier wird ein quantitativer Zusammenhang zwischen Einblasort, Temperatur, Russ und NO festgestellt. Es wurden also Verbrennungsbedingungen gefunden, die einen optimalen Kompromiss zwischen NO- und Russemissionen ermöglichen und den niedrigsten NO_x-Emissionen pro Masseneinheit Kraftstoff von in Betrieb befindlichen Flugzeugtriebwerken entsprechen oder darunter liegen.

Die Verbrennung von Düsentreibstoff in einem geschlossenen Sprühsystem bietet erstmals eine Methode zur Erzeugung von Russ mit vergleichbarer Morphologie und Zusammensetzung wie bei Flugzeugen mit hohem Schub. Das Verständnis der Russbildung und des Russwachstums bei der ESC-Verbrennung von Düsenkraftstoff kann dazu beitragen, die Modellierung und Auslegung von Flugzeugtriebwerken durch ein besseres Verständnis der beteiligten Prozesse zu verbessern. Darüber hinaus ist die Quantifizierung des Zielkonflikts zwischen Russ- und NO-Emissionen für die Entwicklung von Triebwerken, die beide Schadstoffe minimieren, von entscheidender Bedeutung. In Zukunft könnte die ESC zur Kalibrierung von Regulierungsinstrumenten, zur Prüfung neuartiger Düsenkraftstoffe oder zur Herstellung ausreichend grosser Mengen für die weitere Erforschung der biologischen Auswirkungen von Russ verwendet werden.

Chapter 1

Eliminating aircraft soot emissions[1]

Abstract

Soot from aircraft engines deteriorates air quality around airports and can contribute to climate change primarily by influencing cloud processes and contrail formation. Simultaneously, aircraft engines emit CO_2, nitrogen oxides (NO_x) and other pollutants which also negatively affect human health and the environment. While urgent action is needed to reduce all pollutants, strategies to reduce one pollutant may increase another, calling for a need to decrease, for example, the uncertainty associated with soot's contribution to net Radiative Forcing (RF) in order to design targeted policies that minimize the formation and release of all pollutants. Aircraft soot is characterized by rather small median mobility diameters, d_m = 8 – 60 nm, and at high thrust, low (< 25%) organic carbon to total carbon (OC/TC) ratios while at low thrust the OC/TC can be quite high. Computational models could aid in the design of new aircraft combustors to reduce emissions, but current models struggle to capture the soot d_m, and volume fraction, f_v measured experimentally. This may be in part due to oversimplification of soot's irregular morphology in models and a still poor understanding of soot inception. Nonetheless, combustor design can significantly reduce soot emissions through extensive oxidation or near-premixed, lean combustion. For example, lean premixed prevaporized combustors significantly reduce emissions at high thrust by allowing injected fuel to fully vaporize before ignition while low temperatures from very lean jet fuel combustion limit the formation of NO_x. Alternative fuels can be used alongside improved combustor technologies to reduce soot emissions. However, current policies and low supply promote the blending of alternative fuels at low ratios (~1%) for all flights, rather than using high ratios (> 30%) in a few flights which could meaningfully reduce soot emissions. Here, existing technologies for reducing such emissions through combustor and fuel design will be reviewed to identify strategies that eliminate them.

[1] A version of this chapter is published in *Aerosol Research* (2024), **2**, 207-223.

1.1 Introduction

Aviation is a growing industry with a significant impact on human health and the environment due to the emission of combustion by-products, including soot aerosols. The latter is one of the most important contributors to climate change [1] and a component of air pollution known to cause cancer, cardiovascular and respiratory diseases, and it has been correlated with various other illnesses [2]. Regulations around the world have been limiting soot emissions since the 1970s. The International Civil Aviation Organization (ICAO) until recently limited only the 'smoke number', essentially visible black smoke from aircraft engines which caused dangerous reductions in visibility around airports [3]. Modern engines have no visible smoke but still produce invisible nanoparticles [4]. In 2020, smoke number was replaced with a limit on the mass concentration of non-volatile Particulate Matter (nvPM) and in 2023 an additional limit was placed on the number concentration of nvPM for all new engines with a rated thrust greater than 26.7 kN [5]. Thus, jet engine manufacturers must design new engines to meet the new nvPM standards without exceeding the regulations limiting nitrogen oxides (NO_x), unburned hydrocarbons (UHC) or carbon monoxide (CO) emissions while still maintaining strict safety standards. These regulations are aimed at improving local air quality, so engines are assessed based on a standardized landing and take-off (LTO) cycle most relevant for emissions near the ground.

Soot emissions can impact the climate by warming the atmosphere through direct Radiative Forcing (RF) and indirectly by altering cloud processes and decreasing snow albedo [1]. Aviation is unique in that it emits soot at high altitude with very different atmospheric conditions (e.g., temperature and pressure) from those on the ground. This may influence the formation of contrails [6]. Lee et al. [7] estimated the climate forcing contribution of CO_2, contrail cirrus, NO_x, soot aerosols, SO_2 aerosols and water vapor from aviation in 2018. By these estimates, contrails account for 57.4 mWm^{-2} or 55% of aviation's net radiative forcing but with 95% confidence intervals from 27 – 67% of the net RF illustrating the high uncertainty. The exact RF of contrail cirrus depends on the atmospheric conditions along the flight track and time of day. At night, contrails have an exclusively warming effect while during the day there can be a warming and a cooling effect [8].

The estimate of direct RF from soot was relatively low, 0.9 mWm^{-2} [7]. However, inventories of global soot emissions from aircraft can vary by two orders of magnitude [9]. Present inventories are based on the LTO cycle which focuses on landing and take-off at sea-level rather than high-altitude cruise. As these emissions are measured only at ground level for the LTO cycle, the emissions most relevant for climate considerations are only indirectly

estimated [10]. In addition, the LTO cycle does not exactly match the real time at each thrust for example, the LTO cycle assumes idle/taxi is 7% but real aircraft use between 3 – 17% thrust for these conditions. [11]. Estimates of the RF of soot are from climate models which may underestimate the contribution of soot [12]. While CO_2 remains in the atmosphere for 100 years or more, soot and contrails have short atmospheric lifetimes on the order of a week [1] or hours [13], respectively, so their global warming potential is most important in the short term. This presents an opportunity to make immediate reductions in global warming and 'buying time' for the implementation of technologies to lower CO_2 emissions [14]. This may be important for the aviation industry which in 2022, adopted an ambitious goal of net-zero carbon emissions by 2050.

These uncertainties highlight the importance of further research to better quantify the role of soot in both contrail formation [15] and direct radiative forcing [12]. Such uncertainties make it difficult to accurately assess priorities in emission reductions as there are often trade-offs between emissions. For example, reductions in soot often result in an increase in NO_x from diesel engines [16]. Similarly, contrail formation can be avoided by diverting flights to airspace with unfavorable conditions for contrail formation (e.g. warmer temperatures) but may result in higher fuel consumption and, thus, CO_2 emissions [17]. The large uncertainty associated with the contribution of soot to climate change is in part due to the oversimplification of soot morphology in climate models which typically assume soot to be coated spheres. In reality, soot is an agglomerate composed of polydisperse primary particles (PP), illustrated in Figure 1.1, with a nanostructure of layered graphene sheets (Fig. 1.1: inset).

The relative amounts of Organic Carbon (OC) or Elemental Carbon (EC) compared to the Total Carbon (TC) is typically used to quantify the chemical composition of the particles. The OC is defined by the ICAO as "…carbon volatilized in Helium while heating a quartz fiber filter sample to 870 °C during thermal optical transmittance analysis including char formed during pyrolysis of some materials". Conversely, EC is "…light absorbing carbon that is not removed from a filter sample heated to 870 °C in an inert atmosphere during thermal optical transmittance analysis, excluding char" [5]. So, while quantifying OC/EC ratios is important for understanding the light absorption of soot [18], the split between EC and OC is method-dependent [19] rather than a discrete property. The size of irregular agglomerates such as soot is quantified by equivalent diameters such as the mobility diameter, d_m (Fig. 1.1: broken line). Using a realistic soot morphology rather than equivalent spheres in climate models increases the estimated direct RF by 20% on average revealing large direct RF = 3 – 5 W/m^2 in hot spot earth regions, in line with field observations [12].

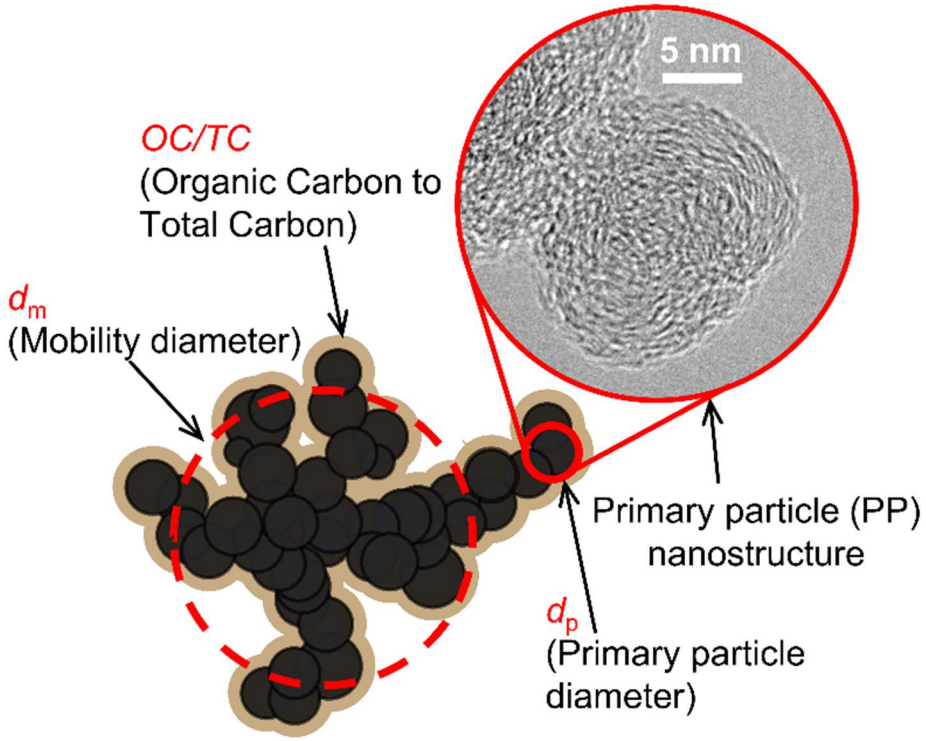

Figure 1.1: A schematic of a soot nanoparticle highlighting commonly quantified properties which are relevant for assessing the health and climate impact of such particles including the mobility diameter, d_m (broken line), primary particle diameter, d_p (red solid line) and Organic Carbon (brown shaded area) to Total Carbon ratio, OC/TC. The inset shows a high-resolution transmission electron micrograph (HRTEM) of a soot primary particle, from enclosed spray combustion of jet fuel produced at an equivalence ratio of 1.25 [20], where the individual graphene layers can be seen. Volatile compounds that may be adsorbed on the surface usually evaporate under the vacuum of the microscope so cannot be visualized easily with HRTEM.

Furthermore, limited access to real jet engines has made it difficult to assess the efficiency of soot to act as ice condensation nuclei (ICN) and thus to enhance contrail formation. To date, experiments on the ICN activity of soot have been done primarily using commercial carbon blacks or miniCAST soot generated by burning hydrocarbon gases [21]. MiniCAST particles tend to have much larger d_m (> 100 nm) than that produced by real aircraft (< 100 nm) if the organic carbon to total carbon ratio (OC/TC) is sufficiently small [22]. Recently, enclosed spray combustion of jet A1 fuel has been shown to be a promising laboratory surrogate for aircraft soot produced at high thrust (i.e. cruise) with sufficiently small d_m and OC/TC [20]. This is important for the calibration of optical instruments which may be sensitive to the OC/TC ratio in addition to particle morphology [22].

Technology for battery-electric or hydrogen-powered planes will not be available in the short-to-medium term for long-haul flights [23]. Significant investment in airport infrastructure would be needed to accommodate such changes in technology [24]. Emissions from aviation need to be addressed urgently to meet climate goals and prevent further health degradation and mortality from air pollution. However, aircraft engines have many competing demands

including continued reduction of gaseous emissions, CO_2 net-zero goals, safety requirements and regulations on noise. Thus, a firm understanding of the environmental and health impacts of soot as well as a fundamental understanding of its formation and growth in aircraft engines is essential for weighing the costs and benefits of mitigation strategies. The regulatory term nvPM refers to particles that remain solid when heated to 350 °C. In aircraft emissions, this is primarily soot and concentrations are measured with instruments designed for soot with a low OC/TC ratio [25] so the terms nvPM and soot will be used interchangeably. Regulations on aircraft emissions apply only to turbofan and turbojet engines with rated thrust > 26.7 kN. As such, most scientific research has been conducted on engines in this category and will also be the category discussed in this paper. However, it is worth noting that small business jets with thrusts < 26.7 kN may produce more nvPM emissions than large aircraft such as the Boeing 737 which do fall under the ICAO regulations and need further research for accurate emissions inventories [26]. In addition, while the European Union (EU) voted to ban leaded aviation gasoline (Avgas) used in small piston-engine aircraft in 2022, most other countries still allow its use and it is now considered one of few major sources of ambient lead in the US [27]. Possible mechanisms for the formation and dynamics of soot from regulated jet engines will be discussed. Then, strategies already in use or under development for the elimination of jet engine soot emissions will be reviewed.

1.2 Formation and dynamics of aircraft soot

Although aircraft combustor design can vary significantly, the soot produced by aircrafts have some morphological and compositional differences from other sources such as diesel engines. Aircrafts tend to produce soot with median d_m in the range of 8 [28] to 60 nm [29]. Such small d_m are associated with greater lung deposition efficiency [30] and translocate from the lungs to other organs more effectively than particles with d_m > 100 nm [31]. The OC/TC tends to be quite low (< 25%) [32] when the aircraft operates at high thrust (> 50%) while the reverse is true at low thrust. Lubricating oil may contribute to the organic fraction of particles emitted from aircraft engines however, the contribution of lubricating oil is highly dependent on engine design and lubricating oil recovery systems [33]. The emission of lubricating oil particles is independent of the thrust as it is a non-combustion source. Therefore, it only plays a significant role when soot emissions are low, for example, during idle [33]. The OC/TC influences the optical properties of soot and thus its RF [18]. Aircraft soot has PP diameters, d_p (Fig. 1.1: solid line), from approximately 5 [34] up to 24 nm with lower thrusts tending to produce smaller d_p [35] which influences soot reactivity [36] and optical properties [37]. These same properties are also influenced by PP nanostructure which is related to their maturity [38]. Aircraft tend to

produce rather disordered soot with a turbostratic structure with more defects on its surface than the bulk [39]. The conditions under which soot forms determine its final morphology and composition and *vice versa* [40].

Figure 1.2 depicts the cross-section of a single annular aircraft combustor (SAC), one of the common combustor designs in modern engines. The combustor is typically an annular tube that receives high pressure air from the compressor, adds energy to the system through combustion and uses it to drive the turbine. Liquid jet fuel is injected at one end of the SAC, typically with a swirling mechanism to atomize the fuel, promoting evaporation. However, perfect mixing is not achieved. So locally fuel-rich pockets allow for soot formation even if the global mixture is fuel-lean. Where the fuel is injected, there is significant recirculation allowing soot to grow in these fuel-rich pockets [41]. When there is insufficient oxygen for complete conversion to carbon dioxide, fuels decompose into radicals and intermediate species, such as acetylene which then grow into small aromatics [42]. These aromatic compounds eventually evolve into polycyclic aromatic hydrocarbons (PAHs) which are the key gaseous precursors to soot [44]. The presence of these soot precursors has been confirmed experimentally with atomic force microscopy [45]. With respect to aviation, experimental studies have shown a correlation between jet fuel aromatic content, sooting tendency [46] and nvPM emissions [47]. So, fuel composition plays a key role in the formation of soot and thus provides one possible route for its elimination as discussed in detail in the next section.

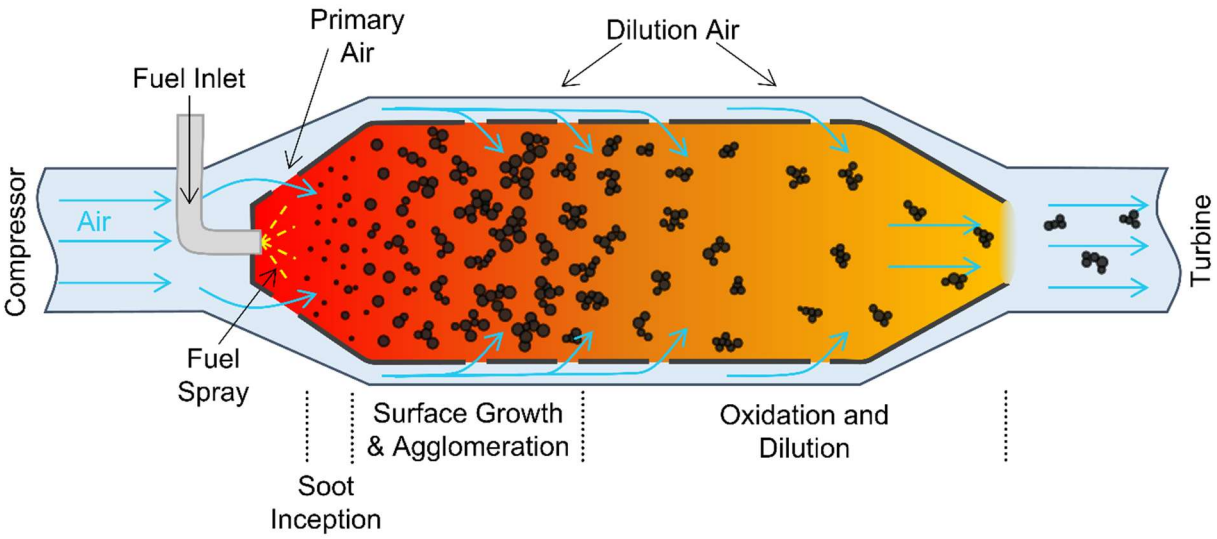

Figure 1.2: A simplified schematic of an aircraft single annular combustor (SAC) adapted from [43] with a qualitative depiction of the soot dynamics from soot inception to surface growth & agglomeration and then oxidation before being vented to the turbine and eventually the exhaust.

Although the exact mechanisms of soot nucleation (i.e. the transition from the gas to solid phase) are still an area of active research [48], the dynamics of soot inception [49] and growth from nascent to mature soot [50] leading to its final structure are becoming better understood.

Nascent soot particles are as small as $d_m \sim 2$ nm [51], amorphous [52] and liquid-like [53] with a carbon to hydrogen (C/H) ratio < 2 [54]. As they age, nascent soot carbonizes (lose hydrogen) and solidifies [55]. Soot then simultaneously undergoes surface growth and agglomeration [56]. Surface growth of soot is well described by the hydrogen-abstraction carbon-addition (HACA) mechanism [44] although other pathways have also been proposed [42]. During the first few milliseconds of particle growth, surface growth precursors are depleted then agglomeration takes over as the primary growth mechanism and d_m increases markedly while d_p stays approximately constant [56]. In the free molecular regime, particles grow into large agglomerates through ballistic cluster-cluster coagulation while in the continuum regime this becomes diffusion-limited cluster agglomeration. Particles which coagulate in the free molecular regime have a slightly more compact structure than those in the continuum regime as shown by their asymptotic mass fractal dimensions of 1.91 and 1.78, respectively [57].

This soot growth sequence has been observed and quantified for soot formation in premixed flames, diesel engines, miniCAST soot generator [50] and even for enclosed spray combustion of jet A1 fuel resulting in aircraft-like soot [58]. After primary air injection for the initial combustion, dilution air is added at various locations along the combustor length. This oxidizes a sizable portion of the soot which was initially created. Transmission Electron Microscopy (TEM) has shown that aircraft soot is significantly oxidized and the small d_m may be in part due to fragmentation of larger agglomerates after extensive oxidation [59]. So, in the early stages of the combustor the number and size of soot is likely larger than what is eventually emitted. The final morphology of the particles, including the d_p, d_m and number of PPs per agglomerate, n_p, depends on the initial volume fraction, residence time, temperature and pressure [60].

While conditions can vary significantly depending on the engine, soot in an aircraft combustor experiences both high temperature and pressure. In addition, pressures are increased at high thrust which has been correlated with increased soot concentration and size [61]. Higher pressures improve the efficiency of engines and so as engine materials have been improved to withstand higher pressures, the pressure ratios in engines have also increased. So, soot may begin growing in the free molecular regime but enters the transition regime as it grows, in particular at high thrust, when pressures are the highest and soot particles tend to grow to the largest sizes. This is in line with mass-mobility measurements of aircraft soot which shows an increase in the mass-mobility exponent, D_{fm}, from 1.86 ± 0.37 to 2.79 ± 0.07 as thrust increases from 7 to 118%, respectively [30]. However, mass-mobility measurements are not part of the regulatory framework for aircraft nvPM.

Low thrusts lead to the longest soot residence time in the combustor but tend to produce the smallest particles both in terms of d_m and d_p which can be attributed to the smaller amount of fuel resulting in a lower volume fraction of nascent soot (i.e. less nucleation) and allowing for a longer residence time in oxygen rich zones which oxidizes the soot reducing both the number and size of particles [62]. At the same time, the OC/TC increases at low thrust which could be attributed to the poor combustion efficiency at these conditions. At high thrust the residence time is short but initial number concentrations are higher due to high fuel flow. The time in oxidating zones is reduced also, resulting in a larger number concentration, d_p [35] and d_m [30]. Simulations of aircraft combustors have shown that soot forms intermittently in locally rich regions of the flame and, due to recirculation, soot spends 4 – 5 times longer in the combustor than the dominant fluid time scales [63]. The high-temperature residence time of soot in a combustor can only be estimated from simulations that account for the geometry, fluid flow rates, temperature and pressure in a given combustor.

Modeling soot emissions accurately remains a challenge [64] because soot formation in combustors is intermittent. So, simulations must take place over a large time frame to achieve a statistically representative time-averaged result [65]. Furthermore, the transport and chemistry of soot must be solved simultaneously in order to capture the real volume fraction, f_v, and particle size distributions (PSD) [41]. The most detailed simulations to date have utilized laboratory combustors such as the Cambridge Rich Quench Lean (RQL) burner [41, Fig. 2]. These laboratory burners are optically accessible for laser diagnostics allowing for a detailed comparison to the evolution of soot f_v and PSD. However, the laboratory burners use ethylene, a gas, instead of liquid jet fuel and pressures are up to 5 bar [64]. Modern aircraft engines may have pressures up to an order of magnitude higher than this at certain conditions [66]. Nonetheless, such simulations can give insight into the formation and growth of soot in aircraft combustors capturing some of the trends observed experimentally. Specifically, simulations show that soot forms near the shear layers between the fuel and oxidizer streams and then enters an inner recirculation zone where it grows further [41]. Fuel rich pockets can also break off from the main jet and become entrained in the recirculation zone driving the intermittent soot growth within the combustor [64]. Soot was shown to grow by both acetylene-based surface growth (e.g., HACA) and condensation via aromatics [41]. Simultaneously, significant oxidation reduces the particle size and can induce fragmentation increasing the number concentration [41] which is supported by experimental data [59]. Introduction of dilution air part way through the burner oxidizes soot in the lean combustion zone as well as lowers the rate of soot formation near the nozzle [64]. Higher pressures in the model combustor result in larger

soot f_v, a trend which was captured by simulations but the total f_v for the high pressure condition was underpredicted by a factor of 4 [64]. Therefore, simulations can give insight into the formation of soot in aircraft combustors but significant improvements are needed to have truly predictive models which can aid in combustor design [65]. It is worth noting that these simulations focus on capturing the number and mass emissions from combustors, but do not seem to account for the realistic morphology of soot particles which are highly irregular agglomerates rather than spheres. The assumption that soot is spherical rather than an agglomerate with polydisperse primary particles can significantly change the resulting estimate of soot d_m, number and, most importantly, f_v [67].

1.3 Means for the elimination of aircraft soot

1.3.1 Sustainable aviation fuels

Alternative aviation fuels include any fuels aside from kerosene-based jet fuels and Avgas. This includes, for example, hydrogen, ammonia and jet fuels made without fossil fuels. Sustainable Aviation fuels (SAF) are non-fossil jet fuels that are attractive due to their potential to act as a drop-in solution for reducing CO_2 emissions as these fuels can be used directly in existing engines. The ICAO specifies fuels must be "completely interchangeable and compatible with conventional jet fuel" in order to prevent the safety risks of mishandling and high costs of additional infrastructure [68]. Alternative jet fuels can be considered 'drop-in' when they do not require new fuel systems, distribution networks or new aircraft [68]. Sustainable Aviation Fuels (SAF) are produced mainly from biological feedstocks (e.g. soybeans, sugarcane, biomass, etc.) [69]. These are converted into liquid hydrocarbon fuels through processes such as Hydroprocessed Esters and Fatty Acids (HEFA), Fischer-Tropsch (F-T) or Alcohol-to-Jet (ATJ) to name a few [70]. Similarly, e-fuels use CO_2 capture and sustainable energy sources such as solar to produce synthetic jet fuels [71]. Currently, SAF are only certified for use when blended with conventional jet fuel although efforts are being made to certify 100% SAF in the future. Flights powered with 100% SAF have already been performed for research purposes [72]. The CO_2 reduction from such fuels comes primarily from the synthetic or biological CO_2 captured during the production process. Actual CO_2 released from the engine remains about the same as conventional jet fuel. So, a Life Cycle Analysis (LCA) is needed to account for the so-called Well-to-Wake emissions [73]. The total reduction in Green House Gas (GHG) emissions will depend on both the GHG emissions associated with production of the petroleum based jet fuel as well as the net GHG emissions from growing, transporting and burning the SAF fuels. The ICAO, under the Carbon Offsetting and Reduction Scheme for International Aviation (CORSIA), certifies alternative fuels as SAF based on a standardized LCA. While the exact

reduction in GHGs will change as technologies evolve, an LCA of the best case scenarios show up to a 68% reduction in CO_2 emissions if SAFs account for > 85% of all aviation fuels [69].

In addition to reducing net-CO_2 emissions, SAFs also have the potential to reduce soot emissions and thus the health impact and non-CO_2 radiative forcing of aircraft emissions which is typically excluded from LCA analysis [69]. These fuels tend to have a lower aromatic content than fossil fuels which has been correlated to the number of particles emitted by an aircraft [47]. As discussed previously, aromatic species are key precursors to soot formation and thus a decrease in fuel aromatics may reduce the rate of soot nucleation. The hydrogen-to-carbon ratio (H/C) of the fuel has been shown to have an even greater anti-correlation with aircraft soot emissions than fuel aromatic content [47]. While H/C has long been associated with the sooting tendency of a fuel [46], the mechanism for this is less clear as it is difficult to separate from effects such as lower flame temperatures [74]. Blends of a HEFA-based SAF with Jet A1 up to 50% (the current upper limit for a SAF blend) showed a ~35% reduction in number based nvPM and ~60% reduction in mass based nvPM [75]. These reductions correlated best with the H/C content of the blends. The size distributions of the soot produced shifted to smaller mobility diameters from d_m = 49 to 22.5 nm and narrowed the distribution from a geometric standard deviation, σ_g = 1.99 to 1.58 with pure Jet A1 and a 50% blend, respectively [75]. With pure Jet A1, the σ_g approaches that of the self-preserving limit for agglomerates coagulating in the free-molecular regime [57] while the σ_g produced with the SAF blends are significantly smaller. This could be due to the decreased number concentration from extended surface growth and less agglomeration. Currently, alternative fuels are designed primarily with the goals of reducing life-cycle CO_2 emissions and matching the properties of conventional jet fuels. However, there is an opportunity to also optimize jet fuel composition for minimum soot emissions. Schripp et al. showed that different SAF could be blended to obtain a desired H/C, while maintaining regulatory specifications for jet fuels [76]. Soot emissions of these fuels were first tested in a laboratory flame, then the optimal mixture was used in a real jet engine to confirm the trends seen in the laboratory resulting in emission reductions of particle mass and number by 29 and 37%, respectively, when using a 38% SAF blend with Jet A1 [76]. Laboratory tests are essential for speeding up the design of alternative fuels since real jet engines are inaccessible to many researchers and too costly to operate for initial screening tests. A standardized flame for assessing the sooting properties of jet fuels would assist in the development of alternative fuels however, there is currently no standardized method for such experiments. Enclosed spray combustion is a promising unit for such in lab approaches [21].

Several publications have shown that the benefits of a SAF blend are thrust-dependent. For example, a 32% blend of HEFA-synthetic paraffinic kerosene and Jet A1 at idle operation showed a 60 and 70% reduction in number- and mass-based nvPM, respectively [29]. The same blend at 65% thrust resulted in only a 12% reduction in number-based nvPM and at take-off the reduction was only 7%. In this case, the use of such SAF blends may improve local air quality by reducing emissions in the vicinity of airports but may not make a significant impact on cruise conditions which are most concerning for climate change. It is worth noting that the majority of studies on aircraft soot emissions are done at ground level which has significantly different atmospheric conditions than cruise in the upper atmosphere. Ideally, cruise emissions should be measured behind an aircraft in-flight, but this is rarely done due to the cost and logistical challenges. One of the few in-flight studies comparing conventional jet fuel to a 50% HEFA blend showed a 50 and 70% reduction in particle number and mass emissions, respectively, behind an aircraft with a medium thrust setting of ~ 50% [77]. At the high thrust setting, the particle number reduction was only 25% [77], supporting the trend observed on the ground. The wide range of values listed here highlights the need for more studies both at the ground level and in-flight.

Currently, SAF must be blended with conventional jet fuel (up to 50%) for safety reasons although 100% blends may be allowed by 2030. In practice, supply issues keep the use of SAF low accounting for an estimated 0.1 – 0.15% of global jet fuel use in 2022 despite a tripling in the supply of SAF from 2021 to 2022. If the SAF supply is limited and individual flights only have a very small fraction of SAF in the fuel, there will likely be no effect on the soot emissions [75]. So, while alternative fuels could provide a short-term solution to reducing aircraft emissions, the speed at which this is adopted is still limited. Targeted use of the limited SAF supply could be used in the short term to maximize the benefits of such fuels while supply is limited. For example, contrails with the greatest warming effect are commonly at dusk during the winter [78] so fueling flights at such times with high SAF blends could have the biggest benefit. One analysis found that compared to a 1% SAF blend for all transatlantic flights, fueling the 2% of flights producing the highest RF with a 50% SAF blend could take the total RF reduction from 0.6% up to 6% [79]. The European Commission and the US have implemented policies to mandate the uptake of SAF which may prohibit the targeted use of SAF. For example, starting in 2025 it will be required that “all aviation fuel supplied to aircraft operators at (European) Union airports contains a minimum share of SAF” [80]. Thus, while the supply of SAF is limited, it will be used in more aircraft at lower blending ratios missing an

opportunity to reduce soot emissions. Intelligent changes to policy on the use of alternative fuels could thus reduce the net-RF of aviation without needing to increase the supply of SAF.

1.3.2 Aircraft Combustor Design & Operation

The limitations of alternative jet fuels highlight the continued need for improved and novel engine technologies which could be used also with alternative fuels to minimize the total impact of aviation on the environment. Here, only combustion engines will be considered as electric aircrafts are estimated to account for only a quarter of all passenger-miles in 2050 [81]. Since nvPM regulations only recently came into effect, most aircraft combustors are designed primarily to lower NO_x, but some designs can also reduce soot. Alternative fuels have not been shown to reduce NO_x emissions compared to conventional jet fuel [77]. Combustor designs must balance limits for all regulated gas and particulate emissions, fuel efficiency, safety and cost. Rich Quench Lean (RQL) combustors have been used by the aviation industry since at least the 1980s to reduce NO_x emissions while maintaining sufficient combustion stability [82]. Today, they are the most common type of combustor listed in the ICAO emissions database [83]. Briefly, RQL combustors have three zones, depicted in Figure 1.3. First, there is a fuel-rich zone that allows for more stable combustion which is important for the safety of the aircraft. Rich conditions have lower combustion efficiency and promote the formation of soot, UHCs, and CO. In the quenching zone, a large volume of cool air is injected to provide oxygen for completing the conversion of UHCs and CO to CO_2 while lowering the temperature to minimize NO_x formation. The air flow for the rich combustion stage and quenching zone are controlled separately and further dilution air may be added before the gases are sent to the turbine. Although the mixing and residence times in RQL combustors were originally optimized for reducing NO_x [84] proper design and operation can also reduce soot emissions through oxidation during the lean burn stage. In fact, it was shown that a judicious injection of fresh oxygen in a manner similar to RQL combustors can promote oxidation of soot removing up to 99.6% of the initial soot volume fraction from jet fuel combustion [85]. When quenching air is introduced farther downstream in the combustor, soot has more time to form and grow. Hence, oxidation is less effective. Earlier injection of air with sufficient turbulent mixing has the opposite effect, minimizing soot emissions [86]. However, if quenching air is injected too early this could increase NO_x emissions or reduce combustion stability.

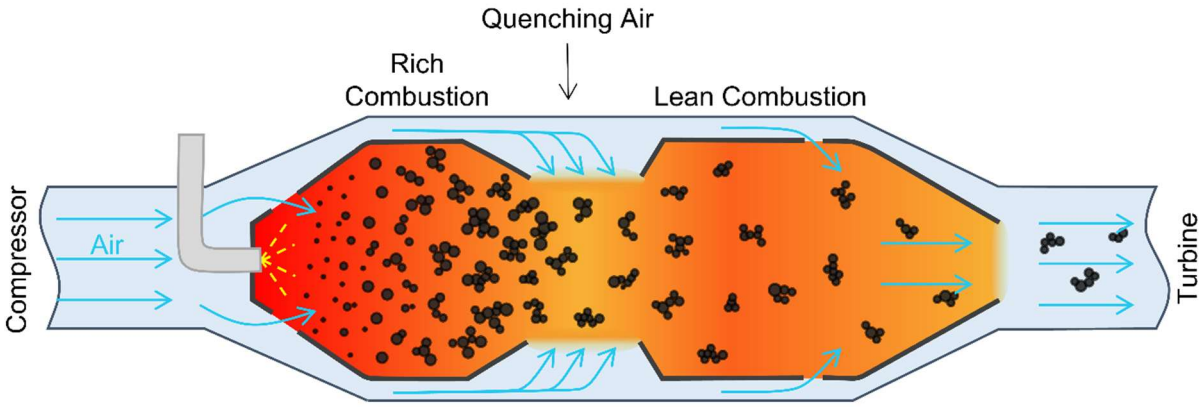

Figure 1.3: A simplified schematic of a Rich Lean Quench (RQL) aircraft combustor adapted from [84] where there is first a fuel rich combustion zone, followed by a large flow of quenching air to lower the temperature and dilute to a globally lean combustion zone. The dynamics of soot are qualitatively depicted from inception to surface growth, agglomeration and oxidation.

In 1995, the first Double Annular Combustor (DAC) was used commercially. This combustor design has two stages as the name implies, depicted in Figure 1.4. At low thrust (e.g., idle) only the pilot stage is used with a low air to fuel ratio and low flowrate to ensure good ignition and to reduce CO and UHC emissions. When sufficiently high thrust is achieved, both the pilot and main stage are ignited with a high air to fuel ratio (lean burn) and high flowrates [87]. This had the desired effect of reducing the NO_x emissions over the LTO cycle by ~30% compared to a single annular combustor on the same engine [88]. Soot emissions from a DAC equipped engine vary significantly with thrust. At low thrust, when only the pilot stage is ignited, soot emissions are high, and increase with increasing thrust in both number and mobility diameter [87]. When both stages are ignited at thrust ~25%, the soot concentration and size drop significantly [87]. Similarly, a DAC using only the pilot stage showed an increased mass concentration of organic particulate matter compared to when both stages were used [26].

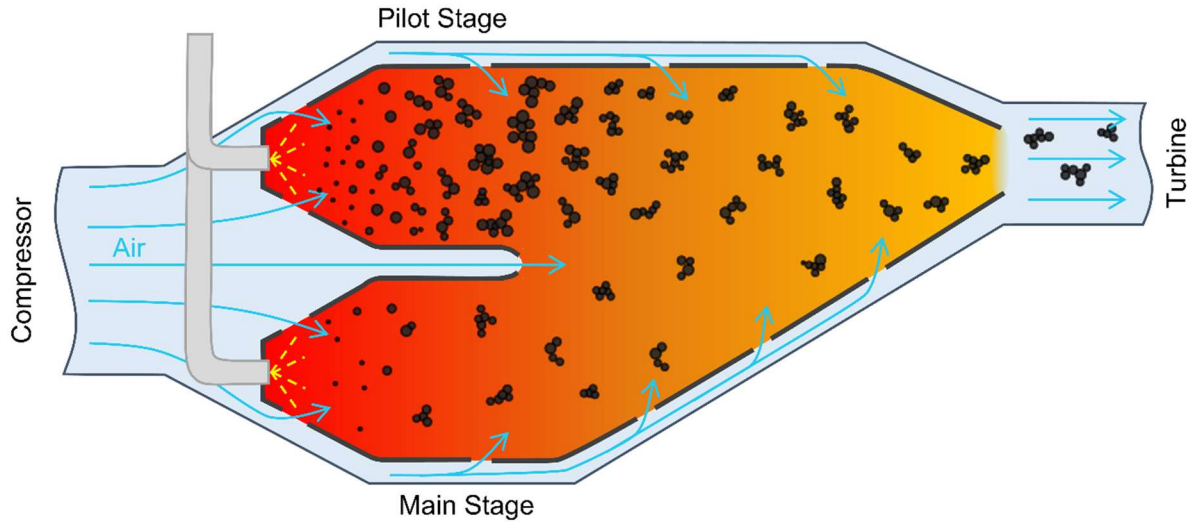

Figure 1.4: Simplified schematic of a Double Annular Combustor (DAC) adapted from [43] and a qualitative depiction of the dynamics of soot surface growth, agglomeration and oxidation within the combustor.

The morphology of soot produced in both stages is in the range observed in other combustors.

As demonstrated by the low emissions of DAC when operated in the lean combustion mode, lean burn engines have the potential for extremely low emissions if the combustion stability issues can be overcome. In fact, lean combustion technologies typically produce an order of magnitude less soot than an RQL combustor [89]. Lean burn combustors were first developed for stationary gas turbines used for energy generation where safety requirements are less strict and are now being transferred to aviation as technology improves. Such technologies include Lean Direct Injection (LDI) or the Multipoint Lean Direct Injection concept (MLDI) [89]. Direct injection is used to reduce the risk of autoignition that comes with premixed combustion. The use of multiple injectors, depicted in Figure 1.5, along with intense mixing creates conditions similar to lean, premixed combustion. In an LDI combustor a central pilot injector is surrounded by multiple main fuel injectors with little to no dilution added after the initial air supply near the fuel injectors. The MLDI concept is similar to the LDI combustor with an altered injector layout. Globally lean combustion with good mixing is unfavorable for soot production as there are few locally fuel-rich areas. At the same time, low temperatures from the lean burn reduce NO_x emissions significantly [89]. Regulatory measurements of nvPM emissions from an LDI combustor show nvPM mass and number emission levels on par with RQL combustors with similar rated thrusts [83]. To the best of our knowledge, no studies have characterized the size, morphology or chemical composition of soot from an LDI equipped engine. The limited data for such combustors makes the real emissions performance of such an engine difficult to assess.

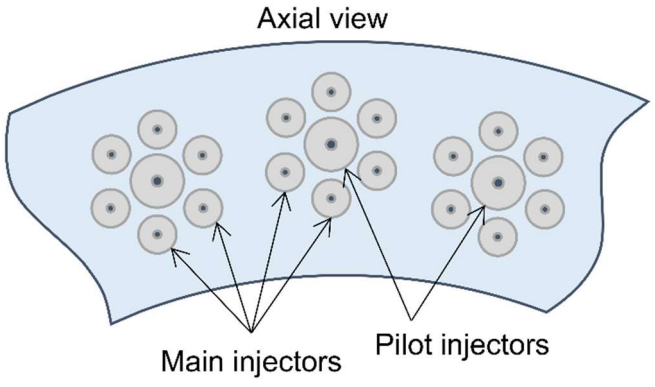

Figure 1.5: A simplified schematic of a Lean Direct Injection (LDI) combustor adapted from [90] which features a central pilot injector surrounded by multiple main injectors. These combustors usually have most or all the air flow into the combustor around the fuel injectors without subsequent dilution to provide intense mixing for lean combustion with close to premixed combustion.

Lean Premixed Prevaporized (LPP) combustors aim to completely vaporize the jet fuel prior to ignition in order to have lean, premixed combustion (Figure 1.6). Without locally fuel-rich conditions, little to no soot will form. As with the LDI combustors, there is little dilution

after the initial injection of primary air for combustion. Premixed combustion with high pressures comes with a risk of autoignition in the mixing zone so careful design of the combustor is needed to prevent such instabilities. These combustors use special fuel injectors to achieve near-premixed lean combustion conditions which tend to form significantly less soot. Both the LDI and LPP combustor designs achieve stable combustion through complex combustor design which could lead to increased cost and maintenance. So, lean conditions are favorable for emissions reduction but come with engineering challenges. Theoretically, new jet fuels with lower lean blow-off (LBO) limits could extend the lean operating range of an engine and conversely, fuels with an insufficient LBO could pose a safety risk [91].

Recently, a novel research engine called the Lean Azimuthal Flame (LEAF) combustor (not yet in commercial use) using "flameless oxidation" has been developed for soot-free and low NO_x combustion [92]. This concept can be further improved through co-combustion of small amounts of hydrogen which extends the operating window [93]. The use of hydrogen helps to stabilize the combustion without the use of a fuel-rich pilot flame that can increase soot production as with the DAC combustors. Such concepts which require an additional fuel that cannot be used in all engines require significantly more capital to implement because additional infrastructure needs to be built to support, for example, hydrogen storage and fueling. Furthermore, such parallel infrastructure poses a safety risk if an aircraft is filled with the wrong fuel and therefore such solutions are not promoted by the [68]. So, combustors which achieve lean, premixed conditions are promising for achieving both low soot and low NO_x emissions but pose design challenges.

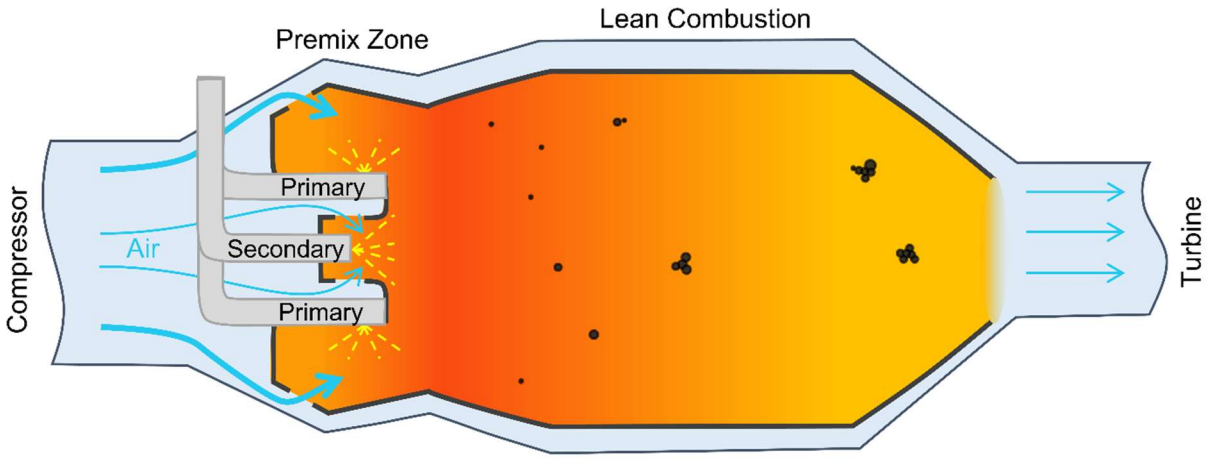

Figure 1.6: A simplified schematic of a Lean Premixed Prevaporized (LPP) combustor adapted from [43] which contains multiple injectors that spray fuel into the premix zone where the jet fuel completely vaporizes without ignition. Then, in the combustion zone the premixed fuel is ignited under fuel-lean conditions which nearly eliminate soot while low temperatures prevent the formation of NO_x.

The ICAO provides a public database of regulated emissions with the earliest nvPM emission test dates starting in 2014 [83]. These data are collected and reported by the engine manufacturers following the standards laid out in the ICAO Annex 16 for engine emissions certification [5]. Emissions are tested across the entire LTO cycle which includes idle/taxi (7% thrust), approach (30%), climb-out (80%) and take-off (100%) for both nvPM mass and number. Figure 1.7 shows the nvPM number emissions normalized by the fuel flow (#/kg) at (a) idle/taxi and (b) take-off for simplicity, although approach and climb-out data are also available [83]. Mass nvPM data shows similar trends. Values for approach and climb-out tend to fall between those measured at the extremes for both number and mass nvPM. Combustor names are provided for all entries in the database and can be grouped by type if sufficient information is given by the manufacturer. The RQL combustors make up the majority of reported data (134 entries), followed by SAC (38), LPP (26), LDI (7) and DAC (2). The SAC (squares) have some of the highest emissions in the database, but a group of SAC are approximately an order of magnitude lower at idle/taxi (Fig. 1.7a). These lower emission SAC are modified for better performance (CFM Tech Insertion) which seems to improve emissions at low (7 and 30%) thrust with little change at high (80 and 100%) thrust. The data for RQL combustors (circles) have the most variation quite likely due to the fact that there are significantly more entries for RQL combustors compared to all other combustor types. This highlights the fact that RQL burners can have quite low particulate emissions if designed and operated properly, particularly for engines with lower static rated thrust. At take-off (Fig. 1.7b), the LPP combustors (triangles) clearly outperform all other combustors in the database. At idle/taxi (Fig. 1.7a) LPP combustors still perform well but some RQL and modified-SAC combustors have similar or lower emissions. In an LPP combustor, all injectors are on during high thrust operation and premixed combustion can be achieved resulting in lower emissions.

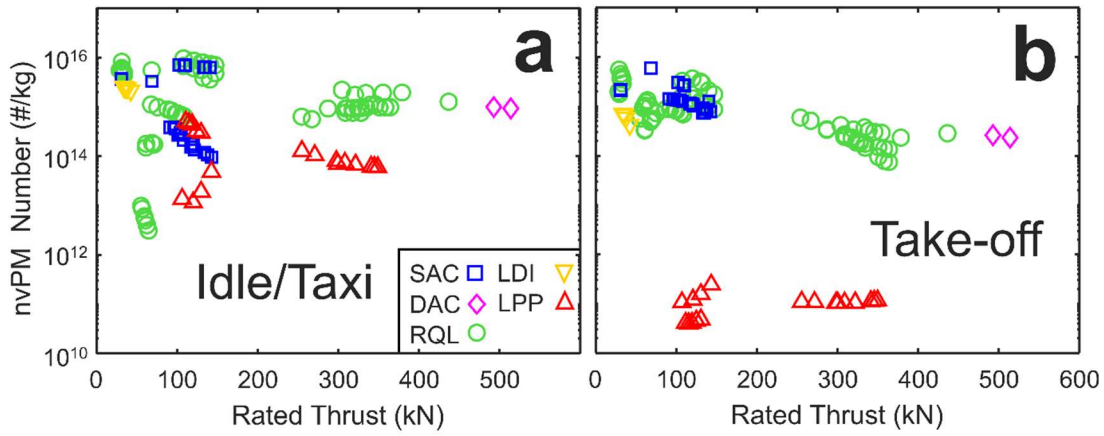

Figure 1.7: The nvPM number as a function of an engine's rated thrust at (a) idle/taxi (7% thrust), (b) take-off (100%). Combustor types represented in the database include SAC (squares), DAC (diamonds), RQL (circles), LDI (inverted triangles), LPP (triangles). The total nvPM number is normalized by the fuel flow (kg).

Conversely, at low thrust only some of the injectors are used to lower the power output without creating conditions which are too lean for stable combustion which may explain the higher emissions at idle/taxi compared to take-off. A similar phenomenon has been observed in scientific studies of DAC engines where emissions were reduced significantly when both combustor stages were in use at approximately thrusts > 30% [87]. The small number of entries for DAC and LDI combustors makes it difficult to draw conclusions about such combustors but the data that are provided for both fall in approximately the middle of the nvPM emission range. So, at present LPP combustors seem to perform at least as well as other combustors at idle/taxi and significantly reduce emissions at take-off resulting in the lowest overall emissions in the ICAO database. It is worth noting that engine operation can also reduce emissions, for example reduced thrust take-off has been shown to reduce fuel consumption, NO_x and black carbon (soot) emissions by 1.0 – 23.2%, 10.7 – 47.7%, and 49.0 – 71.7% respectively [94].

While the ICAO database provides information on the mass and number of nvPM emissions, it does not include any morphological or chemical characterization of the particles. Furthermore, the data are collected by the engine manufacturers, rather than independent researchers. Thus far, the vast majority of academic studies on soot emissions from aircraft engines have been conducted on large commercial aircraft (rated thrust >26.7 kN) most with SAC combustors [29,32,35,37,95–97]. A few studies have explored soot from DAC [25,87,96] and RQL [47,98,99] engines. The limited number of studies characterizing soot emissions from ‘low emission’ engine technology highlights the need for more research on such engines if they will be adopted in the future. Commercial deployment of new engine technologies takes a significant amount of time and money and so, when a new technology is deployed it remains in use for many years with the life span of an average aircraft spanning from 20 – 30 years [100]. This makes it essential to identify which technologies offer the best emissions profile before it is commercially scaled up, for example through the use of computational fluid dynamics (CFD).

1.4 Conclusions

Soot from aviation has a negative effect on human health and can contribute to climate change through direct radiative forcing and increasing the formation of persistent contrails. New regulations have been put into place to limit soot emissions in addition to other pollutants such as NO_x, UHC and CO. The strategies for reducing one type of pollutant may increase another with soot and NO_x emissions often at odds with one another. Non-CO_2 aircraft emissions are estimated to be two thirds of aviation’s net-RF, but the uncertainties associated with the non-

CO_2 terms are very high. The difficulty in reducing soot emissions from aviation comes primarily from the competing requirements which include safety, reduction of gaseous pollutants and cost. A better understanding of the role of soot and other non-CO_2 emissions is needed to properly assess trade-offs between design requirements and avoid improving emissions of one pollutant while increasing another's or compromising safety.

Aircrafts tend to produce soot with relatively small d_m which has greater health impacts than larger soot particles. Soot nucleates in locally fuel-rich zones (created by the jet fuel spray) then grows through surface growth, condensation and agglomeration. The OC/TC ratio of aircraft soot depends on thrust. Low thrust is associated with high OC/TC and high with low OC/TC. Extensive oxidation reduces the number concentration and size of soot resulting in smaller particles than other combustion sources (e.g. diesel). Significant progress is still needed to accurately quantify this process in realistic aircraft combustors. Some progress has been made in recent years matching experimental data from laboratory combustors but there are important differences between laboratory combustors and real aircraft combustors and simulations are not yet able to match the output of these simplified combustors at all conditions. The high cost and 20 – 30 year lifespan of aircraft necessitates robust models to aid in combustor design and operation for further technological advancements.

Sustainable Aviation Fuels (SAF) have the potential to significantly reduce soot emissions due to the lower aromatic and H/C content typically associated with these fuels in addition to reductions in lifetime CO_2 emissions. Although most literature on the use of such fuels does show that it reduces soot emissions, the reduction appears to be thrust dependent. So, it has the greatest effect on reducing low-thrust emissions which are important for local air quality (e.g., idle) although modest reductions have also been observed at high altitude cruising conditions. Several SAFs are approved for commercial use but lack of sufficient supply makes it a tiny proportion of the global jet fuel supply (0.1-0.15% in 2022). If SAFs are blended at small proportions with conventional jet fuel, the soot reduction benefits might be hardly seen. Targeted use of high SAF blends on certain flights rather than low SAF blends for all flights could be the best use of a limited resource. Supply issues likely will not be overcome soon, so policies mandating the use of SAF fuels should be designed in a way that encourages the use of a targeted approach that will also lower soot emissions, not just life cycle CO_2.

Soot is primarily produced during fuel-rich combustion. So, throughout the years efforts have been made to move toward fuel-lean combustion processes. The RQL combustors use a lean quenching stage after an initial rich burn to ensure good combustion stability while still reducing NO_x and in some cases soot. The design of the quenching stage is essential for

balancing combustion efficiency, NO_x, and soot emissions from such engines. The DAC combustors similarly take advantage of a pilot stage with low air to fuel ratios for combustion stability at low thrust and a second main stage combustor which can be used at medium to high thrust for lean combustion with a high air to fuel ratio. When both stages are in use, DAC combustors have very low soot emissions but when only the pilot stage is used, soot emissions can be higher than in a traditional burner particularly at medium-low thrust (e.g., ~20%). More recently, advances have been made on truly lean engine technologies. This can be achieved either by using multiple injectors and high mixing rates to achieve nearly premixed combustion or through mixing zones which allow for full evaporation of fuel before ignition. These lean burn engines promise the lowest emissions of soot and NO_x due to the lower temperatures and lack of fuel-rich zones. High complexity in such burners may result in higher maintenance costs. Finally, hydrogen can be used to help stabilize lean combustion such as in the LEAF combustor which is both soot-free and low NO_x but is still under development in academic laboratories. However, the ICAO is discouraging such solutions which require fuels that are not "drop-in" (e.g. hydrogen), as incompatibilities between engines and fuels could pose safety risks and require significant capital investment in infrastructure.

The combined use of fuels with low sooting propensity and operating at lean combustion conditions have the potential to reduce or even eliminate soot emissions from aircraft engines. However, caution should be used whenever there is a trade-off with other emissions (i.e. NO_x) as there is still significant uncertainty in the contribution of soot to direct RF and its role in contrail formation. The development of computational models which can accurately predict soot production from various combustor designs and modes of operation will be essential for minimizing soot emissions from aircraft while balancing other considerations. This will rely on further fundamental research to better understand soot nucleation rates to close the soot mass balance and match field data.

1.5 References

[1] Bond TC, Doherty SJ, Fahey DW, Forster PM, Berntsen T, DeAngelo BJ, Flanner MG, Ghan S, Kärcher B, Koch D, Kinne S, Kondo Y, Quinn PK, Sarofim MC, Schultz MG, Schulz M, Venkataraman C, Zhang H, Zhang S, Bellouin N, Guttikunda SK, Hopke PK, Jacobson MZ, Kaiser JW, Klimont Z, Lohmann U, Schwarz JP, Shindell D, Storelvmo T, Warren SG, Zender CS. Bounding the role of black carbon in the climate system: A scientific assessment. *J Geophys Res Atmos* (2013) **118**, 5380–552.

[2] Niranjan R, Thakur AK. The toxicological mechanisms of environmental soot (black carbon) and carbon black: Focus on oxidative stress and inflammatory pathways. *Front Immunol* (2017) **8**, 763.

[3] George RE, Nevitt JS, Verssen JA. Jet aircraft operations: Impact on the air

environment. *J Air Pollut Control Assoc* (1972) **22**, 507–15.

[4] Durdina L, Brem BT, Setyan A, Siegerist F, Rindlisbacher T, Wang J. Assessment of particle pollution from jetliners: From smoke visibility to nanoparticle counting. *Environ Sci Technol* (2017) **51**, 3534–41.

[5] ICAO. Annex 16 to the convention on international civil aviation: environmental protection, Vol. II - aircraft engine emissions. Montreal, CA: (2017).

[6] Kärcher B. Formation and radiative forcing of contrail cirrus. *Nat Commun* (2018) **9**, 1824.

[7] Lee DS, Fahey DW, Skowron A, Allen MR, Burkhardt U, Chen Q, Doherty SJ, Freeman S, Forster PM, Fuglestvedt J, Gettelman A, De León RR, Lim LL, Lund MT, Millar RJ, Owen B, Penner JE, Pitari G, Prather MJ, Sausen R, Wilcox LJ. The contribution of global aviation to anthropogenic climate forcing for 2000 to 2018. *Atmos Environ* (2021) **244**, 117834.

[8] Stuber N, Forster P, Rädel G, Shine K. The importance of the diurnal and annual cycle of air traffic for contrail radiative forcing. *Nature* (2006) **441**, 864–7.

[9] Agarwal A, Speth RL, Fritz TM, Jacob SD, Rindlisbacher T, Iovinelli R, Owen B, Miake-Lye RC, Sabnis JS, Barrett SRH. SCOPE11 Method for Estimating Aircraft Black Carbon Mass and Particle Number Emissions. *Environ Sci Technol* (2019) **53**, 1364–73.

[10] Stettler MEJ, Boies AM, Petzold A, Barrett SRH. Global civil aviation black carbon emissions. *Environ Sci Technol* (2013) **47**, 10397–404.

[11] Masiol M, Harrison RM. Aircraft engine exhaust emissions and other airport-related contributions to ambient air pollution: A review. *Atmos Environ* (2014) **95**, 409–55.

[12] Kelesidis GA, Neubauer D, Fan LS, Lohmann U, Pratsinis SE. Enhanced light absorption and radiative forcing by black carbon agglomerates. *Environ Sci Technol* (2022) **56**, 8610–8.

[13] Bock L, Burkhardt U. The temporal evolution of a long-lived contrail cirrus cluster: Simulations with a global climate model. *J Geophys Res* (2016) **121**, 3548–65.

[14] Montzka SA, Dlugokencky EJ, Butler JH. Non-CO_2 greenhouse gases and climate change. *Nature* (2011) **476**, 43–50.

[15] Marcolli C, Mahrt F, Kärcher B. Soot PCF: Pore condensation and freezing framework for soot aggregates. *Atmos Chem Phys* (2021) **21**, 7791–843.

[16] Kim D, Ekoto I, Colban WF, Miles PC. In-cylinder CO and UHC imaging in a light-duty diesel engine during PPCI low-temperature combustion. *SAE Int J Fuels Lubr* (2009) **1**, 933–56.

[17] Teoh R, Schumann U, Majumdar A, Stettler MEJ. Mitigating the climate forcing of aircraft contrails by small-scale diversions and technology adoption. *Environ Sci Technol* (2020) **54**, 2941–50.

[18] Kelesidis GA, Bruun CA, Pratsinis SE. The impact of organic carbon on soot light absorption. *Carbon* (2021) **172**, 742–9.

[19] Cavalli F, Viana M, Yttri KE, Genberg J, Putaud J-P. Toward a standardised thermal-optical protocol for measuring atmospheric organic and elemental carbon: the EUSAAR protocol. *Atmos Meas Tech* (2010) **3**, 79–89.

[20] Trivanovic U, Kelesidis GA, Pratsinis SE. High-throughput generation of aircraft-like

soot. *Aerosol Sci Technol* (2022) **56**, 732–43.

[21] Gao K, Zhou CW, Meier EJB, Kanji ZA. Laboratory studies of ice nucleation onto bare and internally mixed soot-sulfuric acid particles. *Atmos Chem Phys* (2022) **22**, 5331–64.

[22] Durdina L, Lobo P, Trueblood MB, Black EA, Achterberg S, Hagen DE, Brem BT, Wang J. Response of real-time black carbon mass instruments to mini-CAST soot. *Aerosol Sci Technol* (2016) **50**, 906–18.

[23] Schäfer AW, Barrett SRH, Doyme K, Dray LM, Gnadt AR, Self R, O'Sullivan A, Synodinos AP, Torija AJ. Technological, economic and environmental prospects of all-electric aircraft. *Nat Energy* (2019) **4**, 160–6.

[24] Agnolucci P, Akgul O, McDowall W, Papageorgiou LG. The importance of economies of scale, transport costs and demand patterns in optimising hydrogen fuelling infrastructure: An exploration with SHIPMod (Spatial hydrogen infrastructure planning model). *Int J Hydrogen Energy* (2013) **38**, 11189–201.

[25] Lobo P, Durdina L, Smallwood GJ, Rindlisbacher T, Siegerist F, Black EA, Yu Z, Mensah AA, Hagen DE, Miake-Lye RC, Thomson KA, Brem BT, Corbin JC, Abegglen M, Sierau B, Whitefield PD, Wang J. Measurement of aircraft engine non-volatile PM emissions: Results of the Aviation-Particle Regulatory Instrumentation Demonstration Experiment (A-PRIDE) 4 campaign. *Aerosol Sci Technol* (2015) **49**, 472–84.

[26] Durdina L, Brem BT, Schönenberger D, Siegerist F, Anet JG, Rindlisbacher T. Nonvolatile Particulate Matter Emissions of a Business Jet Measured at Ground Level and Estimated for Cruising Altitudes. *Environ Sci Technol* (2019) **53**, 12865–72.

[27] National Academies of Sciences Engineering and Medicine. Options for Reducing Lead Emissions from Piston-Engine Aircraft. (2021).

[28] Durdina L, Brem BT, Elser M, Sch D, Siegerist F, Anet JG. Reduction of Nonvolatile Particulate Matter Emissions of a Commercial Turbofan Engine at the Ground Level from the Use of a Sustainable Aviation Fuel Blend. *Environ Sci Technol* (2021) **55**, 14576–85.

[29] Abegglen M, Durdina L, Brem BT, Wang J, Rindlisbacher T. Effective density and mass – mobility exponents of particulate matter in aircraft turbine exhaust : Dependence on engine thrust and particle size. *J Aerosol Sci* (2015) **88**, 135–47.

[30] Rissler J, Swietlicki E, Bengtsson A, Boman C, Pagels J, Sandström T, Blomberg A, Löndahl J. Experimental determination of deposition of diesel exhaust particles in the human respiratory tract. *J Aerosol Sci* (2012) **48**, 18–33.

[31] Cassee FR, Héroux ME, Gerlofs-Nijland ME, Kelly FJ. Particulate matter beyond mass: Recent health evidence on the role of fractions, chemical constituents and sources of emission. *Inhal Toxicol* (2013) **25**, 802–12.

[32] Marhaba I, Ferry D, Laffon C, Regier TZ, Ouf F, Parent P. Aircraft and MiniCAST soot at the nanoscale. *Combust Flame* (2019) **204**, 278–89.

[33] Timko MT, Albo SE, Onasch TB, Fortner EC, Yu Z, Miake-Lye RC, Canagaratna MR, Ng NL, Worsnop DR. Composition and sources of the organic particle emissions from aircraft engines. *Aerosol Sci Technol* (2014) **48**, 61–73.

[34] Liati A, Schreiber D, Alpert PA, Liao Y, Brem BT, Corral Arroyo P, Hu J, Jonsdottir HR, Ammann M, Dimopoulos Eggenschwiler P. Aircraft soot from conventional fuels

and biofuels during ground idle and climb-out conditions: Electron microscopy and X-ray micro-spectroscopy. *Environ Pollut* (2019) **247**, 658–67.

[35] Liati A, Brem BT, Durdina L, Vögtli M, Dasilva YAR, Eggenschwiler PD, Wang J. Electron microscopic study of soot particulate matter emissions from aircraft turbine engines. *Environ Sci Technol* (2014) **48**, 10975–83.

[36] Messerer A, Niessner R, Pöschl U. Comprehensive kinetic characterization of the oxidation and gasification of model and real diesel soot by nitrogen oxides and oxygen under engine exhaust conditions: Measurement, Langmuir-Hinshelwood, and Arrhenius parameters. *Carbon* (2006) **44**, 307–24.

[37] Kelesidis GA, Kholghy MR, Zuercher J, Robertz J, Allemann M, Duric A, Pratsinis SE. Light scattering from nanoparticle agglomerates. *Powder Technol* (2020) **365**, 52–9.

[38] Baldelli A, Trivanovic U, Sipkens TA, Rogak SN. On determining soot maturity: A review of the role of microscopy- and spectroscopy-based techniques. *Chemosphere* (2020) **252**, 126532.

[39] Parent P, Laffon C, Marhaba I, Ferry D, Regier TZ, Ortega IK, Chazallon B, Carpentier Y, Focsa C. Nanoscale characterization of aircraft soot : A high-resolution transmission electron microscopy , Raman spectroscopy , X-ray photoelectron and near-edge X-ray absorption spectroscopy study. *Carbon* (2016) **101**, 86–100.

[40] Vander Wal RL, Bryg VM, Hays MD. Fingerprinting soot (towards source identification): Physical structure and chemical composition. *J Aerosol Sci* (2010) **41**, 108–17.

[41] Gkantonas S, Sirignano M, Giusti A, D'Anna A, Mastorakos E. Comprehensive soot particle size distribution modelling of a model Rich-Quench-Lean burner. *Fuel* (2020) **270**, 117483.

[42] Wang H. Formation of nascent soot and other condensed-phase materials in flames. *Proc Combust Inst* (2011) **33**, 41–67.

[43] Foust MJ, Thomsen D, Stickles R, Cooper C, Dodds W. Development of the GE aviation low emissions TAPS combustor for next generation aircraft engines. *50th AIAA Aerosp Sci Meet Incl New Horizons Forum Aerosp Expo* (2012), 1–9.

[44] Frenklach M. Reaction mechanism of soot formation in flames. *Phys Chem Chem Phys* (2002) **4**, 2028–37.

[45] Commodo M, Kaiser K, De Falco G, Minutolo P, Schulz F, D'Anna A, Gross L. On the early stages of soot formation: Molecular structure elucidation by high-resolution atomic force microscopy. *Combust Flame* (2019) **205**, 154–64.

[46] Yang Y, Boehman AL, Santoro RJ. A study of jet fuel sooting tendency using the threshold sooting index (TSI) model. *Combust Flame* (2007) **149**, 191–205.

[47] Brem BT, Durdina L, Siegerist F, Beyerle P, Bruderer K, Rindlisbacher T, Rocci-Denis S, Andac MG, Zelina J, Penanhoat O, Wang J. Effects of fuel aromatic content on nonvolatile particulate emissions of an in-production aircraft gas turbine. *Environ Sci Technol* (2015) **49**, 13149–57.

[48] Carbone F, Gleason K, Gomez A. Soot research: Relevance and priorities by mid-century. Combust. Chem. Carbon Neutral Futur., Elsevier Inc. (2023), p. 27–61.

[49] Sharma A, Mukut KM, Roy SP, Goudeli E. The coalescence of incipient soot clusters. *Carbon* (2021) **180**, 215–25.

[50] Kelesidis GA, Goudeli E, Pratsinis SE. Morphology and mobility diameter of carbonaceous aerosols during agglomeration and surface growth. *Carbon* (2017) **121**, 527–35.

[51] Camacho J, Liu C, Gu C, Lin H, Huang Z, Tang Q, You X, Saggese C, Li Y, Jung H, Deng L, Wlokas I, Wang H. Mobility size and mass of nascent soot particles in a benchmark premixed ethylene flame. *Combust Flame* (2015) **162**, 3810–22.

[52] Commodo M, D'Anna A, De Falco G, Larciprete R, Minutolo P. Illuminating the earliest stages of the soot formation by photoemission and Raman spectroscopy. *Combust Flame* (2017) **181**, 188–97.

[53] Kholghy M, Saffaripour M, Yip C, Thomson MJ. The evolution of soot morphology in a laminar coflow diffusion flame of a surrogate for Jet A-1. *Combust Flame* (2013) **160**, 2119–30.

[54] Schulz F, Commodo M, Kaiser K, De Falco G, Minutolo P, Meyer G, D'Anna A, Gross L. Insights into incipient soot formation by atomic force microscopy. *Proc Combust Inst* (2019) **37**, 885–92.

[55] Dobbins RA. Soot inception temperature and the carbonization rate of precursor particles. *Combust Flame* (2002) **130**, 204–14.

[56] Kelesidis GA, Goudeli E, Pratsinis SE. Flame synthesis of functional nanostructured materials and devices: Surface growth and aggregation. *Proc Combust Inst* (2017) **36**, 29–50.

[57] Goudeli E, Eggersdorfer ML, Pratsinis SE. Coagulation-agglomeration of fractal-like particles: Structure and self-preserving size distribution. *Langmuir* (2015) **31**, 1320–7.

[58] Trivanovic U, Pereira Martins M, Benz S, Kelesidis GA, Pratsinis SE. Dynamics of soot surface growth and agglomeration by enclosed spray combustion of jet fuel. *Fuel* (2023) **342**, 127864.

[59] Vander Wal RL, Bryg VM, Huang CH. Aircraft engine particulate matter: Macro-micro- and nanostructure by HRTEM and chemistry by XPS. *Combust Flame* (2014) **161**, 602–11.

[60] Kelesidis GA, Benz S, Pratsinis SE. Process design for carbon black size and morphology. *Carbon* (2023) **213**, 118255.

[61] Chu H, Qi J, Feng S, Dong W, Hong R, Qiu B, Han W. Soot formation in high-pressure combustion: Status and challenges. *Fuel* (2023) **345**, 128236.

[62] Durdina L, Brem BT, Abegglen M, Lobo P, Rindlisbacher T, Thomson KA, Smallwood GJ, Hagen DE, Sierau B, Wang J. Determination of PM mass emissions from an aircraft turbine engine using particle effective density. *Atmos Environ* (2014) **99**, 500–7.

[63] Chong ST, Raman V, Mueller ME, Im HG. The role of recirculation zones in soot formation in aircraft combustors. *Proc ASME Turbo Expo* (2018) **4B**, 1–9.

[64] Chong ST, Hassanaly M, Koo H, Mueller ME, Raman V, Geigle KP. Large eddy simulation of pressure and dilution-jet effects on soot formation in a model aircraft swirl combustor. *Combust Flame* (2018) **192**, 452–72.

[65] Franzelli B, Tardelli L, Stöhr M, Geigle KP, Domingo P. Assessment of LES of intermittent soot production in an aero-engine model combustor using high-speed measurements. *Proc Combust Inst* (2023) **39**, 4821–9.

[66] Nguyen TH, Tri Nguyen P, Garnier F. Evaluation of the relationship between the aerothermodynamic process and operational parameters in the high-pressure turbine of an aircraft engine. *Aerosp Sci Technol* (2019) **86**, 93–105.

[67] Kelesidis GA, Goudeli E. Self-preserving size distribution and collision frequency of flame-made nanoparticles in the transition regime. *Proc Combust Inst* (2021) **38**, 1233–40.

[68] ICAO. Sustainable Aviation Fuels Guide. (2018).

[69] Staples MD, Malina R, Suresh P, Hileman JI, Barrett SRH. Aviation CO_2 emissions reductions from the use of alternative jet fuels. *Energy Policy* (2018) **114**, 342–54.

[70] Brooks KP, Snowden-Swan LJ, Jones SB, Butcher MG, Lee GSJ, Anderson DM, Frye JG, Holladay JE, Owen J, Harmon L, Burton F, Palou-Rivera I, Plaza J, Handler R, Shonnard D. Low-carbon aviation fuel through the alcohol to jet pathway. *Biofuels Aviat. Feed. Technol. Implement., Elsevier Inc.* (2016), p. 109–50.

[71] Schäppi R, Rutz D, Dähler F, Muroyama A, Haueter P, Lilliestam J, Patt A, Furler P, Steinfeld A. Drop-in fuels from sunlight and air. *Nature* (2022) **601**, 63–8.

[72] Märkl RS, Voigt C, Sauer D, Dischl RK, Kaufmann S, Harlaß T, Hahn V, Roiger A, Weiß-rehm C, Burkhardt U, Schumann U, Marsing A, Scheibe M, Dörnbrack A, Renard C, Gauthier M, Swann P, Madden P, Luff D, Sallinen R, Schripp T, Clercq P Le. Powering aircraft with 100 % sustainable aviation fuel reduces ice crystals in contrails. *Atmos Chem Phys* (2023), egusphere-2023-2638. Preprint.

[73] Han J, Elgowainy A, Cai H, Wang MQ. Life-cycle analysis of bio-based aviation fuels. *Bioresour Technol* (2013) **150**, 447–56.

[74] Xue X, Hui X, Vannorsdall P, Singh P, Sung CJ. The blending effect on the sooting tendencies of alternative/conventional jet fuel blends in non-premixed flames. *Fuel* (2019) **237**, 648–57.

[75] Lobo P, Christie S, Khandelwal B, Blakey SG, Raper DW. Evaluation of non-volatile particulate matter emission characteristics of an aircraft auxiliary power unit with varying alternative jet fuel blend ratios. *Energy and Fuels* (2015) **29**, 7705–11.

[76] Schripp T, Grein T, Zinsmeister J, Oßwald P, Köhler M, Müller-Langer F, Hauschild S, Marquardt C, Scheuermann S, Zschocke A, Posselt D. Technical application of a ternary alternative jet fuel blend – Chemical characterization and impact on jet engine particle emission. *Fuel* (2021) **288**, 119606.

[77] Moore RH, Thornhill KL, Weinzierl B, Sauer D, D'Ascoli E, Kim J, Lichtenstern M, Scheibe M, Beaton B, Beyersdorf AJ, Barrick J, Bulzan D, Corr CA, Crosbie E, Jurkat T, Martin R, Riddick D, Shook M, Slover G, Voigt C, White R, Winstead E, Yasky R, Ziemba LD, Brown A, Schlager H, Anderson BE. Biofuel blending reduces particle emissions from aircraft engines at cruise conditions. *Nature* (2017) **543**, 411–5.

[78] Teoh R, Schumann U, Gryspeerdt E, Shapiro M, Molloy J, Koudis G, Voigt C, Stettler MEJ. Aviation contrail climate effects in the North Atlantic from 2016 to 2021. *Atmos Chem Phys* (2022) **22**, 10919–35.

[79] Teoh R, Schumann U, Voigt C, Schripp T, Shapiro M, Engberg Z, Molloy J, Koudis G, Stettler MEJ. Targeted use of sustainable aviation fuel to maximize climate benefits. *Environ Sci Technol* (2022) **56**, 17246–55.

[80] European Commission. Proposal for a Regulation of the European Parliment and of the council on ensuring a level playing field for sustainable air transport. (2021).

[81] Prabhakar N, Heyerdahl L, Jha A, Karbowski D. Energy impacts of electric aircraft: An overview. *AIAA Aviat 2022 Forum* (2022).

[82] Novic AS, Troth DLL, Notardonato J, Novick AS, Troth DLL, Notardonato J. Multifuel evaluation of Rich/Quench/Lean combustor. *Proc. ASME 1983 Int. Gas Turbine Conf. Exhib.*, (1983), p. 1–8.

[83] ICAO. ICAO Aircraft Engine Emissions Databank (2023). https://www.easa.europa.eu/en/domains/environment/icao-aircraft-engine-emissions-databank (accessed August 8, 2023).

[84] Rizk NK, Mongia HC. Ultra-low NOx rich-lean combustion. *Am Soc Mech Eng* (1990), 90-GT-87.

[85] Kelesidis GA, Nagarkar A, Trivanovic U, Pratsinis SE. Toward elimination of soot emissions from jet fuel combustion. *Environ Sci Technol* (2023) **57**, 10276–83.

[86] El Helou I, Skiba AW, Mastorakos E. Experimental investigation of soot production and oxidation in a lab-scale Rich–Quench–Lean (RQL) burner. *Flow, Turbul Combust* (2021) **106**, 1019–41.

[87] Boies AM, Stettler MEJ, Swanson JJ, Johnson TJ, Olfert JS, Johnson M, Eggersdorfer ML, Rindlisbacher T, Wang J, Thomson K, Smallwood G, Sevcenco Y, Walters D, Williams PI, Corbin J, Mensah AA, Symonds J, Dastanpour R, Rogak SN. Particle emission characteristics of a gas turbine with a double annular combustor. *Aerosol Sci Technol* (2015) **49**, 842–55.

[88] Mongia HC. GE aviation low emissions combustion technology evolution. *SAE Tech Pap* (2007), 776–90.

[89] Liu Y, Sun X, Sethi V, Nalianda D, Li YG, Wang L. Review of modern low emissions combustion technologies for aero gas turbine engines. *Prog Aerosp Sci* (2017) **94**, 12–45.

[90] Fric T. Low-emission combustor having perforated plate for lean direct injection, U.S. Patent number: 5 437 158, Publication Date: Aug. 01, 1995.

[91] Undavalli V, Gbadamosi Olatunde OB, Boylu R, Wei C, Haeker J, Hamilton J, Khandelwal B. Recent advancements in sustainable aviation fuels. *Prog Aerosp Sci* (2023) **136**, 100876.

[92] Oliveira PM De, Fredrich D, Falco G De, Helou I El, Anna AD, Giusti A, Mastorakos E. Soot-free low-NO_x aeronautical combustor concept: The lean azimuthal flame for kerosene sprays. *Energy and Fuels* (2021) **35**, 7092–106.

[93] Miniero L, Pandey K, De Falco G, D'Anna A, Noiray N. Soot-free and low-NO combustion of Jet A-1 in a lean azimuthal flame (LEAF) combustor with hydrogen injection. *Proc Combust Inst* (2023) **39**, 4309–18.

[94] Koudis GS, Hu SJ, Majumdar A, Jones R, Stettler MEJ. Airport emissions reductions from reduced thrust takeoff operations. *Transp Res Part D Transp Environ* (2017) **52**, 15–28.

[95] Beyersdorf AJ, Timko MT, Ziemba LD, Bulzan D, Corporan E, Herndon SC, Howard R, Miake-Lye R, Thornhill KL, Winstead E, Wey C, Yu Z, Anderson BE. Reductions in aircraft particulate emissions due to the use of Fischer-Tropsch fuels. *Atmos Chem Phys* (2014) **14**, 11–23.

[96] Johnson TJ, Olfert JS, Symonds JPR, Johnson M, Rindlisbacher T, Swanson JJ, Boies AM, Thomson K, Smallwood G, Walters D, Sevcenco Y, Crayford A, Dastanpour R,

Rogak SN, Durdina L, Bahk YK, Brem B, Wang J. Effective density and mass-mobility exponent of aircraft turbine particulate matter. *J Propuls Power* (2015) **31**, 573–80.

[97] Elser M, Brem BT, Durdina L, Schönenberger D, Siegerist F, Fischer A, Wang J. Chemical composition and radiative properties of nascent particulate matter emitted by an aircraft turbofan burning conventional and alternative fuels. *Atmos Chem Phys* (2019) **19**, 6809–20.

[98] Saffaripour M, Tay LL, Thomson KA, Smallwood GJ, Brem BT, Durdina L, Johnson M. Raman spectroscopy and TEM characterization of solid particulate matter emitted from soot generators and aircraft turbine engines. *Aerosol Sci Technol* (2017) **51**, 518–31.

[99] Delhaye D, Ouf FX, Ferry D, Ortega IK, Penanhoat O, Peillon S, Salm F, Vancassel X, Focsa C, Irimiea C, Harivel N, Perez B, Quinton E, Yon J, Gaffie D. The MERMOSE project: Characterization of particulate matter emissions of a commercial aircraft engine. *J Aerosol Sci* (2017) **105**, 48–63.

[100] Ceruti A, Marzocca P, Liverani A, Bil C. Maintenance in aeronautics in an Industry 4.0 context: The role of augmented reality and additive manufacturing. *J Comput Des Eng* (2019) **6**, 516–26.

Chapter 2

High-throughput generation of aircraft-like soot[2]

Abstract

High-throughput, laboratory units for generation of aircraft-like soot are needed to quantify and understand the impact of such emissions on public health and climate change due to the high costs and limited access to aircraft engines. Enclosed spray combustion of jet fuel is used here to generate high soot concentrations, up to 255 mg/m^3, three orders of magnitude higher than those typically obtained by widely-used soot generators that use vapor-fed flames. This is attributed mostly to the use of real jet fuels. The large mass concentrations enable routine characterization of the soot specific surface area (SSA) and pore size distribution (PSD) by N_2 adsorption. The geometric mean mobility diameter, $\bar{d}_{\mathrm{m}}$, of soot agglomerates was systematically varied from 15 to 180 nm by varying the equivalence ratio (EQR) at constant fuel feed rates, while the organic to total carbon (OC/TC) ratio is low (< 20 %) at all conditions. The geometric mean primary particle (PP) diameter, $\bar{d}_{\mathrm{p}}$, standard deviation, $\sigma_{g,p}$, and mass-mobility exponent, D_{fm}, were hardly altered in that EQR range. These measured D_{fm} and $\sigma_{g,p}$ indicate that soot PPs were sinter-bonded by surface growth, in agreement with aircraft emissions literature. Most importantly, soot made at EQR ≤ 1.34 has mainly small pores (< 2 nm) and similar morphology (D_{fm} = 2.52 ± 0.17), SSA (160 – 239 m^2/g), OC/TC (< 20 %), $\bar{d}_{\mathrm{m}}$ (15 – 61 nm) and $\bar{d}_{\mathrm{p}}$ (14 nm) with those from high-thrust aircraft emissions.

[2] A version of this chapter is published in *Aerosol Science & Technology* (2022), **56**, 732-743.

2.1 Introduction

Aviation is a significant source of ultrafine soot (d_m < 100 nm) in the atmosphere (Westerdahl et al. 2008). These particles are most concerning as they have greater and more systemic inflammatory and cytotoxic responses than fine (d_m < 2.5 μm) and coarse (d_m < 10 μm) particulate emissions [1]. The SSA which is important for assessing the toxicity of such nanoparticles [2] along with the PSD (Marcolli et al. 2021) of soot also determine the rate of its atmospheric aging [3], direct radiative forcing and propensity to act as cloud condensation nuclei. Thus, determination of SSA and PSD of aircraft soot emissions is essential to understand and quantify their impact on climate and public health. This is not trivial as there are hardly any laboratory generators of soot to provide sufficient quantities for its SSA and PSD characterization.

The size, morphology and composition of aircraft soot emissions vary significantly with the applied thrust of their engines [4]: 80 – 100 % thrust is used at take-off (Koudis et al. 2017), 85 % while climbing, 60 % during cruise [4], 30 % during approach and 7 % during taxi/idle [5]. These landing and take-off points are referenced to maximum sea-level-static thrust [5], which may differ when not at sea-level such as at cruise [6]. During aircraft engine operation at high thrust (> 50 %), small agglomerates of soot nanoparticles are emitted having $\bar{d}_m$ ranging from 11 [7] up to 61 nm [6] and $\bar{d}_p$ ranging from 10 nm at 50 % thrust [7] to 18 nm at maximum thrust (100 %) [8]. The morphology of these agglomerates is quantified by their D_{fm} that ranges from 2.6 to 2.8 at high-thrust levels [6]. The organic (OC) to total carbon (TC) mass ratio of soot emitted from high-thrust aircraft engines is consistently small (< 25 %) [9]. The mass concentration of soot within an aircraft plume is rather high ranging from 0.3 to 18'200 μg/m^3 [10]. These soot emissions are sampled at 16 – 25 L/min [11]. Accurate characterization of soot SSA and PSD by N_2 adsorption requires a total sample surface area of at least 5 m^2 [12]. Given that the SSA of carbonaceous nanoparticles is 24 – 807 m^2/g [13], aircraft soot emissions should be sampled for 1 – 24 h. This is beyond the common sampling times of about 10 – 20 min allowed for aircraft engine tests [11]. So, the mass concentration of aircraft soot emissions is not high enough to enable the characterization of their SSA and PSD by N_2 adsorption and other techniques. Typically, the SSA of high-thrust aircraft soot has been determined indirectly with large uncertainty by microscopy [14], mass-mobility and laser induced incandescence measurements ranging from 255 to 1339 m^2/g [7]. These techniques cannot provide though the PSD and total (internal and external) SSA of aircraft soot. Furthermore, the large uncertainty regarding the SSA of aviation emissions can be attributed to the porosity and necking between soot PPs that is not accounted for by the above methods [15]. So, benchmarking the SSA

obtained from such techniques with the total SSA measured from N_2 adsorption is essential to limit the uncertainty regarding the impact of aircraft soot on public health and climate.

In this regard, laboratory generators of aircraft-like soot emissions [16] can assist in their characterization and determine their climate and public health impact. However, most of the currently available generators cannot produce particles with both small $\bar{d}_m$ and low OC/TC that are typical for high-thrust aircraft emissions [16]. For example, the Argonaut Scientific burner produces soot with low OC/TC (≤ 12 %) but large $\bar{d}_m$ (≥ 89 nm) [17]. The McKenna burner typically produces soot with $\bar{d}_m$ < 50 nm that contains rather large amounts of organic carbon (≥ 30 %) [18]. The miniCAST generator is a good source of low-thrust aircraft-like soot having $\bar{d}_m$ between 11 and 88 nm and OC/TC ≥ 50 % [19]. Despite the recent synthesis of soot nanoparticles with low OC/TC using miniCAST with an air pre-mix and lean flame, their $\bar{d}_m$ was still well above 50 nm [20] and the $\bar{d}_m$ range commonly measured for aircraft soot [16]. The above generators rely on combustion of propane [20] or ethylene [21] that much differ from the heavy hydrocarbons in jet fuels [22]. Just doping ethylene flames with 13 wt % of vaporized jet fuel tripled the soot mass concentration [22]. Still, the impact of the jet fuel droplet formation and vaporization that is present in real aircraft engines [23] is not accounted for in gaseous flames [22]. Recently, jet fuel spray combustion was used to produce soot with similar d_m and OC content to that from high-thrust aircraft emissions [24]. None of the above generators, however, can produce high mass concentrations of aircraft-like soot with $\bar{d}_m \leq 50$ nm, to the best of our knowledge. So, such generators need to be operated for several hours (e.g. at least 5 h for the latest miniCAST generator by Ess and Vasilatou [20] to collect enough soot for determination of its SSA and PSD [13].

Here, enclosed and nitrogen-quenched spray combustion [25] of jet fuel is used for high-throughput synthesis of high-thrust aircraft-like soot enabling routine measurement of its SSA and PSD. Enclosing the spray flame prevents uncontrolled soot oxidation by air entrainment and enhances the emitted soot mass concentration. This enables the offline characterization of soot by N_2 adsorption and other techniques that are not possible by conventional spray combustion of jet fuel [24]. By varying the EQR, the $\bar{d}_m$ of soot is controlled and its morphology is characterized by the measured D_{fm} and compared to theoretical power laws for agglomerates [26] and aggregates [27]. The goal of this work is the high-throughput generation of soot having properties similar to that of aviation emissions as running actual aircraft engines for soot generation is too cumbersome and expensive. This is essential for the calibration of laser diagnostics to assist the accurate detection, characterization [16] and filtration [28] of such emissions, as well as for determination of their impact on public health [2] and climate [29].

The burner used here can be readily implemented similar to those marketed by ParteQ. Data from such burners can be used to support policy discussions related to sustainable aviation fuels (SAFs) [30], as well as to investigate the effect of transitioning from aromatic-containing jet A1 to paraffinic or cycloparaffinic SAFs [31] on soot production and particle properties.

2.2 Experimental

2.2.1 Particle production

Figure 2.1 shows a schematic of the experimental set-up. Soot was produced by jet A1 fuel (Birrfeld Airport, Lupfig, Switzerland) spray combustion using an external-mixing, twin fluid nozzle [32] enclosed in two, 30 cm long quartz glass tubes (each with a 42 mm inner diameter) in series [25]. The spray was ignited and sustained by a supporting premixed methane/oxygen flame (CH_4 = 1.25 L/min, O_2 = 2.25 L/min). Here, 4.5 mL/min of fuel flowed through a

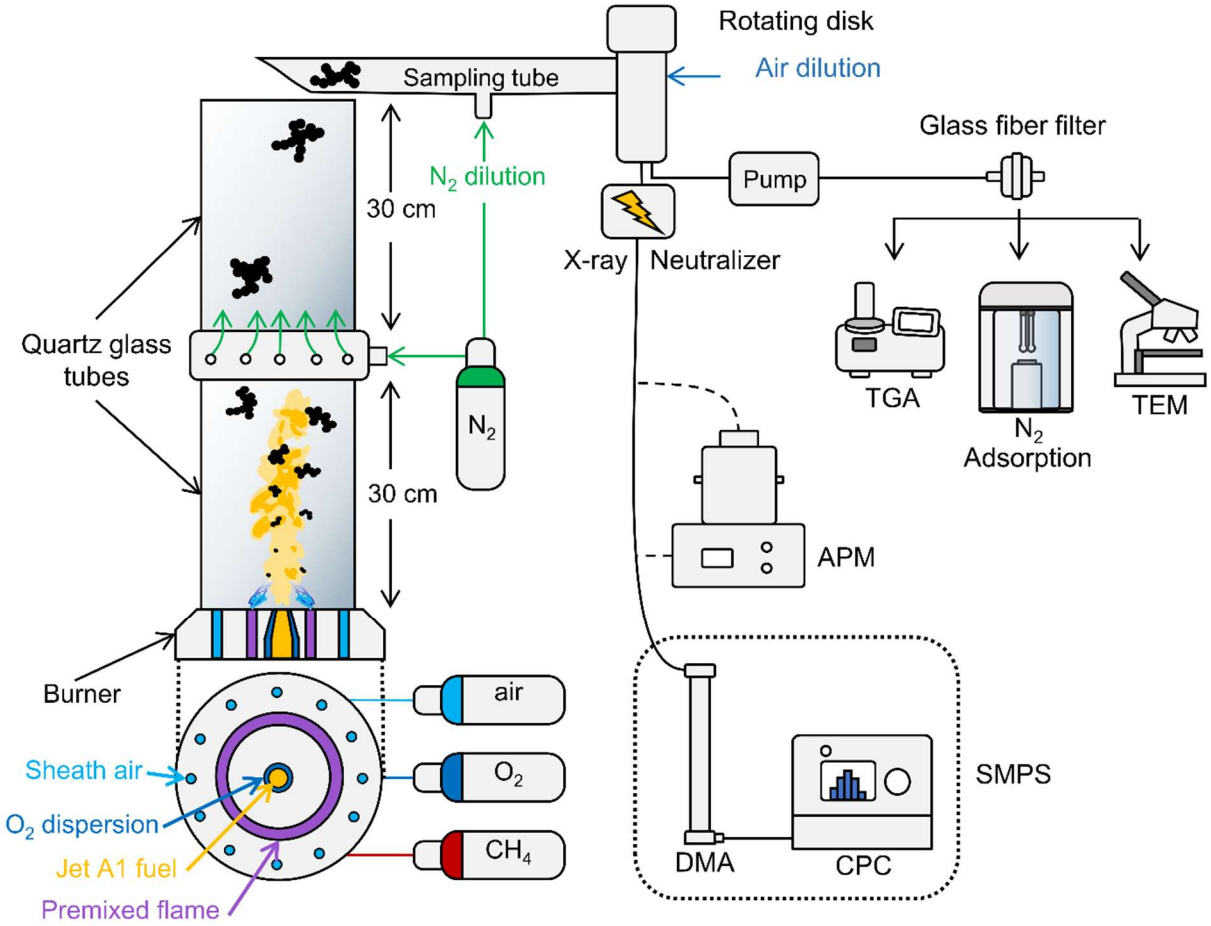

Figure 2.1: Schematic of experimental set-up with spray combustion (not to scale) enclosed in two 30 cm long quartz glass tubes with 20 L/min of nitrogen added between the tubes with a torus ring [34]. Particles are sampled [35] after the second glass tube and diluted with nitrogen. Most of the flow is then sent through a glass fiber filter for offline N_2 adsorption analysis, thermal gravimetric analysis (TGA) and transmission electron microscopy (TEM) of the collected soot. The remaining flow is further diluted with a rotating disk dilution system and sent through an X-ray neutralizer followed by a differential mobility analyzer (DMA) and condensation particle counter (CPC), which typically make up a scanning mobility particle spectrometer (SMPS). Broken lines represent tubing which was added only temporarily for tandem aerosol particle mass (APM) APM–SMPS measurements.

capillary (0.413 mm inner diameter) using a syringe pump (Teledyne 1000D) and was dispersed into a fine spray with 1.5 – 3.0 L/min of O_2 to vary the equivalence ratio (EQR) from 1.59 to 1.25, as calculated accounting for both fuels (i.e. CH_4 and jet A1) and all three O_2 sources (i.e. supporting premixed flame, dispersion gas & sheath air streams) in Appendix C. Increasing EQR beyond 1.59 results in too large soot agglomerates (e.g. $\bar{d}_{\mathrm{m}}$ = 180 nm, Figure C1a) that are beyond the scope of this work while EQR below 1.25 results in too low soot concentrations for SSA and PSD determination. Sheath air was fed through 12 evenly spaced holes surrounding the spray flame at 20 L/min. A torus ring with 12 jet outlets between the two tubes was used to introduce 20 L/min of N_2 in an upward swirled pattern to quench the flame and dilute the exhaust aerosol (Teleki et al. 2009). Maximum axial temperatures, T = 1500 and 1730 K are measured here at EQR = 1.59 and 1.34, respectively, at the centerline of the spray flame. The T = 1730 K obtained at EQR = 1.34 that gives soot with similar characteristics (OC/TC, $\bar{d}_{\mathrm{m}}$, $\bar{d}_p$) to aircraft emissions at high-thrust [9] is consistent with the maximum T = 1850 K measured at the centerline of a gas turbine combustor [33].

2.2.2 Particle sampling and on-line characterization

A straight tube [35] was used to sample 12 L/min of soot aerosol at the top of the second tube (i.e. ~ 63 cm above the burner) while 10 L/min of N_2 dilution were added directly to the sampling tube downstream of its inlet. A rotating disk diluter (MD 19-1E, Matter Engineering AG) further diluted the aerosol by a factor of 1000 with clean air. The diluted aerosol is directed to an X-ray neutralizer (TSI 3087) and a differential mobility analyzer (DMA, TSI 3081) coupled with a condensation particle counter (CPC, TSI 3775) that commonly make up a scanning mobility particle spectrometer (SMPS). This was used to measure the mobility size distribution, as well as the d_{m} of rather monodisperse ($\sigma_{\mathrm{g,m}}$ ~ 1.18) soot agglomerates with mass, m, selected by an aerosol particle mass (APM) analyzer [15]. The latter d_{m} was obtained only for singly charged soot agglomerates that have the largest number-based fraction in the d_{m} distribution [36]. The number of PPs per agglomerate, n_{p}, is related to m and d_{m} by [15]:

$$n_p = \frac{m}{\bar{m}_p} = k_m \left(\frac{d_m}{\bar{d}_p}\right)^{D_{fm}} \tag{2.1}$$

where k_{m} is the mass-mobility prefactor, and $\bar{m}_{\mathrm{p}}$ is the geometric mean PP mass.

2.2.3 Offline analysis

The sampled soot that by-passes the rotating disk diluter was collected on a glass fiber filter for offline analyses. In particular, the OC/TC of soot was obtained by thermogravimetric analysis (TGA) [37]. Modifying the protocol of Klingshirn et al. [37], the samples were first placed in

N_2 to volatilize OC and then in air to oxidize the elemental carbon (EC). The sample heating begun at 30 °C in N_2 and was ramped up to 900 °C at 20 °C/min. The temperature was held at 900 °C for 10 minutes before dropping back to 30 °C at 20 °C/min. The same temperature profile was then repeated in air. From the TGA mass loss (Figure C2), the OC/TC was estimated as the ratio of mass lost under N_2 divided by the total mass lost in both stages. A small amount of inorganics (1 – 7 wt %) could not be oxidized. This was attributed to glass fibers from the collection filters and was not included in the calculation of OC/TC. OC/TC was also determined by thermal optical analysis (TOA) using an OCEC Carbon Aerosol Analyzer (Sunset Laboratory, Model 3) following the modified EUSAAR2 protocol [38].

The specific surface area, SSA, of 20 – 30 mg soot samples degassed for 1 h at 200 °C was determined by N_2 adsorption (Micrometrics Tristar II Plus) at relative pressures, p/p^o, from approximately 0 to 0.3 using the Brunauer, Emmet and Teller (BET) method [39]. Furthermore, the PSD of soot was derived based on its isotherms during N_2 adsorption using the Barrett, Joyner and Halenda (BJH) method [40]. Both BET and BJH analysis methods are applied using the Tristar II Plus software.

Soot PPs selected from the entire, polydisperse soot agglomerate population deposited and collected from the glass fiber filter were imaged with transmission electron microscopy (TEM, FEI Tecnai F30 FEG). That way, the d_p distribution obtained here can be compared consistently to those measured similarly from aircraft engines [8]. In particular, powder samples were dispersed in ethanol and ultrasonicated to break up large agglomerates. Then, a drop of ethanol was placed and dried on the TEM grid [41]. The d_p was determined by manually placing ellipses over the PPs in ImageJ [42] and calculating the area-equivalent diameter. The soot $\bar{d}_p$ measured by TEM levels off after counting 200 PPs (Figure C3), consistent with microscopy analysis of premixed flame soot [43] and TiO_2 [44]. The SSA_{TEM} also can be calculated from TEM-counted $\bar{d}_p$ assuming nanoparticles in point contact [45]:

$$SSA_{TEM} = \frac{6}{\bar{d}_p \cdot \rho} \tag{2.2}$$

where ρ = 1800 kg/m^3 is the mature soot bulk density [46].

2.3 Results and Discussion

2.3.1 Impact of EQR on soot d_m and d_p

Figure 2.2 shows the normalized agglomerate number concentration, $dN/d\log(d_m)/N_{tot}$, as a function of mobility diameter, d_m, of soot made at EQR = 1.25 (double dot-broken line), 1.29 (dotted line), 1.34 (dot-broken line), 1.46 (broken line) and 1.59 (solid line). Shade around each

line represents the standard deviation between, at least, 9 individual size distribution measurements at that EQR.

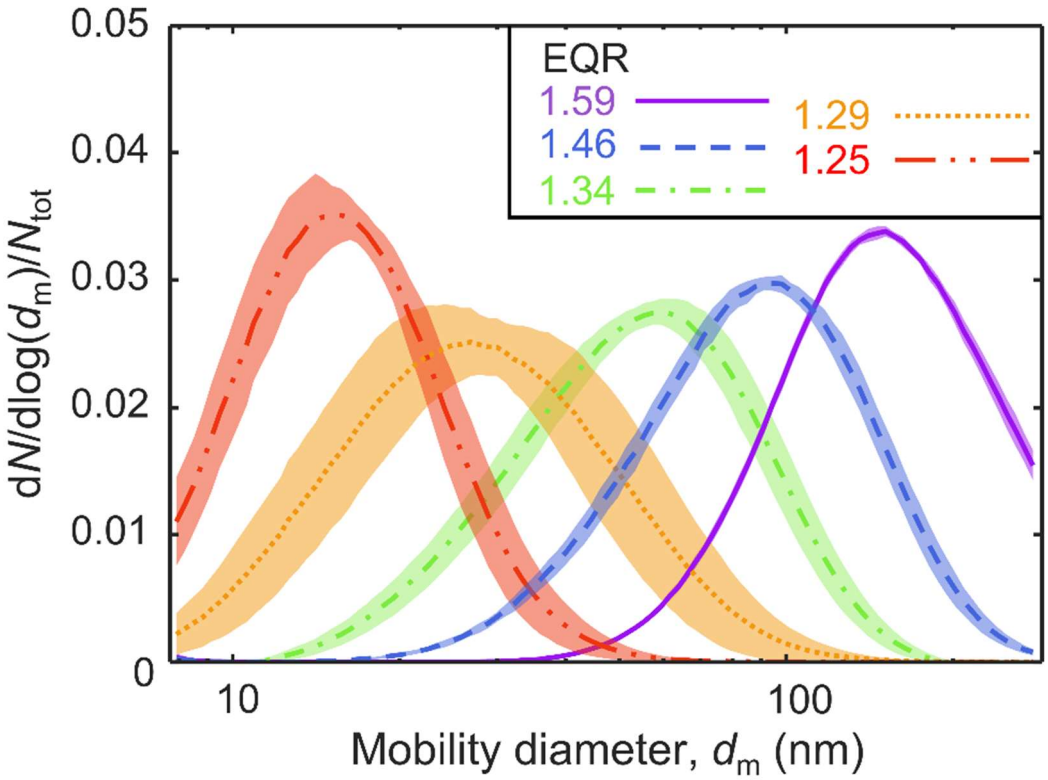

Figure 2.2: Normalized soot number concentration, dN/dlog(d_m)/N_{tot}, as a function of mobility diameter, d_m, at various equivalence ratios (EQR). The shaded areas represent one standard deviation between, at least, 9 measurements.

Clearly, increasing EQR shifts the mobility size distribution to larger d_m. Figure 2.3a shows the $\bar{d}_m$ as a function of EQR (open circles) with error bars representing the standard deviation between at least 9 individual measurements. Increasing EQR from 1.25 to 1.59, increases $\bar{d}_m$ from 15 to 153 nm, due to increasing soot mass concentration with EQR [47] that leads to larger agglomerates [48]. The $\bar{d}_m$ of soot made at EQR ≤ 1.34 is in good agreement with those typically measured from aircraft engines at high (> 50 %) thrust. For example, Abegglen et al. obtained $\bar{d}_m$ between 45 and 61 nm at 65 and 100 % thrust, respectively [6]. Boies et al. measured soot with $\bar{d}_m$ = 11 – 28 nm at thrusts above 50 % [7]. The good agreement between the $\bar{d}_m$ of soot produced here at EQR ≤ 1.34 and that of aircraft emissions can be attributed to the high T (1730 K) of the enclosed spray flame that is consistent with that (1850 K) measured in aircraft combustors [33]. In contrast, the maximum T drops to 1500 K at EQR > 1.34 resulting in soot with larger $\bar{d}_m$ than that of aircraft emissions. It should be noted though that soot coagulates at high pressures (> 1 bar) and short residence times in aircraft combustors [49]. Soot nanoparticles formed at atmospheric pressures can attain similar d_m distributions with those produced at high pressures by coagulation at long residence times [50: Fig. S4]. So, the

long residence times that are present during enclosed spray combustion of jet fuel enable the synthesis of soot nanoparticles with similar $\bar{d}_{\mathrm{m}}$ and $\sigma_{\mathrm{g,m}}$ with those measured from aircraft engines.

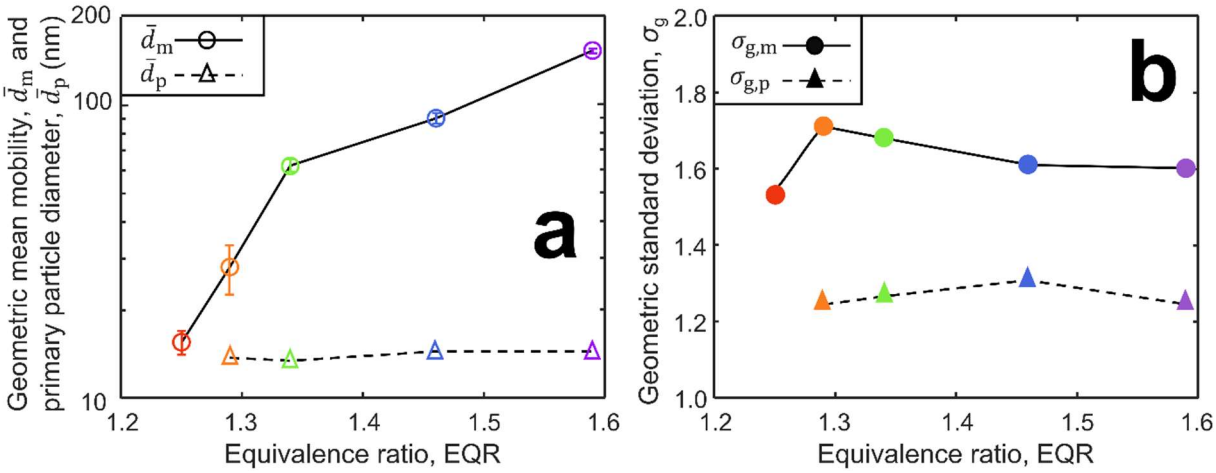

Figure 2.3: a) The geometric mean mobility, $\bar{d}_m$ (open circles), and PP diameter, $\bar{d}_p$ (open triangles), as well as b) the geometric standard deviation of the mobility, $\sigma_{\mathrm{g,m}}$ (filled circles), and PP size distributions, $\sigma_{\mathrm{g,p}}$ (filled triangles), as a function of EQR. Error bars represent the standard deviation between, at least, 9 measurements.

The width of the mobility size distribution is quantified by the geometric standard deviation, $\sigma_{\mathrm{g,m}}$ (Figure 2.3b; filled circles), that hardly changes from 1.53 up to 1.71. The $\sigma_{\mathrm{g,m}}$ measured here at all EQR is smaller than the self-preserving $\sigma_{\mathrm{g,m}} = 2.03$ for agglomerates of PPs in point contact in the free molecular regime [51]. This can be attributed to formation of aggregates (by surface reactions and condensation) that narrow the self-preserving size distribution [27]. Soot agglomerates formed at EQR > 1.25 coagulate largely in the transition regime. Then the $\sigma_{\mathrm{g,m}}$ of 1.68 and 1.71 of soot made at EQR = 1.34 and 1.29 are consistent with the $\sigma_{\mathrm{g,m}} = 1.66$ [6] up to $\sigma_{\mathrm{g,m}} = 1.80$ [11] measured from high-thrust aircraft engine emissions at $\bar{d}_{\mathrm{m}}$ comparable to those from [6] and [11].

The soot PP size distribution was obtained from microscopy images at all EQR (Figure C4). Figure 2.3 shows $\bar{d}_{\mathrm{p}}$ (a; open triangles) and geometric standard deviation of the PP size distribution, $\sigma_{\mathrm{g,p}}$ (b; filled triangles) as a function of EQR. Unlike $\bar{d}_{\mathrm{m}}$, the $\bar{d}_{\mathrm{p}}$ obtained from the entire soot agglomerate population is hardly affected by EQR and ranges from 13.3 to 14.3 nm. This is consistent with the small $\bar{d}_{\mathrm{p}}$ variation in fuel rich miniCAST reactors operating at EQR = 1.12 – 1.33 [52]. Most importantly, the $\bar{d}_{\mathrm{p}} = 13.9 \pm 0.5$ nm averaged over all EQR is consistent with the $\bar{d}_{\mathrm{p}}$ measured for high-thrust aircraft soot from 10 [7] to 18 nm [8] with a mean value of 15.8 ± 2.1 nm [7–9]. Figure C5 shows the distribution of d_{p} from [8] and [9] and the lognormal fittings of the data to obtain the $\bar{d}_{\mathrm{p}}$ for comparison.

Similarly, the $\sigma_{g,p}$ is rather constant at all EQR, ranging from 1.25 to 1.30 and also well below its self-preserving size distribution value of 1.45 [51] indicating again the significance of surface growth during coagulation. The $\sigma_{g,p}$ measured here is consistent with those from open premixed ($\sigma_{g,p}$ = 1.25) [43] and spray flames ($\sigma_{g,p}$ = 1.25) [24] as well as with those estimated by discrete element modelling (DEM) for surface growth and agglomeration ($\sigma_{g,p}$ = 1.2) [27].

The variation of soot d_p with its d_m (that is equivalent to the projected-area diameter at these conditions; [53]) is also elucidated by interfacing mass-mobility data from enclosed spray combustion at EQR = 1.59 (Figure C6; circles), 1.46 (triangles), 1.34 (diamonds) and 1.29 (squares) with a power law [43]. As the d_m of single soot agglomerates increases from 50 to 100 nm, their d_p increases from 10.8 ± 2.2 nm to about 15.2 ± 1.1 nm. This indicates that large soot agglomerates (e.g. d_m = 100 nm) formed at long residence times are mixed with small soot agglomerates (e.g. d_m = 50 nm) produced at short residence times with limited surface growth during enclosed spray combustion [54]. Further increasing of d_m does not affect the soot d_p. The variation of d_p with d_m measured here for soot from enclosed spray combustion is in excellent agreement with that from open one (inverse triangles) [24] and consistent with an empirical power law from engine soot (solid line & shaded area) [54].

2.3.2 Soot morphology

A tandem APM-SMPS was used to quantify the mass-mobility relationship of soot. The n_p distribution was obtained using Equation 2.1 and the APM-SMPS data. Figure 2.4 shows the n_p as a function of normalized mobility diameter, $d_m/\bar{d}_p$ of soot made at EQR 1.59 (circles), 1.46 (triangles), 1.34 (diamonds) and 1.29 (squares). No data are shown for EQR = 1.25 as APM cannot analyze accurately particles with d_m < 50 nm [55]. The average D_{fm} and k_m for all EQR were 2.43 ± 0.1 and 0.68 ± 0.16 (double dot-broken line, Eq. 2.1), respectively. The average k_m of 0.68 (symbols) is on par with the k_m = 0.68 from partially compacted, flame-made soot agglomerates [56]. There appears to be no significant difference in the mass-mobility relationships at different EQR. The variations in the fitted D_{fm} and k_m may be due to the outsized influence of data at the extreme ends of the scale or due to potential differences in PP diameter at different d_m [54]. This small k_m indicates that the present soot agglomerates are rather asymmetric and contain only a few branches, consistent with TEM (Fig. C4) [57]. All APM-SMPS data are bracketed largely between the mass-mobility relationships for agglomerates of monodisperse PPs in point contact with D_{fm} = 2.17 ± 0.1 and k_m = 1.0 (dotted line, Eq. 2.1) [26] and aggregates of PPs made by agglomeration and surface growth with D_{fm} = 2.45 ± 0.05 and k_m = 0.82 (solid line, Eq. 2.1) [48]. Agglomeration seems to be the primary growth mechanism, but surface reactions also contribute as they result in formation of polydisperse and chemically-

bonded PPs. In this regard, n_p, measured for soot from enclosed spray combustion (Fig. 4; symbols) is described best by a DEM-derived power law for agglomerates of polydisperse and chemically-bonded PPs (Eq. 2.1 with D_{fm} = 2.22 and k_m = 1; dot-broken line) [48]. As the data lean largely to the latter relationship, this further indicates that soot grows by surface reactions and agglomeration, consistent with its necking in TEM images (Figure 2.4; inset). High-thrust aircraft engines typically produce soot with D_{fm} from 2.62 [58] to 2.79 [6], similar to D_{fm} of soot made here at EQR = 1.34.

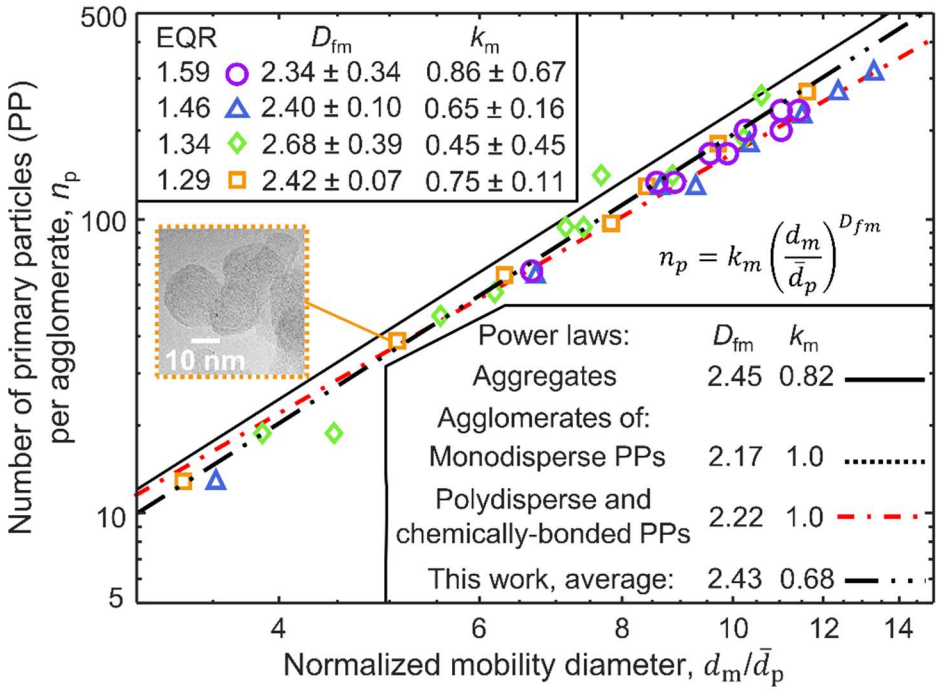

Figure 2.4: The number of soot PPs per agglomerate, n_p, as a function of their normalized mobility diameter, $d_m/\bar{d}_p$ produced at various EQR and measured by APM-SMPS (symbols and double dot-broken line). Power laws derived for aggregates (solid line) [27] and agglomerates of monodisperse PPs in point contact (dotted line) [26] or aggregates of polydisperse and chemically-bonded PPs (dot-broken line) [27] are shown also. The inset shows an exemplary TEM image of soot made at EQR = 1.29.

Figure 2.5 compares the soot effective density, ρ_{eff}, measured here from enclosed spray combustion (circles, triangles, diamonds and squares) to those obtained from various engines summarized by Olfert and Rogak [54; solid line & gray shaded area]. In particular, the ρ_{eff} of soot from enclosed spray combustion is at the lower end of the average engine soot ρ_{eff}, but in excellent agreement with that measured from an airplane (open inverse triangles) [59] and a helicopter engine (filled inverse triangles) [58]. In this regard, the ρ_{eff} of aircraft (open and filled inverse triangles) and enclosed spray flame combustion (circles, triangles, diamonds and squares) soot is in good agreement with that estimated by a DEM-derived power law (dot-broken line & red shaded area) [48]. So, the ρ_{eff} of soot formed during jet fuel combustion in enclosed spray flames and aircraft engines seems to be determined by surface growth and agglomeration.

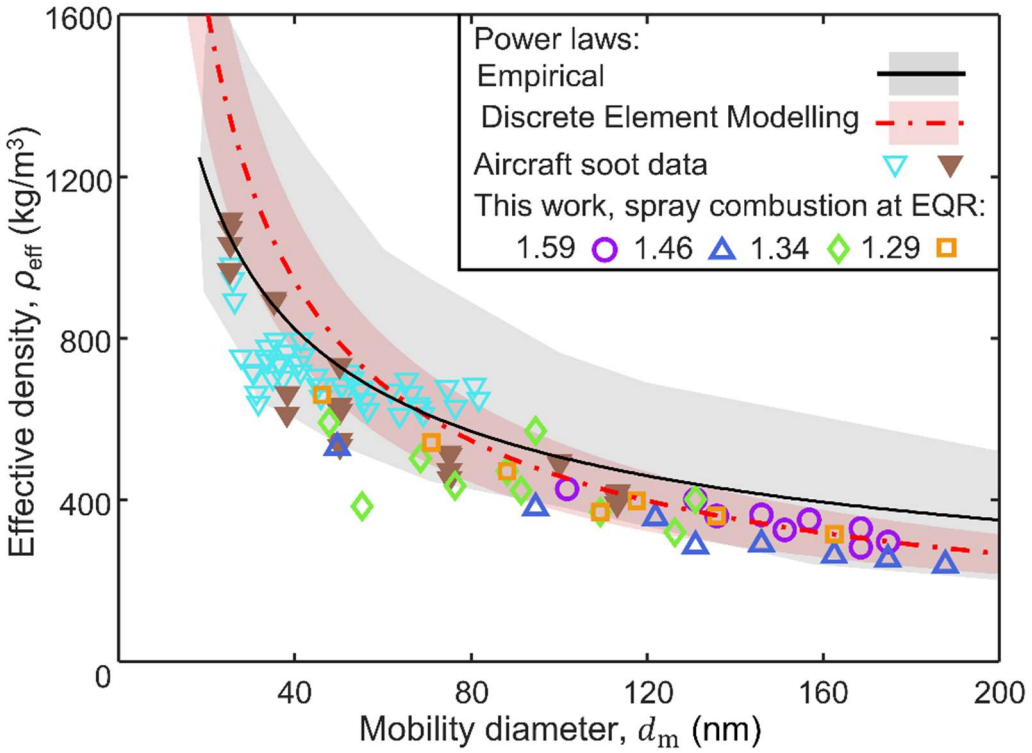

Figure 2.5: Effective density, ρ_{eff}, as a function of d_m of soot from enclosed spray combustion at EQR = 1.59 (circles), 1.46 (triangles), 1.34 (diamonds) and 1.29 (squares) in comparison to data from an airplane (open inverse triangles) [59] and a helicopter engine (filled inverse triangles) [58]. The measured soot ρ_{eff} are compared also to those obtained from a power law derived by DEM for surface growth and agglomeration (red dot-broken line & red shaded area) [48], as well as an empirical power law extracted from engine data (black solid line & gray shaded area) [54].

2.3.3 Organic carbon content of soot

Figure 2.6 shows the soot OC/TC measured by TOA (filled symbols) and TGA (open symbols) as a function of EQR. The OC/TC derived by TOA (Fig. 6; filled symbols) decreases from 19 to 10 % as EQR increases from 1.25 to 1.59. Across the same range, the TGA-derived OC/TC (Fig. 2.6; open symbols) drops from 36 to 11 %. The reduction of OC/TC with increasing EQR and $\bar{d}_m$ can be attributed to the increasing degree of soot maturation and oxidation at such conditions, corroborating DEM simulations [60]. The TOA- (filled symbols) and TGA-derived (open symbols) OC/TC are practically identical for soot formed at EQR > 1.34. At EQR ≤ 1.34 though, the TGA-derived OC/TC is up to 17 % larger than that obtained by TOA. This is consistent with TGA measurements of aircraft soot that resulted in 20 % larger OC/TC than that measured by TOA (Table 2.1) [37]. The difference between the TOA- and TGA-derived OC/TC can be attributed to the larger temperature used in the latter analysis (650 vs. 900 °C) that may result in charring or desorption of semi-volatile organic compounds [61]. This disparity could also indicate the presence of inorganic volatile compounds in soot formed at EQR ≤ 1.34 that are not accounted for by TOA [62].

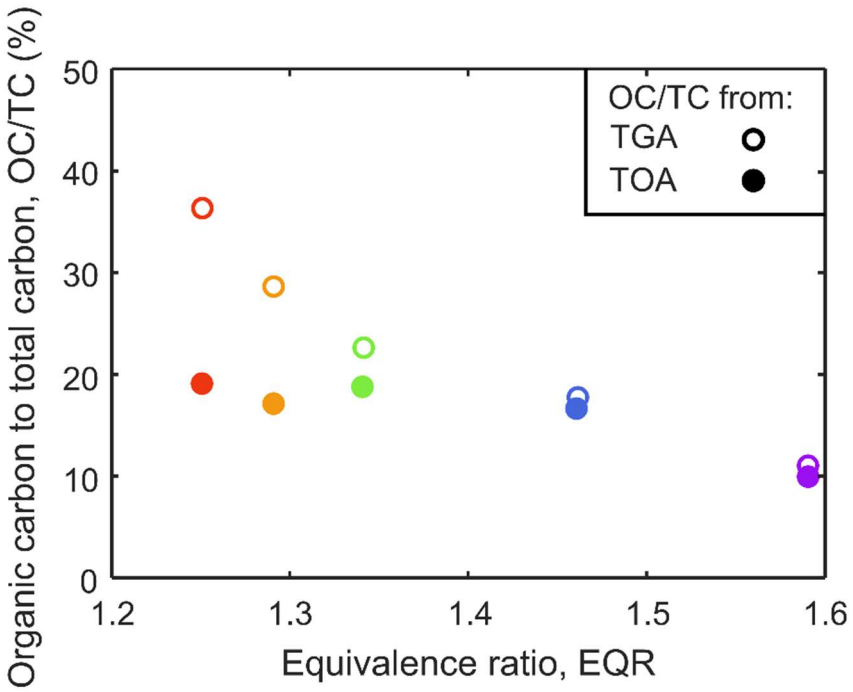

Figure 2.6: The present OC/TC of soot from TGA (open symbols) and TOA (filled symbols) as a function of EQR.

It should be noted that soot made at EQR > 1.34 has larger $\bar{d}_{\mathrm{m}}$ than that measured from aircraft emissions [6]. In contrast, soot made at EQR ≤ 1.34 has similar $\bar{d}_{\mathrm{m}}$ (15 – 61 nm) [6], TOA- [4,9,37,63] and TGA-derived [37] OC/TC with those obtained from aircraft soot, as shown in Table 2.1. Furthermore, the OC/TC = 17 – 19 % measured here by TOA for soot from enclosed spray combustion of jet fuel at EQR = 1.25 – 1.34 is within the SAE ARP6320A requirements of TOA-derived OC/TC < 20 % for calibration of aircraft emission instrumentation [11].

Table 2.1: The OC/TC of soot from various aircraft engines, as well as from enclosed spray combustion at EQR = 1.25 – 1.34 measured by TOA and/or TGA.

	OC/TC (%)	
	by TOA	by TGA
Turbofan engine [63]	14 – 25	–
// // [4]	14 – 25	–
Powerjet // [9]	12 – 24	–
Turbojet // [37]	8 – 19	15 – 40
This work: Enclosed spray combustion at EQR = 1.25 – 1.34	17 – 19	22 – 36

2.3.4 Soot mass concentrations

Figure 2.7 compares the produced soot mass concentration as a function of $\bar{d}_{\mathrm{m}}$ from enclosed (circles) and open spray combustion units (squares) [24] as well as a 5201 miniCAST with low organic carbon content (≤ 25 %) [20] (triangles). The mass concentrations of miniCAST soot shown in Fig. 2.7 (triangles) have been corrected to eliminate the impact of dilution [20]. The

soot mass concentrations from spray combustion are measured directly by APM-SMPS. Enclosing the spray combustion unit substantially increased the soot production rate and mass concentration of soot with $\bar{d}_{\mathrm{m}} \leq 50$ nm in comparison to open units [24] and miniCAST soot generators [20]. The mass concentrations from the latter were originally determined indirectly with an aethalometer using a mass absorption cross-section, *MAC*, of 7.77 m^2/g for a wavelength of 880 nm [20] (Figure C7; filled triangles). This *MAC* is much larger than the typically accepted value of 4.69 m^2/g at 880 nm for mature soot [46]. The presence of organic carbon can further reduce the *MAC* of soot [60]. Here, the soot mass concentrations from a miniCAST generator [20] are obtained using the latter *MAC* that accounts for the realistic organic carbon content of soot made at these conditions (triangles). Accounting for the realistic soot composition increased the miniCAST mass concentrations by a factor of 2.4 (Figure C7; filled triangles), consistent with similar analysis for premixed flames [60].

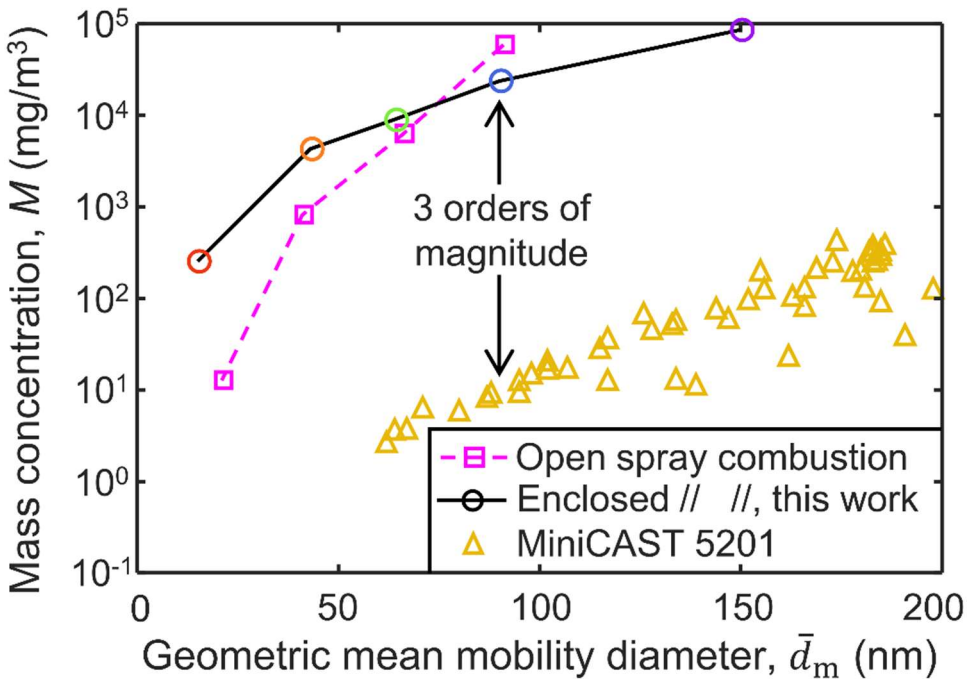

Figure 2.7: The mass concentration, *M*, of soot produced from enclosed (circles) and open spray combustion units (squares) [24] as a function of $\bar{d}_m$ as well as a 5201 miniCAST (triangles) [20] with its data corrected with a realistic *MAC*.

For all soot generators, the emitted mass concentration increases with $\bar{d}_{\mathrm{m}}$ as expected. The spray combustion units systematically produce much more soot than the miniCAST. For example, the soot mass concentrations with $\bar{d}_{\mathrm{m}}$ = 65 nm from enclosed spray combustion were three orders of magnitude higher than the miniCAST, while the molar flow rate (calculated in the SI) in the enclosed unit (0.02 mol/min; circles) was only an order of magnitude higher than that in the miniCAST (0.003 mol/min; triangles). This is consistent with laser induced incandescence measurements [22] revealing that doping a diffusion ethylene flame with 13 wt

% of jet fuel tripled the maximum soot mass concentration. The large increase of soot mass concentrations by combusting jet fuel instead of propane or ethylene could be attributed to the fast evaporation of jet fuel droplets resulting in high molecular weight hydrocarbons that enhance soot nucleation and its mass concentration [22]. So, combustion of sprays facilitates soot formation as liquid jet fuel is composed of heavier hydrocarbons [64] than common gaseous hydrocarbons used in current lab soot generators [20].

The enclosed spray combustion unit is able to produce up to 20 times higher mass concentrations of aircraft-like soot $\bar{d}_{\mathrm{m}}$ < 50 nm than the open one. This is despite the nearly thrice lower fuel flow rate used here (4.5 mL/min) than in the open one (12 mL/min). The latter has a lean EQR of 0.35 [24], while the enclosed unit has a rich EQR (1.25 – 1.59). Increasing EQR increases the emitted soot volume fraction and mass concentration [65]. Furthermore, enclosing the unit prevents the entrainment of atmospheric air in the flame [66] and limits soot oxidation. The N_2 injection through the torus ring at HAB = 30 cm of the enclosed unit reduces the flame temperature [34] and further mitigates soot oxidation.

2.3.5 Soot pore size distribution (PSD) and specific surface area (SSA)

The increased mass concentrations from the enclosed spray combustion unit enable the collection of enough soot (≥ 10 mg) for N_2 adsorption and determination of PSD and SSA. So, the SSA of soot made at various EQR in Table 2.2 have been obtained from N_2 adsorption (Figure C8). The external SSA_{TEM} of soot based on the measured $\bar{d}_{\mathrm{p}}$ (Figure 2.3a) using Eq. 2.2 is shown also in Table 2.2. The SSA_{TEM} from aircraft soot was calculated based on $\bar{d}_{\mathrm{p}}$ reported in the literature from 10 [7] to 18 nm [8] which results in SSA_{TEM} from 333 to 185 m^2/g, respectively, bracketing the present range of SSA_{TEM} from enclosed spray combustion soot. This indicates that the *SSA* and PSD measured here for enclosed spray combustion soot are equivalent to those of real aircraft soot. At EQR > 1.34 the SSA_{TEM} is smaller than the *SSA* suggesting that internal pores contribute also to the total SSA of soot.

Table 2.2: The specific surface area spray combustion soot at four EQR by the N_2 adsorption, SSA, and with transmission electron microscopy (TEM), SSA_{TEM}. The $\bar{d}_{\mathrm{p}}$ from the literature is used to estimate the SSA_{TEM} of aircraft soot from $\bar{d}_{\mathrm{p}}$ = 10 [7] to 18 nm [8].

	SSA [m^2/g]	SSA_{TEM} [m^2/g]
EQR = 1.59	258	233
// 1.46	282	233
// 1.34	239	251
// 1.29	160	245
Aircraft soot	-	185 – 333

The presence of internal pores in the spray combustion soot at EQR > 1.29 was further investigated by deriving the PSD from the full N_2 adsorption isotherm using the BJH method. Figure 2.8 shows the specific pore surface area concentration, dA/dlog(w), as a function of the pore width, w, derived for soot made at EQR = 1.59 (solid line), 1.46 (broken line), 1.34 (dot-broken line) and 1.29 (dotted line). At all EQR there is a sharp increase in the area concentration of pores with w = 1.4 nm, i.e. the lower detection limit of the N_2 adsorption instrument used here. However, at EQR of 1.46 and 1.59, there are also peaks of the surface area concentration at approximately w = 2.5 nm. These pores can explain the larger SSA than SSA_{TEM} measured at these conditions (Table 2.2). These pores can be caused by internal oxidation which occurs at low temperatures (< 1100 K) [67]. Rich flames with high EQR exhibit lower temperatures than lean flames, as the peak flame temperature is attained at near stoichiometric conditions [47]. This could explain the enhanced internal porosity measured here at EQR = 1.46 and 1.59.

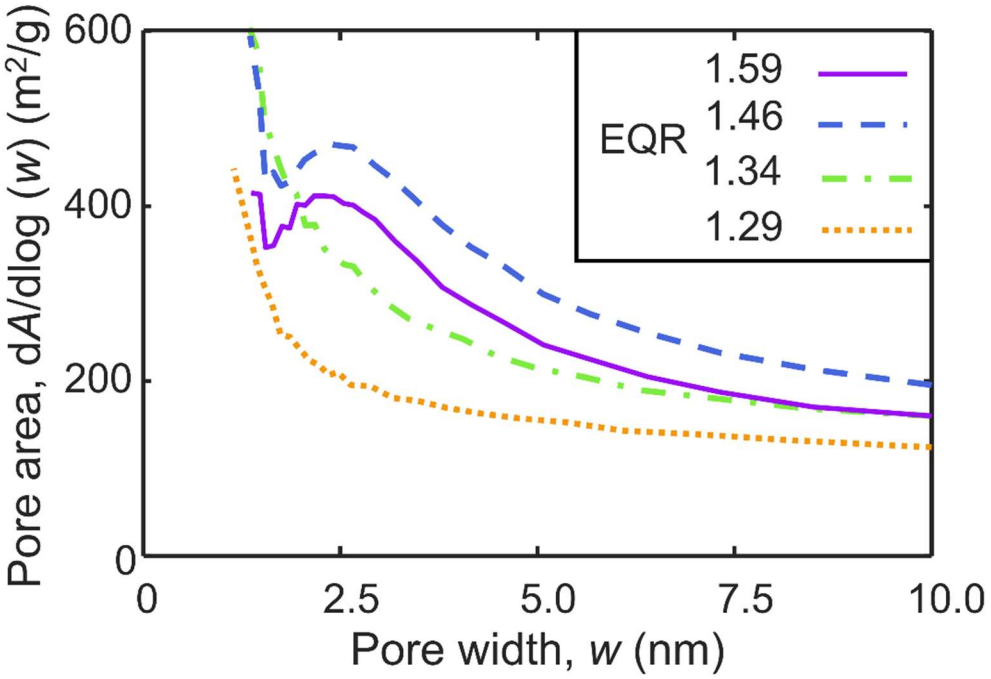

Figure 2.8: Specific pore surface area concentration, dA/dlog(w), as a function of pore width, w, of soot made at EQR = 1.59 (solid line), 1.46 (broken line), 1.34 (dot-broken line) and 1.29 (dotted line) using the Barrett-Joyner-Halenda (BJH) method.

2.4 Conclusions

An enclosed jet A1 fuel spray combustion unit is used to produce soot with controlled geometric mean mobility diameter, $\bar{d}_m$, from 15 to 153 nm by varying the combustion equivalence ratio (EQR). The morphology of the resulting soot agglomerates quantified by their mass-mobility exponent, D_{fm} = 2.43 ± 0.1 and prefactor, k_m = 0.68 ± 0.16 as well as the PP diameter, $\bar{d}_p$ = 13.9 nm, are largely constant regardless of EQR. These D_{fm} and k_m indicated necked soot agglomerates by surface growth, consistent with microscopy images and in agreement with data

from aircraft emissions. Specifically, soot agglomerates made here at EQR ≤ 1.34 have similar morphology, $\bar{d}_{\mathrm{m}}$ and $\bar{d}_{\mathrm{p}}$ with those from high-thrust aircraft emissions.

The produced mass concentrations were, at least, three orders of magnitude larger than those obtained by the widely used miniCAST soot generator and for soot with $\bar{d}_{\mathrm{m}}$ = 30 nm more than 20 times larger than those attained by an open spray combustion unit using 2 – 3 times higher jet A1 fuel feed rates. The large production rates attained here facilitated the collection of soot to determine its specific surface area (SSA) and PSD. Thus, enclosed units can be used to produce large mass concentrations of aircraft-like soot, enabling the offline characterization of its SSA and PSD. Last but probably not least, the SSA of soot produced at EQR ≥ 1.46 is enhanced through the presence of pores with 2 – 4 nm width formed by internal oxidation. The SSA and PSD measured here for aircraft-like soot, for the first time to the best of our knowledge, can assist to determine the atmospheric aging rate of aviation emissions [68] and thus their atmospheric implications. The SSA of aviation emissions is also essential to derive robust soot oxidation rates [67] and optimize the engine performance. Furthermore, the soot generator developed here based on enclosed spray combustion of liquid fuels can be used also to inform current policy-relevant discussions related to sustainable aviation fuels (SAFs) [30] and to better understand how transitioning from aromatic-containing jet A1 to paraffinic or cycloparaffinic SAFs [31] would change soot particle production and particle properties.

2.5 References

[1] Cassee FR, Héroux ME, Gerlofs-Nijland ME, Kelly FJ. Particulate matter beyond mass: Recent health evidence on the role of fractions, chemical constituents and sources of emission. *Inhal Toxicol* (2013) **25**, 802–12.

[2] Schmid O, Stoeger T. Surface area is the biologically most effective dose metric for acute nanoparticle toxicity in the lung. *J Aerosol Sci* (2016) **99**, 133–43.

[3] Zhang R, Khalizov AF, Pagels J, Zhang D, Xue H, McMurry PH. Variability in morphology, hygroscopicity, and optical properties of soot aerosols during atmospheric processing. *Proc Natl Acad Sci* (2008) **105**, 10291–6.

[4] Elser M, Brem BT, Durdina L, Schönenberger D, Siegerist F, Fischer A, Wang J. Chemical composition and radiative properties of nascent particulate matter emitted by an aircraft turbofan burning conventional and alternative fuels. *Atmos Chem Phys* (2019) **19**, 6809–20.

[5] ICAO. Annex 16 to the convention on international civil aviation: environmental protection: volume II aircraft engine emissions. (2008).

[6] Abegglen M, Durdina L, Brem BT, Wang J, Rindlisbacher T. Effective density and mass – mobility exponents of particulate matter in aircraft turbine exhaust : Dependence on engine thrust and particle size. *J Aerosol Sci* (2015) **88**, 135–47.

[7] Boies AM, Stettler MEJ, Swanson JJ, Johnson TJ, Olfert JS, Johnson M, Eggersdorfer ML, Rindlisbacher T, Wang J, Thomson K, Smallwood G, Sevcenco Y, Walters D,

Williams PI, Corbin J, Mensah AA, Symonds J, Dastanpour R, Rogak SN. Particle emission characteristics of a gas turbine with a double annular combustor. *Aerosol Sci Technol* (2015) **49**, 842–55.

[8] Liati A, Brem BT, Durdina L, Vögtli M, Dasilva YAR, Eggenschwiler PD, Wang J. Electron microscopic study of soot particulate matter emissions from aircraft turbine engines. *Environ Sci Technol* (2014) **48**, 10975–83.

[9] Marhaba I, Ferry D, Laffon C, Regier TZ, Ouf F, Parent P. Aircraft and MiniCAST soot at the nanoscale. *Combust Flame* (2019) **204**, 278–89.

[10] Agarwal A, Speth RL, Fritz TM, Jacob SD, Rindlisbacher T, Iovinelli R, Owen B, Miake-Lye RC, Sabnis JS, Barrett SRH. SCOPE11 method for estimating aircraft black carbon mass and particle number emissions. *Environ Sci Technol* (2019) **53**, 1364–73.

[11] Lobo P, Durdina L, Smallwood GJ, Rindlisbacher T, Siegerist F, Black EA, Yu Z, Mensah AA, Hagen DE, Miake-Lye RC, Thomson KA, Brem BT, Corbin JC, Abegglen M, Sierau B, Whitefield PD, Wang J. Measurement of aircraft engine non-volatile PM emissions: Results of the Aviation-Particle Regulatory Instrumentation Demonstration Experiment (A-PRIDE) 4 campaign. *Aerosol Sci Technol* (2015) **49**, 472–84.

[12] Karg E, Ferron GA, Schumann G, Schmid O. Specific BET Surface Area Measurement of Low-Mass-Samples. *12th ETH Conf Combust Gener Nanoparticles*, (2008).

[13] Ouf F-X, Bourrous S, Vallières C, Yon J, Lintis L. Specific surface area of combustion emitted particles: Impact of primary particle diameter and organic content. *J Aerosol Sci* (2019) **137**, 105436.

[14] Bourrous S, Ribeyre Q, Lintis L, Yon J, Bau S, Thomas D, Cécile V, Ouf F-X. A semi-automatic analysis tool for the determination of primary particle size, overlap coefficient and specific surface area of nanoparticles aggregates. *J Aerosol Sci* (2018) **126**, 122–32.

[15] Eggersdorfer ML, Gröhn AJ, Sorensen CM, McMurry PH, Pratsinis SE. Mass-mobility characterization of flame-made ZrO_2 aerosols: Primary particle diameter and extent of aggregation. *J Colloid Interface Sci* (2012) **387**, 12–23.

[16] Durdina L, Lobo P, Trueblood MB, Black EA, Achterberg S, Hagen DE, Brem BT, Wang J. Response of real-time black carbon mass instruments to mini-CAST soot. *Aerosol Sci Technol* (2016) **50**, 906–18.

[17] Kazemimanesh M, Moallemi A, Olfert JS, Kostiuk LW. Probe sampling to map and characterize nanoparticles along the axis of a laminar methane jet diffusion flame. *Proc Combust Inst* (2017) **36**, 881–8.

[18] Maricq MM. Examining the relationship between black carbon and soot in flames and engine exhaust. *Aerosol Sci Technol* (2014) **48**, 620–9.

[19] Moore RH, Ziemba LD, Dutcher D, Beyersdorf AJ, Chan K, Crumeyrolle S, Raymond TM, Thornhill KL, Winstead EL, Anderson BE. Mapping the operation of the miniature combustion aerosol standard (Mini-CAST) soot generator. *Aerosol Sci Technol* (2014) **48**, 467–79.

[20] Ess MN, Vasilatou K. Characterization of a new miniCAST with diffusion flame and premixed flame options: Generation of particles with high EC content in the size range 30 nm to 200 nm. *Aerosol Sci Technol* (2019) **53**, 29–44.

[21] Kazemimanesh M, Moallemi A, Thomson K, Smallwood G, Lobo P, Olfert JS. A

novel miniature inverted-flame burner for the generation of soot nanoparticles. *Aerosol Sci Technol* (2019) **53**, 184–95.

[22] Saggese C, Singh A V., Xue X, Chu C, Kholghy MR, Zhang T, Camacho J, Giaccai J, Miller JH, Thomson MJ, Sung CJ, Wang H. The distillation curve and sooting propensity of a typical jet fuel. *Fuel* (2019) **235**, 350–62.

[23] Mueller ME, Pitsch H. Large eddy simulation of soot evolution in an aircraft combustor. *Phys Fluids* (2013) **25**, 110812.

[24] Kholghy MR, DeRosa VG. Morphology, composition and optical properties of jet engine-like soot made by a spray flame. *Combust Flame* (2021) **231**, 111480.

[25] Teleki A, Heine MC, Krumeich F, Akhtar MK, Pratsinis SE. In situ coating of flame-made TiO_2 particles with nanothin SiO_2 films. *Langmuir* (2008) **24**, 12553–8.

[26] Sorensen CM. The mobility of fractal aggregates: A review. *Aerosol Sci Technol* (2011) **45**, 755–69.

[27] Kelesidis GA, Goudeli E, Pratsinis SE. Morphology and mobility diameter of carbonaceous aerosols during agglomeration and surface growth. *Carbon* (2017) **121**, 527–35.

[28] Mader BT, Flagan RC, Seinfeld JH. Sampling atmospheric carbonaceous aerosols using a particle trap impactor/denuder sampler. *Environ Sci Technol* (2001) **35**, 4857–67.

[29] Lohmann U, Friebel F, Kanji ZA, Mahrt F, Mensah AA, Neubauer D. Future warming exacerbated by aged-soot effect on cloud formation. *Nat Geosci* (2020) **13**, 674–80.

[30] Chao H, Agusdinata DB, DeLaurentis D, Stechel EB. Carbon offsetting and reduction scheme with sustainable aviation fuel options: Fleet-level carbon emissions impacts for U.S. airlines. *Transp Res Part D Transp Environ* (2019) **75**, 42–56.

[31] Huq NA, Hafenstine GR, Huo X, Nguyen H, Tifft SM, Conklin DR, Stück D, Stunkel J, Yang Z, Heyne JS, Wiatrowski MR, Zhang Y, Tao L, Zhu J, McEnally CS, Christensen ED, Hays C, van Allsburg KM, Unocic KA, Meyer HM, Abdullah Z, Vardon DR. Toward net-zero sustainable aviation fuel with wet waste–derived volatile fatty acids. *Proc Natl Acad Sci* (2021) **118**, 1-11.

[32] Mädler L, Kammler HK, Mueller R, Pratsinis SE. Controlled synthesis of nanostructured particles by flame spray pyrolysis. *J Aerosol Sci* (2002) **33**, 369–89.

[33] Meier U, Heinze J, Freitag S, Hassa C. Spray and flame structure of a generic injector at aeroengine conditions. *Proc ASME Turbo Expo* (2011) **3**, 61–72.

[34] Teleki A, Buesser B, Heine MC, Krumeich F, Akhtar MK, Pratsinis SE. Role of gas - aerosol mixing during in situ coating of flame-made titania particles. *Ind Eng Chem Res* (2009) **48**, 85–92.

[35] Goudeli E, Gröhn AJ, Pratsinis SE. Sampling and dilution of nanoparticles at high temperature. *Aerosol Sci Technol* (2016) **50**, 591–604.

[36] Wiedensohler A. An approximation of the bipolar charge distribution for particles in the submicron size range. *J Aerosol Sci* (1988) **19**, 387–9.

[37] Klingshirn CD, West ZJ, DeWitt MJ, Higgins A, Graham J, Corporan E. Quantification of elemental and total carbon in combustion particulate matter using thermal-oxidative analysis. *J Air Waste Manag Assoc* (2019) **69**, 1003–13.

[38] Cavalli F, Viana M, Yttri KE, Genberg J, Putaud J-P. Toward a standardised thermal-

optical protocol for measuring atmospheric organic and elemental carbon: the EUSAAR protocol. *Atmos Meas Tech* (2010) **3**, 79–89.

[39] Brunauer S, Emmett PH, Teller E. Adsorption of gases in multimolecular layers. *J Am Chem Soc* (1938) **60**, 309–19.

[40] Barrett EP, Joyner LG, Halenda PP. The determination of pore volume and area distributions in porous substances. I. Computations from nitrogen isotherms. *J Am Chem Soc* (1951) **73**, 373–380.

[41] Strobel R, Krumeich F, Stark WJ, Pratsinis SE, Baiker A. Flame spray synthesis of Pd/Al_2O_3 catalysts and their behavior in enantioselective hydrogenation. *J Catal* (2004) **222**, 307–14.

[42] Schneider CA, Rasband WS, Eliceiri KW. NIH Image to ImageJ: 25 years of image analysis. *Nat Methods* (2012) **9**, 671–5.

[43] Kelesidis GA, Kholghy MR, Zuercher J, Robertz J, Allemann M, Duric A, Pratsinis SE. Light scattering from nanoparticle agglomerates. *Powder Technol* (2020) **365**, 52–9.

[44] Tsantilis S, Kammler HK, Pratsinis SE. Population balance modeling of flame synthesis of titania nanoparticles. *Chem Eng Sci* (2002) **57**, 2139–56.

[45] Rissler J, Messing ME, Malik AI, Nilsson PT, Erik Z, Bohgard M, Sanati M, Pagels JH, Rissler J, Messing ME, Malik AI, Nilsson PT, Erik Z, Rissler J, Messing ME, Malik AI, Nilsson PT, Nordin EZ, Bohgard M, Sanati M, Pagels JH. Effective density characterization of soot agglomerates from various sources and comparison to aggregation theory effective density characterization of soot agglomerates from various sources and comparison to aggregation theory. *Aerosol Sci Technol* (2013) **47**, 792–805.

[46] Bond TC, Bergstrom RW. Light absorption by carbonaceous particles: An investigative review. *Aerosol Sci Technol* (2006) **40**, 27–67.

[47] Glassman I, Yetter RA. Combustion. Academic Press; (2007).

[48] Kelesidis GA, Goudeli E, Pratsinis SE. Flame synthesis of functional nanostructured materials and devices: Surface growth and aggregation. *Proc Combust Inst* (2017) **36**, 29–50.

[49] Jones WP, Marquis AJ, Vogiatzaki K. Large-eddy simulation of spray combustion in a gas turbine combustor. *Combust Flame* (2014) **161**, 222–39.

[50] Kelesidis GA, Goudeli E. Self-preserving size distribution and collision frequency of flame-made nanoparticles in the transition regime. *Proc Combust Inst* (2021) **38**, 1233–40.

[51] Goudeli E, Eggersdorfer ML, Pratsinis SE. Coagulation-agglomeration of fractal-like particles: Structure and self-preserving size distribution. *Langmuir* (2015) **31**, 1320–7.

[52] Saffaripour M, Tay LL, Thomson KA, Smallwood GJ, Brem BT, Durdina L, Johnson M. Raman spectroscopy and TEM characterization of solid particulate matter emitted from soot generators and aircraft turbine engines. *Aerosol Sci Technol* (2017) **51**, 518–31.

[53] Rogak SN, Flagan RC, Nguyen H V. The mobility and structure of aerosol agglomerates. *Aerosol Sci Technol* (1993) **18**, 25–47.

[54] Olfert J, Rogak S. Universal relations between soot effective density and primary

particle size for common combustion sources. *Aerosol Sci Technol* (2019) **53**, 485–92.

[55] Tajima N, Sakurai H, Fukushima N, Ehara K. Design considerations and performance evaluation of a compact aerosol particle mass analyzer. *Aerosol Sci Technol* (2013) **47**, 1152–62.

[56] Kholghy MR, Kelesidis GA, Pratsinis SE. Reactive polycyclic aromatic hydrocarbon dimerization drives soot nucleation. *Phys Chem Chem Phys* (2018) **20**, 10926–38.

[57] Heinson WR, Sorensen CM, Chakrabarti A. Does shape anisotropy control the fractal dimension in diffusion-limited cluster-cluster aggregation? *Aerosol Sci Technol* (2010) **44**, i-iv.

[58] Olfert JS, Dickau M, Momenimovahed A, Saffaripour M, Thomson K, Smallwood G, Stettler MEJ, Boies A, Sevcenco Y, Crayford A, Johnson M. Effective density and volatility of particles sampled from a helicopter gas turbine engine. *Aerosol Sci Technol* (2017) **51**, 704–14.

[59] Johnson TJ, Olfert JS, Symonds JPR, Johnson M, Rindlisbacher T, Swanson JJ, Boies AM, Thomson K, Smallwood G, Walters D, Sevcenco Y, Crayford A, Dastanpour R, Rogak SN, Durdina L, Bahk YK, Brem B, Wang J. Effective density and mass-mobility exponent of aircraft turbine particulate matter. *J Propuls Power* (2015) **31**, 573–80.

[60] Kelesidis GA, Pratsinis SE. A perspective on gas-phase synthesis of nanomaterials: Process design, impact and outlook. *Chem Eng J* (2021) **421**, 129884.

[61] Schauer JJ, Mader BT, Deminter JT, Heidemann G, Bae MS, Seinfeld JH, Flagan RC, Cary RA, Smith D, Huebert BJ, Bertram T, Howell S, Kline JT, Quinn P, Bates T, Turpin B, Lim HJ, Yu JZ, Yang H, Keywood MD. ACE-Asia intercomparison of a thermal-optical method for the determination of particle-phase organic and elemental carbon. *Environ Sci Technol* (2003) **37**, 993–1001.

[62] Corbin JC, Moallemi A, Liu F, Gagné S, Olfert JS, Smallwood GJ, Lobo P. Closure between particulate matter concentrations measured ex situ by thermal–optical analysis and in situ by the CPMA–electrometer reference mass system. *Aerosol Sci Technol* (2020) **54**, 1293–309.

[63] Delhaye D, Ouf FX, Ferry D, Ortega IK, Penanhoat O, Peillon S, Salm F, Vancassel X, Focsa C, Irimiea C, Harivel N, Perez B, Quinton E, Yon J, Gaffie D. The MERMOSE project: Characterization of particulate matter emissions of a commercial aircraft engine. *J Aerosol Sci* (2017) **105**, 48–63.

[64] Saffaripour M, Zabeti P, Kholghy M, Thomson MJ. An experimental comparison of the sooting behavior of synthetic jet fuels. *Energy and Fuels* (2011) **25**, 5584–93.

[65] Maricq MM, Harris SJ, Szente JJ. Soot size distributions in rich premixed ethylene flames. *Combust Flame* (2003) **132**, 328–42.

[66] Waser O, Groehn AJ, Eggersdorfer ML, Pratsinis SE. Air entrainment during flame aerosol synthesis of nanoparticles. *Aerosol Sci Technol* (2014) **48**, 1195–206.

[67] Kelesidis GA, Pratsinis SE. Estimating the internal and surface oxidation of soot agglomerates. *Combust Flame* (2019) **209**, 493–9.

[68] Marcolli C, Mahrt F, Kärcher B. Soot PCF: Pore condensation and freezing framework for soot aggregates. *Atmos Chem Phys* (2021) **21**, 7791–843.

Chapter 3

Dynamics of soot formation by enclosed spray combustion of jet fuel[3]

Abstract

Understanding the dynamics of soot formation and growth during combustion of jet fuel is essential for mitigation of aircraft engine emissions. Here, soot formation during enclosed spray combustion of jet fuel is investigated by microscopy, scanning mobility particle, X-ray diffraction & Raman spectroscopy measurements and discrete element modeling (DEM) along the flame centerline at various Effective eQuivalence Ratios (EQR). The DEM-derived mobility and primary particle size distribution dynamics are in excellent agreement with those measured at 5 – 63 cm height above the burner (HAB) for the experimentally measured temperature and soot volume fraction. At low EQR (1.46 and 1.59) soot surface growth is rather limited and stops at about residence time, t = 4 – 7 ms, resulting in median soot primary particle diameters, $\bar{d}_{\mathrm{p}}$, of ~ 14 nm. At longer t (high HAB), agglomeration takes over and increases the median mobility diameter from 16 to 88 or 145 nm at EQR of 1.46 or 1.59, respectively, without altering its $\bar{d}_{\mathrm{p}}$ and having the disorder over graphitic Raman band ratio, D/G = 0.90 ± 0.01, an interlayer distance, d_{002} = 3.68 ± 0.01 Å and a crystallite length, L_{c} = 1.24 ± 0.02 nm. In contrast, increasing EQR from 1.59 to 1.88, enhances soot surface growth, increases $\bar{d}_{\mathrm{p}}$ up to 23 nm and results in more graphitic soot having D/G = 0.80 ± 0.01, d_{002} = 3.63 ± 0.01 Å and L_{c} = 1.47 ± 0.01 nm. Furthermore, the L_c and D/G of soot are linearly proportional and inversely proportional, respectively, to its $\bar{d}_{\mathrm{p}}$ that is determined largely by surface growth.

[3] A version of this chapter is published in *Fuel* (2023) **342**, 127864.

3.1 Introduction

Aircraft engines are significant sources of ultrafine soot agglomerates [1] that have large inflammatory and cytotoxic responses [2] and contribute to global warming through their direct radiative forcing [3], as well as by facilitating ice nucleation and formation of contrail cirrus clouds [4]. The mobility diameter, d_m, of such agglomerates determines their transport and lifetime in the atmosphere [5] as well as their deposition in our respiratory system [6]. The primary particle (PP) diameter, d_p, and nanostructure of soot largely determine its oxidative reactions [7] and cytotoxicity [8]. So, understanding the relation between combustion conditions and soot size, composition and morphology is essential to quantify and mitigate the impact of such emissions on climate change and public health.

The size distribution of soot agglomerates from jet fuel combustion in an aircraft engine varies significantly with the applied thrust as summarized recently [9]. The nanostructure of aircraft soot emissions is commonly quantified by the disorder and graphitic bands of their Raman spectrum that is hardly affected by thrust [10]. Monitoring the dynamics of soot nanoparticles during combustion in an aircraft engine is essential to explain the impact of thrust on formation of soot and assist mitigation of its emissions. This can be done by probe or thermophoretic sampling that require though substantial modifications of the engine design [11]. So, aircraft soot emissions have been sampled only at the exhaust of the engine [12].

In this regard, monitoring the dynamics of soot in flame reactors that generate soot with equivalent characteristics to aircraft soot can provide the much needed understanding of soot formation in aircraft engines [13]. The soot d_m and d_p dynamics [14] have been measured using scanning mobility particle sizers (SMPS) and microscopy in laminar premixed ethylene [15], propene [16], ethane or acetylene [17] flames at various EQRs [18] that lead to similar median $\bar{d}_m$ and $\bar{d}_p$ with those of aircraft soot emissions [19]. However, such premixed flame soot contains large amounts of organic carbon [20] and thus is less graphitic than aircraft soot [10]. Furthermore, the light hydrocarbons (e.g. ethylene, propene, ethane, acetylene) used in the above reactors result in lower soot mass concentrations than those from jet fuel combustion [9] due to limited soot nucleation [21].

Recently, it was shown that enclosed spray combustion of jet fuel produces soot agglomerates at high concentrations with similar morphology, size distribution and organic carbon content with those of aircraft emissions [9]. The high concentrations allowed for analysis of the specific surface area, SSA, with N_2 adsorption which is typically not feasible due to the low mass of soot collected from the aircraft exhausts. Here, the dynamics of soot formation and growth are monitored during enclosed spray combustion of jet fuel [9] along the burner

centerline. The flame EQR is varied from 1.46 to 1.88 to quantify its impact on the evolution of the soot size distribution and composition by mobility, microscopy and Raman spectroscopy measurements along with discrete element modeling, DEM, simulations. Understanding soot dynamics during enclosed spray combustion of jet fuel can assist the development of robust models to guide the design and operation of aircraft engines with minimal soot emissions.

3.2 Experimental

Soot was generated by jet A1 fuel ($C_{11.6}H_{22}$ [22], Birrfeld Airport, Lupfig, Switzerland) enclosed spray combustion [9] using an external-mixing, twin fluid nozzle [23] enclosed in two, 30 cm long stainless steel and quartz tubes (each with a 42 mm inner diameter) in series [24], as shown in the experimental diagram (Appendix D: Fig. D1). So, 4.5 mL/min of fuel were dispersed into a fine spray with 0.66 – 2.0 L/min of O_2 to vary the EQR from 1.46 to 1.88. Given that the true fuel/oxidizer ratio is not known throughout the flame, the Effective eQuivalence Ratio (EQR) is calculated accounting for all oxygen sources [9], is:

$$EQR = \frac{\left(\frac{Fuel}{Air}\right)_{Actual}}{\left(\frac{Fuel}{Air}\right)_{Stoichiometric}} \tag{3.1}$$

The spray was ignited and sustained by a supporting premixed methane/oxygen flame (CH_4 = 1.25 L/min, O_2 = 2.25 L/min). Sheath air was fed through 12 evenly spaced holes surrounding the spray flame at 20 L/min. A torus ring with 12 jet outlets between the two tubes was used to introduce 20 L/min of N_2 in an upward swirled pattern to quench the flame and dilute the exhaust aerosol [25].

The flame temperature, *T*, was measured with the spray present using a 1 mm (nominal) bead diameter, R-type thermocouple (Intertechno-Friag AG) and corrected for radiative heat losses [26]. In the absence of flames, the spray produces droplets of about 36 μm in diameter at HAB = 6 cm and EQR = 1.46 (Fig. D2). However, these droplets evaporate within a millisecond (HAB << 5 cm, Fig. 3.3) during combustion [27], as *T* increases up to 1603 K at HAB = 5 cm which is much larger than the autoignition *T* = 483 K of jet A1 fuel [28]. Phase-Doppler anemometery and computational fluid dynamics of ethanol combustion in the same burner also indicated that the spray droplets completely evaporate by HAB = 5 cm (i.e. the smallest HAB measured here) [29]. Given that higher temperatures are encountered in enclosed than open burners, fuel droplets evaporate much faster in enclosed ones. For example, in the enclosed flame shown in Fig. 3.1a of [30] droplets are exposed to prolonged higher temperatures than in the open flame of Fig. 3.1g of [30] that has a much narrower high temperature zone in its center. So, the probe does not perturb the spray at HAB = 5 cm, as the

droplets have already evaporated completely. The thermocouple does not affect the fuel vaporization and subsequent soot aerosol dynamics (Fig. D3) and catalytic effects on the Pt thermocouple surface seem to be negligible. Nonetheless, the mobility and primary particle size distributions were measured here in the absence of a thermocouple. The *T* profile was measured here in a premixed ethylene flame to validate the energy balance used for the radiation correction [26]. The excellent agreement between the premixed flame *T* (Fig. D4: symbols & solid line) measured here and that obtained by Oktem et al. [31] (Fig. D4: broken line) validates the present energy balance calculations.

Soot was extracted from the centerline of the flame using a straight sampling probe with in-flow tube inner diameter of 2.5 mm becoming 5 mm after a 15 mm long entrance [32] at HAB = 5, 10, 15, 20 and 25 cm through five evenly spaced, sealable holes in the bottom stainless steel tube (Fig. D1), as well as at the top of the quartz tube (HAB ~ 63 cm). Since the flame is enclosed by a stainless steel tube, any perturbations induced by the sampling probe cannot be observed. However, measurements at HAB = 63 cm do not seem to be affected by the presence of the thermocouple (Fig. D3). Therefore, the sampling probe does not affect the spray at the HAB = 5 – 63 cm investigated here. The sampled aerosol was rapidly diluted and quenched by mixing with N_2, followed by compressed air from a rotating disk diluter and directed to an SMPS, as well as to a glass fiber filter for offline analysis. The total dilution ratio ranges from 30 to 45. The dilution ratios used here keep the total number concentration of the sampled aerosol at about ~ 10^6 #/cm^3, limiting perturbations of the measured mobility size distribution due to coagulation in the sampling line [32]. The present sampling and dilution system can reduce the temperature of the sampled aerosol down to 264 ºC even at low HAB = 10 cm [32].

The Raman spectra of filter-collected soot nanoparticles were obtained using a 515 nm laser having 50 mW power (Renshaw inVia). The laser was focused with a x20 magnification optical microscope which gives a 2 μm spot size, 10 % laser power was focused on the sample for 120 s and three spectral acquisitions per spot [33]. Raman spectra were obtained and averaged over three positions on the filter surface. The intensities of the disorder (D ~ 1350 cm^{-1}) and graphitic (G ~ 1580 cm^{-1}) bands [33] were obtained after straight line subtraction of the baseline [34]. The ratio of D/G was obtained by simply comparing the intensity (height) of the two peaks. This ratio has been related to the average size of crystalline domains to quantify the degree of soot graphitization based on graphite material studies [35]. The D/G ratio is used here for a comparison of soot graphitization at various HAB and EQR. Soot graphitization was also investigated by X-ray diffraction (XRD) with the method described in detail elsewhere [36]. Briefly, an AXS D8 diffractometer (Bruker) at a scan rate of 0.0197 °/s over the range of

diffraction angles from 2θ = 10˚ – 70˚ was used to obtain the peak angle and full width half maximum (FWHM) of the 002 peak. From this, Bragg's law can be used to quantify the crystallite length, L_c and interlayer distance, d_{002} [37].

Soot collected on the filter was imaged by transmission electron microscopy (TEM, FEI Tecnai F30 FEG). The nanoparticles were dispersed in ethanol and placed in an ultrasonic bath for 15 min to break up large agglomerates [23]. A drop of ethanol solution was then placed on lacey carbon TEM grids with a 200 mesh copper support (LC200-Cu-150, Electron Microscopy Sciences) and allowed to dry. The d_p was measured by manually placing ellipses over the PPs in ImageJ [38] and calculating the area-equivalent diameter. More than 200 PPs were measured for each HAB and EQR to determine the $\bar{d}_p$. The $\bar{d}_p$ levels off after 200 PPs are counted (Fig. D5, consistent with microscopy analysis of soot [39] and TiO_2 [40] nanoparticles.

3.3 Theory

Soot formation by surface growth and agglomeration is investigated by DEM assuming extremely fast soot inception [13] and an initial number/size of soot nuclei [41] attained after complete fuel spray vaporization and combustion. Soot oxidation is not considered as it seems negligible during enclosed spray combustion of jet fuel since the soot volume fraction, f_v, increases by surface growth at small HAB and levels off at HAB > 25 cm (Fig. D6). So, oxidation does not reduce soot f_v at the combustion conditions employed here and can be neglected. Coalescence is not included in the present DEM, as soot nanoparticles with $d_m \geq 2$ nm hardly coalesce due to their large C content [42]. So, necking between soot primary particles occurs by surface growth [41].

The DEM-derived dynamics of nascent [41] and mature [43] soot (e.g. in premixed flame reactors [39]) have been detailed and validated previously. In brief, 1000 monodisperse soot particles with initial diameter of 2 nm and number density of $4.5 \cdot 10^{16}$ #/m^3 are randomly distributed in a cubic cell. This initial soot diameter is the smallest identified in laminar premixed ethylene flames [44]. Similarly, the initial soot number density that is used here is the largest one measured in a premixed ethylene flame at 0.55 cm HAB [44]. The temperature, T, of the cubic cell is varied as a function of the Knudsen number, Kn, to follow closely the T measurements of enclosed spray combustion of jet fuel (Fig. D7). So, the particle velocities are rescaled using a Gaussian thermostat [45] to follow the Maxwell-Boltzmann distribution obtained based on the measured T. So, the HAB is related to the residence time by matching the Kn from the DEM to that from the measured values.

The Hydrogen Abstraction Carbon Addition (HACA) mechanism [46] is used to account for soot surface growth as DEM simulates soot formation after inception has stopped [38]. The H, H_2 and C_2H_2 concentrations involved in soot surface growth by HACA [46] are included in the present DEM [41]. The maximum computed soot f_v can be varied from 5 to 100 ppb by increasing the H concentration from 0.36 to 7.5 mmol/m^3 [41]. At constant H concentration, varying the acetylene concentration does not affect the computed f_v, as H abstraction from the soot surface is the rate limiting step of the HACA mechanism [46]. The initial number of hydrogen atoms and acetylene molecules is varied to attain the measured maximum soot volume fraction of about 100 ppb.

During enclosed spray combustion, nanoparticles are formed at a wide range of residence times due to turbulence and recirculation [30]. The present DEM follows only the average residence time of the flame neglecting turbulence and any recirculation if present given the low soot volume fractions, $f_v \leq 100$ ppb, during enclosed spray combustion of jet fuel (Fig. D6). The computed mobility diameter, d_m, is obtained based on the projected area, A_{proj}, of the DEM-derived soot agglomerates [47]:

$$d_m = 2 \cdot \sqrt{\frac{A_{proj}}{\pi}} \tag{3.2}$$

The measured d_m is obtained based on the electrical mobility of the sampled soot nanoparticles [48]. In the free molecular and transition regimes, the d_m obtained using the agglomerate A_{proj} (Eq. 3.2) is identical to that measured based on its electrical mobility [47]. The gas mean free path, λ, is defined as [49]:

$$\lambda = \frac{2 \cdot \eta}{p \cdot \sqrt{\frac{8 \cdot MW}{\pi \cdot R \cdot T}}} \tag{3.3}$$

where MW and η are the molecular weight and viscosity of air, respectively, p is the pressure, R the universal gas constant and T the temperature. The residence time and soot dynamics are derived here by DEM only at EQR = 1.46 and 1.59, as Kn (used here to impose the measured T profile in the simulations) could not be measured as a function of HAB at EQR > 1.59. This due to the large particle number concentrations limiting probe sampling at HAB < 63 cm.

3.4 Results and Discussion

3.4.1 Flame temperature

Fig. 3.1 shows the flame T as a function of HAB during enclosed spray combustion of jet fuel at EQR = 1.46 (triangles), 1.59 (circles), 1.73 (squares) and 1.88 (diamonds). The T reaches its

maximum at HAB = 5 – 10 cm. As HAB increases, *T* decreases almost linearly reaching 900 – 1220 K at 25 cm, consistent with *T* profiles in premixed ethylene flames [50]. After N_2 is introduced at HAB = 30 cm, *T* is further reduced reaching 600 – 690 K at HAB = 63 cm regardless of EQR. Increasing EQR from 1.46 to 1.88 decreases the maximum *T* from 1603 to 1300 K due to the reduced combustion efficiency [51] consistent with *T* measurements in ethanol spray flames [29]. The maximum *T* here is about 300 K lower than the theoretical adiabatic flame *T* of jet A1 vapor in a premixed combustor at each EQR from all O_2 sources [51].

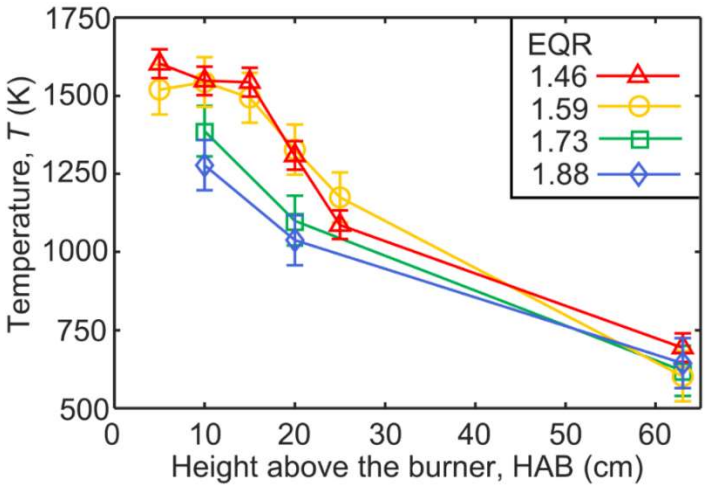

Fig. 3.1: Flame temperature, *T*, as a function of HAB during enclosed spray combustion of jet A1 fuel at effective equivalence ratio, EQR = 1.46 (triangles), 1.59 (circles), 1.73 (squares) & 1.88 (diamonds).

3.4.2 Soot dynamics along the burner axis

During enclosed spray combustion of jet fuel at EQR = 1.46 (Fig. D8: triangles) and 1.59 (Fig. D8: circles), soot particles experience residence times of about 100 and 400 ms, respectively, at HAB = 30 cm. These residence times derived by DEM are on par with the 60 – 400 ms obtained by computational fluid dynamics in an identical enclosed burner at a similar HAB [30]. At HAB = 63 cm, these residence times are 400 and 2500 ms at EQR = 1.46 and 1.59, respectively. Fig. 3.2 shows the measured (symbols) and DEM-derived (lines) mobility diameter, d_m, distributions of soot at EQR 1.46 and HAB of 5 (d), 15 (c), 25 (b) and 63 cm (a) and the corresponding *T* (Fig. 3.1) and representative DEM-derived agglomerate schematics. The shaded area shows the variability of at least 10 SMPS measurements per HAB. For example, increasing HAB from 5 to 25 cm increases the median mobility diameter, $\bar{d}_m$, from 16 to 63 nm, consistent with soot $\bar{d}_m$ dynamics in premixed flames [15]. After introducing N_2 at HAB = 30 cm, the flame *T* is further reduced (Fig. 3.1) diluting the aerosol and slowing down coagulation. The mobility size distribution measured here is in excellent agreement with that reported in (Fig. 3.2a, triangles, [9]), further validating the experimental methods used in this work. So, $\bar{d}_m$ increases only up to 88 nm at HAB = 63 cm. The DEM-derived d_m distributions

(lines) span a limited range of d_m because they only account for particles which have experienced a single residence time [41], while in-flame measurements at such turbulent conditions include particles from multiple residence times that are dominated by those around the centerline [52]. At all HABs, the DEM-derived d_m distributions (lines) are in agreement with the measured ones (symbols). Good agreement between DEM simulations and measurements is obtained at all EQR (Fig. D9 for EQR = 1.59) indicating that DEM can follow accurately soot dynamics during enclosed spray combustion of jet fuel given the measured T and volume fraction profiles.

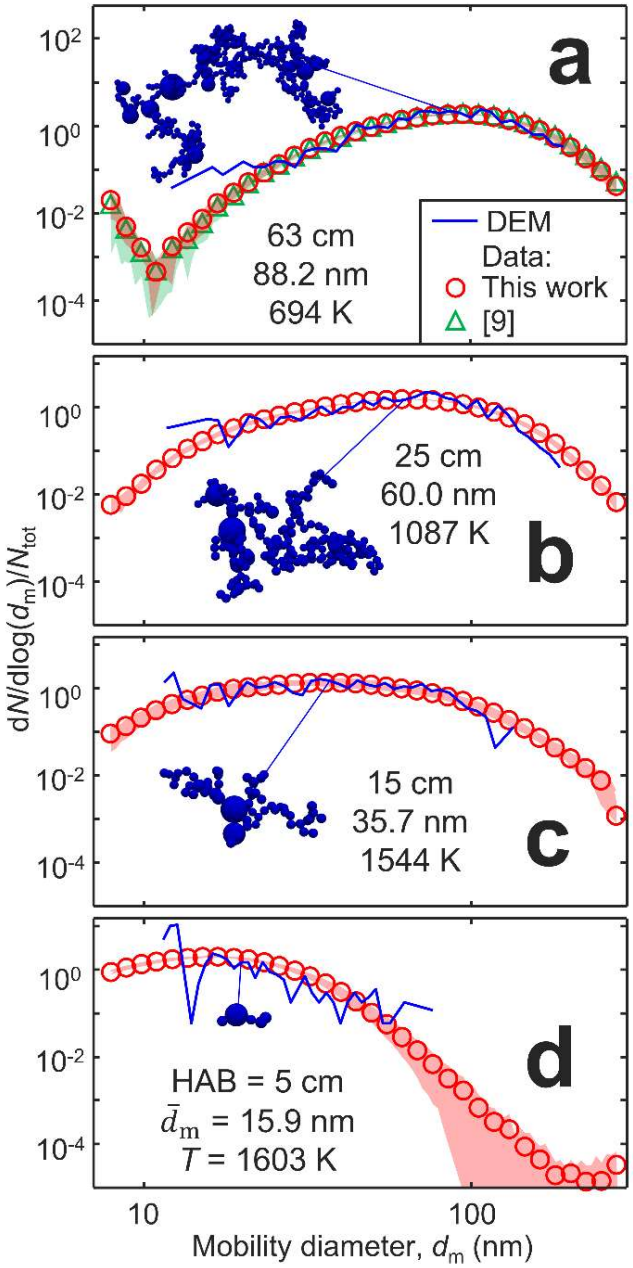

Fig. 3.2: Mobility diameter, d_m, distributions of soot from enclosed spray combustion of jet fuel at EQR = 1.46 and HAB = 5 (d), 15 (c), 25 (b) and 63 cm (a) from experiments (symbols, shaded area) and DEM simulations (lines) along with representative schemes of the corresponding agglomerate having that $\bar{d}_m$. Circles represent this work, triangles represent data from [9].

Fig. 3.3 shows the measured (symbols) and DEM-derived (lines) soot $\bar{d}_{\mathrm{m}}$ (circles, solid line) and $\bar{d}_{\mathrm{p}}$ (triangles, broken line), as a function of Knudsen number, *Kn*, (bottom abscissa) for EQR = 1.46 with exemplary schematics of DEM-calculated agglomerates. The soot *Kn* was estimated from the measured *T* and $\bar{d}_{\mathrm{m}}$ obtained at various HAB (top abscissa). It was also derived by DEM as a function of *t* (second top abscissa). The DEM-derived $\bar{d}_{\mathrm{m}}$ and $\bar{d}_{\mathrm{p}}$ are in excellent agreement with the measurements, quantitatively explaining soot dynamics during enclosed combustion of jet fuel. For example, at *t* < 12 ms and HAB < 5 cm, soot grows largely by surface growth, consistent with soot formation in premixed flames [43]. There, soot nanoparticles are rather spherical, having $\bar{d}_{\mathrm{m}} = \bar{d}_{\mathrm{p}}$ that increases up to about 13 nm at *t* = 7 ms. From then on, agglomeration dominates and increases $\bar{d}_{\mathrm{m}}$ up to 88 nm at HAB = 63 cm, while $\bar{d}_{\mathrm{p}}$ remains rather constant. At higher EQR (i.e. 1.59), both soot number density [53] and coagulation rate increase [50] as agglomeration largely takes over at *t* > 4 ms at this EQR (Fig. D8).

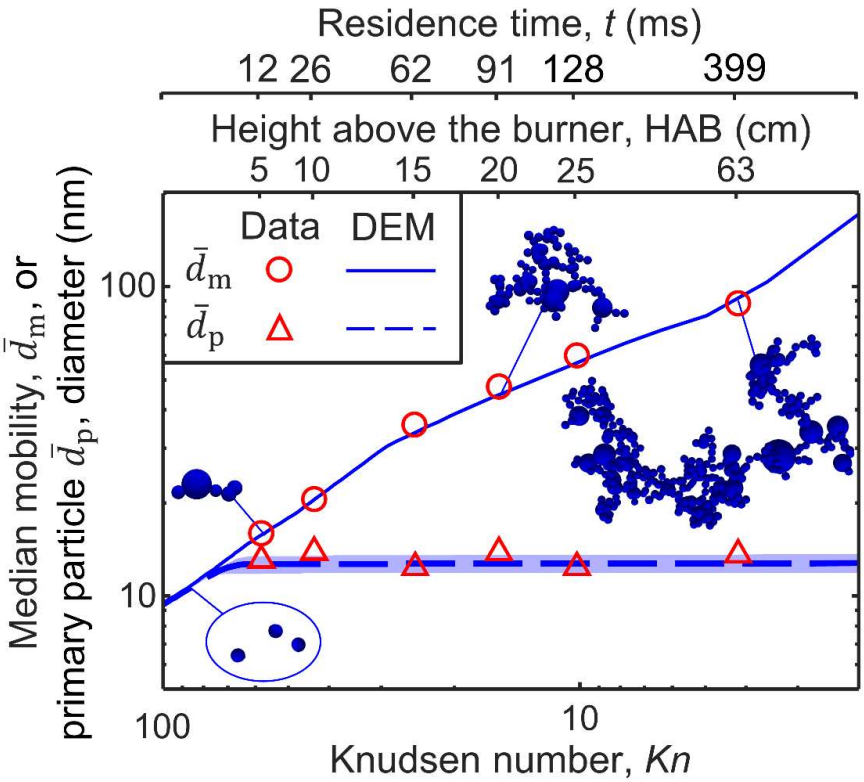

Fig. 3.3: Median mobility, $\bar{d}_m$, (circles, solid line) and primary particle $\bar{d}_p$, (triangles, broken line) diameters as a function of *Kn* (bottom abscissa), HAB (top abscissa) or residence time, *t*, (second top abscissa) measured (symbols) or derived by DEM (lines) at EQR = 1.46.

Fig. 3.4 shows the PP size distributions produced at EQR = 1.46 and measured at HAB = 63 cm (symbols) and derived by DEM at *t* = 0.8 (dot-broken line), 1.7 (broken line) and 12 (dotted line) that overlays with that of 399 ms or HAB = 63 cm (solid line). The PP size distributions measured at HAB = 5 – 25 cm (Fig. D10) are practically identical with that

measured at HAB = 63 cm (Fig. 3.4: symbols), consistent with the simulations at t = 12 – 399 ms. So, the evolution of the PP size distribution during the early stages of soot formation can be elucidated by DEM as it is not possible to measure it there with our instruments. For instance, young soot PPs with $\bar{d}_p$ = 7.4 nm and geometric standard deviation, $\sigma_{g,p}$ = 1.2 are formed by surface growth and aggregation at t = 0.8 ms. As t increases to 1.7 and 12 ms, surface growth dominates, shifting $\bar{d}_p$ to 12.7 nm (Fig. 3.3, triangles) and $\sigma_{g,p}$ is largely constant, ~ 1.26. Even though coagulation increases agglomerate size (Fig. 3.3, circles), the soot PP size (d_p) distribution does not change at t > 7 ms, as surface growth has levelled off [41]. The DEM-derived PP size distributions obtained at t = 12 and 399 ms overlap and are in agreement with the measured ones. This further validates the present DEM simulations and indicates that surface growth stops at short residence times (t < 7 ms) during enclosed combustion of jet fuel.

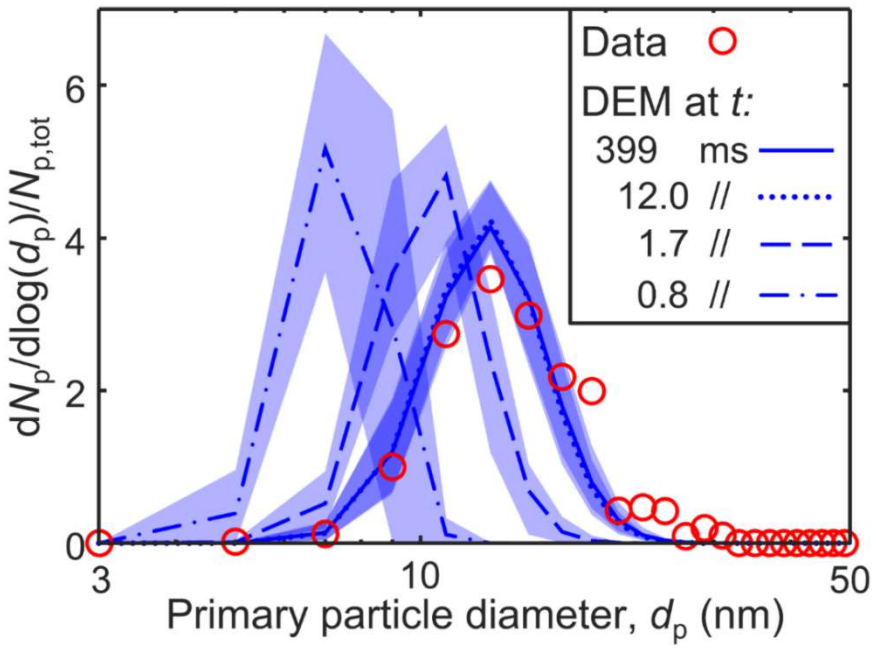

Fig. 3.4: The PP distributions of soot made at EQR = 1.46 and measured at HAB = 63 cm (symbols) or derived by DEM at t = 0.8 (dot-broken line), 1.7 (broken line), 12 (dotted line) and 399 ms (solid line).

Fig. 3.5 shows the Raman spectra along with the ratio of the disorder (D ~ 1350 cm^{-1}) over the graphitic (G ~ 1580 cm^{-1}) band measured at HAB = 5 (double dot-broken line), 10 (dot-broken line), 25 (broken line) and 63 cm (solid line) from soot made at EQR = 1.46 that are quite similar to those made at EQR = 1.59 (Fig. D11). More graphitic soot nanoparticles having D/G = 0.85 ± 0.01 are formed at HAB = 5 cm and T = 1600 K (Fig. 3.1). As HAB increases from 5 to 10 cm, T decreases (Fig. 3.1) and D/G increases up to 0.88 ± 0.01. The Raman spectra dynamics of soot produced at EQR = 1.59 is shown in Fig. D11. Based on the uncertainty error bars, the increase of D/G from 0.85 to 0.9 is not within the experimental noise. This increase is similar to that of D/G of premixed flame soot that had been attributed to increasing soot maturity

[54]. X-ray photoelectron spectroscopy suggests that this increase of soot D/G can be attributed to reactions at the soot surface that increase the sp^3-hybridized carbon content [55]. Above HAB = 10 cm, D/G asymptotically reaches 0.87 – 0.89. Similar asymptotic D/G are obtained at EQR = 1.59 (Fig. D11). This is attributed to coagulation at low $T < 1500$ K (Fig. 3.1) that does not affect soot nanostructure [54] as limited oxidation is expected to take place in the enclosed flame environment especially after injection of 20 L/min of N_2 at 30 cm HAB. The Raman spectra of soot generated here at EQR ≤ 1.59 and HAB = 63 cm are in agreement with that of aircraft soot (Fig. 3.5, dotted line) [10]. At the same time, the spectra are quite different from that produced by a diesel engine [33] which produced a D/G ratio of 0.80 and a slight shift in the D peak relative to that of aircraft soot (Fig. D11, dotted line). This indicates that the nanostructure of soot produced here at low EQR is similar to that of aircraft emissions.

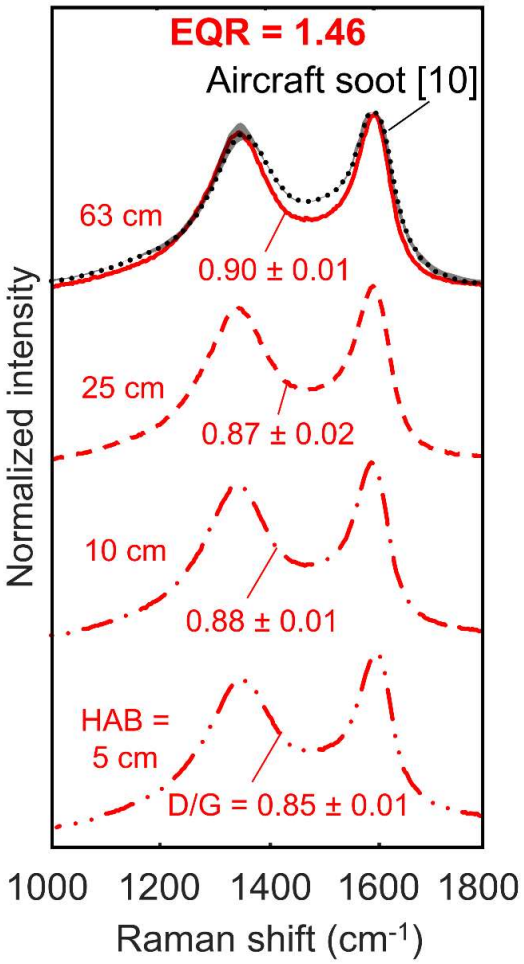

Fig. 3.5: Normalized intensity as a function of Raman shift measured from soot produced by enclosed combustion of jet fuel spray at EQR = 1.46 and HAB = 5 cm (double dot-broken line), 10 (dot-broken line), 25 (broken line) and 63 cm (solid line) in comparison to that of aircraft soot (dotted line [10]).

3.4.3 Impact of EQR on soot PP size distribution and nanostructure

Fig. 3.6a shows the d_p distributions along with the median $\bar{d}_p$ and $\sigma_{g,p}$ of soot produced by enclosed spray combustion of jet fuel at EQR = 1.46 – 1.88 at HAB = 63 cm. The d_p distribution

is hardly affected at EQR of 1.46 and 1.59, resulting in a $\bar{d}_p$ of about 14 nm, consistent with our previous work [9]. Increasing EQR to 1.73 or 1.88 though, increases $\bar{d}_p$ to 20 or 23 nm, consistent with measurements in rich premixed [39] and diffusion flames [55]. This can be attributed to enhanced surface growth [43] or prolonged high temperature residence times [41] at high EQR.

Fig. 3.6b shows the Raman spectra along with the D/G of soot produced at EQR = 1.46 – 1.88 at HAB = 63 cm. The Raman spectrum of soot made at EQR = 1.59 is almost identical to that obtained at EQR = 1.46 and the same HAB (Fig. 3.5) having D/G = 0.90 ± 0.01. Further increasing EQR to 1.73 and 1.88 decreases D/G to 0.83 ± 0.01 and 0.80 ± 0.01, respectively. This indicates that soot nanoparticles produced at EQR > 1.59 are more graphitic than those made at lower EQR. This is despite the low T at EQR > 1.59 (Fig. 3.1) which results in less graphitic nanoparticles in premixed flame reactors [54]. The valley between the D and G peaks, as well as their full width at half maximum increases with increasing EQR. This is due to the secondary D2, D3 and D4 Raman bands that are attributed to surface graphene defects, amorphous carbon, polyenes and/or ionic impurities [56]. The width and intensity of these bands increase with increasing organic to total carbon (OC/TC) mass ratio and thus could indicate the adsorption of disordered polyaromatic hydrocarbons on soot [57]. The organic to total carbon (OC/TC) mass ratio was also measured for soot from enclosed spray combustion of jet fuel at EQR = 1.46 – 1.88 and HAB = 63 cm, as described in [9] (Fig. D12). Increasing EQR from 1.46 to 1.59 decreases the OC/TC of soot from 17.6 to 10.9 %, consistent with past OC/TC measurements of soot made at identical conditions [9]. Further increasing EQR to 1.88 enhances OC/TC up to 14.4 % and explains the increase D/G the FWHM of the D and G peaks, corroborating data of premixed flame soot [57].

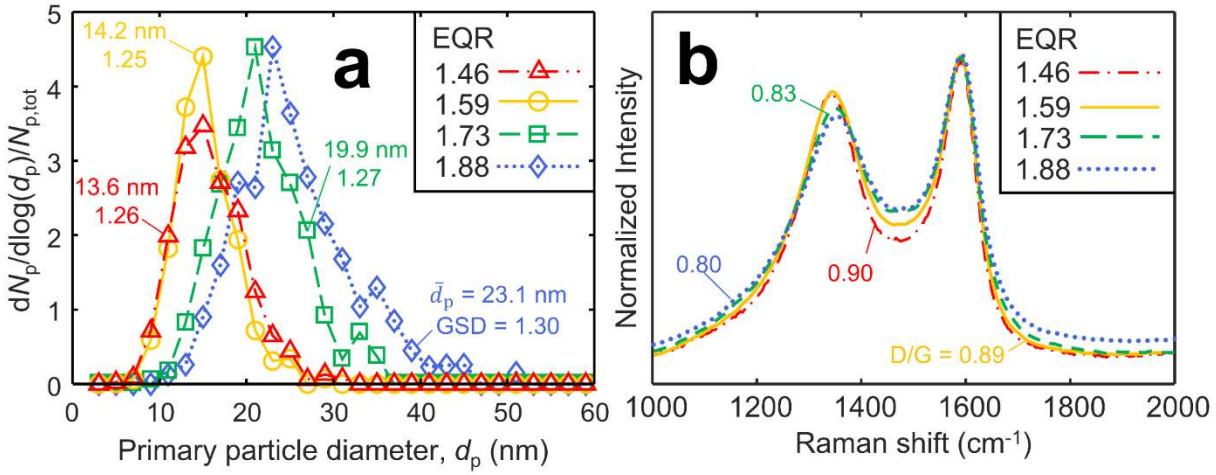

Fig. 3.6: Soot d_p distributions (a) and Raman spectra (b) obtained from enclosed spray combustion of jet fuel at EQR = 1.46 (triangles, dot-broken line), 1.59 (circles, solid line), 1.73 (squares, broken line) and 1.88 (diamonds, dotted line) at HAB = 63 cm.

Fig. 3.7 presents the soot D/G as a function of its $\bar{d}_p$ at EQR = 1.46 – 1.88, with selected TEM images of soot. Increasing EQR from 1.46 to 1.88 increases soot $\bar{d}_p$ from 14 to 23 nm while the soot D/G decreases from 0.9 to 0.8. This D/G drop with increasing $\bar{d}_p$ is in excellent agreement with measurements in turbulent diffusion flames (D/G from 11 to 5 for $\bar{d}_p$ increasing from 15 to 25 nm using a 785 nm laser for Raman) [58]. Aerodynamically classifying soot from an inverted ethylene diffusion flame similarly showed a correlation between impactor stage (i.e. aerodynamic diameter, d_a) and the D/G ratio from a 785 nm laser where D/G dropped from 13.5 at stage 4 (d_a = 22 – 38 nm) to 8.5 at stage 10 (d_a = 560 – 950 nm) [34]. So, while exposure to high temperatures at relatively long residence times has been shown to graphitize soot [59], $\bar{d}_p$ increases with increasing graphitic content of soot formed by diffusion and spray flames where the high-temperature residence time is short.

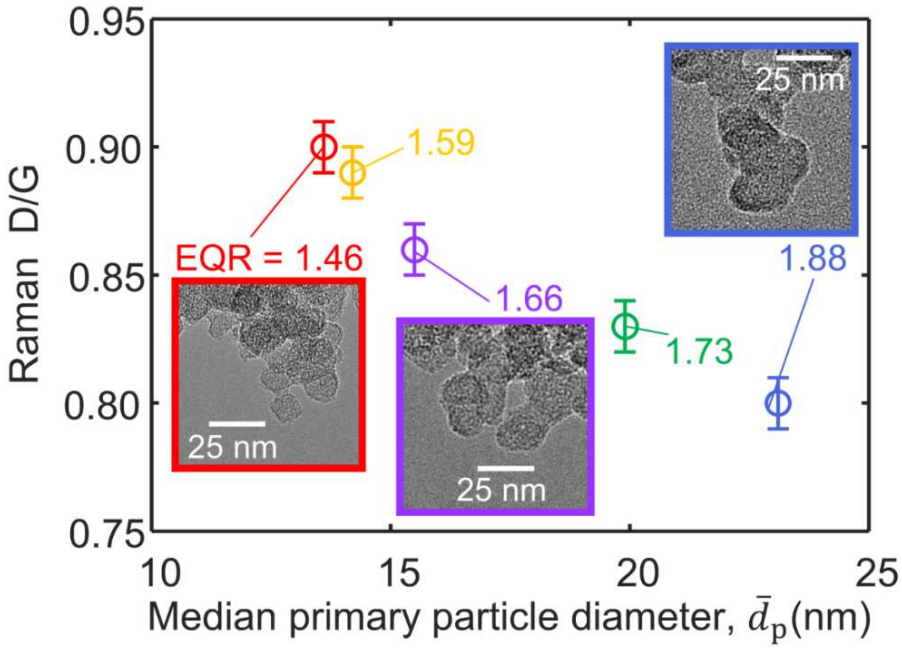

Fig. 3.7: Soot D/G ratio as a function of its median PP diameter, $\bar{d}_p$, measured here by enclosed spray combustion of jet fuel at EQR = 1.46 – 1.88 at HAB = 63 cm, with TEM images of soot at EQR of 1.46, 1.66 and 1.88.

To further verify this, the nanostructure of soot from enclosed spray combustion of jet fuel was analyzed with high resolution transmission electron microscopy (HRTEM; Fig. D13). Such images reveal that soot primary particles formed at EQR = 1.46 are rather amorphous and contain polyaromatic hydrocarbons (PAHs) arranged in small crystallites. As EQR increases, soot nanostructure becomes more ordered, and the length of their crystallites increases. This corroborates the Raman spectra obtained here and indicates that increasing EQR results in larger soot primary particles with higher graphitic content. In this regard, Fig. 3.8 shows the mean interlayer distance, d_{002} (circles), and crystallite length, L_c (triangles), as a function of mean d_p

of soot produced by enclosed spray combustion at EQR = 1.46 – 1.88 obtained from XRD patterns as described in [36]. As EQR increases and soot primary particles become larger by surface growth, d_{002} decreases and L_c increases. This further confirms that soot primary particles become more graphitic at increasing EQR and d_p. This can be attributed to enhanced surface growth through the HACA mechanism [46] that is required to produce large, graphitic soot nanoparticles [60] obtained here at HAB = 63 cm. This is also consistent with measurements [53] and simulations [61] in premixed flames showing that increasing EQR increases the soot d_m, decreases its optical band gap and thus enhances its graphitic content.

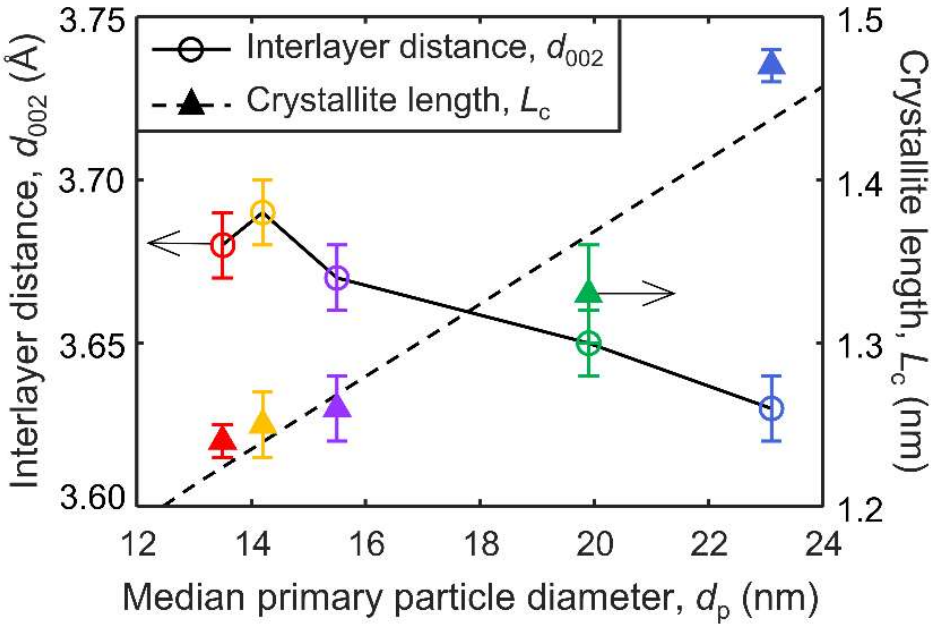

Fig. 3.8: Mean interlayer distance, d_{002} (circles) and crystallite length, L_c (triangles) as a function of median d_p of soot produced by enclosed spray combustion of jet fuel at EQR = 1.46 – 1.88.

3.5 Conclusions

The dynamics of soot formed during enclosed spray combustion of jet A1 [9] were investigated numerically and experimentally at HAB = 5 – 63 cm and EQR = 1.46 – 1.88. The soot mobility (Fig. 3.2), primary particle (Fig. 3.3) size distributions and nanostructure (Fig. 3.5) measured here as a function of height above the burner (HAB) elucidate in detail the dynamics of soot formation during enclosed spray combustion of jet fuel. These data are explained quantitatively by a discrete element model (DEM) for surface growth and agglomeration [41] that is used to describe such soot aerosol dynamics in spray flames for the first time to the best of our knowledge. The d_m and d_p distributions derived from DEM are in excellent agreement with experimental measurements at all conditions for the experimentally measured temperature and soot volume fraction. At HAB > 5 cm, the $\bar{d}_p$ does not increase as surface growth is limited at EQR = 1.46 or 1.59 ending after t = 7 and 4 ms, respectively, corresponding to HAB < 5 cm, as

elucidated by DEM. At these short t, $\bar{d}_p$ = 14 nm and does not grow from HAB = 5 to 63 cm while $\bar{d}_m$ increases by agglomeration to 88 or 145 nm at EQR = 1.46 or 1.59, respectively. At these low HAB, the soot nanostructure is slightly more graphitic and becomes more disordered after the maximum temperature is attained between HAB = 5 – 10 cm for all EQR. At HAB = 63 cm and EQR ≤ 1.59, the soot nanostructure is rather disordered with D/G = 0.90 ± 0.01. As the EQR increases from 1.59 to 1.88, the $\bar{d}_p$ increases to 23 nm through enhanced surface growth and becomes more graphitic having D/G = 0.80 ± 0.01 despite the lower flame temperatures with increasing EQR. This is consistent with observations in turbulent diffusion flames [58]. Thus, the D/G of soot is linearly inversely proportional to its $\bar{d}_p$ that is determined largely by surface growth.

3.6 References

[1] Westerdahl D, Fruin SA, Fine PL, Sioutas C. The Los Angeles International Airport as a source of ultrafine particles and other pollutants to nearby communities. *Atmos Environ* (2008) **42**, 3143–55.

[2] Cassee FR, Héroux ME, Gerlofs-Nijland ME, Kelly FJ. Particulate matter beyond mass: Recent health evidence on the role of fractions, chemical constituents and sources of emission. *Inhal Toxicol* (2013) **25**, 802–12.

[3] Kelesidis GA, Neubauer D, Fan LS, Lohmann U, Pratsinis SE. Enhanced light absorption and radiative forcing by black carbon agglomerates. *Environ Sci Technol* (2022) **56**, 8610–8.

[4] Kärcher B. Formation and radiative forcing of contrail cirrus. *Nat Commun* (2018) **9**, 1824.

[5] Bond TC, Doherty SJ, Fahey DW, Forster PM, Berntsen T, DeAngelo BJ, Flanner MG, Ghan S, Kärcher B, Koch D, Kinne S, Kondo Y, Quinn PK, Sarofim MC, Schultz MG, Schulz M, Venkataraman C, Zhang H, Zhang S, Bellouin N, Guttikunda SK, Hopke PK, Jacobson MZ, Kaiser JW, Klimont Z, Lohmann U, Schwarz JP, Shindell D, Storelvmo T, Warren SG, Zender CS. Bounding the role of black carbon in the climate system: A scientific assessment. *J Geophys Res Atmos* (2013) **118**, 5380–552.

[6] Rissler J, Swietlicki E, Bengtsson A, Boman C, Pagels J, Sandström T, Blomberg A, Löndahl J. Experimental determination of deposition of diesel exhaust particles in the human respiratory tract. *J Aerosol Sci* (2012) **48**, 18–33.

[7] Hagen FP, Kretzler D, Häber T, Bockhorn H, Suntz R, Trimis D. Carbon nanostructure and reactivity of soot particles from non-intrusive methods based on UV-VIS spectroscopy and time-resolved laser-induced incandescence. *Carbon* (2021) **182**, 634–54.

[8] Schmid O, Stoeger T. Surface area is the biologically most effective dose metric for acute nanoparticle toxicity in the lung. *J Aerosol Sci* (2016) **99**, 133–43.

[9] Trivanovic U, Kelesidis GA, Pratsinis SE. High-throughput generation of aircraft-like soot. *Aerosol Sci Technol* (2022) **56**, 732–43.

[10] Parent P, Laffon C, Marhaba I, Ferry D, Regier TZ, Ortega IK, Chazallon B, Carpentier

Y, Focsa C. Nanoscale characterization of aircraft soot : A high-resolution transmission electron microscopy , Raman spectroscopy , X-ray photoelectron and near-edge X-ray absorption spectroscopy study. *Carbon* (2016) **101**, 86–100.

[11] Zhang R, Kook S. Structural evolution of soot particles during diesel combustion in a single-cylinder light-duty engine. *Combust Flame* (2015) **162**, 2720–8.

[12] Saffaripour M, Thomson KA, Smallwood GJ, Lobo P. A review on the morphological properties of non-volatile particulate matter emissions from aircraft turbine engines. *J Aerosol Sci* (2020) **139**, 105467.

[13] Wang H. Formation of nascent soot and other condensed-phase materials in flames. *Proc Combust Inst* (2011) **33**, 41–67.

[14] Bladh H, Johnsson J, Olofsson NE, Bohlin A, Bengtsson PE. Optical soot characterization using two-color laser-induced incandescence (2C-LII) in the soot growth region of a premixed flat flame. *Proc Combust Inst* (2011) **33**, 641–8.

[15] Zhao B, Yang Z, Johnston M V., Wang H, Wexler AS, Balthasar M, Kraft M. Measurement and numerical simulation of soot particle size distribution functions in a laminar premixed ethylene-oxygen-argon flame. *Combust Flame* (2003) **133**, 173–88.

[16] Lin H, Gu C, Camacho J, Lin B, Shao C, Li R, Gu H, Guan B, Wang H, Huang Z. Mobility size distributions of soot in premixed propene flames. *Combust Flame* (2016) **172**, 365–73.

[17] Mei J, Wang M, Hou D, Tang Q, You X. Comparative study on nascent soot formation characteristics in laminar premixed acetylene, ethylene, and ethane flames. *Energy and Fuels* (2018) **32**, 11683–93.

[18] Maricq MM, Harris SJ, Szente JJ. Soot size distributions in rich premixed ethylene flames. *Combust Flame* (2003) **132**, 328–42.

[19] Ess MN, Vasilatou K. Characterization of a new miniCAST with diffusion flame and premixed flame options: Generation of particles with high EC content in the size range 30 nm to 200 nm. *Aerosol Sci Technol* (2019) **53**, 29–44.

[20] Maricq MM. Examining the relationship between black carbon and soot in flames and engine exhaust. *Aerosol Sci Technol* (2014) **48**, 620–9.

[21] Saggese C, Singh A V., Xue X, Chu C, Kholghy MR, Zhang T, Camacho J, Giaccai J, Miller JH, Thomson MJ, Sung CJ, Wang H. The distillation curve and sooting propensity of a typical jet fuel. *Fuel* (2019) **235**, 350–62.

[22] Dagaut P, Cathonnet M. The ignition, oxidation, and combustion of kerosene: A review of experimental and kinetic modeling. *Prog Energy Combust Sci* (2006) **32**, 48–92.

[23] Mädler L, Kammler HK, Mueller R, Pratsinis SE. Controlled synthesis of nanostructured particles by flame spray pyrolysis. *J Aerosol Sci* (2002) **33**, 369–89.

[24] Teleki A, Heine MC, Krumeich F, Akhtar MK, Pratsinis SE. In situ coating of flame-made TiO_2 particles with nanothin SiO_2 films. *Langmuir* (2008) **24**, 12553–8.

[25] Teleki A, Buesser B, Heine MC, Krumeich F, Akhtar MK, Pratsinis SE. Role of gas - aerosol mixing during in situ coating of flame-made titania particles. *Ind Eng Chem Res* (2009) **48**, 85–92.

[26] Shaddix CR. A new method to compute the radiant correction of bare-wire thermocouples. *33rd ASME Natl. Heat Transf. Conf. Mediterr. Combust. Symp.*, Naples, Italy: (2017).

[27] Kitano T, Nishio J, Kurose R, Komori S. Evaporation and combustion of multicomponent fuel droplets. *Fuel* (2014) **136**, 219–25.

[28] Glassman I, Yetter RA. Combustion. Academic Press; (2007).

[29] Gröhn AJ, Pratsinis SE, Wegner K. Fluid-particle dynamics during combustion spray aerosol synthesis of ZrO_2. *Chem Eng J* (2012) **191**, 491–502.

[30] Waser O, Brenner O, Groehn AJ, Pratsinis SE. Process design for size-controlled flame spray synthesis of $Li_4Ti_5O_{12}$ and electrochemical performance. *Chem Process Eng* (2017) **38**, 51–66.

[31] Öktem B, Tolocka MP, Zhao B, Wang H, Johnston M V. Chemical species associated with the early stage of soot growth in a laminar premixed ethylene – oxygen – argon flame. *Combust Flame* (2005) **142**, 364–73.

[32] Goudeli E, Gröhn AJ, Pratsinis SE. Sampling and dilution of nanoparticles at high temperature. *Aerosol Sci Technol* (2016) **50**, 591–604.

[33] Sadezky A, Muckenhuber H, Grothe H, Niessner R, Pöschl U. Raman microspectroscopy of soot and related carbonaceous materials: Spectral analysis and structural information. *Carbon* (2005) **43**, 1731–42.

[34] Baldelli A, Rogak SN. Morphology and Raman spectra of aerodynamically-classified soot samples. *Atmos Meas Tech Discuss* (2019) **12**, 4339–46.

[35] Tuinstra F, Koenig J. Raman Spectrum of Graphite. *J Chem Phys* (1970) **53**, 1126–30.

[36] Kelesidis GA, Rossi N, Pratsinis SE. Porosity and crystallinity dynamics of carbon black during internal and surface oxidation. *Carbon* (2022) **197**, 334–40.

[37] Iwashita N, Park CR, Fujimoto H, Shiraishi M, Inagaki M. Specification for a standard procedure of X-ray diffraction measurements on carbon materials. *Carbon* (2004) **42**, 701–14.

[38] Schneider CA, Rasband WS, Eliceiri KW. NIH Image to ImageJ: 25 years of image analysis. *Nat Methods* (2012) **9**, 671–5.

[39] Kelesidis GA, Kholghy MR, Zuercher J, Robertz J, Allemann M, Duric A, Pratsinis SE. Light scattering from nanoparticle agglomerates. *Powder Technol* (2020) **365**, 52–9.

[40] Tsantilis S, Kammler HK, Pratsinis SE. Population balance modeling of flame synthesis of titania nanoparticles. *Chem Eng Sci* (2002) **57**, 2139–56.

[41] Kelesidis GA, Goudeli E, Pratsinis SE. Flame synthesis of functional nanostructured materials and devices: Surface growth and aggregation. *Proc Combust Inst* (2017) **36**, 29–50.

[42] Mitchell P, Frenklach M. Particle aggregation with simultaneous surface growth. *Phys Rev E* (2003) **67**, 061407.

[43] Kelesidis GA, Goudeli E, Pratsinis SE. Morphology and mobility diameter of carbonaceous aerosols during agglomeration and surface growth. *Carbon* (2017) **121**, 527–35.

[44] Camacho J, Liu C, Gu C, Lin H, Huang Z, Tang Q, You X, Saggese C, Li Y, Jung H, Deng L, Wlokas I, Wang H. Mobility size and mass of nascent soot particles in a benchmark premixed ethylene flame. *Combust Flame* (2015) **162**, 3810–22.

[45] Woodcock L V. Isothermal molecular dynamics calculations for liquid salts. *Chem Phys Lett* (1971) **10**, 257–61.

[46] Appel J, Bockhorn H, Frenklach M. Kinetic modeling of soot formation with detailed chemistry and physics: Laminar premixed flames of C2 hydrocarbons. *Combust Flame* (2000) **121**, 122–36.

[47] Rogak SN, Flagan RC, Nguyen H V. The mobility and structure of aerosol agglomerates. *Aerosol Sci Technol* (1993) **18**, 25–47.

[48] Hinds WC. Aerosol Technology: Properties, Behavior, and Measurement of Air Borne Particles. second ed. Hoboken, New Jersey: John Wiley & Sons; (1999).

[49] Friedlander SK. Smoke, Dust and Haze: Fundamentals of Aerosol Dynamics. New York: Oxford University Press; (2000).

[50] Ciajolo A, D'Anna A, Barbella R, Tregrossi A, Violi A. The effect of temperature on soot inception in premixed ethylene flames. *Symp Combust* (1996) **26**, 2327–33.

[51] Gülder ÖL. Flame temperature estimation of conventional and future jet fuels. *J Eng Gas Turbines Power* (1986) **108**, 376–80.

[52] Chowdhury S, Boyette WR, Roberts WL. Time-averaged probability density functions of soot nanoparticles along the centerline of a piloted turbulent diffusion flame using a scanning mobility particle sizer. *J Aerosol Sci* (2017) **106**, 56–67.

[53] Liu C, Singh A V., Saggese C, Tang Q, Chen D, Wan K, Vinciguerra M, Commodo M, De Falco G, Minutolo P, D'Anna A, Wang H. Flame-formed carbon nanoparticles exhibit quantum dot behaviors. *Proc Natl Acad Sci* (2019) **116**, 12692–7.

[54] Dasappa S, Camacho J. Evolution in size and structural order for incipient soot formed at flame temperatures greater than 2100 K. *Fuel* (2021) **291**, 120196.

[55] Ghazi R, Tjong H, Soewono A, Rogak SN, Olfert JS. Mass, mobility, volatility, and morphology of soot particles generated by a mckenna and inverted burner. *Aerosol Sci Technol* (2013) **47**, 395–405.

[56] Bonpua J, Yagües Y, Aleshin A, Dasappa S, Camacho J. Flame temperature effect on sp^2 bonds on nascent carbon nanoparticles formed in premixed flames ($T_{f,max} > 2100$ K): A Raman spectroscopy and particle mobility sizing study. *Proc Combust Inst* (2019) **37**, 943–51.

[57] Bocchicchio S, Commodo M, Sgro LA, Chiari M, D'Anna A, Minutolo P. Thermo-optical-transmission OC/EC and Raman spectroscopy analyses of flame-generated carbonaceous nanoparticles. *Fuel* (2022) **310**, 122308.

[58] Trivanovic U, Sipkens TA, Kazemimanesh M, Baldelli A, Jefferson AM, Conrad BM, Johnson MR, Corbin JC, Olfert JS, Rogak SN. Morphology and size of soot from gas flares as a function of fuel and water addition. *Fuel* (2020) **279**, 118478.

[59] Vander Wal RL, Tomasek AJ, Pamphlet MI, Taylor CD, Thompson WK. Analysis of HRTEM images for carbon nanostructure quantification. *J Nanoparticle Res* (2004) **6**, 555–68.

[60] Hayashida K, Nagaoka S, Ishitani H. Growth and oxidation of graphitic crystallites in soot particles within a laminar diffusion flame. *Fuel* (2014) **128**, 148–54.

[61] Kelesidis GA, Pratsinis SE. Soot light absorption and refractive index during agglomeration and surface growth. *Proc Combust Inst* (2019) **37**, 1177–84.

Chapter 4

Trade-off between soot and NO emissions during enclosed spray combustion of jet fuel[4]

Abstract

Aviation emissions of soot and nitrogen oxides are strictly regulated as they adversely impact human health and environment. Jet fuel combustion conditions that decrease one pollutant concentration typically increase the other, making it hard to simultaneously reduce both. Although it's difficult to study such conditions due to high temperatures and gas flowrates of aircraft engines, recently it was shown that Enclosed Spray Combustion (ESC) of jet fuel results in soot with similar characteristics to that from aircrafts making ESC an attractive unit for studying aviation-like emissions. Furthermore, judicious swirl-injection of air downstream of the ESC burner drastically reduces soot emissions. Here, the trade-off between soot and nitric oxide (NO) emissions is explored, for the first time, during ESC of jet A1 fuel that is widely used in aviation. Injecting air shortly after the ESC burner decreases soot but increases NO emissions, while such injection further downstream has the inverse outcome. This interplay between soot and NO emissions was correlated quantitatively with the gas temperature shortly after air injection. Consequently, combustion conditions for an optimal trade-off between soot and NO emissions are identified that are at or below the lowest NO_x emissions per unit mass of fuel from existing aircraft engines.

[4] A version of this chapter has been submitted for publication in *Environmental Science & Technology*

4.1 Introduction

Aviation is an important source of pollution including particulate matter and oxides of nitrogen (NO_x) impacting air quality near airports [1]. Furthermore, such non-CO_2 emissions have a significant impact on climate. They account for about two-thirds of aviation's impact on net radiative forcing [2]. So, the International Civil Aviation Organization (ICAO) has long regulated the emissions of NO_x and more recently of non-volatile particulate matter, nvPM [3]. The regulatory term nvPM refers to particles that remain solid when heated to 350 °C [3] of which soot is a significant component. Reducing soot and NO_x emissions simultaneously is challenging as combustion conditions which reduce one typically promote the formation of the other as has long been demonstrated in diesel engines [4]. Thus, the design of aircraft combustors which reduce both soot and NO_x while also maintaining strict safety and performance standards is challenging and trade-offs must be carefully weighed.

During combustion of hydrocarbons, soot is formed by incomplete combustion at low temperatures and removed through oxidation at high ones. The competition between agglomeration and oxidation determines the emitted soot particle size, morphology and concentration. Combustion systems promote the oxidation of soot by increasing the flame temperature or O_2 concentration which will in turn increase the soot oxidation rate [5].

However, the high temperatures that promote such soot oxidation also drive the formation of thermal NO_x [6]. Recently it was shown that swirl-injection of increasing concentrations of O_2 into Enclosed Spray Combustion (ESC) of Jet A fuel can reduce soot total number concentration, N_{tot}, and volume fraction, f_v, by up to 95.4 and 99.6%, respectively [7]. This is similar to the concept of Rich-Quench-Lean (RQL) aircraft combustors which are comprised of an initial fuel-rich phase, followed by quenching with air to form a lean-burn zone [8]. The RQL concept was originally developed to lower NO_x emissions by rapidly reducing the temperature and prevent the formation of thermal NO_x [9] rather than to eliminate soot. If temperatures are dropped too low, soot cannot be efficiently oxidized leading to increased soot emissions [8]. So, the quenching stage in RQL combustors must be optimized to achieve temperatures that minimize both soot and NO_x. Several studies have used lab-scale RQL burners to investigate the effect of air dilution on soot concentrations [10], mobility size distributions [11], nanostructure, composition and morphology [7]. Similarly, models of NO_x formation in RQL combustors have been developed [12]. However, to the best of our knowledge there are no systematic studies which examine the effect of air quenching and its location in an RQL-like system on both the characteristics of soot and NO_x emissions. Furthermore, there are few studies on NO_x emissions from real fuels [13]. Here, the impact of air quenching location

on the resulting soot and NO emissions during ESC of jet fuel is investigated while exploring conditions to balance emissions from both pollutants.

4.2 Experimental

4.2.1 Particle synthesis and sampling

Soot and NO were generated by ESC of jet A1 fuel (Birrfeld Airport, Lupfig, Switzerland) [14], as depicted in Figure 4.1. Here, 4 mL/min of fuel flowed through a capillary tube and 1 L/min of O_2 from the concentric annulus to disperse the fuel into a fine spray. This is ignited with a small, premixed methane flame (CH_4 = 1.25 L/min, O_2 = 2.25 L/min) and surrounded by a 17 L/min sheath flow of air. This results in an Effective eQuivalence Ratio (EQR) of approximately 1.78 accounting for all flows entering the system at a Height Above the Burner, HAB = 0, as described in detail elsewhere [14]. The flows at HAB = 0 and initial EQR are held constant throughout the experiments. The system was enclosed in two quartz glass tubes separated by a torus ring supplying a 20 L/min mixture of N_2 and O_2 in an upward, swirled motion [15]. When N_2 only is fed to the ring, this quenches and dilutes the flame preventing soot oxidation [14].

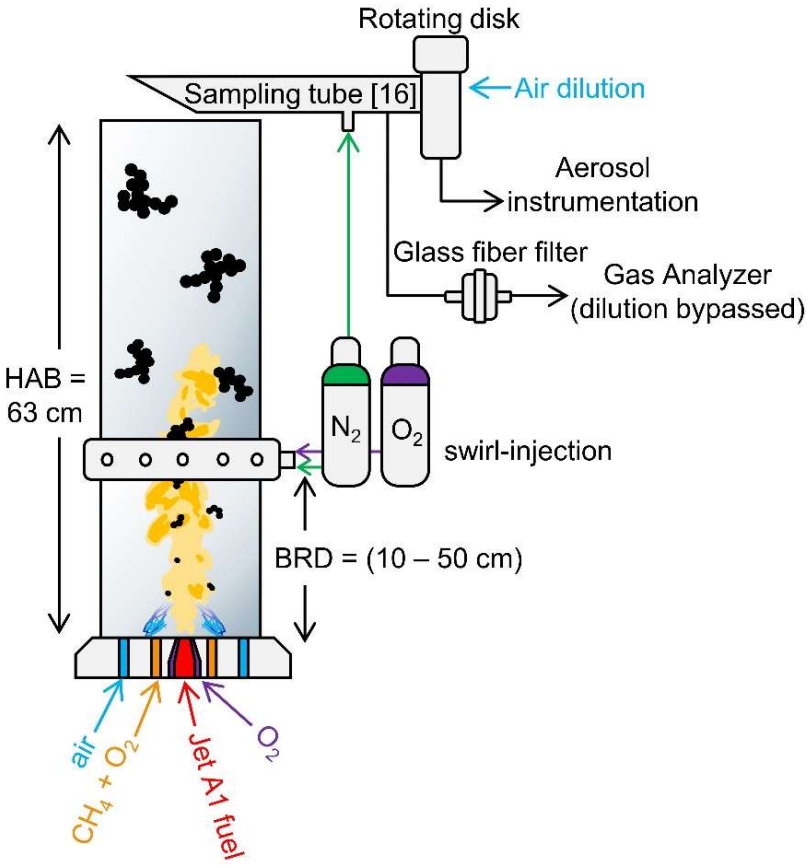

Figure 4.1: Schematic (not-to-scale) of the experimental set up. Jet A1 fuel from a capillary tube is dispersed by O_2 into a fine spray that was ignited by a small, premixed methane flame. All of this was enclosed in two quartz glass tubes in series that are separated by a torus ring [15] totaling 63 cm in length. The Burner to Ring Distance (BRD) is determined by the length of the first tube. The torus ring swirl-injects a mixture of N_2 and O_2 at 20 L/min to quench and dilute the flame. Exhaust is sampled immediately after the second quartz glass tube [16] for online and offline analysis.

Adding O_2 to the ring allows for controlled oxidation of the soot in the second tube [7]. Here, 0 (N_2 only), 5, 10, 15 and 20 vol. % O_2 (air) are used. The Burner to Ring Distance (BRD) denotes the distance from the burner (HAB = 0 cm) to the bottom surface of the torus ring. The BRD was adjusted by using various tubes with lengths of 10, 20, 30, 40 and 50 cm to achieve a combined length of 63 cm when accounting for the two tubes plus the torus ring.

4.2.2 Online measurements

The particle mobility size, d_m, was measured with a Scanning Mobility Particle Spectrometer (SMPS) which consists of an X-ray neutralizer (TSI 3087), a Differential Mobility Analyzer (DMA, TSI 3081) and a Condensation Particle Counter (CPC, TSI 3775). To prevent coagulation, particles sent to the SMPS are diluted in the straight tube sampler first with a dilution factor of ~ 41.3 using nitrogen and air from a rotating disk diluter (MD 19-1E, Matter Engineering AG). The resulting mobility size distributions were fit to a log normal distribution to obtain the median mobility diameter, d_m, Geometric Standard Deviation (GSD) and total number concentration, N_{tot}, of the distribution.

Undiluted exhaust from the straight tube sampler was passed through a glass fiber filter to remove particles from the flow for gas analysis with an infrared photometer (ABB EL3040 with Uras26) sampled at a rate of 1 Hz. This allowed for measurement of Nitric Oxide (NO), in mg/m^3 and converted to parts per million (ppm) assuming room temperature (25 °C) and pressure (1 atm).

The temperature of the flame, T, was measured with an R-type thermocouple (Intertechno-Firag AG) with a 1 mm (nominal) bead diameter and corrected for radiative losses [17]. The in-flame temperatures were measured by replacing the typical quartz glass tube with a steel tube containing sealable sampling ports every 5 cm. Although the thermocouple has not been shown to significantly influence the particles produced by the flame [17], no other measurements were taken while the thermocouple was inserted in the flame.

4.2.3 Offline characterization of soot

Particles deposited on glass fiber filters were used for offline analysis including Transmission Electron Microscopy (TEM, FEI Tecnai F30 FEG). Particles from the filter were dispersed in ethanol and then were placed in an ultrasonic bath to break up large agglomerates for 15 minutes [18]. After the ultrasonic bath, a drop of the ethanol solution was placed on a lacey carbon TEM grid with a 200 copper mesh support (LC200-Cu-150, Electron Microscopy Sciences). The resulting images were used to measure the primary particle diameter, d_p, of soot by manually placing ellipses over the primary particles with the software ImageJ [19]. From this, the area-

equivalent diameter is calculated from more than 200 primary particles at each condition. At least 200 primary particles were counted as the median d_p leveled off by then as shown in Figure E1 of Appendix E and consistent with microscopy analysis of soot [20] and TiO_2 [21]. Exemplary TEM images are shown in Figure E2.

4.3 Results and Discussion

4.3.1 Flame temperature

Figure 4.2 shows the centerline flame temperatures 5 cm before (filled symbols) and after swirl-injection of air (open symbols) at BRD = 10 (inverse triangles), 20 (diamonds), 30 (circles), 40 (triangles) and 50 cm (squares). The temperatures at BRD = 30 cm (circles) are consistent with the corresponding literature [7]. All temperatures 5 cm before air injection, T_{pre}, continuously decrease from 1350 K at BRD = 10 cm to 811 K at BRD = 50 cm, as all these locations are after the maximum temperature of ESC [17: Fig. 1]. Immediately after air injection, the temperature increases at all BRD (except 50 cm) indicating the oxidation of unburned jet fuel and/or soot before dropping further downstream as expected. With BRD = 50 cm there is no such maximum in T as the temperature is too low already for further fuel/soot oxidation. In fact, this temperature profile is identical to that measured when injecting only N_2 (Figure E3a), proving that no fuel/soot oxidation takes place.

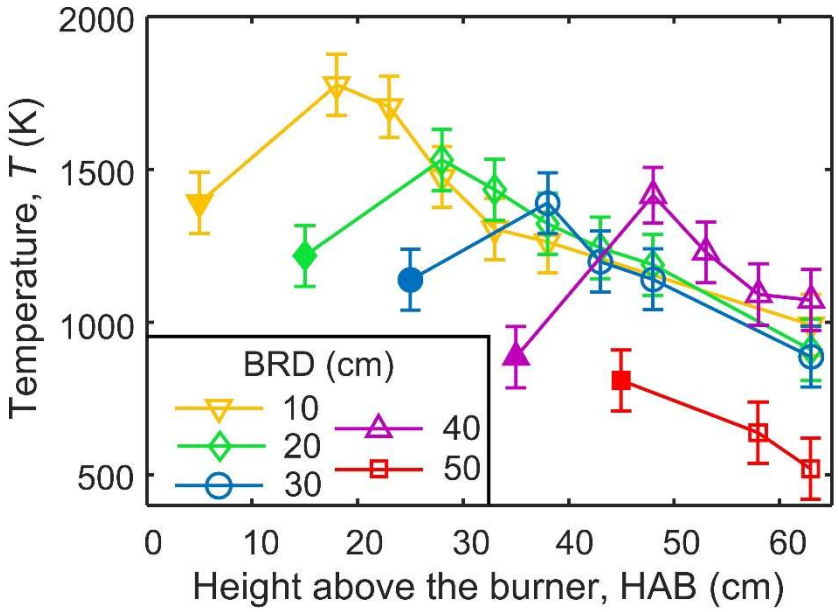

Figure 4.2: Centerline temperature by ESC of jet A1 fuel before (filled symbols) and after swirl-injection of air (open symbols) through a torus ring at BRD = 10 (inverse triangles), 20 (diamonds), 30 (circles), 40 (triangles) and 50 cm (squares).

4.3.2 Soot concentration and size

The total number concentration, N_{tot}, of soot at the end of the enclosure (HAB = 63 cm) is shown in Figure 4.3 when BRD = 50 (squares), 40 (triangles), 30 (circles), 20 (diamonds) and

10 cm (inverse triangles) with various O_2 volume fractions in N_2 supplied were through the torus ring. Higher O_2 vol% lead to larger reductions in N_{tot}, consistent with the literature [7]. The initial concentration with the torus ring supplying N_2 only (0 vol% O_2), was nearly the same for all five BRD, about 4 x 10^7 #/cm^3. At BRD = 50 cm, there is virtually no change in soot number concentration even when adding air (20 vol% O_2). This is another indication of no soot oxidation when BRD = 50 cm and consistent with Figure 4.2. Conversely, for BRD ≤ 40 cm, reductions of at least 99.6% in the number concentration are achieved by gas injection with 15 vol % O_2 through the torus ring. At lower BRD, less O_2 is needed to achieve significant N_{tot} reductions. For example, injecting just 10% O_2 at HAB = 10 cm resulted in a 99.9% reduction in N_{tot}. This is consistent with a model Rich Quench Lean (RQL) combustor burning ethylene exhibiting also a decrease in soot number and volume concentrations when dilution air is injected earlier on in the flame [22]. The approximately four orders of magnitude reduction in N_{tot} when air is injected compared to N_2 is similar to that achieved by passing soot through a lean-premixed flame [23] suggesting that the swirl-injection of gas by the torus ring here results in turbulent conditions and intense mixing akin to a premixed flame.

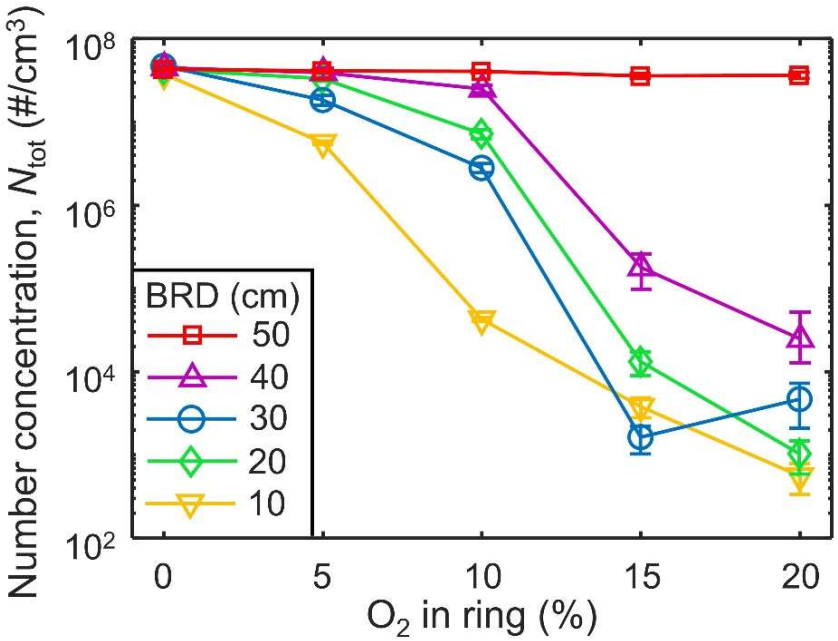

Figure 4.3: The total soot number concentration, N_{tot}, as a function of the volume fraction of O_2 supplied through the torus ring at BRD of 50 (squares), 40 (triangles), 30 (circles), 20 (diamonds) and 10 cm (inverse triangles).

The soot mobility size distributions are shown in Figure 4.4 when air was injected at BRD = 50 (dot-dashed line), 40 (dashed line), 30 (solid line), 20 (dotted line) and 10 cm (double dot-dashed line). At BRD = 50 cm, the median d_m of 180 ± 1.2 nm is close to that obtained when pure N_2 is fed through the torus ring, 196 ± 2.9 nm (Figure E4). The GSD of 1.59 ± 0.01 is slightly above the quasi-self-preserving GSD = 1.48 ± 0.03 for flame reactors [24]. In

contrast, at BRD = 40 and 30, the distributions drop to median d_m = 15 ± 2.7 and 22 ± 2.9 nm, respectively, and the concentration is significantly reduced for more than 10 vol % O_2 in the swirl gas. This drastic reduction in size and concentration suggests that significant oxidation has taken place removing most of the soot originally produced and consistent with Figure 4.3. The distributions have also widened to 1.89 ± 0.41 and 1.90 ± 0.20 at BRD = 40 and 30 cm, respectively. This widening could be also due to some fragmentation during soot oxidation. A similar widening of the size distribution has been observed from ESC of jet fuel under slightly different conditions [7], during oxidation of soot from a premixed flame burning a JP-8 jet fuel surrogate [23] and during simulations of diesel soot oxidation [25]. Further lowering the location of the torus ring to BRD = 20 or 10 cm, results in such low soot concentrations (N_{tot} < 50 #/cm after dilution) that a lognormal distribution cannot be fit to the results.

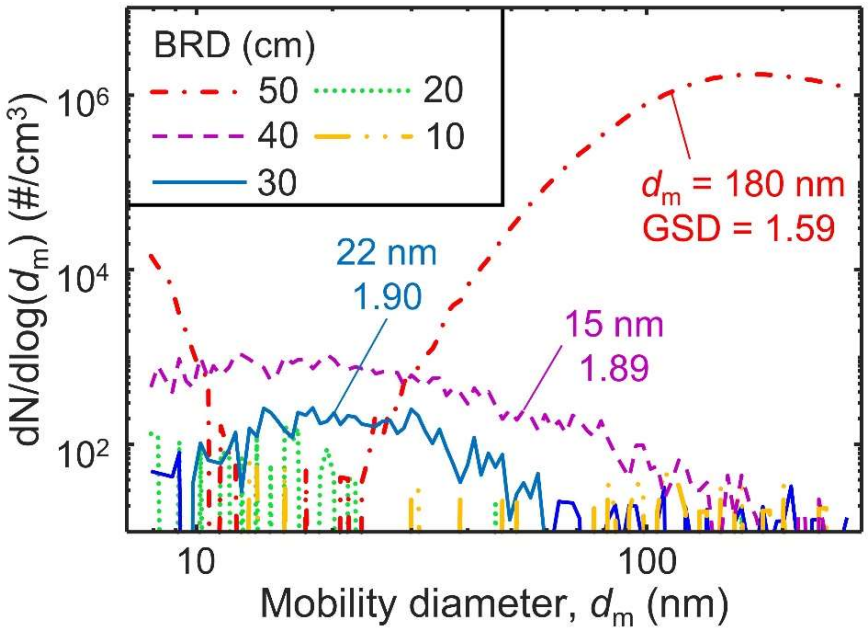

Figure 4.4: The soot mobility size distributions at BRD = 50 (dot-dashed line), 40 (dashed line), 30 (solid line), 20 (dotted line) and 10 cm (double dot-dashed line) with air injection.

Evidently, injection of N_2 containing even small amounts of O_2 when BRD = 10 cm is most effective for removing soot. The high temperatures there (Figure 4.2, inverse triangles) increase the soot oxidation rate [26] but other factors may also contribute to the fast removal of soot. A BRD = 10 cm coincides with the maximum temperatures measured in these flames at HAB ~ 10 cm (Figure E3a-d) ranging from 1391 – 1878 K. Soot inception in laminar diffusion flames begins in a similar temperature range of 1332 – 1913 K for various hydrocarbons [6]. Qualitatively, soot begins to deposit visibly on the walls of the quartz glass tubes near HAB = 10 cm (Figure E5). In addition, while the N_{tot} from injection of pure N_2 (0 vol% O_2 injected) was practically identical for all BRD (Figure 4.3), the initial mobility size distributions (Figure E4) shifted to smaller mobility diameters when pure N_2 was injected at lower BRD (i.e. earlier

in the flame). This N_2 essentially diluted the soot aerosol and reduced its coagulation-agglomeration rate. The primary particle sizes with such N_2 quenching were similar for all BRD as well, Figure E6a, suggesting that agglomerates formed at lower BRD contained fewer primary particles resulting in a lower volume fraction (Figure E7, open symbols). This suggests that quenching at BRD = 10 cm interferes with soot formation. Furthermore, less mature soot particles tend to have more disordered carbon [27] which is easier to oxidize compared to ordered material [28]. When BRD ≥ 20 cm, the $T_{pre} \leq 1217$ K so injecting air quite likely does not interfere with soot formation.

4.3.3 Nitric oxide emissions

Figure 4.5 shows the nitric oxide, NO, emissions at the end of the ESC enclosure when BRD = 10 (inverse triangles), 20 (diamonds), 30 (circles), 40 (triangles) and 50 cm (squares). The error bars represent the standard deviation between at least three experiments. There is a nearly linear trend between BRD and NO with the highest NO emissions of 446 ± 82 ppm occurring at BRD = 10 cm and the lowest NO = 138 ± 18 ppm at BRD = 50 cm. In this regard, injecting air later in the flame is desirable to minimize NO. Increasing the O_2 concentration from 0 to 20 % results in also a linear increase in NO from 208 ± 35 ppm with pure N_2 quenching up to 325 ± 32 ppm with air quenching when BRD = 30 cm (Figure E8). This is expected as lower BRD increased post-injection temperatures (Figure 4.2) while N_2 quenching reduced them (Figure E3) and increased NO has long been associated with higher temperatures due to the Zeldovich mechanism of NO formation [29].

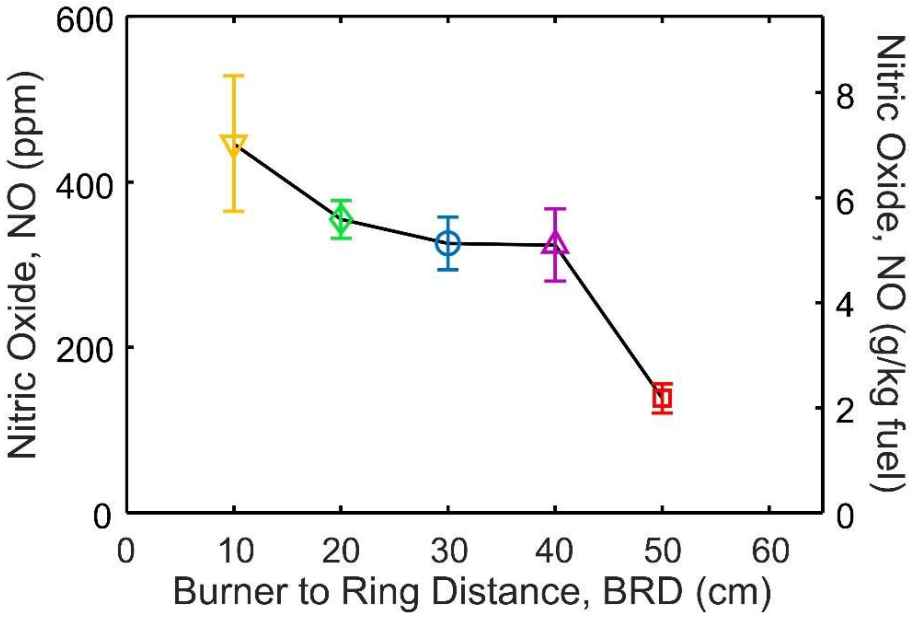

Figure 4.5: The nitric oxide (NO) emissions in parts per million (left axis) or normalized by the amount of fuel that would be burned over the 32.9 min landing and take-off (LTO) cycle (right axis) as a function of the BRD of swirl-injection of air.

The NO_x emissions from aviation are typically expressed as grams of NO_x produced over the standardized Landing and Take-Off (LTO) cycle normalized by the kilograms of fuel burned over this time (g NO_x/kg fuel) [3]. While the laboratory burner cannot be cycled through the LTO cycle, for the same length of time (32.9 minutes) the NO emissions here can be converted to 7.03 ± 1.29, 5.59 ± 0.036, 5.13 ± 0.50, 5.10 ± 0.69 and 2.18 ± 0.28 g/kg when BRD = 10, 20, 30, 40 and 50 cm, respectively (Figure 4.5, right axis). The permissible NO_x from an engine depends on both its maximum rated thrust and pressure ratio where more NO_x is permitted from engines with higher thrust and pressure ratios [3]. This allows for a balance between reducing fuel consumption through the use of more efficient engines (i.e. higher pressure ratios) and the air quality impacts of NO_x [30]. The dependence on pressure ratio and rated thrust makes it difficult to compare the results here directly to regulatory limits. However, the present values are at the bottom or below the range of NO_x reported in the publicly available ICAO aircraft emissions databank for existing engines from approximately 5.20 to 279 g/kg over the LTO cycle [31]. It is important to note that the present system is orders of magnitude smaller than a real aircraft engine and the NO_x emissions of aircrafts tend to decrease with lower fuel flow in real engines [32]. Here, the fuel flow is 4 mL/min or 5.38 x 10^{-5} kg/s while the lowest fuel flow in the ICAO database is 0.023 kg/s [31]. Although higher fuel flowrates are associated with higher NO_x emissions from aircrafts, the magnitude of this effect seems to vary significantly between different engine types indicating that the NO_x can be reduced through engine design [32]. Thus, the relative magnitude and trend of NO emissions shown in Figure 4.5 and S8 are more important than the absolute values.

Some NO is produced in the flame before the injection of air due to the first temperature peak at approximately HAB = 10 cm (Figure E3) and presence of N_2 in the sheath air. This is why some NO is still detected when BRD = 50 cm or when N_2 is injected (Figure E9). The so-called penalty for oxidizing soot is the NO formed during the second temperature peak post-air injection which adds to the NO formed earlier in the flame. For this reason, the NO emissions measured at the end of the enclosure are correlated to the temperature 5 cm downstream of the air injection as shown in Figure 4.6 (left axis). When BRD = 50 cm (square), the post-injection temperature, T_{post}, is the lowest, 640 K, and correspondingly the NO is also at its lowest, 138 ppm. For BRD = 20 – 40 cm, T_{post} = 1531 – 1415 K which is within the standard deviation between measurements of approximately 100 K. Accordingly, the mean NO values measured vary from 355 to 324 ppm across the same range again with significant overlap in their standard deviations. At BRD = 10 cm, the post-injection temperature was significantly higher, 1777 K,

and the emitted NO was 446 ppm. A linear relationship between NO and T_{post} can be described as:

$$[NO] = 0.26 \cdot T_{post} - 36 \quad (4.1)$$

where [NO] is in ppm and T_{post} in K with an $R^2 = 0.99$. So, NO increases at a rate of 0.26 ppm/K across the range studied here. This correlation holds true also when pure N_2 is injected in the flame (Figure E10) further confirming that the post-injection temperature is an important metric for determining the NO emitted rather than the maximum temperature which is similar for all BRD (Figure E3).

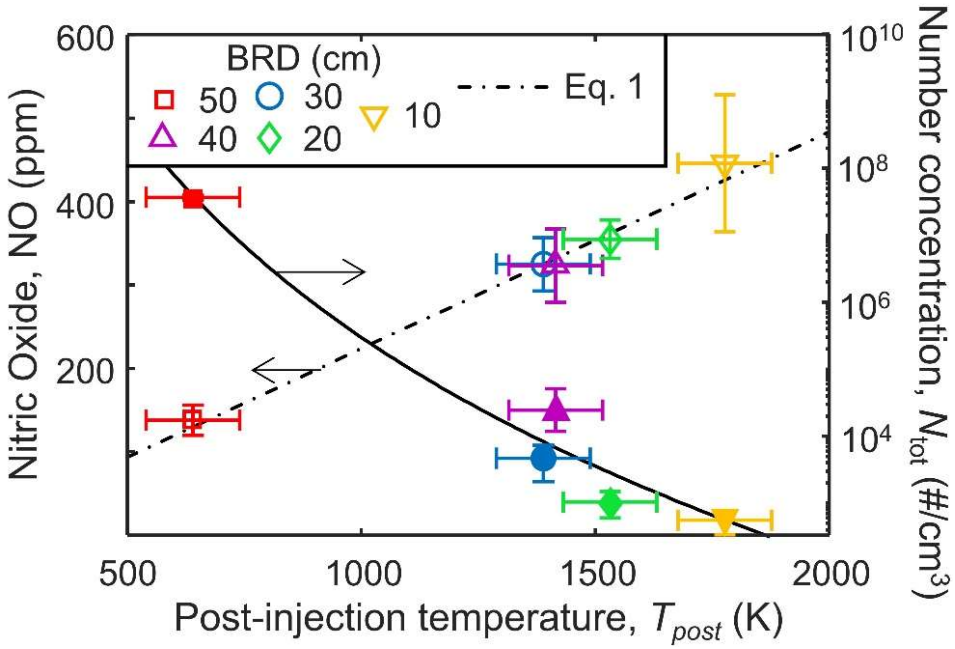

Figure 4.6: The temperature 5 cm after swirl-injection of air, T_{post}, (Figure 4.2), and the associated NO (open symbols) and total number concentration N_{tot}, (filled symbols) emitted from the enclosure when BRD = 50 (squares), 40 (triangles), 30 (circles), 20 (diamonds) and 10 cm (inverse triangles).

The temperature after swirl-injection of air is inversely related to the concentration of soot produced (Figure 4.6; filled symbols). When oxidation of soot occurs at high temperatures, the process is limited by the reaction rate and occurs primarily on the soot surface, shrinking the soot particles [33]. In contrast, at low temperatures the reaction occurs slowly enough for O_2 to diffuse into the particle and cause internal oxidation which reduces the mass and increases the porosity of soot without a significant change in its structure and primary particle diameter [33]. The significance of internal oxidation starts around 973 [34] to 1073 K [26]. When BRD $\leq$ 40 cm, all T_{post} are significantly above this threshold.

When BRD = 50 cm, the temperature just before air injection is 811 K and drops well below the threshold for surface oxidation after the torus ring. This suggests that air injection at BRD = 50 cm does not induce oxidation and if it does, it should be internal oxidation preserving

the size of the particles. Here, the primary particle diameter of soot produced when BRD = 50 cm is not affected by the composition of the quenching gas (Figure E6b). The median d_m is only slightly decreased from 196 nm with N_2 injection (Figure E4) to 180 nm with air (Figure 4.4; dot-broken line). Also, with BRD = 50 cm only 10 cm are left to the end of the enclosure so, soot has less time to oxidize. On the other hand, at BRD = 30 cm the d_m is reduced significantly from 142 nm (Figure E4) with pure N_2 injection down to just 15 nm with air (Figure 4.4, solid line), a 90% reduction.

As both NO and soot are pollutants which must be minimized due to increasingly strict regulations, an trade-off is needed. Figure 4.7 shows the NO (left axis, open symbols) and N_{tot} (right axis, filled symbols) as a function of BRD. The best trade-off between NO and N_{tot} is when BRD = 30 cm. The mean NO is nearly identical to that produced when BRD = 40 cm, however the N_{tot} of soot is lower. However, the NO and N_{tot} at BRD = 30 cm are similar to those achieved at BRD = 20 and 40 cm. When BRD is below 20 cm or above 40 cm, the trade-offs between soot and NO become more apparent and a significant penalty is paid either in increased NO (BRD = 10 cm) or increased soot (BRD = 50 cm). Interestingly, there is an abrupt change from significant soot oxidation and elevated NO at BRD = 40 cm to negligible oxidation and low NO at BRD = 50 cm.

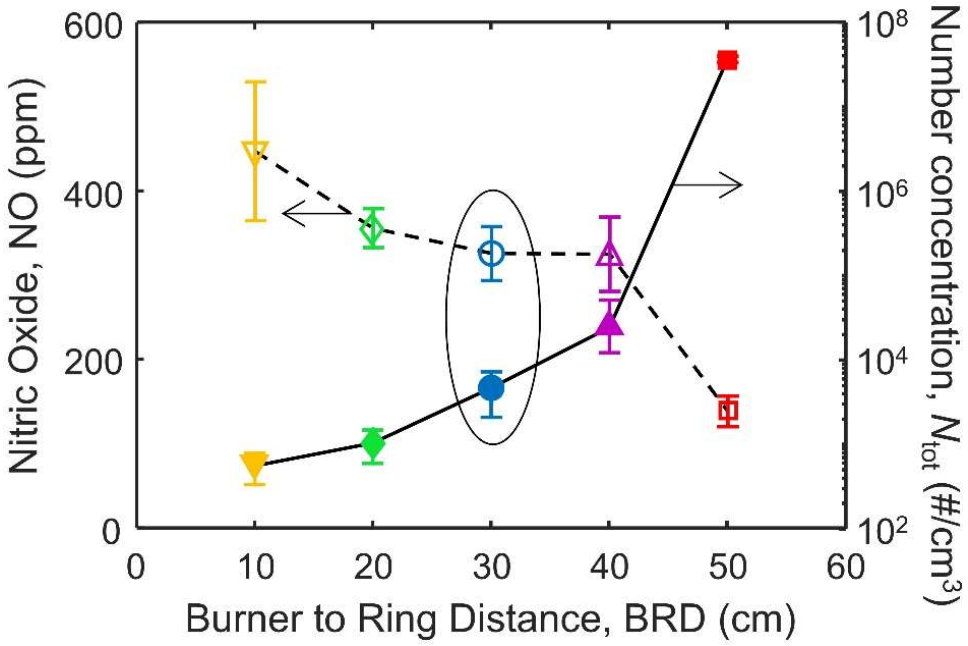

Figure 4.7: The NO (left axis, open symbols) and N_{tot} (right axis, filled symbols) measured at the exit of the enclosure when BRD = 10 (inverse triangles), 20 (diamonds), 30 (circles), 40 (triangles) and 50 cm (squares).

The temperature just before the torus ring is similar at 885 and 881 K at BRD = 40 and 50 cm, respectively. After air injection, this changes significantly with T_{post} = 1415 and 640 at BRD = 40 and 50 cm, respectively. Thermal Gravimetric Analysis (TGA) of aircraft soot in air

showed the onset of soot mass loss at around 700 K, which then dropped off steeply around 830 K [35], similar to the temperature threshold observed here. In addition, during TGA, temperatures are ramped up slowly in a controlled environment while during ESC, the oxidation of soot releases heat which accelerates the oxidation further causing the increase in T_{post} relative to T_{pre} and significant differences in both N_{tot} and NO observed here. The exact temperature at which this tipping point is reached will depend in part on the structure of the particles [36] which here has been shown to be similar to that of aircraft soot [17]. Thus, the location of air quenching can significantly impact both NO and soot emissions as both emissions are related to the temperature in the flame.

4.4 Summary & Conclusions

A torus ring was used to swirl-inject air into ESC of jet A1 fuel through a torus ring at burner to ring distances, BRD = 10, 20, 30, 40 and 50 cm. Maximum flame temperatures occur at approximately 10 cm height above the burner so, when BRD = 10 cm, the highest temperature is 1777K downstream of the torus ring. This BRD in turn results in the lowest soot concentrations, N_{tot} = 560 #/cm^3 but the highest NO (446 ppm). At the other extreme (when BRD = 50 cm), post-injection temperatures are significantly lower, i.e. 640 K. Then, NO is significantly lower at 138 ppm, but the soot concentration is orders of magnitude higher at 3.7 x 10^7 #/cm^3. The temperatures, NO and N_{tot} measured with air quenching at BRD = 50 cm were nearly identical to that measured with N_2 quenching. This suggests that negligible soot oxidation is taking place then. The post-injection temperature was a most important metric for determining NO emissions with a linear correlation for the range of temperatures studied here. At BRD = 20 – 40 cm, temperatures and thus NO emissions are quite similar with nearly identical means of 325 and 324 ppm obtained at BRD = 30 and 40 cm, respectively. The N_{tot} was reduced by more than 99.9% for all three BRD, but the greatest reduction of 99.998% was achieved at BRD = 20 cm. Thus, BRD = 30 cm offers the best trade-off between NO and soot emissions. Beyond it, temperatures are either too high, promoting NO formation or too low to oxidize soot. These results indicate the potential of optimal aircraft engine design with respect to minimizing both NO and soot emissions through the NO and soot (aerosol) residence time at high temperatures.

4.5 References

[1] Hudda N, Durant LW, Fruin SA, Durant JL. Impacts of aviation emissions on near-airport residential air quality. *Environ Sci Technol* (2020) **54**, 8580–8.

[2] Lee DS, Fahey DW, Skowron A, Allen MR, Burkhardt U, Chen Q, Doherty SJ, Freeman S, Forster PM, Fuglestvedt J, Gettelman A, De León RR, Lim LL, Lund MT, Millar RJ,

Owen B, Penner JE, Pitari G, Prather MJ, Sausen R, Wilcox LJ. The contribution of global aviation to anthropogenic climate forcing for 2000 to 2018. *Atmos Environ* (2021) **244**, 117834.

[3] ICAO. Annex 16 to the convention on international civil aviation: environmental protection, Vol. II - aircraft engine emissions. Montreal, CA: (2017).

[4] Kim D, Ekoto I, Colban WF, Miles PC. In-cylinder CO and UHC imaging in a light-duty diesel engine during PPCI low-temperature combustion. *SAE Int J Fuels Lubr* (2009) **1**, 933–56.

[5] Kelesidis GA, Pratsinis SE. Estimating the internal and surface oxidation of soot agglomerates. *Combust Flame* (2019) **209**, 493–9.

[6] Glassman I, Yetter RA. Combustion. Academic Press; (2007).

[7] Kelesidis GA, Nagarkar A, Trivanovic U, Pratsinis SE. Toward elimination of soot emissions from jet fuel combustion. *Environ Sci Technol* (2023) **57**, 10276–83.

[8] Liu Y, Sun X, Sethi V, Nalianda D, Li YG, Wang L. Review of modern low emissions combustion technologies for aero gas turbine engines. *Prog Aerosp Sci* (2017) **94**, 12–45.

[9] Rizk NK, Mongia HC. Ultra-Low NOx Rich-Lean Combustion. *Am Soc Mech Eng* (1990), 90-GT-87.

[10] El Helou I, Skiba AW, Mastorakos E. Experimental investigation of soot production and oxidation in a lab-scale Rich–Quench–Lean (RQL) burner. *Flow, Turbul Combust* (2021) **106**, 1019–41.

[11] Gkantonas S, Sirignano M, Giusti A, D'Anna A, Mastorakos E. Comprehensive soot particle size distribution modelling of a model Rich-Quench-Lean burner. *Fuel* (2020) **270**, 117483.

[12] Prakash A. Prediction of NOx emissions for an RQL aero-engine ombustor using a stirred reactor modelling approach. *52nd AIAA/SAE/ASEE Jt Propuls Conf 2016* (2016), 1–10.

[13] Saggese C, Wan K, Xu R, Tao Y, Bowman CT, Park JW, Lu T, Wang H. A physics-based approach to modeling real-fuel combustion chemistry – V. NO_x formation from a typical Jet A. *Combust Flame* (2020) **212**, 270–8.

[14] Trivanovic U, Kelesidis GA, Pratsinis SE. High-throughput generation of aircraft-like soot. *Aerosol Sci Technol* (2022) **56**, 732–43.

[15] Teleki A, Heine MC, Krumeich F, Akhtar MK, Pratsinis SE. In situ coating of flame-made TiO_2 particles with nanothin SiO_2 films. *Langmuir* (2008) **24**, 12553–8.

[16] Goudeli E, Gröhn AJ, Pratsinis SE. Sampling and dilution of nanoparticles at high temperature. *Aerosol Sci Technol* (2016) **50**, 591–604.

[17] Trivanovic U, Pereira Martins M, Benz S, Kelesidis GA, Pratsinis SE. Dynamics of soot surface growth and agglomeration by enclosed spray combustion of jet fuel. *Fuel* (2023) **342**, 127864.

[18] Mädler L, Kammler HK, Mueller R, Pratsinis SE. Controlled synthesis of nanostructured particles by flame spray pyrolysis. *J Aerosol Sci* (2002) **33**, 369–89.

[19] Schneider CA, Rasband WS, Eliceiri KW. NIH Image to ImageJ: 25 years of image analysis. *Nat Methods* (2012) **9**, 671–5.

[20] Kelesidis GA, Kholghy MR, Zuercher J, Robertz J, Allemann M, Duric A, Pratsinis SE. Light scattering from nanoparticle agglomerates. *Powder Technol* (2020) **365**, 52–9.

[21] Tsantilis S, Kammler HK, Pratsinis SE. Population balance modeling of flame synthesis of titania nanoparticles. *Chem Eng Sci* (2002) **57**, 2139–56.

[22] De Falco G, Helou I El, de Oliveira PM, Sirignano M, Yuan R, D'Anna A, Mastorakos E. Soot particle size distribution measurements in a turbulent ethylene swirl flame. *Proc Combust Inst* (2021) **38**, 2691–9.

[23] Echavarria CA, Jaramillo IC, Sarofim AF, Lighty JAS. Burnout of soot particles in a two-stage burner with a JP-8 surrogate fuel. *Combust Flame* (2012) **159**, 2441–8.

[24] Kelesidis GA, Goudeli E. Self-preserving size distribution and collision frequency of flame-made nanoparticles in the transition regime. *Proc Combust Inst* (2021) **38**, 1233–40.

[25] Harris SJ, Maricq MM. The role of fragmentation in defining the signature size distribution of diesel soot. *J Aerosol Sci* (2002) **33**, 935–42.

[26] Stanmore BR, Brilhac JF, Gilot P. The oxidation of soot: A review of experiments, mechanisms and models. *Carbon* (2001) **39**, 2247–68.

[27] Baldelli A, Trivanovic U, Sipkens TA, Rogak SN. On determining soot maturity: A review of the role of microscopy- and spectroscopy-based techniques. *Chemosphere* (2020) **252**, 126532.

[28] Hayashida K, Nagaoka S, Ishitani H. Growth and oxidation of graphitic crystallites in soot particles within a laminar diffusion flame. *Fuel* (2014) **128**, 148–54.

[29] Zeldovich YB. Formation of nitrogen in combustion and explosions. *Acta Physicochim USSR* (1946) **21**, 577–628.

[30] Miller CJ, Prashanth P, Allroggen F, Grobler C, Sabnis JS, Speth RL, Barrett SRH. An environmental cost basis for regulating aviation NO_x emissions. *Environ Res Commun* (2022) **4**, 055002.

[31] ICAO. ICAO Aircraft Engine Emissions Databank (2023). https://www.easa.europa.eu/en/domains/environment/icao-aircraft-engine-emissions-databank (accessed August 8, 2023).

[32] Turgut ET, Usanmaz O. An assessment of cruise NO_x emissions of short-haul commercial flights. *Atmos Environ* (2017) **171**, 191–204.

[33] Kelesidis GA, Rossi N, Pratsinis SE. Porosity and crystallinity dynamics of carbon black during internal and surface oxidation. *Carbon* (2022) **197**, 334–40.

[34] Ma X, Zangmeister CD, Zachariah MR. Soot oxidation kinetics: A comparison study of two tandem ion-mobility methods. *J Phys Chem C* (2013) **117**, 10723–9.

[35] Klingshirn CD, West ZJ, DeWitt MJ, Higgins A, Graham J, Corporan E. Quantification of elemental and total carbon in combustion particulate matter using thermal-oxidative analysis. *J Air Waste Manag Assoc* (2019) **69**, 1003–13.

[36] Vander Wal RL, Tomasek AJ. Soot oxidation: Dependence upon initial nanostructure. *Combust Flame* (2003) **134**, 1–9.

Chapter 5

Outlook and Research Recommendations

Carbonaceous nanoparticles have a long history dating back as early as 2000 BC when they were used for ink [1] and more recently in the 20th century when significant research and policy efforts were made to reduce air pollution [2]. Despite this long history, carbonaceous nanoparticles remain an important research area due to continuously advancing combustion technologies and the urgent need to address threats to the climate [3] and human health [4]. Advancing the understanding of how such particles interact with atmospheric processes and the human bodies will be essential for making intelligent trade-offs between soot and other pollutants (Chapter 1). In this regard, extensive experimentation with sprays of jet fuel was used to develop Enclosed Spray Combustion (ESC) as a method to produce soot with characteristics matching that observed in soot from aircrafts at high thrust as described in Chapter 2. Thus, ESC provides a platform to better understand soot produced from real fuels in a laboratory setting that can be used to address these gaps in the literature. Three major gaps in the literature include: the role of soot in contrail formation, biological mechanisms that cause the adverse health effects of particulate matter and accurate modeling of soot in aircraft combustors.

First, contrails are estimated to make up approximately half of aviation's net radiative forcing (RF) [5]. This highlights the need to understand the role of soot in contrail formation so that trade-offs (Chapter 1) can be properly assessed. Some studies have shown that reducing soot from aircraft engines reduces the number of nucleated ice crystals (i.e. contrails) [6] while others show that aircraft soot tends to be a poor ice nucleating particles at cirrus cloud temperatures [7]. Most laboratory studies on the ice condensation properties of soot have been conducted with miniCAST soot that produces relatively large (d_m > 100 nm) particles which use hydrocarbon gases rather than real jet fuel [8]. ESC of jet fuel (Chapter 2) could be used to conduct controlled experiments on the ice nucleating properties of aircraft-like soot to reduce the uncertainty in the RF of aviation. Furthermore, ESC could be used to assess changes to the ice nucleating properties of soot particles produced with novel aviation fuels which may have different properties to those from conventional jet fuel (Appendix B).

Second, fine particulate matter (PM), which includes soot, has been linked to cancer [9] cardiovascular and respiratory diseases [4]. While many studies have observed correlations

between PM and disease, causal relationships have not yet been established because the biological mechanisms behind the diseases have not been established [10]. Proposed mechanisms for soot toxicity include localized oxidative stress where soot is in contact with tissue causing DNA damage and systemic inflammation due to immune responses to soot [9]. One important metric for determining the toxicity of nanoparticles is its Specific Surface Area (SSA) where higher SSA of carbon black and inorganic nanomaterials is associated with greater toxicity [11]. However, this is rarely measured for soot particles due to the large quantities needed for such measurements. Therefore, it is not clear if the increased toxicity with SSA is true only for external surface are, or if it also applies to internal surface area due to increased porosity of particles. The ESC burner developed in this thesis (Chapter 2) can produce large quantities of soot from real fuels allowing for the characterization of the SSA of aircraft-like soot for the first time. *In vitro* studies to characterize the cytotoxicity of soot require several milligrams of soot, a quantity that cannot be easily obtained from aircraft engines so, carbon black is often used as a substitute [11]. The high throughput of ESC could therefore be used to fill this gap and to examine any differences in toxicity caused by different types of jet fuel such as from sustainable aviation fuels. Furthermore, characterization of the effective density of ESC soot (Chapter 2) can be used to improve particle inhalation models which determine the lung-deposited dose and location of soot [12].

Third, models of soot formation and dynamics in turbulent flames with real fuels must be improved to better predict soot emissions from aircraft engines so that trade-offs between pollutants can be minimized. Models of soot dynamics in Rich-Quench-Lean (RQL)-like systems today typically compare to laboratory burners with ethylene [13] which is very different from the liquid fuels used in real engines. In Chapter 3, Discrete Element Modeling (DEM) was applied to elucidate soot dynamics during spray combustion of jet fuel capturing the evolution of soot mobility and primary particle diameter. In addition, one of the most important trade-offs are between reduction of soot (Appendix A) and oxides of nitrogen (NO_x). The quantitative correlation between air injection location, temperature, nitric oxide (NO) and soot provided in Chapter 4 can serve as a starting point for understanding such trade-offs. Future work should aim to interface such DEM models with computational fluid dynamics (CFD) and NO_x kinetics to capture soot morphology, concentration and NO_x emissions. ESC could be used as experimental validation to advance such models.

Improving the large uncertainties associated with the climate impact of soot and its health impacts is essential for choosing the best strategies to mitigate its effects. In particular, an understanding of the role of soot in contrail formation is urgently needed to guide climate

policy while an understanding of the health effects could improve air quality measures. Similarly, improved models are essential for improving engine design and developing novel combustion technologies that minimize the negative effects of soot and other pollutants.

5.1 References

[1] Ulrich G. Flame Synthesis of Fine Particles. *Chem Eng News* (1984) **62**, 22–9.

[2] Mosley S. Environmental History of Air Pollution and Protection. vol. 4. (2014).

[3] Bond TC, Doherty SJ, Fahey DW, Forster PM, Berntsen T, DeAngelo BJ, Flanner MG, Ghan S, Kärcher B, Koch D, Kinne S, Kondo Y, Quinn PK, Sarofim MC, Schultz MG, Schulz M, Venkataraman C, Zhang H, Zhang S, Bellouin N, Guttikunda SK, Hopke PK, Jacobson MZ, Kaiser JW, Klimont Z, Lohmann U, Schwarz JP, Shindell D, Storelvmo T, Warren SG, Zender CS. Bounding the role of black carbon in the climate system: A scientific assessment. *J Geophys Res Atmos* (2013) **118**, 5380–552.

[4] Cassee FR, Héroux ME, Gerlofs-Nijland ME, Kelly FJ. Particulate matter beyond mass: Recent health evidence on the role of fractions, chemical constituents and sources of emission. *Inhal Toxicol* (2013) **25**, 802–12.

[5] Lee DS, Fahey DW, Skowron A, Allen MR, Burkhardt U, Chen Q, Doherty SJ, Freeman S, Forster PM, Fuglestvedt J, Gettelman A, De León RR, Lim LL, Lund MT, Millar RJ, Owen B, Penner JE, Pitari G, Prather MJ, Sausen R, Wilcox LJ. The contribution of global aviation to anthropogenic climate forcing for 2000 to 2018. *Atmos Environ* (2021) **244**, 117834.

[6] Kärcher B. Formation and radiative forcing of contrail cirrus. *Nat Commun* (2018) **9**, 1824.

[7] Testa B, Durdina L, Alpert PA, Mahrt F, Dreimol CH, Edebeli J, Spirig C, Decker ZCJ, Anet J, Kanji ZA. Soot aerosol from commercial aviation engines are poor ice nucleating particles at cirrus cloud temperatures. *Atmos Chem Phys* (2023), egushpere-2023-2441. Preprint.

[8] Gao K, Zhou CW, Meier EJB, Kanji ZA. Laboratory studies of ice nucleation onto bare and internally mixed soot-sulfuric acid particles. *Atmos Chem Phys* (2022) **22**, 5331–64.

[9] Niranjan R, Thakur AK. The toxicological mechanisms of environmental soot (black carbon) and carbon black: Focus on Oxidative stress and inflammatory pathways. *Front Immunol* (2017) **8**, 763.

[10] Shiraiwa M, Selzle K, Pöschl U. Hazardous components and health effects of atmospheric aerosol particles: Reactive oxygen species, soot, polycyclic aromatic compounds and allergenic proteins. *Free Radic Res* (2012) **46**, 927–39.

[11] Schmid O, Stoeger T. Surface area is the biologically most effective dose metric for acute nanoparticle toxicity in the lung. *J Aerosol Sci* (2016) **99**, 133–43.

[12] Lizonova D, Nagarkar A, Demokritou P, Kelesidis GA. Effective density of inhaled environmental and engineered nanoparticles and its impact on the lung deposition and dosimetry. *Part Fibre Toxicol* (2024) **21**, 1–11.

[13] Gkantonas S, Sirignano M, Giusti A, D'Anna A, Mastorakos E. Comprehensive soot particle size distribution modelling of a model Rich-Quench-Lean burner. *Fuel* (2020) **270**, 117483.

Appendix A

Toward elimination of soot emissions from jet fuel combustion[5]

Abstract

Soot from jet fuel combustion in aircraft engines contributes to global warming through the formation of contrail cirrus clouds that make up to 56 % of the total radiative forcing from aviation. Here, the elimination of such emissions is explored through N_2 injection (containing 0–25 vol % O_2) at the exhaust of enclosed spray combustion of jet fuel that nicely emulates aircraft soot emissions. It is shown that injecting N_2 containing 5 vol % of O2 enhances the formation of polyaromatic hydrocarbons (PAHs) that adsorb on the surface of soot. This increases soot number density and volume fraction by 25 and 80 %, respectively. However, further increasing the O_2 concentration to 20 or 25 vol % enhances oxidation and nearly eliminates soot emissions from jet fuel spray combustion, reducing the soot number density and volume fraction by 87.3 or 95.4 and 98.3 or 99.6 %, respectively. So, a judicious injection of air just after the aircraft engine exhaust can drastically reduce soot emissions and halve the radiative forcing due to aviation, as shown by soot mobility, X-ray diffraction, Raman spectroscopy, nitrogen adsorption, microscopy, and thermogravimetric analysis (for the organic to total carbon ratio) measurements.

[5] A version of this appendix has been published in *Environmental Science & Technology*

A1. Introduction

About a million tons of carbonaceous (soot) nanoparticles are released every year by aviation through incomplete combustion of jet fuel [1]. These emissions have a major impact on the health of airport workers and communities living near airports due to their cytotoxicity [2]. In addition, soot nanoparticles typically form clusters (agglomerates) that strongly absorb light, reducing visibility and increasing the radiative forcing, RF, and thus the Earth's temperature [3]. Most importantly, aircraft soot emissions act as ice nuclei and form contrail cirrus clouds [4]. The RF from such contrails makes up about 56 % of the total RF induced by aviation [5]. Thus, eliminating soot emissions from aircraft engines is essential to limit their impact on public health and substantially reduce their climate forcing [6].

To this end, bio-based (e.g., hydrotreated esters and fatty acids, HEFA [7]) or synthetic fuels derived by the Fischer–Tropsch (FT) process [8] have been explored to reduce the soot emissions from the combustion of petroleum-based jet fuels in aircraft engines. For example, a 50:50 blend of jet A and HEFA fuels decreased the total number concentration, N_t, of soot nanoparticles [7] by 50–70 %. Similarly, the combustion of a 60:40 blend of jet A1 and FT-derived fuels lowered by 34–50 % the soot N_t. [8] Blending jet fuel with such alternative fuels decreases the mean mobility [7], d_m, and primary particle diameters [9], d_p, of soot by about 15 and 30 %, respectively. Raman and microscopy analyses indicate that the combustion of biofuels results in more amorphous soot than jet fuels, while FT-derived fuels yield more graphitic soot [9].

Despite the rather large (50 – 70 %) reduction of aircraft soot emissions, using blends of jet with bio-based or synthetic fuels reduces only up to 20 % the RF from contrail cirrus clouds [6]. In this regard, climate modeling revealed that a 90 % decrease of soot N_t can reduce this RF [6] up to 50 %. This can be attained through gas (or air) injection downstream of the aircraft combustors [10]. For example, the design of quite a few of the current aircraft combustors is based on the rich quench lean (RQL) concept [11] where swirling and cross-flow jets are used in the primary zone to produce high concentrations of soot [12]. This zone is followed by a lean dilution zone, where additional air is injected to oxidize that soot [12]. Similarly, O_2 was introduced downstream of model laboratory RQL combustors burning ethylene [13] to oxidize soot and reduce its volume fraction [14], f_v, and N_t up to 99%. However, soot produced by ethylene combustion contains a higher organic and amorphous carbon content than aircraft soot from jet fuel combustion [15]. In particular, Raman spectroscopy showed that the oxidative reactivity of soot increases with its amorphous carbon content [16]. Recently, the impact of air injection downstream of jet fuel combustion was elucidated in a laboratory RQL

combustor [17]. The rather small air flow rates used there resulted in low O_2 concentrations downstream of the combustor [17] that reduced soot f_v up to 40 %. The limited reduction of soot f_v in current RQL combustors can be attributed to the inhomogeneity of temperature and gas profiles that result in regions with high concentrations of soot that survive oxidation and exit the combustor [18]. Large reductions (> 90 %) of soot N_t and f_v have been attained by dilution and combustion of ethylene [19] or jet fuel [20] soot in a lean premixed flame [21]. However, this exhaust treatment system does not resemble the dilution zones in common RQL combustors [18]. Similarly, "soot-free" combustion of jet fuel was attained recently in a laboratory-scale lean azimuthal flame (LEAF) combustor of jet A1 fuel by enhancing soot oxidation while injecting hydrogen [22].

Here, enclosed spray combustion (ESC) of jet fuel (Figure S1) that produces surrogate aircraft soot emissions [23] is used to explore their elimination. During ESC of jet fuel, soot nanoparticles grow by surface reactions [24] and agglomeration [25], attaining similar morphology, size distribution, and organic carbon content with those of aviation emissions [23]. Most importantly, the Raman spectrum of soot from ESC of jet fuel is in excellent agreement with that measured from aircraft soot [26] (Figure S2). This indicates that the oxidative reactivity of such surrogate aircraft soot is similar to that of aviation emissions [16], So, the elimination of such soot is investigated here by injecting N_2 containing 0 – 25 vol % of O_2 downstream of ESC of jet fuel. The impact of such O addition on the soot mobility, primary particle size distributions, f_v, N_t, composition, and nanostructure is elucidated below for the first time to the best of our knowledge. That way, the transformation of soot during oxidation is quantified, providing a basis for optimization of the RQL concept that is already used by some aircraft engine manufacturers [11].

A2. Materials and Methods

Soot nanoparticles were generated by ESC. Briefly, soot was produced by jet A fuel (POSF 10325 [27]) spray combustion using an external-mixing, twin fluid nozzle [28] enclosed in two, 30 cm long quartz tubes (each with a 42 mm inner diameter) in series [29] (Figure S1). So, 4 mL/min of fuel was dispersed into a fine spray with 1 L/min of O2. The resulting spray was ignited and sustained by a supporting premixed methane/oxygen flame (CH_4 = 1.25 L/min, O_2 = 2.25 L/min). Sheath air was fed through 12 evenly spaced holes surrounding the spray flame at 17.2 L/min. A torus ring [30] with 12 jet outlets between the two tubes (height above burner, HAB = 30 cm) was used to introduce 20 L/min of N_2 with or without O_2 in an upward swirled pattern to quench the flame as well as to dilute and oxidize the exhaust soot emissions. The O_2 concentration, [O_2], was varied from 0 to 25 vol %. The steel torus ring was made using two

pieces of pipe welded to a tube (Figure S3) having a 0.38 cm inner diameter and 12 outlets, each having a 0.06 cm diameter [30] with an upward azimuth angle of 10°.

The temperature profile, T, was measured using a 1 mm (nominal) bead diameter and an R-type thermocouple (Intertechno-Firag AG) and corrected for radiative heat losses [31]. The T measurements and energy balance used here have been described and validated for ESC of jet A1 fuel [31]. The centerline flame T profiles during ESC of jet A (Figure A.1a: circles) and A1 (squares) fuel are quite similar. Figure A.1b shows that the centerline *T* by ESC of jet A1 fuel at HAB = 35 (circles) and 63 cm (triangles) increases with increasing oxygen content in the injected nitrogen jets from the torus ring at HAB = 30 cm, as expected.

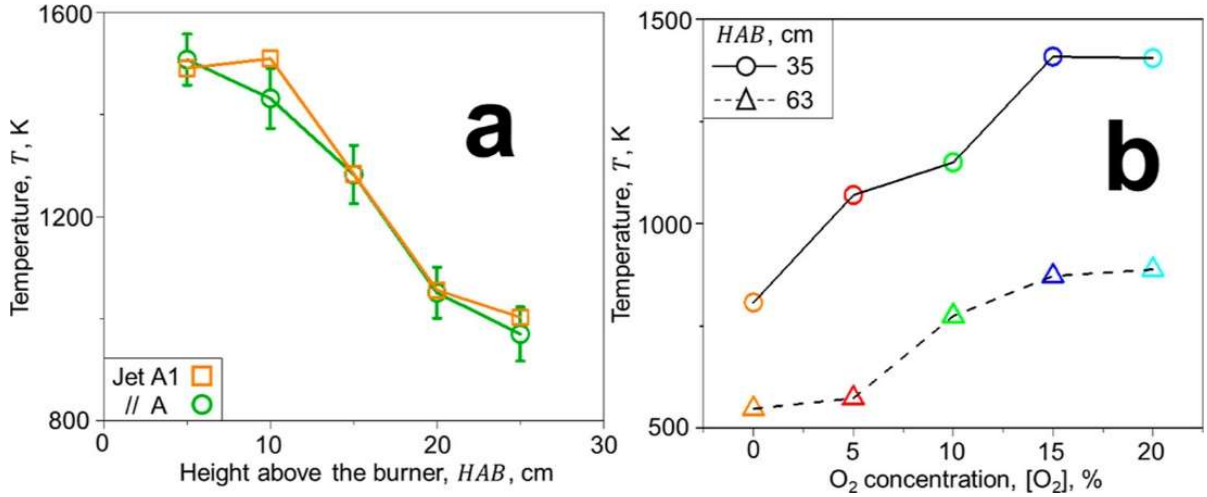

Figure A.1: Centerline temperature (a) by ESC of jet fuel A (circles) and A1 (squares) as a function of HAB, and (b) by ESC of jet fuel A1 as a function of [O2] in the injected N_2 jets from the torus ring at HAB = 35 (circles) and 63 cm (triangles).

Soot was extracted from the centerline of the flame at HAB = 63 cm using a straight tube sampler [32]. The sampled aerosol was rapidly diluted and quenched by mixing with N_2, followed by compressed air from a rotating disk diluter. The total dilution factor was set to 33.24 at all conditions investigated here. The distribution of the soot mobility diameter, d_m, and its total number concentration, N_t, were obtained by averaging five 65 s scans of a scanning mobility particle sizer [32]. The soot f_v was estimated based on the measured dm and d_p distributions, accounting for the soot agglomerate structure [33]:

$$f_v = \frac{\pi}{6}\sum_{i=1}^{k} N_i d_{m,i}^{2.22} d_p^{-0.78} \qquad \text{(A.1)}$$

where N_i is the number concentration of soot agglomerates having $d_{m,i}$ and mean d_p. The index k varies from 1 to 100, i.e., the largest number of dm bins measured by the scanning mobility particle sizer. The exponents for d_p and $d_{m.i}$ in Eq. A.1 were validated with aerosol particle mass analyzer data in premixed [34], diffusion [25] and spray [23] flames. Equation A.1 has been

derived by capitalizing on a power law for the soot effective density that was obtained by discrete element modeling of soot agglomeration and surface growth [25]. This equation has been used to measure accurately the soot f_v in laminar premixed [35], diffusion flames, and diesel engines [36], accounting for the realistic morphology of soot [33].

Soot was also collected on a glass fiber filter for off-line analysis. Then, Raman spectra of such soot nanoparticles were obtained using a 515 nm laser having 50 mW power (Renshaw inVia). The laser was focused with a ×20 magnification optical microscope, which gives a 2 μm spot size, while a 10 % laser power was focused on the sample for 120 s and three acquisitions [37]. The intensities of the disorder (D ~ 1350 cm^{-1}) and graphitic (G ~ 1580 cm^{-1}) bands [37] were obtained after straight line subtraction of the baseline [38].

The X-ray diffraction (XRD) patterns of soot at diffraction angles, 2θ = 10 – 70°, were also obtained by an AXS D8 diffractometer (Bruker) at a scan rate of 0.0197 °/s. Here, the average interlayer distance, d, of soot was obtained by analyzing the 002 XRD peak using Bragg's law [39]:

$$d = \frac{n \cdot \lambda}{2sin\theta_{002}} \tag{A.2}$$

where n = 1 is the order of diffraction, λ = 0.154 nm is the wavelength of the diffractometer, and θ_{002} is the center angle of the 002 peak. Similarly, the average crystallite length, L_c, of spray flame soot was obtained by [39]:

$$L_c = \frac{K \cdot \lambda}{\beta_{002} cos\theta_{002}} \tag{A.3}$$

where K = 0.89 is the peak shape factor [40] and β_{002} is the full width of the half maximum of the 002 peak. The crystallites d and L_c were determined here using Eqns. A.2 and A.3 with the θ_{002} and β_{002} derived from the measured XRD patterns that were validated using the patterns of commercial carbon blacks [41].

The organic to total carbon (OC/TC) mass ratio of soot was obtained by thermogravimetric analysis (TGA) [42]. The samples were first placed in N_2 to volatilize OC and then in air to oxidize the elemental carbon (EC). The sample heating began at 30 °C in N_2 and was ramped up to 900 °C at 20 °C/min. The temperature was held at 900 °C for 10 min before dropping back to 30 °C at 20 °C/min. The same temperature profile was then repeated in air. From the TGA mass loss, the OC/TC was estimated as the ratio of mass lost under N_2 divided by the total mass lost in both stages.

Soot nanoparticles were analyzed by N_2 adsorption on a Tristar II Plus surface area and a porosity system (Micromeritics) at 77.3 K after degassing in vacuum (VacPrep 061, Micromeritics) at 200 °C overnight. The specific surface area, SSA, was derived from N_2 adsorbed at five relative pressures ranging from 0.05 to 0.25 using the Brunauer–Emmett–Teller method [43].

Soot nanoparticles were also imaged using transmission electron microscopy (TEM, FEI Tecnai F30 FEG). The nanoparticles were dispersed in ethanol and placed in an ultrasonic bath for 15 min to break up large agglomerates [23]. A drop of ethanol solution was then placed on lacey carbon TEM grids with a 200 mesh copper support (LC200-Cu-150, Electron Microscopy Sciences) and allowed to dry. The primary particle diameter, d_p, was measured by manually placing ellipses over the primary particles in ImageJ [44] and calculating the area-equivalent diameter. About 150–200 primary particles were counted for each [O_2] condition to obtain statistically significant size distributions [23].

A3. Results and Discussion

Extensive recirculation results in radially rather uniform conditions away from the burner, as has been shown for temperature, T, by computational fluid dynamics (CFD) analysis (e.g., Figure 1a in ref [45]). To further confirm this for the soot aerosol, its average mobility diameter, d_m, f_v, and N_t were measured at the centerline (r/R = 0) and in-between the tube wall and centerline (r/R = 0.5; Table S1) at HAB = 25 cm (i.e., well below the location of the torus ring with the 12 N_2-jets containing O_2). The soot N_t, f_v, and d_m at the centerline are similar (within the measurement variation) to those obtained in-between the tube wall and centerline there. This indicates that the soot aerosol has been largely homogenized across the tube radius when it reaches the torus ring (HAB = 30 cm). Further downstream, the soot size distribution becomes even more uniform across the tube due to its intense mixing with the O_2-containing N_2 jets, as shown in Figure S4 for two radial locations at HAB = 35 and 63 cm, as well as by the corresponding N_t and mean d_m (Table S2). This indicates that the soot aerosol is well mixed across the enclosing tube, corroborating CFD simulations at similar gas-aerosol mixing configurations [30].

Figure A.2 shows the soot mobility (a) and primary particle (b) size distributions at the centerline of HAB = 63 cm along with their mean soot d_m and d_p from ESC of jet fuel and mixed with N_2 jets containing 0 – 25 vol % O_2. In the absence of oxidation, ([O_2] = 0 vol %), soot nanoparticles form large agglomerates that have a broad dm distribution with mean d_m = 181 nm (Figure A.2a: solid red line), in good agreement with those measured from ESC of jet A1 fuel at similar equivalence ratios [23]. The primary particles making up these

agglomerates have a relatively narrow size distribution with a geometric standard deviation, σ_g = 1.27 with d_p = 12 nm (Figure A.2b: solid red line). Increasing [O_2] to 5 vol % hardly alters the soot mobility size distribution (dotted line). In contrast, the primary particle size distribution shifts to larger d_p, consistent with the literature on low O_2 (< 10 vol %) addition that enhances the formation of PAHs [46] through the generation of reactive O_2 species [47]. Most likely, the increase of soot d_p at [O_2] = 5 vol % can be attributed to such PAHs that adsorb on the soot surface (as confirmed here by TGA and Raman spectroscopy, Figure A.4f,h). The mobility and primary particle size distributions measured here for soot from ESC of jet fuel at [O_2] = 5 vol % are consistent with those measured for soot made in laminar flow reactors at low O_2 concentrations [47]. Increasing the O_2 concentration in the injected N_2 jets increases the flame T at HAB = 35 cm from 780 K at [O_2] = 0 vol % up to 1400 K at [O_2] = 20 vol % (Figure A.1b). At such a high T, surface oxidation takes place [48] reducing both soot dm and dp. In particular, increasing [O_2] up to 20 and 25 vol % enhances soot oxidation, reducing its d_m to 59 and 37 nm and its d_p to 10 and 8 nm. The broad d_m distributions at large [O_2] are similar to those obtained after diluting and combusting ethylene [19] and jet fuel [20] soot with air in lean premixed flames. These broad distributions can be attributed to fragmentation by oxidation suggested by measurements and simulations of diesel soot oxidation [49]. Furthermore, the d_p distribution narrows drastically by surface oxidation at large [O_2], i.e., from 1.27 at [O_2] = 0 vol % down to σ_g of 1.13 and 1.14 at [O_2] = 20 and 25 vol %, respectively.

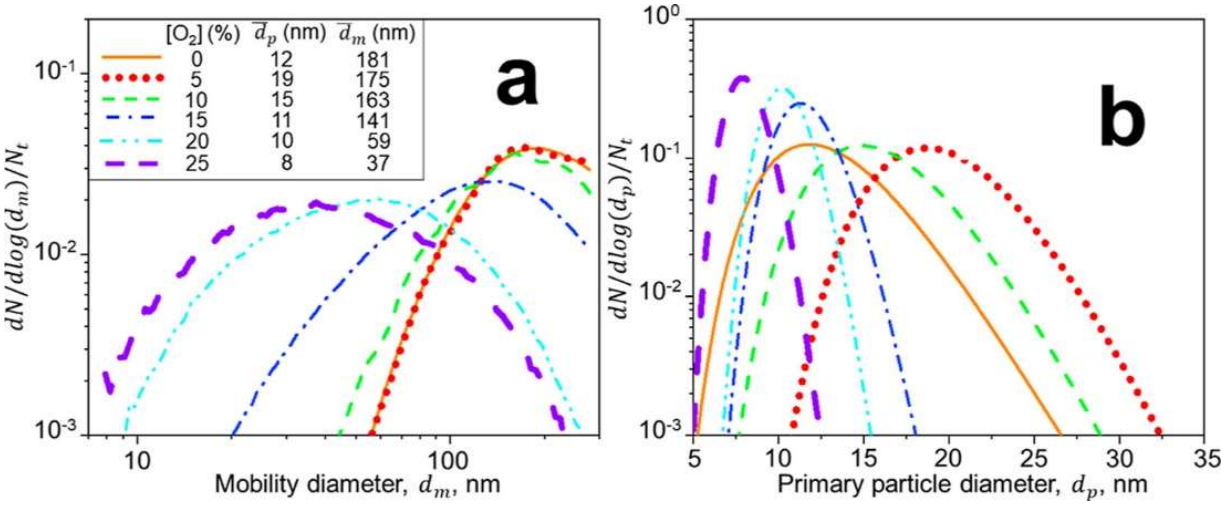

Figure A.2: Impact of O_2-containing N_2 jets on soot characteristics. Mobility (a) and primary particle (b) size distributions along with the mean mobility, d_m, and primary particle, d_p, diameters of soot from ESC of jet fuel and mixed with N_2 jets having O2 concentrations, [O_2] = 0 (solid line), 5 (dotted line), 10 (broken line), 15 (dot-broken line), 20 (double dot-broken line), and 25 vol % (thick broken line).

The mobility and primary particle size distributions measured here can be used to obtain the N_t (Figure A.3: triangles and a broken line) and f_v (circles and a solid line). The latter is derived by accounting for the realistic agglomerate structure of soot that is essential to close its

mass balance [33]. Increasing [O_2] from 0 to 5 vol % enhances soot f_v by 80 % (Figure A.3) due to the PAH formation and adsorption on the soot surface [46], consistent with the soot f_v increase after injection of small amounts of air downstream of synthetic fuel combustion [17]. Soot N_t also increases by 25 %. This could be attributed to the inception of nascent soot enabled by the low concentrations [47] of O_2. Increasing [O_2] to 20 vol % almost eliminates soot emissions by reducing f_v and N_t by 98.3 and 87.3 %, respectively. Further increasing [O_2] to 25 vol % hardly affects f_v and N_t, reducing them by 99.6 and 95.4 %, respectively. The reduction of soot N_t obtained here is on par with the 99.9 % N_t reduction measured after air dilution and combustion in a lean premixed flame [20]. This indicates that rather uniform soot concentration profiles are attained here (Figure S4 and Table S2), similar to those in premixed flames [20].

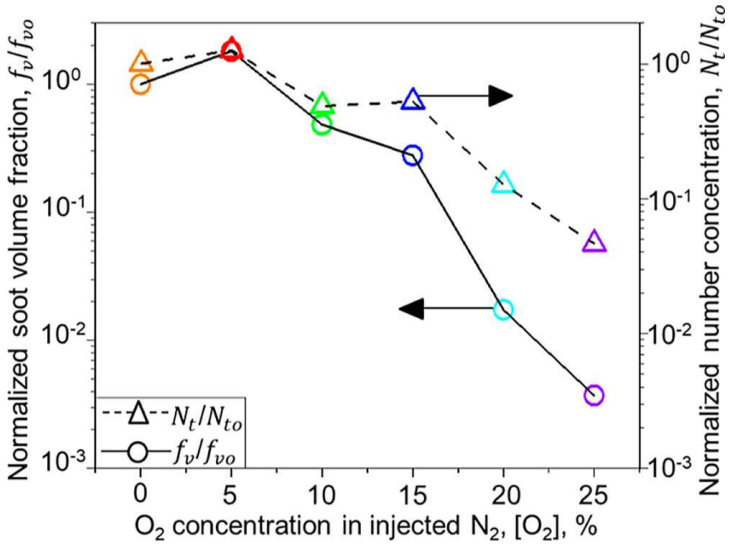

Figure A.3: Reducing soot emissions by downstream injection of O_2-containing N_2. Normalized volume fraction, f_v/f_{vo} (circles and a solid line), and total number density, N_t/N_{to} (triangles and a broken line), of soot produced from ESC of jet A fuel and mixed downstream with 20 L/min of O_2-containing N_2 jets as a function of their [O_2] normalized by the $f_{vo} = 1.4 \times 10^{-8}$ and $N_{to} = 6.7 \times 107$ cm^{-3} at [O_2] = 0 vol %.

Furthermore, the soot f_v reduction measured here is 50 % larger than that attained in a laboratory-scale RQL combustor [17]. This could be attributed to potentially more homogeneous mixing of soot with oxidizing gas by employing the current jet configuration. The soot $f_v = 5 \times 10^{-11}$ obtained here at [O_2] = 25 vol % is on par with the $f_v = 3 \times 10^{-11}$ to 6×10^{-11} measured in a so-called "soot-free" LEAF combustor [22]. In fact, the corresponding $N_t = 3.1 \times 10^6$ #/cm^3 is 3 orders of magnitude lower than the $N_t = 3.5 – 7.5 \times 10^9$ #/cm^3 measured in LEAF [22]. The largest 95.4 % N_t reduction of jet fuel emissions attained here using O_2-containing N_2 jets is about 25 – 60 % greater than that obtained by blending jets with HEFA [7] or FT-derived [8] fuels.

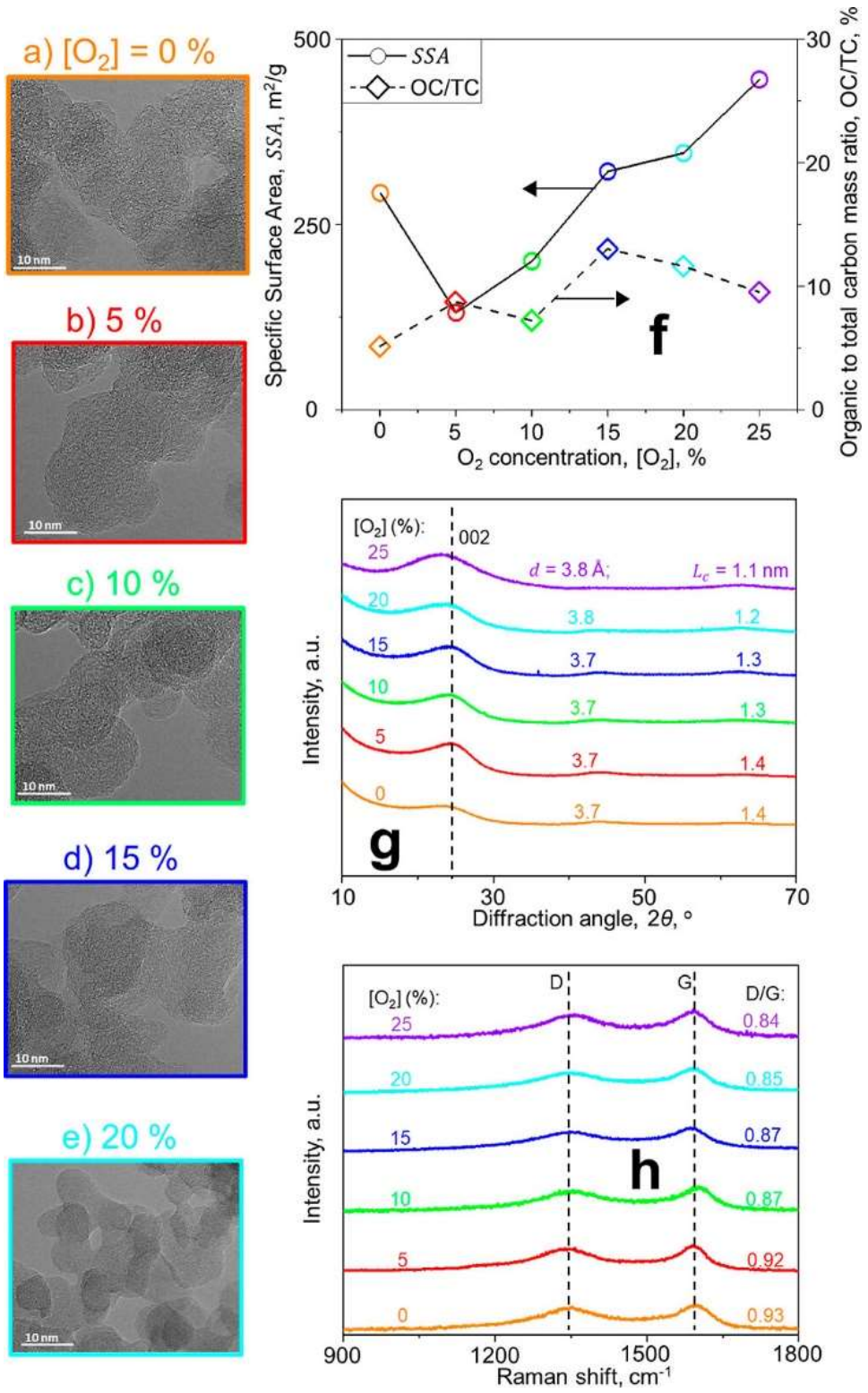

Figure A.4: Characterization of soot nanostructure and composition. Microscopy images (a–e), specific surface area, SSA (f: left ordinate), and organic to total carbon (OC/TC) mass ratio (f: right ordinate); XRD patterns (g) and Raman spectra (h) of soot from ESC of jet fuel and mixed with N_2 jets having [O_2] of 0 – 25 vol %.

Figure A.4f shows the specific surface area, SSA (circles and a solid line), and organic to total carbon (OC/TC) mass ratio (diamonds and a broken line) of soot produced here at the conditions shown in Figure A.3. The SSA of soot correlates with its cytotoxicity [50] and thus

it is essential to quantify its impact on public health. At $[O_2]$ = 0 vol %, soot nanoparticles have SSA = 292.3 m^2/g and OC/TC = 5.1 %, consistent with those measured from ESC of jet A1 fuel at similar equivalence ratios [23]. Varying $[O_2]$ from 0 to 5 vol % decreases the SSA of soot to 130.6 m^2/g and increases its OC/TC to 8.7%, as small amounts of O_2 enhance PAH formation [46] and thus the soot OC/TC. As $[O_2]$ further increases up to 25 vol %, soot nanoparticles are oxidized and their diameter decreases (as discussed in Figure A.2), increasing their SSA up to 445.5 m^2/g. This 50% enhancement of soot SSA attained here is on par with the 30 % increase obtained by blending jet with alternative fuels [9]. Introducing dilution jets with $[O_2]$ more than 5 vol % enhances slightly the adsorption of PAHs and increases the OC/TC of the soot up to 10 – 13 %. This can reduce the light absorption of soot [51] and thus its direct radiative forcing [3] by up to 17 %. Atmospheric transformations of particle composition and morphology (e.g., during water processing [52]) should be accounted for to most accurately quantify the impact of aircraft soot emissions on public health and climate.

The impact of O_2-containing N_2 dilution jets on soot nanostructure is quantified by X-ray diffraction (XRD) and Raman spectroscopy. Figure A.4g shows the XRD patterns along with the mean interlayer distance, d, and crystallite length, L_c, of soot produced at various $[O_2]$. The pattern of unoxidized ESC soot ($[O_2]$ = 0 vol %) exhibits a rather broad 002 peak (broken line) at a diffraction angle, 2θ, of about 24° that yields d = 3.7 Å and L_c = 1.4 nm, in agreement with the XRD pattern of unoxidized carbon black [41] and aircraft soot [26]. Surface oxidation at $[O_2]$ = 5 – 15 vol % hardly affects d and L_c of soot, consistent with the XRD patterns of carbon black oxidized at similar O_2 concentrations [41]. Further increasing $[O_2]$ to 20 – 25 vol % shifts the peak to smaller diffraction angles, increasing d to 3.8 Å and reducing L_c to 1.2 – 1.1 nm. This indicates that oxidation at such large $[O_2]$ makes soot less graphitic, more amorphous, and subsequently more reactive [16].

Figure A.4h shows the Raman spectra along with the mean ratio of the disorder (D) over the graphitic (G) band of soot produced at various $[O_2]$. Increasing $[O_2]$ from 0 to 5 vol % hardly alters the nanostructure and the Raman spectrum of soot. However, further increasing $[O_2]$ from 5 to 20 and 25 vol % reduces D/G to 0.85 and 0.84. This D/G reduction indicates that the average PAH size of soot decrease [53] due to oxidation and small PAH adsorption, consistent with Raman spectroscopy measurements of oxidized carbon black [54], and soot from premixed [55] and diffusion [56] flames. The small PAH sizes attained after soot oxidation with $[O_2]$ = 20 vol % enhance the oxidative reactivity of soot [16] and thus its reactions with ozone in the atmosphere [57]. Most importantly, the amorphous soot emitted after such oxidation has smaller

ice nucleation activity than graphitic soot [58] produced in the absence of downstream O_2 here. This can further limit the formation of contrail cirrus clouds and thus their radiative forcing!

A4. Discussion and Outlook

In conclusion, it is shown that injecting air downstream of jet fuel combustion can drastically reduce its soot emissions. By capitalizing on the quantitative understanding of soot oxidation [48] and, in particular, surface growth and agglomeration dynamics in the ESC reactor and torus ring [31], it was shown that upward injection of 12 swirling O_2-containing N_2 jets facilitates close contact of the soot aerosol with oxidizing gas to enable drastic reduction of soot emissions (Figure A.3). In particular, the injection of N_2 containing 20 – 25 vol % of O_2 enhances the oxidation of soot nanoparticles and decreases their N_t and f_v by 87.3 – 95.4 and 98.3 – 99.6%, respectively. Oxidation at these conditions increases the amorphous and organic carbon content of the emitted soot, reducing its light absorption [51], direct radiative forcing [3], and ice nucleation activity [58]. The number concentration of ice nuclei formed in the contrails of aircraft engines decreases almost linearly as the soot number concentration decreases from 10^{16} down to about 8×10^{13} #/kg of fuel [4]. Recent measurements have shown that aircraft engines combusting jet A1 fuel release 5×10^{15} #/kg of fuel (see Figure 4 in ref [8]). Injection of O_2 downstream of jet A or A1 fuel combustion reduces the soot N_t up to about an order of magnitude (Figure A.3). In this N_t range, the concentration of ice nuclei seems to decrease linearly with the soot concentration [4]. This suggests that the injection of air downstream of aircraft engines may reduce the radiative forcing from their emissions [6] by at least 50%.

To relate the present results to the emissions of actual jet engines, besides matching fuel and oxidant composition (jet fuel A or A1 and air or $[O_2] = 20\%$), one has to match the so-called high temperature particle residence time between ESC and jet engines, as has been shown in the combustion synthesis of nanoparticles (i.e., Figure 7 in ref [59]). The scale-up of the present spray combustion reactor has been explored experimentally and numerically [59] up to 2 orders of magnitude [60] where it was shown that the characteristics of flame-made nanoparticles can be preserved by maintaining similar high-temperature particle residence times across scales. In this regard, the present set of data is essential to derive and validate CFD [59] and moving sectional models for soot oxidation from jet fuel combustion [48]. Such models can be used to obtain robust oxidation rates for aircraft soot emissions and facilitate the design and scale-up of engine exhausts with minimal, if not zero, soot emissions.

A5. References

[1] Agarwal A, Speth RL, Fritz TM, Jacob SD, Rindlisbacher T, Iovinelli R, Owen B, Miake-Lye RC, Sabnis JS, Barrett SRH. SCOPE11 Method for Estimating Aircraft Black Carbon Mass and Particle Number Emissions. *Environ Sci Technol* (2019) **53**, 1364–73.

[2] Delaval MN, Jonsdottir HR, Leni Z, Keller A, Brem BT, Siegerist F, Schönenberger D, Durdina L, Elser M, Salathe M, Baumlin N, Lobo P, Burtscher H, Liati A, Geiser M. Responses of reconstituted human bronchial epithelia from normal and health-compromised donors to non-volatile particulate matter emissions from an aircraft turbofan engine. *Environ Pollut* (2022) **307**, 119521.

[3] Kelesidis GA, Neubauer D, Fan LS, Lohmann U, Pratsinis SE. Enhanced Light Absorption and Radiative Forcing by Black Carbon Agglomerates. *Environ Sci Technol* (2022) **56**, 8610–8.

[4] Kärcher B. Formation and radiative forcing of contrail cirrus. *Nat Commun* (2018) **9**, 1824.

[5] Lee DS, Fahey DW, Skowron A, Allen MR, Burkhardt U, Chen Q, Doherty SJ, Freeman S, Forster PM, Fuglestvedt J, Gettelman A, De León RR, Lim LL, Lund MT, Millar RJ, Owen B, Penner JE, Pitari G, Prather MJ, Sausen R, Wilcox LJ. The contribution of global aviation to anthropogenic climate forcing for 2000 to 2018. *Atmos Environ* (2021) **244**, 117834.

[6] Burkhardt U, Bock L, Bier A. Mitigating the contrail cirrus climate impact by reducing aircraft soot number emissions. *Npj Clim Atmos Sci* (2018), 1–37.

[7] Moore RH, Thornhill KL, Weinzierl B, Sauer D, D'Ascoli E, Kim J, Lichtenstern M, Scheibe M, Beaton B, Beyersdorf AJ, Barrick J, Bulzan D, Corr CA, Crosbie E, Jurkat T, Martin R, Riddick D, Shook M, Slover G, Voigt C, White R, Winstead E, Yasky R, Ziemba LD, Brown A, Schlager H, Anderson BE. Biofuel blending reduces particle emissions from aircraft engines at cruise conditions. *Nature* (2017) **543**, 411–5.

[8] Voigt C, Kleine J, Sauer D, Moore RH, Bräuer T, Le Clercq P, Kaufmann S, Scheibe M, Jurkat-Witschas T, Aigner M, Bauder U, Boose Y, Borrmann S, Crosbie E, Diskin GS, DiGangi J, Hahn V, Heckl C, Huber F, Nowak JB, Rapp M, Rauch B, Robinson C, Schripp T, Shook M, Winstead E, Ziemba L, Schlager H, Anderson BE. Cleaner burning aviation fuels can reduce contrail cloudiness. *Commun Earth Environ* (2021) **2**, 2–11.

[9] Chen L, Hu X, Wang J, Yu Y. Impacts of alternative fuels on morphological and nanostructural characteristics of soot emissions from an aviation piston engine. *Environ Sci Technol* (2019) **53**, 4667–74.

[10] Geigle KP, Hadef R, Meier W. Soot Formation and flame characterization of an aero-engine model combustor burning ethylene at elevated pressure. *J Eng Gas Turbines Power* (2014) **136**, 021505.

[11] Liu Y, Sun X, Sethi V, Nalianda D, Li YG, Wang L. Review of modern low emissions combustion technologies for aero gas turbine engines. *Prog Aerosp Sci* (2017) **94**, 12–45.

[12] Lefebvre AH. The role of fuel preparation in low-emission combustion. *J Eng Gas Turbines Power* (1995) **117**, 617–54.

[13] Geigle KP, Hadef R, Stöhr M, Meier W. Flow field characterization of pressurized sooting swirl flames and relation to soot distributions. *Proc Combust Inst* (2017) **36**, 3917–24.

[14] De Falco G, Helou I El, de Oliveira PM, Sirignano M, Yuan R, D'Anna A, Mastorakos E. Soot particle size distribution measurements in a turbulent ethylene swirl flame. *Proc Combust Inst* (2021) **38**, 2691–9.

[15] Ess MN, Vasilatou K. Characterization of a new miniCAST with diffusion flame and premixed flame options: Generation of particles with high EC content in the size range 30 nm to 200 nm. *Aerosol Sci Technol* (2019) **53**, 29–44.

[16] Hagen FP, Kretzler D, Häber T, Bockhorn H, Suntz R, Trimis D. Carbon nanostructure and reactivity of soot particles from non-intrusive methods based on UV-VIS spectroscopy and time-resolved laser-induced incandescence. *Carbon* (2021) **182**, 634–54.

[17] El Helou I, Foale JM, Pathania RS, Ciardiello R, Skiba AW, Mastorakos E. A comparison between fossil and synthetic kerosene flames from the perspective of soot emissions in a swirl spray RQL burner. *Fuel* (2023) **331**, 125608.

[18] Mueller ME, Pitsch H. Large eddy simulation of soot evolution in an aircraft combustor. *Phys Fluids* (2013) **25**, 110812.

[19] Ghiassi H, Jaramillo IC, Toth P, Lighty JAS. Soot oxidation-induced fragmentation: Part 2: Experimental investigation of the mechanism of fragmentation. *Combust Flame* (2016) **163**, 170–8.

[20] Echavarria CA, Jaramillo IC, Sarofim AF, Lighty JAS. Burnout of soot particles in a two-stage burner with a JP-8 surrogate fuel. *Combust Flame* (2012) **159**, 2441–8.

[21] Neoh KG, Howard JB, Sarofim AF. Effect of oxidation on the physical structure of soot. *Symp Combust* (1985) **20**, 951–7.

[22] Miniero L, Pandey K, De Falco G, D'Anna A, Noiray N. Soot-free and low-NO combustion of Jet A-1 in a lean azimuthal flame (LEAF) combustor with hydrogen injection. *Proc Combust Inst* (2023) **39**, 4309–18.

[23] Trivanovic U, Kelesidis GA, Pratsinis SE. High-throughput generation of aircraft-like soot. *Aerosol Sci Technol* (2022) **56**, 732–43.

[24] Kelesidis GA, Goudeli E, Pratsinis SE. Flame synthesis of functional nanostructured materials and devices: Surface growth and aggregation. *Proc Combust Inst* (2017) **36**, 29–50.

[25] Kelesidis GA, Goudeli E, Pratsinis SE. Morphology and mobility diameter of carbonaceous aerosols during agglomeration and surface growth. *Carbon* (2017) **121**, 527–35.

[26] Parent P, Laffon C, Marhaba I, Ferry D, Regier TZ, Ortega IK, Chazallon B, Carpentier Y, Focsa C. Nanoscale characterization of aircraft soot : A high-resolution transmission electron microscopy, Raman spectroscopy, X-ray photoelectron and near-edge X-ray absorption spectroscopy study. *Carbon* (2016) **101**, 86–100.

[27] Kholghy MR, DeRosa VG. Morphology, composition and optical properties of jet engine-like soot made by a spray flame. *Combust Flame* (2021) **231**, 111480.

[28] Mädler L, Kammler HK, Mueller R, Pratsinis SE. Controlled synthesis of nanostructured particles by flame spray pyrolysis. *J Aerosol Sci* (2002) **33**, 369–89.

[29] Teleki A, Heine MC, Krumeich F, Akhtar MK, Pratsinis SE. In situ coating of flame-made TiO_2 particles with nanothin SiO_2 films. *Langmuir* (2008) **24**, 12553–8.

[30] Teleki A, Buesser B, Heine MC, Krumeich F, Akhtar MK, Pratsinis SE. Role of gas -

aerosol mixing during in situ coating of flame-made titania particles. *Ind Eng Chem Res* (2009) **48**, 85–92.

[31] Trivanovic U, Pereira Martins M, Benz S, Kelesidis GA, Pratsinis SE. Dynamics of soot surface growth and agglomeration by enclosed spray combustion of jet fuel. *Fuel* (2023) **342**, 127864.

[32] Goudeli E, Gröhn AJ, Pratsinis SE. Sampling and dilution of nanoparticles at high temperature. *Aerosol Sci Technol* (2016) **50**, 591–604.

[33] Kelesidis GA, Pratsinis SE. Determination of the volume fraction of soot accounting for its composition and morphology. *Proc Combust Inst* (2021) **38**, 1189–96.

[34] Kelesidis GA, Kholghy MR, Zuercher J, Robertz J, Allemann M, Duric A, Pratsinis SE. Light scattering from nanoparticle agglomerates. *Powder Technol* (2020) **365**, 52–9.

[35] Camacho J, Liu C, Gu C, Lin H, Huang Z, Tang Q, You X, Saggese C, Li Y, Jung H, Deng L, Wlokas I, Wang H. Mobility size and mass of nascent soot particles in a benchmark premixed ethylene flame. *Combust Flame* (2015) **162**, 3810–22.

[36] Rissler J, Messing ME, Malik AI, Nilsson PT, Erik Z, Bohgard M, Sanati M, Pagels JH, Rissler J, Messing ME, Malik AI, Nilsson PT, Erik Z, Rissler J, Messing ME, Malik AI, Nilsson PT, Nordin EZ, Bohgard M, Sanati M, Pagels JH. Effective density characterization of soot agglomerates from various sources and comparison to aggregation theory effective density characterization of soot agglomerates from various sources and comparison to aggregation theory. *Aerosol Sci Technol* (2013) **47**, 792–805.

[37] Sadezky A, Muckenhuber H, Grothe H, Niessner R, Pöschl U. Raman microspectroscopy of soot and related carbonaceous materials: Spectral analysis and structural information. *Carbon* (2005) **43**, 1731–42.

[38] Baldelli A, Rogak SN. Morphology and Raman spectra of aerodynamically-classified soot samples. *Atmos Meas Tech Discuss* (2019) **12**, 4339–46.

[39] Iwashita N, Park CR, Fujimoto H, Shiraishi M, Inagaki M. Specification for a standard procedure of X-ray diffraction measurements on carbon materials. *Carbon* (2004) **42**, 701–14.

[40] Lapuerta M, Oliva F, Agudelo JR, Boehman AL. Effect of fuel on the soot nanostructure and consequences on loading and regeneration of diesel particulate filters. *Combust Flame* (2012) **159**, 844–53.

[41] Kelesidis GA, Rossi N, Pratsinis SE. Porosity and crystallinity dynamics of carbon black during internal and surface oxidation. *Carbon* (2022) **197**, 334–40.

[42] Klingshirn CD, West ZJ, DeWitt MJ, Higgins A, Graham J, Corporan E. Quantification of elemental and total carbon in combustion particulate matter using thermal-oxidative analysis. *J Air Waste Manag Assoc* (2019) **69**, 1003–13.

[43] Brunauer S, Emmett PH, Teller E. Adsorption of Gases in Multimolecular Layers. *J Am Chem Soc* (1938) **60**, 309–19.

[44] Schneider CA, Rasband WS, Eliceiri KW. NIH Image to ImageJ: 25 years of image analysis. *Nat Methods* (2012) **9**, 671–5.

[45] Waser O, Brenner O, Groehn AJ, Pratsinis SE. Process design for size-controlled flame spray synthesis of $Li_4Ti_5O_{12}$ and electrochemical performance. *Chem Process Eng* (2017) **38**, 51–66.

[46] Sánchez NE, Callejas A, Millera Á, Bilbao R, Alzueta MU. Influence of the oxygen

presence on polycyclic aromatic hydrocarbon (PAH) formation from acetylene pyrolysis under sooting conditions. *Energy and Fuels* (2013) **27**, 7081–8.

[47] Mei J, Zhou Y, You X, Law CK. Formation of nascent soot during very fuel-rich oxidation of ethylene at low temperatures. *Combust Flame* (2021) **226**, 31–41.

[48] Kelesidis GA, Pratsinis SE. Estimating the internal and surface oxidation of soot agglomerates. *Combust Flame* (2019) **209**, 493–9.

[49] Harris SJ, Maricq MM. The role of fragmentation in defining the signature size distribution of diesel soot. *J Aerosol Sci* (2002) **33**, 935–42.

[50] Schmid O, Stoeger T. Surface area is the biologically most effective dose metric for acute nanoparticle toxicity in the lung. *J Aerosol Sci* (2016) **99**, 133–43.

[51] Kelesidis GA, Bruun CA, Pratsinis SE. The impact of organic carbon on soot light absorption. *Carbon* (2021) **172**, 742–9.

[52] Kelesidis GA, Furrer FM, Wegner K, Pratsinis SE. Impact of humidity on silica nanoparticle agglomerate morphology and size distribution. *Langmuir* (2018) **34**, 8532–41.

[53] Ferrari AC, Robertson J. Raman spectroscopy of amorphous, nanostructured, diamond-like carbon, and nanodiamond. *Philos Trans R Soc A Math Phys Eng Sci* (2004) **362**, 2477–512.

[54] Seong H, Choi S. Oxidation-derived maturing process of soot, dependent on O_2-NO_2 mixtures and temperatures. *Carbon* (2015) **93**, 1068–76.

[55] De Falco G, Bocchicchio S, Commodo M, Minutolo P, D'Anna A. Raman Spectroscopy of Nascent Soot Oxidation: Structural Analysis During Heating. *Front Energy Res* (2022) **10**, 1–11.

[56] Hayashida K, Nagaoka S, Ishitani H. Growth and oxidation of graphitic crystallites in soot particles within a laminar diffusion flame. *Fuel* (2014) **128**, 148–54.

[57] Lohmann U, Friebel F, Kanji ZA, Mahrt F, Mensah AA, Neubauer D. Future warming exacerbated by aged-soot effect on cloud formation. *Nat Geosci* (2020) **13**, 674–80.

[58] Häusler T, Gebhardt P, Iglesias D, Rameshan C, Marchesan S, Eder D, Grothe H. Ice nucleation activity of graphene and graphene oxides. *J Phys Chem C* (2018) **122**, 8182–90.

[59] Gröhn AJ, Pratsinis SE, Sánchez-Ferrer A, Mezzenga R, Wegner K. Scale-up of nanoparticle synthesis by flame spray pyrolysis: The high-temperature particle residence time. *Ind Eng Chem Res* (2014) **53**, 10734–42.

[60] Mueller R, Mädler L, Pratsinis SE. Nanoparticle synthesis at high production rates by flame spray pyrolysis. *Chem Eng Sci* (2003) **58**, 1969–76.

Appendix B

Impact of sustainable aviation fuels on soot from enclosed spray combustion

Abstract

Sustainable aviation fuels (SAF) are currently one of the most promising short to medium-term solutions to reduce the CO_2 emissions from aviation. Currently, SAF fuels are blended with conventional jet fuels up to a maximum of 50 vol% and reductions in CO_2 are achieved through the capture of CO_2 during the production of the fuels. In addition to CO_2, Aviation emits soot particles which have negative environmental and health effects and as such, should be minimized. These new SAF fuels will also have an effect on the emitted soot particles with early studies showing a tendency towards reduced particle size and number concentration. In order to properly assess the impact of SAF on soot emissions, Enclosed Spray Combustion of jet A1 and blends of up to 50 % Hydroprocessed Esters and Fatty Acids (HEFA) SAF were used to produce aircraft-like soot and compare the size, morphology and nanostructure of the resulting particles. The addition of SAF up to 50 % did not appear to have a significant effect on the morphology, nanostructure or composition of the soot produced. However, slight reductions were observed in the number concentration for all blends between 10 – 50 % and a small reduction in the mobility diameter was observed when the 50 % blend was used.

B1. Introduction

The aviation industry is under growing pressure to reduce its climate impact. One of the most promising solutions to reduce CO_2 emissions currently being developed is sustainable aviation fuels (SAF). These fuels provide an immediate solution for reducing emissions from aviation, because SAF can provide an immediate reduction in emissions without needing new infrastructure or aircrafts. SAF can be produced through various processes, however the most developed is currently hydrotreated ester and fatty acid (HEFA) based SAF. These fuels were refined from vegetable oils, waste oils or fats. Their life cycle CO_2 emissions are reduced by the absorbed CO_2 of the biomass used in the SAF production. The International Civil Aviation Organization (ICAO) stipulates that these fuels must be compatible with existing aircraft engines [1]. Currently, the maximum approved blending ratio is 50% for SAF produced from HEFA based fuels, while for other SAF this limit might be lower. This is to ensure compatibility with older aircraft engines as dictated by the ASTM D7566. Optimistically, SAF could reduce aviation's lifecycle CO_2 emissions by up to 68% if more than 85% of all aviation fuels are replaced with SAF [2]. In addition to CO_2, aircrafts produce soot nanoparticles that negatively impact the climate [3] and human health [4] and are therefore regulated by the ICAO. While there is evidence that SAF could reduce soot [5] as well as CO2 emissions, so far, soot emissions were often neglected in the life cycle assessment of SAF [2]. This may be in part, because the effects of SAF on soot emissions are still unclear and need further investigation.

Blends of SAF and conventional jet fuels have demonstrated significant reductions in non-volatile particle matter (nvPM), composed primarily of soot, from aircraft engines. For example, during a standardized landing and take-off (LTO) cycle at ground level a 32% SAF blend resulted in a 20% mass reduction and 25% reduction in the number of nvPM particles [5]. This reduction might be due to the low aromatic content of SAF [6]. Aromatics are known to act as a precursor for soot formation, so reducing aromatic content may reduce soot formation for SAF blended fuels compared to conventional fuels [7]. Similar reductions were observed during cruise conditions, where a 50% SAF blend resulted in a 50% reduction in soot number and a 70% reduction in mass concentrations [8]. The effect of SAF on soot emissions was shown to be thrust dependent where the greatest reductions occurred at lower thrust levels, which was in agreement with the lower emissions at cruise conditions for SAF [5]. This aligned with findings from the studies of conventional jet fuels, which showed that the fuel composition had a lesser impact on soot emissions at high thrusts [7]. SAF could therefore be used to improve the air quality at airports, where low thrust idling of airplanes is common.

The use of SAF could influence the size of soot particles, including the primary particle diameter (d_p) and the mobility diameter (d_m). Studies had shown varied effects based on SAF blend ratios. For instance, one study found that low SAF blends (20%) slightly increased the d_m of soot, while blends at 40% or higher had comparable or lower d_m than pure jet fuel [9]. Other research had reported a consistent decrease in d_m even with SAF blends as low as 17% [10]. The effect of SAF on d_p and nanostructure was similarly unclear and has not yet been extensively studied. One study found an overall decrease in d_p for 25% Fischer-Tropsch (FT) based SAF and 20% pentanol fuel blends with RP-3 fuel in a piston engine [11]. However, other work showed that pure hydroprocessed renewable jet (HRJ) and FT SAF resulted in a larger d_p of 29 nm and 27 nm respectively, in comparison to Jet A1 fuel with a d_p of 22 nm at low thrust conditions [12]. While smaller primary particles were produced, at high thrust conditions, with a d_p of 20 nm and 23 nm for HRJ and FT SAF, compared to conventional fuel with a d_p of 27 nm [12]. So far there are no data in the literature on the effect of SAF blending with primary particle size, to the best of our knowledge.

SAF blends may have led to greater soot graphitization, which was observed for a 40% pentanol and a 25% Fischer-Tropsch SAF blend with RP-3 [11]. The reference Jet A1 fuel displayed higher levels of amorphous carbon and a lower degree of graphitic crystallization [11]. This could have been due to higher temperatures that led to a greater graphitization of soot [13]. However, the opposite trend was observed in a different engine type, where SAF blends formed more disordered soot, which was attributed to the lower aromatic content [12]. Therefore, the effect of SAF blending on the nanostructure of soot remained unclear. The organic carbon to total carbon (OC/TC) ratio was correlated with soot maturity, which alters its light absorption and is crucial for determining the radiative forcing of soot [14]. A 32% HEFA based SAF blend did not show an influence on the OC/TC ratio compared to Jet A1 fuel [15]. However, these results does not rule out a possible influence of blending on the OC/TC ratio, when other blend ratios were used. Additionally, the OC/TC ratio greatly depended on the engine thrust, so the effect of SAF blending on the OC/TC ratio may also be dependent on the thrust level [15]. One of the most important characteristics for understanding the toxicity of nanoparticles is the specific surface area (SSA) of soot [16]. Nevertheless, no studies so far have investigated the impact of blending SAF on this quantity, despite its potential effect on air quality near airports.

While some soot properties have been characterized for soot produced by pure SAF and some SAF blends, there has not yet been a comprehensive characterization of the morphology, size and nanostructure of soot produced by SAF at various blending ratios. Therefore, this work

synthesizes soot through enclosed spray combustion of varied blend ratios of HEFA SAF to Jet A1 fuel from 0 to 50%. Changing the blend ratio will quantify its impact on the mobility size distribution, the primary particle diameter, the flame temperature, the nanostructure, the OC/TC ratio and the SSA without confounding factors such as engine type and thrust. This understanding could lead to a better utilization of the currently limited SAF supply and might support the development of SAF in regard to their soot emissions as well as to facilitate literature comparison.

B2. Experimental

Following a previously used method for soot generation with conventional fuel, soot was generated by enclosed spray combustion of Jet A1 fuel (Birrfeld Airport, Lupfig, Switzerland) blended with a HEFA based SAF (Bio Thrust, Circular Industries) [17]. The flame was enclosed by two 30 cm long quartz or steel tubes (42 mm diameter inner diameter) in series. The fuel was injected with a flowrate of 4.5 mL/min and then dispersed into a fine spray with 1.5 L/min of O_2 to reach the effective equivalence ratio (EQR) of 1.59. The EQR was calculated based on the chemical composition of $C_{11.6}H_{22}$ for the jet fuel [18], considering all flows in the enclosure [17]. The spray was ignited by a supporting premixed methane/oxygen flame (CH_4 = 1.25 L/min, O_2 = 2.25 L/min). Sheath air was introduced at 20 L/min through 12 evenly spaced holes surrounding the spray flame. Furthermore, a torus ring with 12 jet outlets introduced 20 L/min of N_2 in an upward swirled vortex to quench the flame and dilute the exhaust aerosol, in between the two tubes [19]. The manufacturer provided a conventional Jet A1 fuel (0% SAF) and blends of 18 and 50 vol% SAF. Blends of 10, 30 and 40 vol% were mixed to provide intermediate data points.

At 63 cm height above the burner (HAB) the soot was extracted with a straight tube sampler [20]. The flow was diluted with N_2. One flow fraction was further diluted with a rotating disk diluter (MD19-1E) and distributed for online analysis through an X-ray neutralizer (TSI 3087), that was connected to a condensation particle counter (CPC, TSI 3775) to combine into a scanning mobility particle spectrometer (SMPS). Soot was analyzed for its mobility size distribution with the SMPS. An R-type thermocouple (Intertechno-Firag AG) was used to measure the flame temperature for the different fuels at 5, 10, 15, 20, 25 and 63 cm HAB, whose results were then corrected for radiative heat losses [21]. Soot produced during in-flame temperature measurements were discarded for analysis in case the presence of the thermocouple altered the soot.

The fraction of soot not sent through the rotating disk diluter was collected on a glass fiber filter for offline analysis. Raman spectroscopy was employed to assess the nanostructure of soot

using the methods outlined by Sadezky et al. [23]. Raman spectra were obtained with a 515 nm laser with 50 mW power (Renshaw inVia). The laser, focused through an optical microscope at x20 magnification with a 2 μm spot size, was applied to the soot sample at 10% power for 120s at three distinct locations. Baseline subtraction was performed on the resulting Raman spectra to correct for fluorescence. The intensities of the disordered band (D ~ 1350 cm^{-1}) and the graphitic band (G ~ 1580 cm^{-1}) were compared by calculating the baseline adjusted D/G ratio of the height of these peaks. Further characterization of the nanostructure was made through X-ray diffraction (XRD) analysis of the produced soot. The AXS D8 diffractometer (Burker) was operated at a scan rate of 0.0197°/s between the diffraction angles 2θ = 10° – 70° to acquire the full width half maximum (FWHM) and the peak angle of the 002 peak. Bragg's law was subsequently utilized to quantify the crystallite length (L_c) and the interlayer distance (d_{002}) [24]. Primary particle sizing was carried out with Transmission Electron Microscopy (TEM, FEI Tecnai F30 FEG). The soot samples were dissolved in ethanol and subjected to an ultrasonic bath for 15 min to break up large agglomerates. A drop of this solution was put on a lacey carbon TEM grid with a 200 mesh copper support (LC200-Cu-150, Electron Microscopy Sciences) and allowed to dry. An image processing software (ImageJ) was used to measure the primary particle diameter (d_p) manually. Around 500 primary particles (PP) were evaluated for each fuel blend to determine an average PP diameter ($\bar{d}_p$), however after counting 200 PP the $\bar{d}_p$ had already been seen to level off [25]. The SSA was determined by utilizing 80 – 100 mg of soot, due to the large quantity the combined soot from multiple experiments with the same conditions was used. The soot was degassed at 200 °C for one hour under vacuum (Micrometrics Tristar II Plus) at approximate relative pressures of 0 to 0.3 (p/p°) using the Brunauer, Emmet and Teller method (BET) [26]. Thermogravimetric analysis (TGA) was used to obtain the OC/TC ratio of soot by modifying the protocol of Klingshirn et al. [27] Samples underwent a heating process from 30 °C to 900 °C at a 20 °C/min rate, where they were held at 900 °C for 10 min before cooling down to 30 °C at the same rate. This temperature profile was done for both nitrogen and air. The organic carbon was volatilized in the N_2 atmosphere and then air to oxidize the elemental carbon. The OC/TC ratio was estimated from the resulting mass loss under N_2 divided by the total mass loss of both stages.

B3. Results and Discussion

Figure B.1 shows the mobility size distributions for blending ratios of a) 0, b) 10, c) 18, d) 30, e) 40 and f) 50% SAF. The dN/dlog(d_m) of the number concentrations were shown as a function of the mobility diameter (d_m) where the lines represented the average distribution and

the shaded area depicted one standard deviation that resulted from ten measurements per experiment that were averaged for the repeated experiments. Experiments for the 40% SAF blend was only performed once which may explain the very small variation compared to the other size distributions. For all blending ratios, the distributions appear to follow a typical lognormal distribution. Figure B.2a shows the total number concentration of particles, N_{tot}, from a lognormal fit of the SMPS data. Similarly, Figure B.2b shows the median of the lognormal fit of the data for the different blending ratios. For both N_{tot} and dm, the average standard deviation of the other conditions was plotted as error bars for the 10 and 40% SAF blends, as the experiments was only performed once. In Figure B.2a, N_{tot} was approximately 10^6 #/m^3 for all blending ratios. The SAF blends appeared to consistently have a decrease in

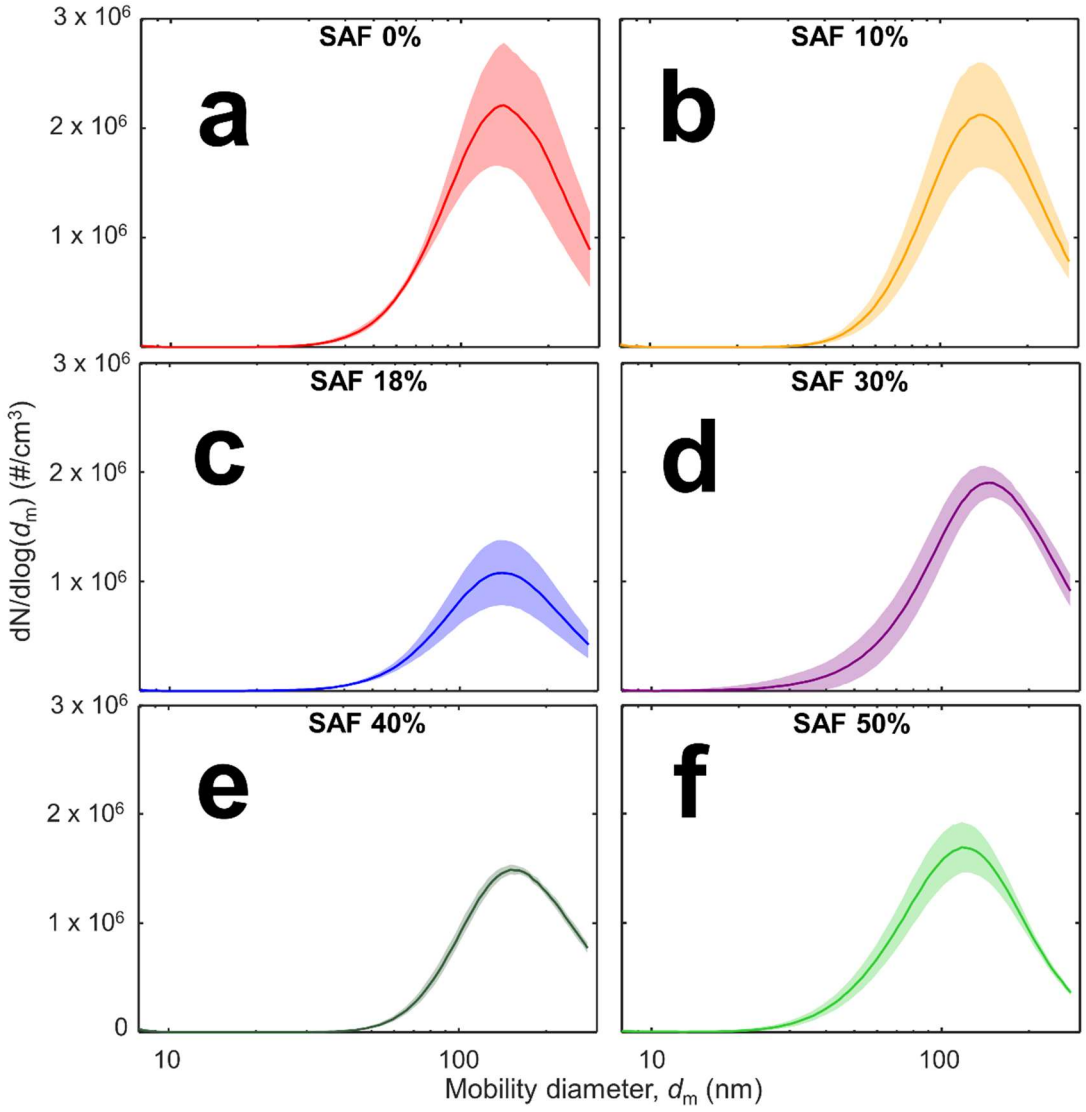

Figure B.1: The mobility size distributions for a SAF blend ratio of a) 0, b) 10, c) 18, d) 30, e) 40 and f) 50% are shown with the dN/dlog(d_m) as a function of the d_m. The average distribution is plotted as a line with a surrounding shaded area, which represented one standard deviation resulting from the average of repeated experiments with ten SMPS scans each. For the 10 and 40% SAF blend only one experiment was carried out.

the average number concentration of approximately 30% compared to the conventional fuel. Nevertheless, the number reductions were within the lower error margin of the pure Jet A1 fuel. The soot produced here was most similar to soot from aircraft engines at high thrust [17]. A study that used a 32% HEFA SAF recorded small number concentration reductions (10 – 15%) at high thrust, which was in line with the small decrease seen in the total number of particles in Figure B.2a [5]. Therefore, the total number of particles did not seem to be strongly correlated to the blend ratio, although there was a consistent slight reduction (~30%) in N_{tot} compared to pure Jet A1.

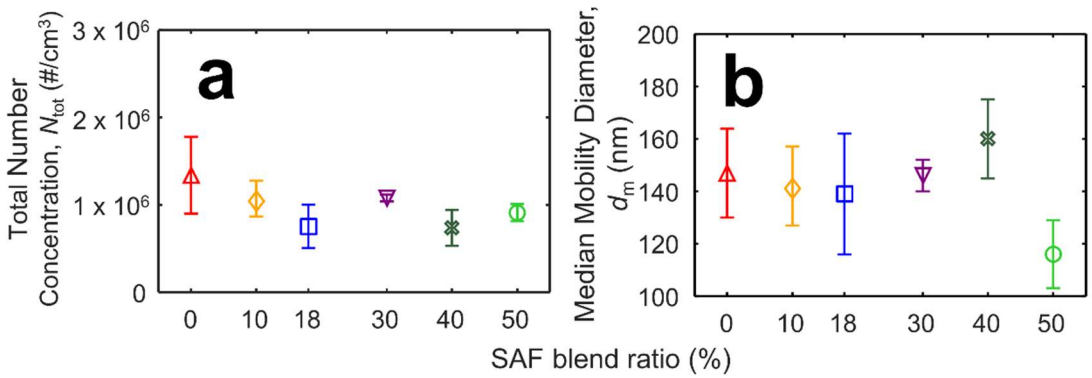

Figure B.2: a) the total number concentration, N_{tot}, and b) median mobility diameter as a function of the SAF blending ratio. Error bars depict the standard deviation between measurements but for the 10 and 40% blends the average standard deviation from the other blending ratios was used as these conditions were only measured once each.

The median mobility diameter, d_m, is shown in Figure B.2b for the different SAF blends. For blending ratios up until 40%, there did not appear to be a difference in the size of the dm compared to the unblended Jet A1 fuel. All values lie within one standard deviation of the 0% SAF. A previous study at the same conditions also reached a d_m of 153 nm for pure SAF, which agreed with the 147 ± 17 nm observed here [17]. For the 50% SAF blend the dm was consistently lower with a d_m of 116 ± 13 nm than for the Jet A1 fuel. This could have indicated that high SAF blends are needed to influence the d_m of soot particles. Low aromatic content was seen to decrease the PP concentration as well as delay soot particle formation [12]. The lower aromatic content of the fuel mixture could have led to fewer primary particles for agglomeration and therefore a decrease in d_m [6]. In the study, smaller differences in aromatic content mattered less for particle concentration and delayed formation, which could explain why only the 50% blend had a d_m decrease [12].

The PP size distributions are shown as histograms in Figure B.3. The fuel blends a) 0, b) 18 and c) 50% were examined through analysis of TEM images with a d_p of 14.6, 15.9 and 14.3 nm and a geometric standard deviation (σ_g) of 1.31, 1.28 and 1.31 nm respectively. While the soot produced by the 18% blend increased by about 1 nm relative to the 0 and 50% blends,

significant overlap of the PP size distributions suggests that this may just be due to random variations between experiments. Therefore, it appears that the blending ratio did not have a strong influence on the average primary particle diameter. This might have been due to the similar temperatures observed for the blends. As surface growth is essential for determining the primary particle size, which is influenced by the temperature [28]. The d_p and σ_g for the SAF 0% were in agreement with prior research at similar conditions that observed a d_p = 14.3 nm and σ_g = 1.25 [17].

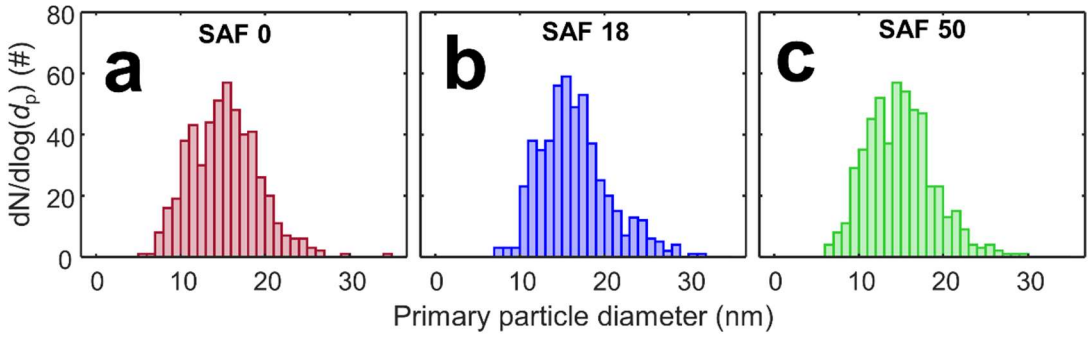

Figure B.3: Histograms of the primary particle diameters measured by TEM for the blend ratios of a) 0, b) 18 and c) 50% are shown.

Figure B.4 shows the centreline flame temperature as a function of HAB with 0 (triangles), 18 (squares) and 50% (circles) SAF. In-flame temperatures from a different batch of Jet A1 (diamonds) are also shown [25]. The error bars represent one standard deviation from at least three measurements. Peak flame temperatures occurred between 5 and 10 cm HAB and showed the largest variation between experiments. These temperature fluctuations might have been in part due to variation of the thermocouple placement. Lower temperatures are reached, when the flame centre is not exactly measured, since the flame is hottest in its centre. Because the lower HAB reached higher temperatures, these differences in the placement were more pronounced in their variability. This observation could be supported by three very high temperatures measured above 1750 K at the 5 and 10 cm HAB, which had massively impacted the variability of the 0 and 50% blend. Otherwise, the temperature profiles shown in Figure B.4 did not demonstrate any major differences for the separate blend ratios. The previous temperature measurement with a different Jet A1 fuel aligned with the temperatures measured for SAF 0%, except for the HAB at 15 and 20 cm. Here the unblended SAF temperatures were lower than the literature values with an approximate decrease of ~300 and ~200 K. These differences could have been due to the usage of a different batch of Jet A1 fuel, which could have affected the exact properties of the fuel. For this reason, in this study SAF was blended with the same batch of Jet A1 used for the 0% condition to remove potential differences between Jet A1 batches.

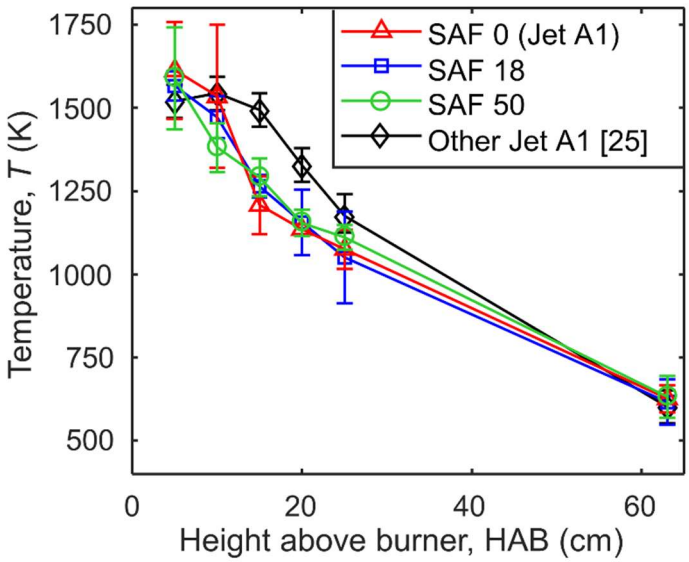

Figure B.4: The centreline temperature profiles as a function of HAB for blending ratios 0 (triangles), 18 (squares) and 50% (circles) HEFA SAF after adjusting for radiative losses. The error bars resulted from at least three measurements taken for each fuel blend and height. Results from a different batch of Jet A1 with the same experimental setup and EQR are plotted with diamonds [25].

Raman spectroscopy was used to obtain the disordered (D) over graphitic (G) ratios (D/G) shown in Figure B.5. The error bars are the standard deviation between three experiments. The 10 and 40% blends used the average standard deviation of the other blends, as they were only measured once. The random variations of the D/G ratios observed in Figure B.5 indicate no clear trend for the blending ratio. This could have been due to the similar temperatures observed for the different blends. Temperature is an important factor for soot graphitisation, where low temperatures lead to amorphous soot and high temperatures lead to more graphitic soot [29]. Therefore, the similar temperature profiles (Figure B.4) result in a similar nanostructure of soot. The aromatic content of SAF compared to Jet A1 fuel should be one of

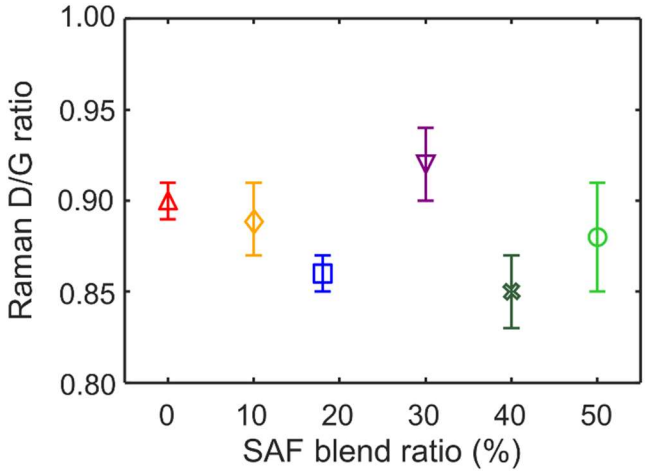

Figure B.5: The D/G ratio as a function of the SAF blend percentage. The standard deviation of the 10 and 40% blends had the average standard deviation resulting from the other measurements, since only one experiment was carried out.

the major differences of the blends. However, it was shown that the aromatic content also did not influence the nanostructure [30]. Therefore, there seemed to be no strong correlation between D/G ratio and the SAF blend ratio, while minor differences were observed. Additionally, further experiments should be done to better capture the variability between the experiments.

Further analysis into the nanostructure was done with XRD analysis for the samples at 0, 18 and 50% SAF blend ratio. The crystallite structure did not change for the 0 and 50% blend ratios. However, more graphitic values were observed in Figure B.6 for the 18% blend. Here a decrease in interlayer distance and an increase in crystallite length was reported. The interlayer distance seemed to be the better indicator for the increase in graphitisation seen for the 18% SAF blend, as the crystallite length was within the error margin of the other blends. These differences pointed to a more developed crystallite region for the 18% blend and therefore to a more graphitic nanostructure than for the other SAF blends. These results supported the observations made from Raman spectroscopy for these blends. The 0% SAF blend was also in agreement with the d_{002} (3.69 ± 0.01 Å) and the Lc (1.24 ± 0.02 nm) literature values for Jet A1 fuel at similar conditions [25].

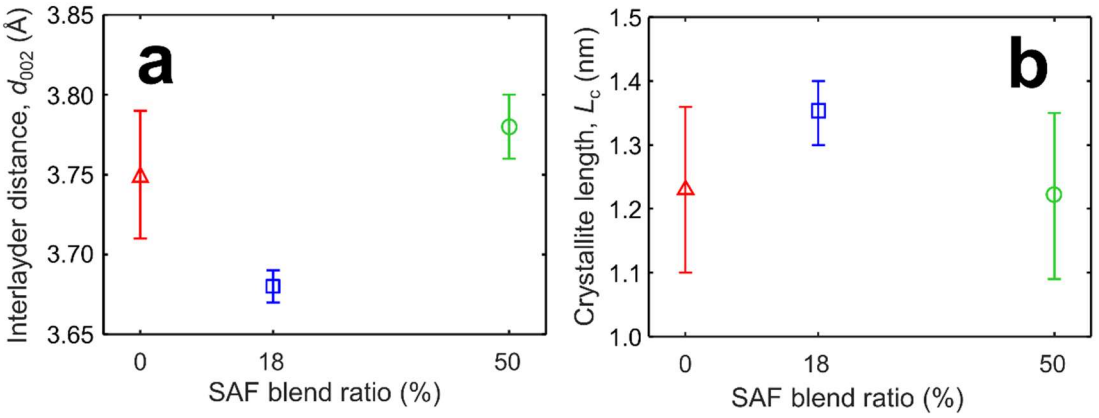

Figure B.6: The interlayer distance (d_{002}) and the crystallite length (L_c) for the 0, 18 and 50% SAF blends are shown. XRD analysis was conducted three times per fuel blend and its standard deviation was added as error bars.

The OC/TC ratio of the soot produced at multiple blending ratios was analysed with TGA, shown in Figure B.7. For the blending ratios 10, 30 and 40% the average standard deviation from the 0, 18 and 50% blends was applied, as these measurements were done once. The OC/TC ratios were lowest for the 0 and 18% blends with similar OC/TC ratios of 11 ± 1% and 10 ± 1% respectively, while the highest ratios were observed for blends of 10 and 30% were both reached 21 ± 2% OC/TC. All of the OC/TC ratios fell within approximately 10 and 20% OC content. The 0% blend OC/TC ratio is in great agreement with a previous experiment at the same conditions that also reached 11% OC/TC ratio for Jet A1 fuel [17].

Due to the random OC/TC ratio variations in Figure B.7, no significant effect of the blending of SAF on the OC/TC ratio was observed. These results agreed with the literature, where a 32% HEFA SAF blend with a turbofan engine, also noted no influence of the blending on the OC/TC ratio from thermal optical analysis (TOA) [15]. In past work, it was shown that TGA agrees well with TOA at the experimental conditions used here [17]. One difference between the study and the values in this work were the standard deviations, which were rather large (± 20%) for the study compared to the variation here (± 2%) [15]. The large spread for the OC/TC ratios from aircraft soot suggested that other factors apart from the fuel blend were important for determining the OC/TC ratio. Temperature could have affected soot maturity, where high temperatures create more mature soot. This mature soot has a lower amount of organic carbon than younger soot, which decreases its OC/TC ratio [31]. Thus, temperature effects from long sampling lines used in research on real aircraft engines may influence the final results [31]. As shown in Figure B.4, the temperature profiles were similar for all blending ratios which may explain the similar OC/TC ratio observed in this study.

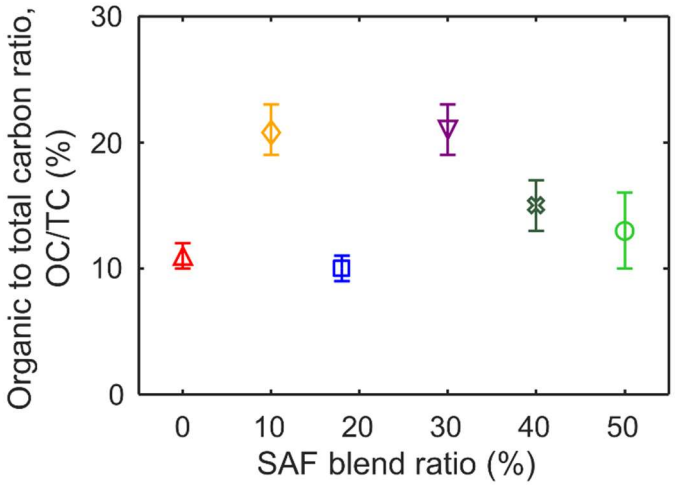

Figure B.7: The OC/TC ratios as a function of the HEFA SAF and Jet A1 blending ratio is shown. Error bars represent the standard deviation between three experiments. For the 10, 30 and 40% blends the average standard deviation was used for comparison, since they were measured once.

Figure B.8 shows the specific surface area (SSA) of soot produced with blends of 0, 18, and 50% SAF. At 0 and 18%, the results were within one standard deviation of each other while at 50% a slight increase in the SSA was observed from 239 ± 19 m^2/g and 215 ± 20 m^2/g at 0% and 18% up to 269 ± 1 m^2/g with the 50% blend. The SSA of conventional Jet A1 (0% SAF) was in agreement with the literature for soot from the same EQR with a different batch of Jet A1, where an SSA of 258 m^2/g was reported that was within one standard deviation of the observed result [17]. The $\bar{d}_p$ for all conditions was similar (Figure B.3), therefore a change in SSA would indicate a change in porosity. The SSA had previously not

been researched for any SAF blends. Thus, the reported values in Figure B.8 are the first of its kind. Due to the large variation between samples, more measurements should be performed in order to confirm a potential increase in SSA at high (≥ 50%) blending ratios.

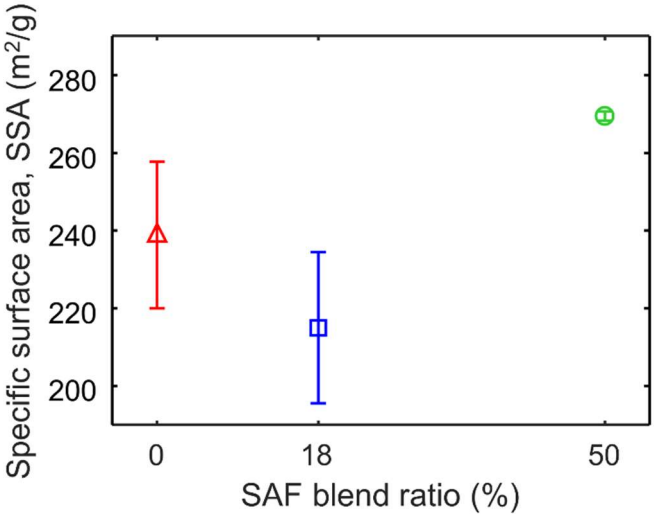

Figure B.8: The SSA for the SAF blends at 0, 18 and 50% are shown. The measured soot was combined from multiple experiments at the same conditions. At each fuel blend the SSA was analysed twice, which resulted in the displayed error bars.

B4. Conclusions

The soot produced from enclosed spray combustion at blending ratios from 0 to 50% HEFA SAF blended with Jet A1 fuel was characterized for its number concentration, mobility size distribution, primary particle diameter, flame temperature, nanostructure, OC/TC ratio and SSA. The blending did not appear to have a strong influence on the number concentrations, where only slight reductions (~30%) were observed with overlapping error bars. Similarly slight reductions were observed in the literature for aircrafts at high thrust with a 10 to 15% decrease in number concentration [5]. The experimental setup in this study had also been reported to produce soot similar to aircrafts at high thrust [17]. The dm of soot was reduced at the 50% blend with a dm = 116 ± 13 nm compared to the 147 ± 17 nm of the pure Jet A1, which was not the case at lower blend ratios (≤ 40%). This might be due to the lower aromatic content of SAF nucleating fewer primary particles for agglomeration. The temperature profiles were largely unaffected by the addition of SAF. Similarly, no effect on the average primary particle diameter was found. While there was some variability in the Raman D/G ratios and crystallite sizes of soot from different blending ratios, there was no apparent trend associated with the blending of SAF. Consistent with data from soot produced by aircraft engines operating with a 32% blend of HEFA based SAF and Jet A1 fuel, there was no trend observed in the OC/TC results due to the blending of SAF up to 50% [15]. For the first time the SSA of soot from a SAF blend was measured. The SSA ranged from 196 – 271 m^2/g at 18 and 50% blends

respectively. There was an increase in the SSA at 50%, however, further measurements are needed to confirm this result. Overall, blending Jet A1 fuel up to 50% with a HEFA-based SAF does not appear to have a strong influence on the resulting soot particles. This is consistent with research from soot produced by aircrafts at high thrust where only small changes to the particle size and number concentrations were observed.

B5. References

[1] ICAO, Guidance on potential policies and coordinated approaches for the deployment of sustainable aviation fuels. Version 2. March 2023.

[2] M.D. Staples, R. Malina, P. Suresh, J.I. Hileman, S.R.H. Barrett, Aviation CO2 emissions reductions from the use of alternative jet fuels, *Energy Policy* (2018) **114**, 342–354.

[3] T.C. Bond, S.J. Doherty, D.W. Fahey, P.M. Forster, T. Berntsen, B.J. Deangelo, M.G. Flanner, S. Ghan, B. Kärcher, D. Koch, S. Kinne, Y. Kondo, P.K. Quinn, M.C. Sarofim, M.G. Schultz, M. Schulz, C. Venkataraman, H. Zhang, S. Zhang, N. Bellouin, S.K. Guttikunda, P.K. Hopke, M.Z. Jacobson, J.W. Kaiser, Z. Klimont, U. Lohmann, J.P. Schwarz, D. Shindell, T. Storelvmo, S.G. Warren, C.S. Zender, Bounding the role of black carbon in the climate system: A scientific assessment, *J Geophys Res Atmos* (2013) **118**, 5380–5552.

[4] R. Niranjan, A.K. Thakur, The toxicological mechanisms of environmental soot (black carbon) and carbon black: Focus on Oxidative stress and inflammatory pathways, *Front Immunol* (2017) **8**, 1664–3224.

[5] L. Durdina, B.T. Brem, M. Elser, D. Schönenberger, F. Siegerist, J.G. Anet, Reduction of nonvolatile particulate matter emissions of a commercial turbofan engine at the ground level from the use of a sustainable aviation fuel blend, *Environ Sci Technol* (2021) **55**, 14576–14585.

[6] S. Sharma, P. Singh, B.A. Almohammadi, B. Khandelwal, S. Kumar, Testing of formulated fuel with variable aromatic type and contents in a compression-ignition engine, *Fuel Process Technol* (2020) **208**, 106413.

[7] B.T. Brem, L. Durdina, F. Siegerist, P. Beyerle, K. Bruderer, T. Rindlisbacher, S. Rocci-Denis, M.G. Andac, J. Zelina, O. Penanhoat, J. Wang, Effects of Fuel Aromatic Content on Nonvolatile Particulate Emissions of an In-Production Aircraft Gas Turbine, *Environ Sci Technol* (2015) **49**, 13149–13157.

[8] R.H. Moore, K.L. Thornhill, B. Weinzierl, D. Sauer, E.D. Ascoli, B. Beaton, A.J. Beyersdorf, D. Bulzan, C. Corr, E. Crosbie, R. Martin, D. Riddick, M. Shook, G. Slover, C. Voigt, R. White, E. Winstead, R. Yasky, L.D. Ziemba, A. Brown, H. Schlager, B.E. Anderson, Biofuel blending reduces aircraft engine particle emissions at cruise conditions, *Nature* (2017) **543**, 411–415.

[9] P. Lobo, D.E. Hagen, P.D. Whitefield, Comparison of PM emissions from a commercial jet engine burning conventional, biomass, and fischer-tropsch fuels, *Environ Sci Technol* (2011) **45**, 10744–10749.

[10] T. Schripp, B.E. Anderson, U. Bauder, B. Rauch, J.C. Corbin, G.J. Smallwood, P. Lobo, E.C. Crosbie, M.A. Shook, R.C. Miake-Lye, Z. Yu, A. Freedman, P.D. Whitefield, C.E. Robinson, S.L. Achterberg, M. Köhler, P. Oßwald, T. Grein, D. Sauer, C. Voigt, H.

Schlager, P. LeClercq, Aircraft engine particulate matter emissions from sustainable aviation fuels: Results from ground-based measurements during the NASA/DLR campaign ECLIF2/ND-MAX, *Fuel* (2022) **325**, 124764.

[11] L. Chen, X. Hu, J. Wang, Y. Yu, Impacts of Alternative Fuels on Morphological and Nanostructural Characteristics of Soot Emissions from an Aviation Piston Engine, *Environ Sci Technol* (2019) **53**, 4667–4674.

[12] C.H. Huang, R.L. Vander Wal, Effect of soot structure evolution from commercial jet engine burning petroleum based JP-8 and synthetic HRJ and FT fuels, *Energy and Fuels* (2013) **27**, 4946–4958.

[13] R.L. Vander Wal, A.J. Tomasek, M.I. Pamphlet, C.D. Taylor, W.K. Thompson, Analysis of HRTEM images for carbon nanostructure quantification, *J Nanoparticle* Res (2004) **6**, 555–568.

[14] G.A. Kelesidis, C.A. Bruun, S.E. Pratsinis, The impact of organic carbon on soot light absorption, *Carbon* (2021) **172**, 742–749.

[15] M. Elser, B.T. Brem, L. Durdina, D. Schönenberger, F. Siegerist, A. Fischer, J. Wang, Chemical composition and radiative properties of nascent particulate matter emitted by an aircraft turbofan burning conventional and alternative fuels, *Atmos Chem Phys* (2019) **19**, 6809–6820.

[16] O. Schmid, T. Stoeger, Surface area is the biologically most effective dose metric for acute nanoparticle toxicity in the lung, *J Aerosol Sci* (2016) **99**, 133–143.

[17] U. Trivanovic, G.A. Kelesidis, S.E. Pratsinis, High-throughput generation of aircraft-like soot, *Aerosol Sci Tech* (2022) **56**, 732–743.

[18] P. Dagaut, M. Cathonnet, The ignition, oxidation, and combustion of kerosene: A review of experimental and kinetic modeling, *Prog Energy Combust Sci* (2006) **32**, 48–92.

[19] A. Teleki, B. Buesser, M.C. Heine, F. Krumeich, M.K. Akhtar, S.E. Pratsinis, Role of gas - Aerosol mixing during in situ coating of flame-made titania particles, *Ind Eng Chem Res* (2009) **48**, 85–92.

[20] E. Goudeli, A.J. Gröhn, S.E. Pratsinis, Sampling and dilution of nanoparticles at high temperature, *Aerosol Sci Tech* (2016) **50**, 591–604.

[21] C.R. Shaddix, A New Method To Compute the Radiant Correction of Bare-Wire Thermocouples, in: 33rd ASME National Heat Transfer ConferenceTenth Mediterranean Combustion Symposium (MCS-10), Naples, Italy, 2017.

[23] A. Sadezky, H. Muckenhuber, H. Grothe, R. Niessner, U. Pöschl, Raman microspectroscopy of soot and related carbonaceous materials: Spectral analysis and structural information, *Carbon* (2005) **43**, 1731–1742.

[24] N. Iwashita, C.R. Park, H. Fujimoto, M. Shiraishi, M. Inagaki, Specification for a standard procedure of X-ray diffraction measurements on carbon materials, *Carbon* (2004) **42**, 701–714.

[25] U. Trivanovic, M. Pereira Martins, S. Benz, G.A. Kelesidis, S.E. Pratsinis, Dynamics of soot surface growth and agglomeration by enclosed spray combustion of jet fuel, *Fuel* (2023) **342**, 127864.

[26] S. Brunauer, P.H. Emmett, E. Teller, Adsorption of Gases in Multimolecular Layers, *J Am Chem Soc* (1938) **60**, 309–319.

[27] C.D. Klingshirn, Z.J. West, M.J. DeWitt, A. Higgins, J. Graham, E. Corporan,

Quantification of elemental and total carbon in combustion particulate matter using thermal-oxidative analysis, *J Air Waste Manage Assoc* (2019) **69**, 1003–1013.

[28] G.A. Kelesidis, E. Goudeli, S.E. Pratsinis, Flame synthesis of functional nanostructured materials and devices: Surface growth and aggregation, *Proc Combust **Inst*** (2017) **36**, 29–50.

[29] R.L. Vander Wal, A.J. Tomasek, Soot nanostructure: Dependence upon synthesis conditions, *Combust Flame* (2004) **136**, 129–140.

[30] Aizawa T, Takahata N, Okabe K, Mizutani Y, Effect of Fuel Aromatics on In-Flame Diesel Soot Nanostructure via HRTEM, *SAE Technical Paper* (2015) 01–1829.

[31] G.A. Kelesidis, C.A. Bruun, S.E. Pratsinis, The impact of organic carbon on soot light absorption, *Carbon* (2021) **172**, 742–749.

Appendix C

Supplementary Information for Chapter 2: High-throughput generation of aircraft-like soot

C1. Equivalence ratio calculation and range

The equivalence ratio of the flames at standard temperature and pressure (STP) was calculated accounting for the fuel flow rate (4.5 mL/min, 0.00038 mol/s), dispersion O_2 flow rate (1.5 – 3.0 L/min, 0.00112 – 0.00223 mol/s), sheath air flow rate (20 L/min, 0.01488 mol/s), and premixed flame flow rate (CH_4/O_2: 1.25/2.25 L/min, 0.00093/0.00167 mol/s). Jet A1 fuel is a complex mixture with no one chemical formula however, for this calculation jet A1 was assumed to be composed of 11.6 carbon atoms and 22 hydrogen atoms on average [1]. From this chemical formula the molar mass was calculated to be 161 g/mol. The density of jet A1 at STP is 811 kg/m^3 [2]. A stoichiometric methane flame has the chemical equation:

$$CH_4 + 2O_2 \rightarrow CO_2 + 2H_2O$$

Thus, in each case twice the molar flow of CH_4, $\dot{m}_{CH4}$, of O_2 is needed to fully combust the CH_4. This amount is subtracted from the O_2 available for combustion with jet fuel giving the 'net' molar flow of O_2. The O_2 required to combust the jet fuel under stoichiometric conditions was calculated given the stoichiometric ratio for hydrocarbon combustion:

$$C_{11.6}H_{22} + 17.1O_2 \rightarrow 11.6CO_2 + 11H_2O \quad \text{(C.1)}$$

Thus, an O_2/jet fuel ratio of 17.1 is needed to achieve stoichiometric conditions. From this the equivalence ratio at each dispersion O_2 flow rate is calculated as:

$$EQR = \frac{17.1}{\left(\frac{Net\ molar\ flow\ of\ O_2}{Molar\ flow\ of\ jet\ fuel}\right)} \quad \text{(C.2)}$$

For example, EQR = 1.34 was calculated as follows: 2.5 L/min of dispersion O_2 is used for this EQR. Using the ideal gas law, where the density of a gas at STP is 22.4 L/mol, the molar flow of dispersion O_2 is:

$$\frac{2.5\ L/min}{60\ s/\ \text{min}\ \cdot\ 22.4\ L/mol} = 0.00186\ mol/s \qquad \text{(C.3)}$$

The same calculation is used to determine the molar flow of CH_4, premixed O_2 and sheath air of which 21% is assumed to be O_2 and 79% N_2. The molar flow of jet fuel is calculated as:

$$\frac{4.5\ mL/min}{60\ s/min} \cdot \frac{811\ kg/m^3}{161\ g/mol} = 0.00038\ mol/s \qquad \text{(C.4)}$$

Subtracting the O_2 required for CH_4 combustion from the premixed O_2, dispersion O_2 and sheath O_2:

$$\left(\dot{m}_{premixed,O2} + \dot{m}_{disp,O2} + \dot{m}_{sheath,O2}\right) - 2\dot{m}_{CH4} = 0.0048\ mol/s \qquad \text{(C.5)}$$

Thus, the EQR is:

$$EQR = \frac{17.1}{\left(\frac{0.0048\ mol/s}{0.00038\ mol/s}\right)} = 1.34$$

The EQR ranging from 1.25 to 1.59 are investigated extensively. However, a larger range is possible with the spray combustion unit set up (Figure C1a). The upper limit, EQR = 1.90 (solid line) is due to the lowest dispersion O_2 flow rate that the mass flow controller could supply, 0.62 L/min.

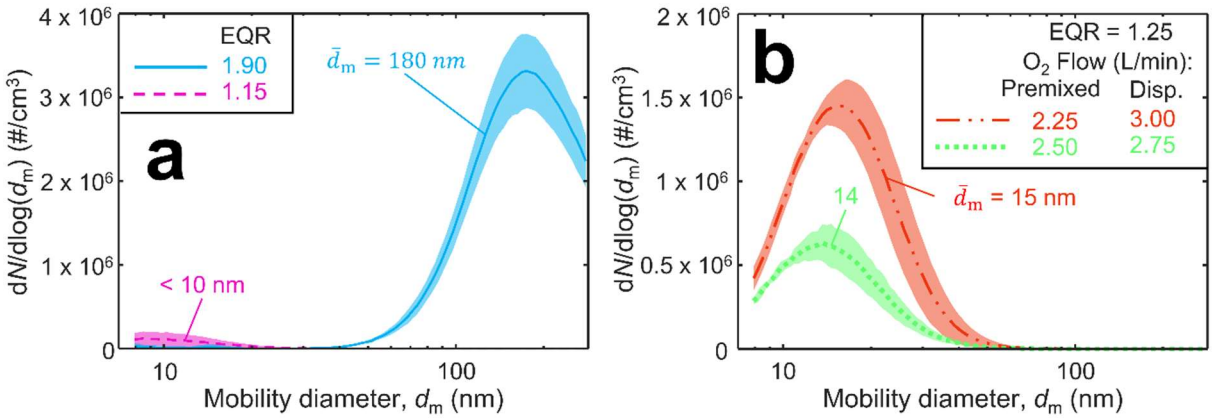

Figure C1: Mobility soot size distributions a) at the maximum, 1.90 (solid line), and minimum, 1.15 (broken line) EQR which could practically be achieved and b) with the same EQR, 1.25, achieved using either the standard premixed O_2 (2.25 L/min) and dispersion O_2 flow of 3 L/min (double-dot dashed line), or 2.50 L/min of premixed O_2 and 2.75 L/min of dispersion O_2 (dotted line).

In principle, a different mass flow controller or higher fuel flow rate could be used to achieve a higher EQR which should further increase the $\bar{d}_m$. On the other hand, the lower limit, EQR = 1.15 (broken line), 3.60 L/min dispersion O_2, was determined by the very low concertation of soot, < 1000 #/cm^3. This value is after the same dilution described in the main text so it is possible that with less dilution this EQR could also be useful. However, without proper dilution the sampling system needs to be reconfigured to avoid overheating. Using different O_2 flowrates in the premixed flame does not significantly affect the mobility size

distribution when comparing the same EQR, Figure C1b. For example, increasing the O_2 flowrate in the supporting flame from 2.25 to 2.5 L/min and equally decreasing the dispersion O_2 flowrate (from 3 to 2.75 L/min) results in soot with similar a mobility size distribution but lower concentration than that made at the same overall EQR of 1.25 (Figure C1b). The range studied extensively from EQR = 1.25 to 1.59, covers the range of aircraft-relevant sizes at which sufficient mass could be collected for N_2 absorption and TGA.

C2. Thermal gravimetric analysis (TGA)

Figure C2 shows the normalized evolution of spray combustion soot at EQR = 1.59 (solid lines), 1.46 (broken lines), 1.34 (dot-broken lines), 1.29 (dotted lines) and 1.25 (double dot-broken lines) with mass loss under a) N_2 and b) air as a function of time. The mass lost under N_2, $\bar{m}_{os}$ (up to 900 °C), is attributed to organic carbon (OC). Mass lost under air, $\bar{m}_s$ (up to 900 °C), that occurs after N_2 is attributed to elemental carbon (EC). The temperature profile applied (thin solid lines) is shown on the right axis. In each case the temperature begins at 30 °C, then increases at a rate of 20 °C/min up to 900 °C where it remains for 10 minutes before returning to 30 °C at 20 °C/min.

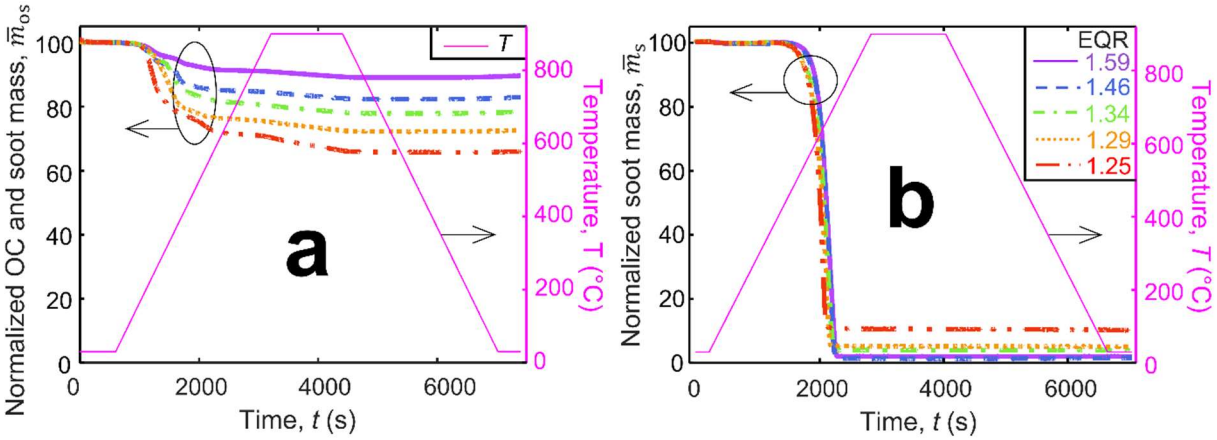

Figure C2: Mass loss profiles a) in N_2 and b) in air of soot made at EQR = 1.59 (solid line), 1.46 (broken line), 1.34 (dot-broken line), 1.29 (dotted line) and 1.25 (double dot-broken line). The mass lost under N_2, $\bar{m}_{os}$, is attributed to OC. Mass lost under air, $\bar{m}_s$, that occurs after N_2 is attributed to EC. The resulting OC/TC are shown in Fig. 2.5. The evolution of temperature, *T*, as a function of time, *t* (thin solid line), is shown on the right-hand axis.

C3. Primary particle sizing

To ensure a sufficient number of primary particles (PPs) were counted to obtain a reliable value of $\bar{d}_p$, the geometric mean was plotted as a function of number of particles counted, Figure C3. Always, an asymptote was reached by about 200 counted, in agreement with the literature [3].

The PPs of soot are polydisperse thus d_p can be represented more accurately as a particle size distribution as is shown in Figure C4 with d_p ranging from 5 to 30 nm. The exemplary TEM

images illustrate significant necking between PPs indicative of surface growth. The images also illustrate the polydispersity of the PP sizes. Liati et al. [4; Fig. 3] provided histograms of the soot primary particle (PP) size distribution along with the respective mode d_p = 20 and 24 nm measured from aircraft engines at 65 and 100 % thrust, respectively. Similarly, Marhaba et al. [5; Fig. 2] provide primary particle size distributions at 70, 85 and 100 % thrust with mode d_p = 13, 13.8 and 13.7, respectively.

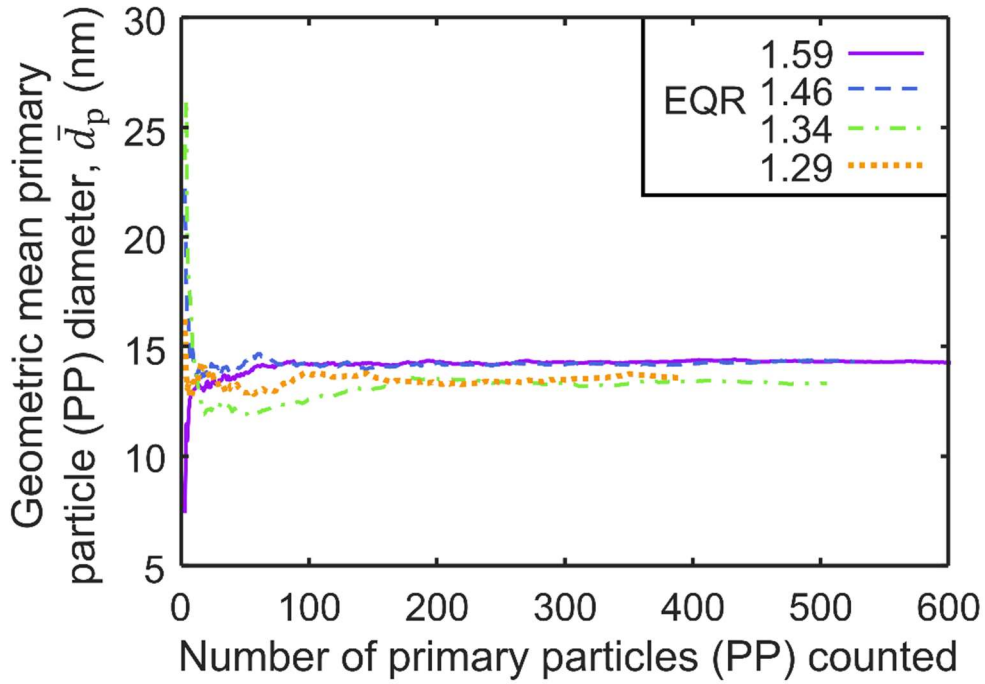

Figure C3: The evolution of $\bar{d}_p$ as a function of the number of PPs counted for EQR = 1.59 (solid line), 1.46 (broken line), 1.34 (dot-broken line) and 1.29 (dotted line).

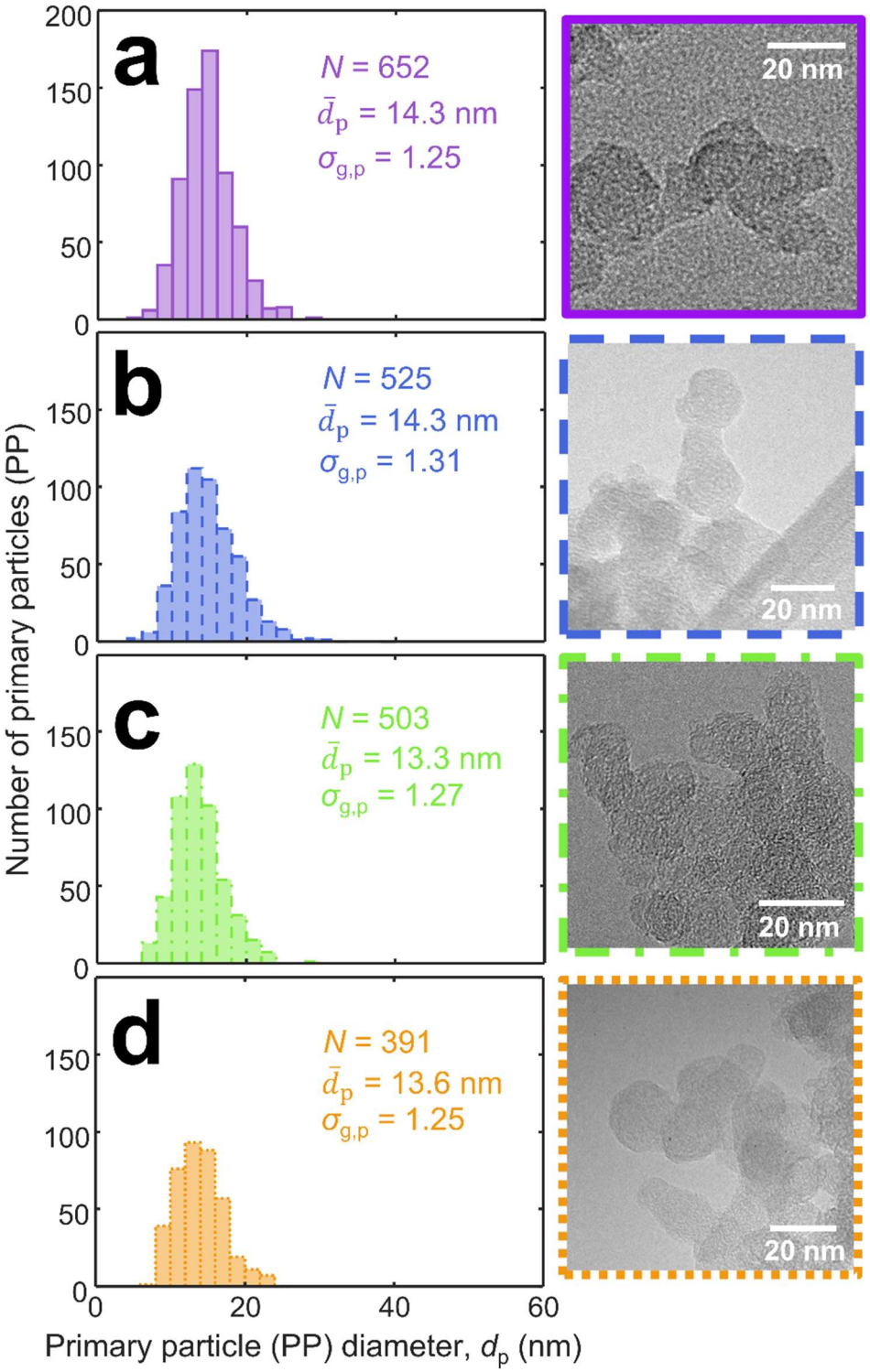

Figure C4: Histograms of the PP diameters measured by TEM with exemplary TEM images from a) EQR = 1.59, b) 1.46, c) 1.34, and d) 1.29.

To facilitate the comparison of PP size distributions of aircraft soot obtained from various studies [4–6] the $\bar{d}_p$ was obtained by fitting a lognormal distribution to the published raw data. Figure C5a shows the raw microscopy data from Liati et al. (symbols) [4] at 100 (circles) and 65% thrust (triangles), along with their lognormal fittings used here that result in $\bar{d}_p$ = 18 (broken line) and 17.4 nm (solid line), respectively.

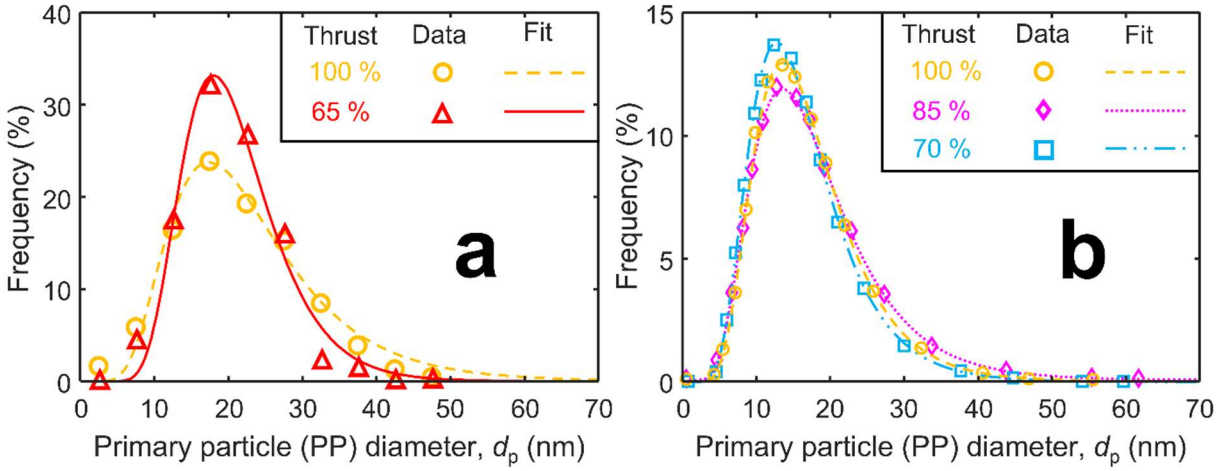

Figure C5: Raw microscopy data (symbols) and lognormal fits (lines) of the primary particle size distribution measured by [4] from aircraft engines at a) 100 (circles, broken line) and 65 % (triangles, solid line), as well as by [5] at b) at 100 (circles, dot-broken line), 85 (diamonds, dotted line) and 70 % (squares, double dot-broken line).

Similarly, Figure C5b shows the raw microscopy data (symbols) from [5] at 100 (circles), 85 (diamonds) and 70 % (squares) thrust along with their lognormal fittings that result in $\bar{d}_p$ = 13.6 (broken line), 13.7 (dotted line) and 12.7 nm (double dot-broken line), respectively.

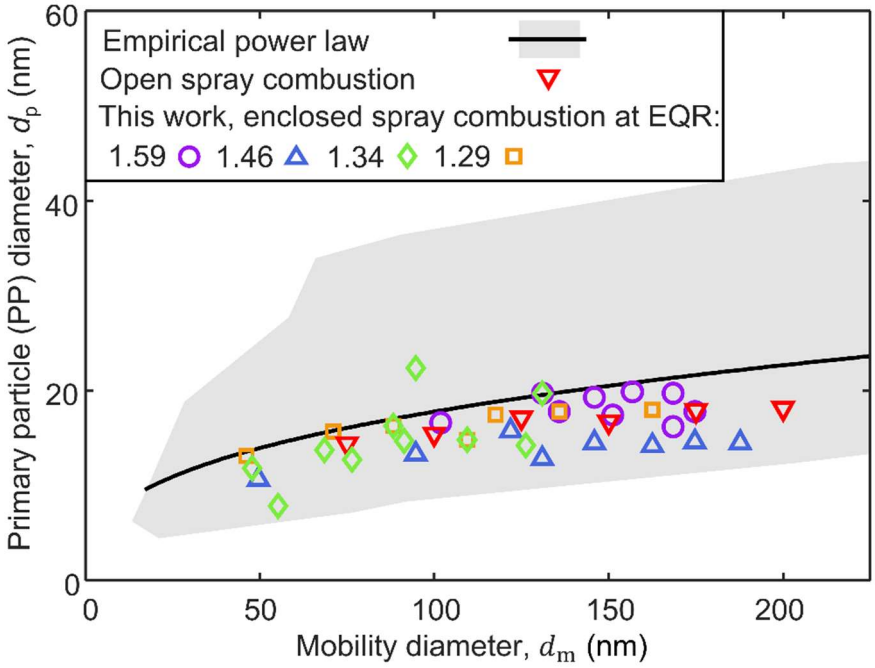

Figure C6: The soot d_p as a function of d_m obtained here by interfacing mass-mobility data from enclosed spray combustion at EQR = 1.59 (circles), 1.46 (triangles), 1.34 (diamonds) and 1.29 (squares) with a power law [3] in comparison to that measured for soot from open spray combustion (inverse triangles) [7] as well as to an empirical power law obtained from engine data (solid line & shaded area) [8].

C4. Mass concentration correction

The mass concentration, *M*, of soot estimated from an aethalometer depends on the assumed mass absorption cross-section (*MAC*) which depends on particle chemical composition and size [9]. The *MAC* originally used by Ess and Vasilatou [10], 7.77 m^2/g at 880 nm, does not

account for the OC/TC and causes a systematic underestimation of the *M* for soot with low OC/TC, i.e. aircraft-like soot. Figure C7 shows the *M* from the enclosed unit studied here (circles) and an open one (squares) [7], along with the corrected miniCAST *M* (open triangles) and the ones directly from Ess and Vasilatou (filled triangles) [10].

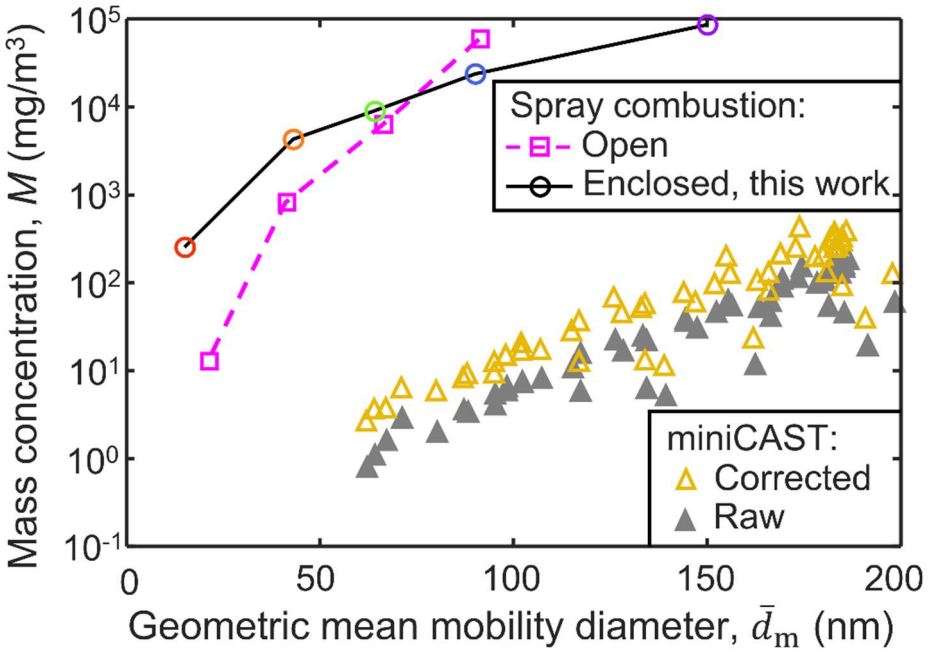

Figure C7: The mass concentration of soot produced by an enclosed (circles) and open (squares) [7] spray combustion unit, as well as a 5201 miniCAST with corrected (open triangles) and raw (filled triangles) [10] mass concentrations using the manufacturer's default *MAC* = 7.77 m²/g at 880 nm as a function of $\bar{d}_m$.

C5. Molar flow rate of spray combustion unit and miniCAST

The molar flow rate, $\dot{m}$, can be calculated as:

$$\dot{m} = \dot{v} \cdot \frac{\rho}{MW} \tag{C.6}$$

where $\dot{v}$ is the volumetric flow rate, ρ is the density and *MW* is the molecular weight. These values for spray combustion and miniCAST soot are listed in Table C1 assuming a chemical equation of $C_{11.6}H_{22}$ for jet A1 [1]. Based on these, the molar flows are $\dot{m}_{jetfuel}$ = 0.02 mol/min and $\dot{m}_{propane}$ = 0.003 mol/min.

Table C1: Properties of fuel used for the enclosed spray combustion unit (this work) and a miniCAST [10] which use jet A1 and propane, respectively.

	$\dot{v}$ (mL/min)	ρ (kg/m³)	MW (g/mol)
Enclosed unit, jet A1	4.5	804	161.4
miniCAST, propane	60 – 70	1.882	44.09

C6. Nitrogen adsorption isotherms

Specific surface area (SSA) and pore size distributions are estimated from N_2 adsorption isotherms, shown in Figure C8, by the Micromeritics Tristar II Plus software.

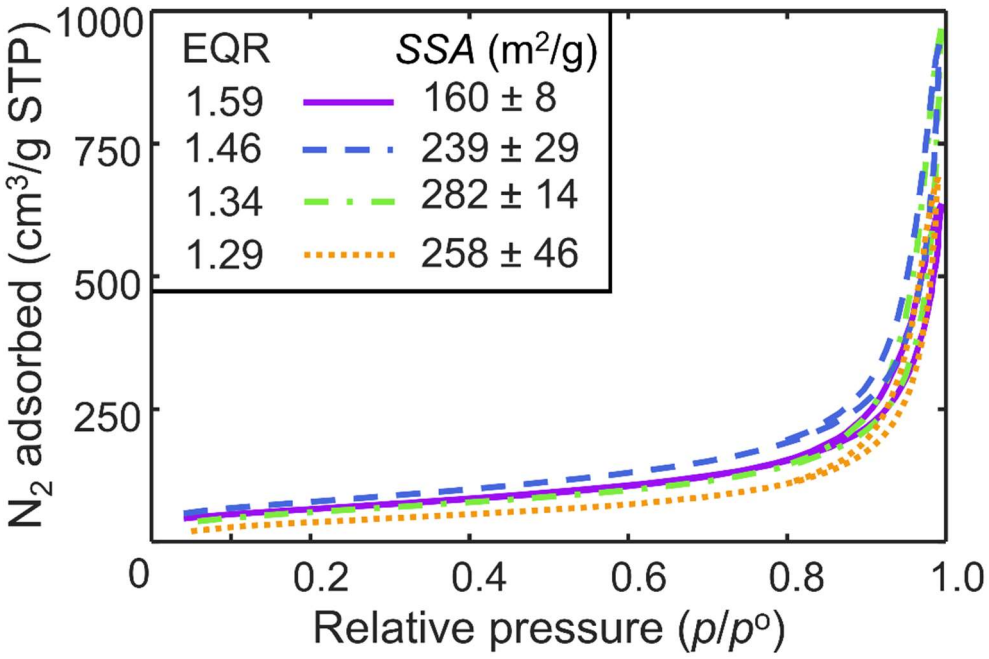

Figure C8: The N_2 adsorption isotherms for soot at EQR = 1.59 (solid line), 1.46 (broken line), 1.34 (dot-broken line) and 1.29 (dotted line).

C7. References

[1] Dagaut P, Cathonnet M. The ignition, oxidation, and combustion of kerosene: A review of experimental and kinetic modeling. *Prog Energy Combust Sci* (2006) **32**, 48–92.

[2] Measurement Canada. Volume correction factors to 15 °C for use with all grades of Jet A, Jet-A1, jet kerosene, turbine fuel. (2016).

[3] Kelesidis GA, Kholghy MR, Zuercher J, Robertz J, Allemann M, Duric A, Pratsinis SE. Light scattering from nanoparticle agglomerates. *Powder Technol* (2020) **365**, 52–9.

[4] Liati A, Brem BT, Durdina L, Vögtli M, Dasilva YAR, Eggenschwiler PD, Wang J. Electron microscopic study of soot particulate matter emissions from aircraft turbine engines. *Environ Sci Technol* (2014) **48**, 10975–83.

[5] Marhaba I, Ferry D, Laffon C, Regier TZ, Ouf F, Parent P. Aircraft and MiniCAST soot at the nanoscale. *Combust Flame* (2019) **204**, 278–89.

[6] Boies AM, Stettler MEJ, Swanson JJ, Johnson TJ, Olfert JS, Johnson M, Eggersdorfer ML, Rindlisbacher T, Wang J, Thomson K, Smallwood G, Sevcenco Y, Walters D, Williams PI, Corbin J, Mensah AA, Symonds J, Dastanpour R, Rogak SN. Particle emission characteristics of a gas turbine with a double annular combustor. *Aerosol Sci Technol* (2015) **49**, 842–55.

[7] Kholghy MR, DeRosa VG. Morphology, composition and optical properties of jet engine-like soot made by a spray flame. *Combust Flame* (2021) **231**, 111480.

[8] Olfert J, Rogak S. Universal relations between soot effective density and primary particle size for common combustion sources. *Aerosol Sci Technol* (2019) **53**, 485–92.

[9] Kelesidis GA, Bruun CA, Pratsinis SE. The impact of organic carbon on soot light absorption. *Carbon* (2021) **172**, 742–9.

[10] Ess MN, Vasilatou K. Characterization of a new miniCAST with diffusion flame and premixed flame options: Generation of particles with high EC content in the size range 30 nm to 200 nm. *Aerosol Sci Technol* (2019) **53**, 29–44.

Appendix D

Supplementary Information for Chapter 3: Dynamics of soot surface growth and agglomeration by enclosed spray combustion of jet fuel

The experimental set-up used here, Figure D1, was almost identical to that used previously [1]. Now, the bottom quartz glass tube was exchanged with a steel tube containing five evenly spaced, sealable holes to allow for soot sampling and temperature measurements with a straight sampling tube [2] and an R-type thermocouple, respectively.

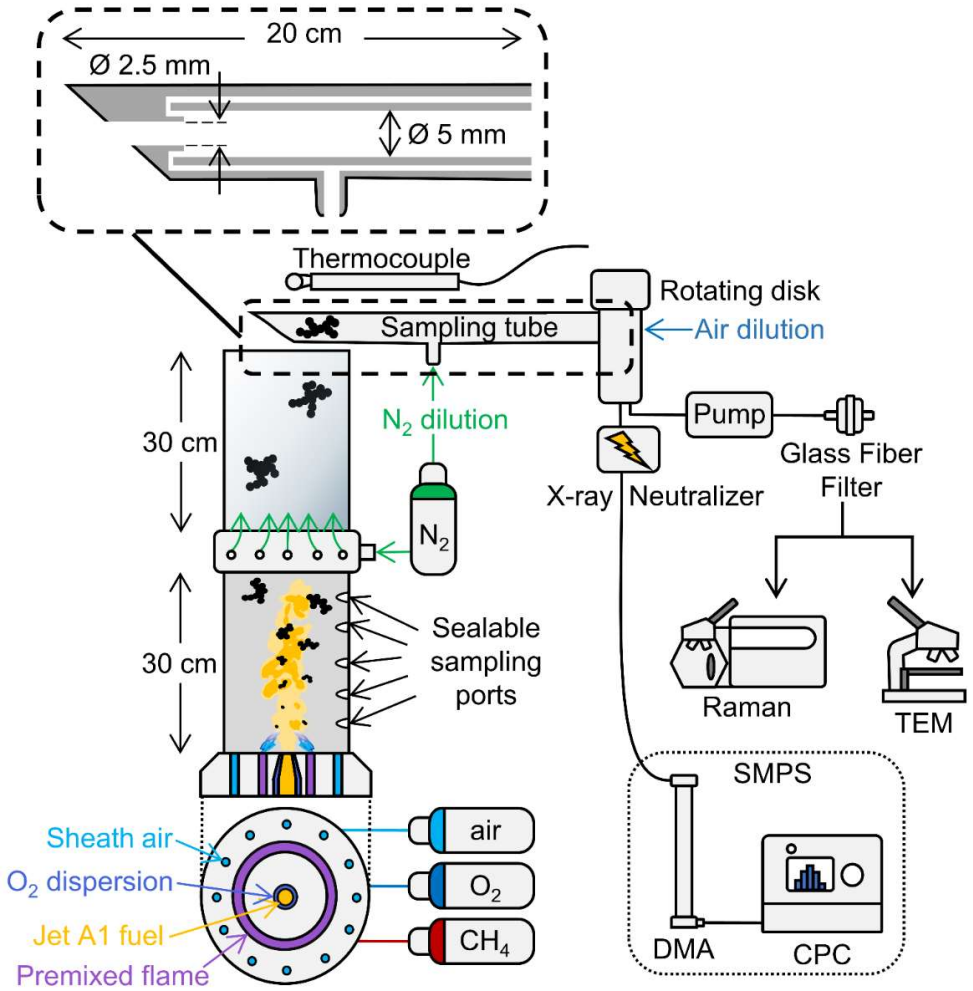

Figure D1: Schematic of the experimental set up used by [1] and modified here to allow for soot sampling and *T* measurements at HAB = 5, 10, 15, 20, 25 and 63 cm.

The diameter of the spray droplets, d_d, was measured using Fraunhofer laser diffraction spectrometry (SympaTec Heleos) in the absence of combustion, 6 cm above the nozzle (Figure D2) as a function of EQR at 1.88 (diamonds), 1.73 (squares), 1.59 (circles) and 1.46 (triangles). For safety reasons, ethanol was used instead of jet A1 for the majority of the spray measurements. However, ethanol droplets (open symbols) give nearly identical droplet size distributions to jet A1 fuel (filled circles). Here, the fuel flow rate is kept constant while the O_2 dispersion is increased to produce a lower EQR. The range of conditions studied here produce large variations in the median droplet diameter, $\bar{d}_d$, from 330 ± 2 µm at EQR = 1.88 down to 36 ± 0.5 µm at EQR = 1.46. The droplet diameter changes only slightly at low EQR (50 ± 1 µm at EQR = 1.59) then increases exponentially from EQR = 1.73 and higher. The correlation between the dispersion gas flow rate and the $\bar{d}_d$ has been shown for similar spray reactors with ethanol [3] and water [4].

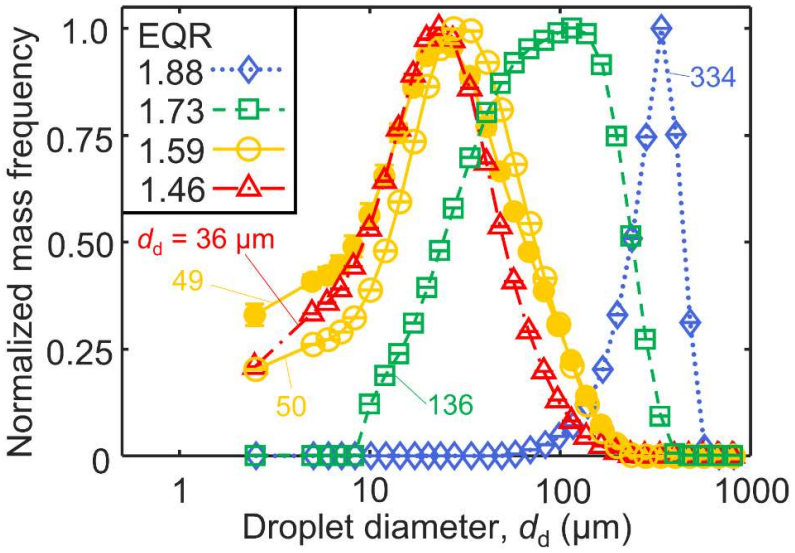

Figure D2: The droplet size distributions of ethanol sprays at EQR = 1.88 (diamonds), 1.73 (squares), 1.59 (open circles), 1.46 (triangles) and a jet fuel spray at EQR = 1.59 (filled circles).

When the flame is ignited, droplets likely do not reach the room temperature sizes. The temperatures in the flame reach up to 1600 K (Fig. 3.1), well above the autoignition temperature, 483 K, of jet A1. Droplets of a jet A1 surrogate with d_d = 15 µm undergoing combustion evaporated within less than 1 ms, much shorter than the 12 ms residence time at HAB = 5 cm shown in Figure D8. Below the autoignition temperature, the evaporation rate of a droplet can be estimated with the procedure from Hinds [5]. Briefly, modeling jet A1 as n-decane [6] which has a molecular weight, MW_{C10H22} = 142 g/mol and chemical formula $C_{10}H_{22}$, the atomic diffusion volume, v_{C10H22}, can be estimated as 209 [7]. The vapor pressure, P_{vap} of n-decane at T = 448 K can be estimated from the Antoine equation with coefficients valid from 368 K to 448 K [7]:

$$log_{10}(P_{vap}) = 4.07857 - \frac{1501.268}{T - 78.67} \quad \text{(D.1)}$$

Then, the diffusion coefficient, D, can be calculated as [7]:

$$D = \frac{10^{-3} \cdot T^{1.75} \left(\frac{1}{MW_{C_{10}H_{22}}} + \frac{1}{MW_{air}}\right)^{1/2}}{P\left[\left(v_{C_{10}H_{22}}\right)^{1/3} + (v_{air})^{1/3}\right]^2} \quad \text{(D.2)}$$

where P is the pressure in atm, and the MW_{air} and v_{air} are 29 g/mol and 20.1 [7], respectively. Finally, the droplet lifetime can be calculated as [5]:

$$t = \frac{\rho d_d^2}{8DMW_{C_{10}H_{22}}\left(\frac{P_{vap}}{T}\right)} \quad \text{(D.3)}$$

where ρ is the density which at 448 K is 606 kg/m^3 [8]. This results in a droplet lifetime of 17 ms assuming the median d_d = 36 µm at EQR = 1.46. While this is slightly longer than the time needed to reach HAB = 5 cm, at the true flame temperatures the droplet lifetime will be much shorter.

Figure D3 shows the mobility size distributions of soot at HAB = 63cm with (squares) and without (circles) a thermocouple inserted at HAB = 10 cm. While the mobility and primary particle size distributions in the main text were measured in the absence of a thermocouple, this indicates that the thermocouple does not affect the fuel evaporation and subsequent soot aerosol dynamics.

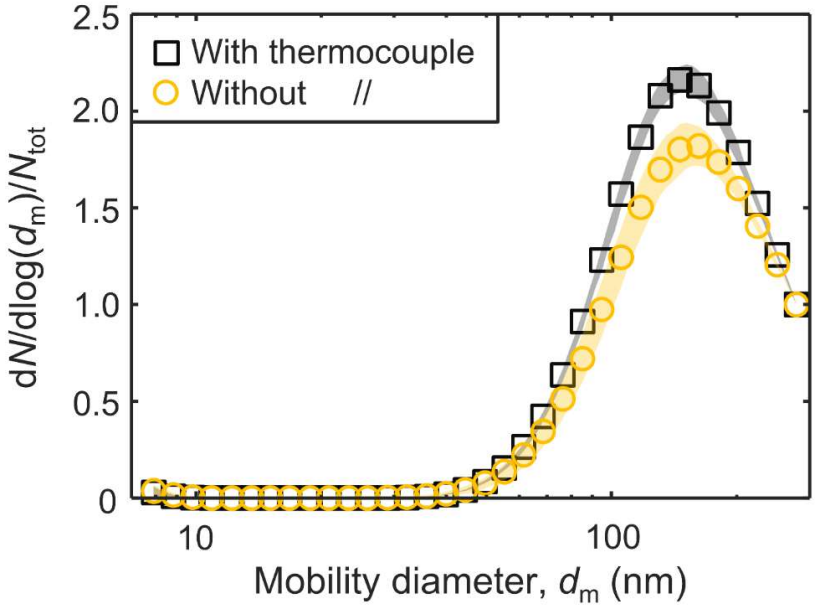

Figure D3: Mobility size distributions of soot produced at EQR = 1.59 and sampled at HAB = 63 cm with (squares) and without (circles) inserting a thermocouple at HAB = 10 cm. The shade shows the

reproducibility of the measurements [1].

Figure D4 shows the temperature profile from a premixed ethylene flame with EQR = 2.5 [9] (broken line). The flame was reproduced using a McKenna burner [10] and the gas compositions and flow rates given in [11]. The temperature profile measured here using a thermocouple (symbols) is in excellent agreement with that obtained in literature [11] (broken line). The flame T was obtained from the measured thermocouple temperature, T_t, corrected for radiative losses based on the following energy balance [9]:

$$h(T - T_t) = \varepsilon_t(T_t^4 - T_w^4) \tag{D.4}$$

where h is the convective heat transfer coefficient, ε_t is the emissivity of the thermocouple and T_w is the temperature of the tube walls. The same ε_t is used for T measurements in both premixed and spray flames as the same thermocouple was used in all conditions. The flame heat transfer coefficient, h, is given by [12]:

$$h = \frac{Nu \cdot k}{d_h} \tag{D.5}$$

where Nu is the Nusselt number, k is the thermal conductivity of the gas mixture and d_h = 42 mm is the diameter of the enclosure [1]. The k of the gas mixture is derived iteratively using MATLAB based on an initial $T = T_{bead}$ + 50 K, the k at that temperature [8] and assuming a mixture of CO_2, H_2O and N_2 calculated based on the chemical mass balance after combustion of ethylene and jet A1 fuels in the premixed and spray flame, respectively. Details of this calculation are described in Appendix C for the spray flame. A Nu = 2 is used for the premixed flame, as is commonly done [9]. For the turbulent spray flame, Nu is obtained from [13]:

$$Nu = 0.431Re^{0.5} \tag{D.6}$$

where the spray flame Re is [12]:

$$Re = \frac{\rho v d_h}{\mu} \tag{D.7}$$

with ρ, v and μ as the fluid density, velocity and dynamic viscosity, respectively. The ρ and μ are derived iteratively similarly to k based on the assumed mixture of CO_2, H_2O and N_2. The velocity at the exit of the spray flame nozzle, v_i, is approximately equal to the speed of sound, 343 m/s, as the pressure drop across the nozzle is maintained slightly above the critical pressure ratio for a sonic flow [3]. As HAB increases, v is estimated by [14]:

$$v = v_i\sqrt{\frac{1}{HAB}} \tag{D.8}$$

Using Eqs. D.2 – 4, *Nu* = 60 – 67 is obtained at HAB = 5 – 63 cm and EQR = 1.46 – 1.88 of the spray flame. Equation (D4) has been used for *T* measurements in premixed [11] and spray [3] flames. This validates the present temperature measurements, as well as the radiative loss correction used here [11].

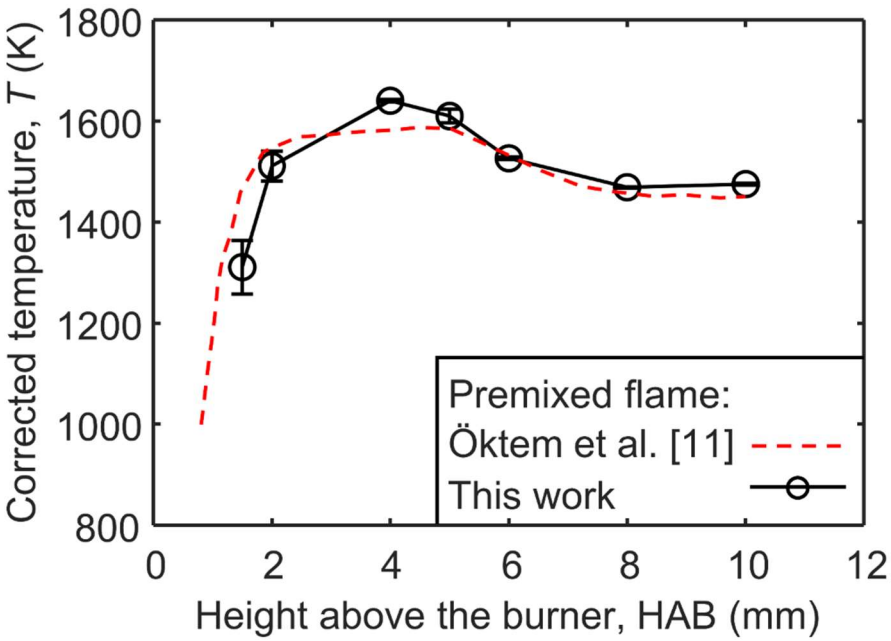

Figure D4: Temperature data from a premixed ethylene flame [11] (broken line) compared to the same flame recreated with the experimental set up used in this work (symbols).

To ensure a sufficient number of primary particles (PPs) were counted to obtain a reliable value of $\bar{d}_{\mathrm{p}}$, the median was plotted as a function of number of particles counted, Figure D5. Always, an asymptote was reached by about 200 counted, in agreement with literature [10].

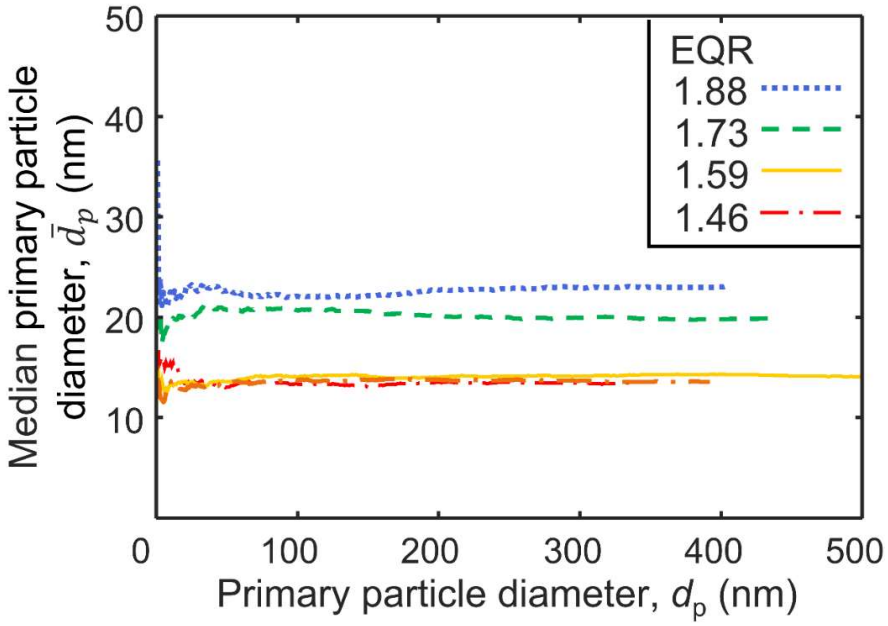

Figure D5: The evolution of $\bar{d}_p$ as a function of the number of PPs counted for HAB = 63 cm and EQR = 1.88 (dotted line), 1.73 (broken line), 1.59 (solid line) and 1.46 (dot-broken line).

Figure D6 shows the volume fraction, f_v, of soot at EQR = 1.46 (triangles) and 1.59 (circles) as a function of HAB. The f_v was calculated based on mass mobility measurements reported in [1] and number concentrations measured by SMPS.

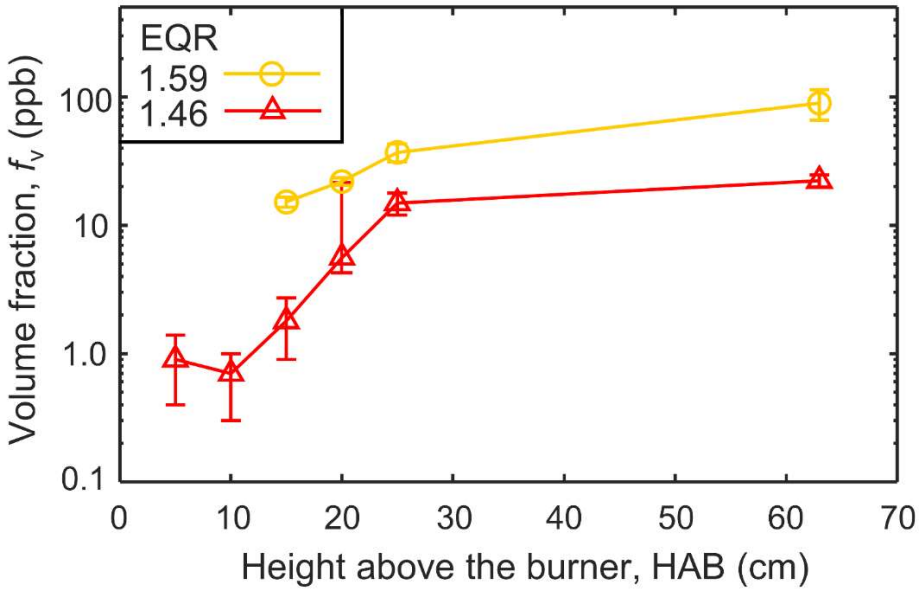

Figure D6: The f_v as a function of HAB at EQR = 1.46 (triangles) and 1.59 (circles). The error bars represent the standard deviation between at least 10 scans of the SMPS.

Figure D7 shows T as a function of Knudsen number, Kn, measured during enclosed spray combustion of jet fuel at EQR = 1.46 (symbols) and used as an input in DEM (line). The soot Kn was estimated from the measured T (Fig. 3.1) and $\bar{d}_m$ (Fig. 3.2) at various HAB. As T drops with increasing HAB, Kn decreases from 80 to 4. The T used in DEM is varied as a function of Kn (line) to follow closely the T measurements of enclosed jet fuel spray combustion.

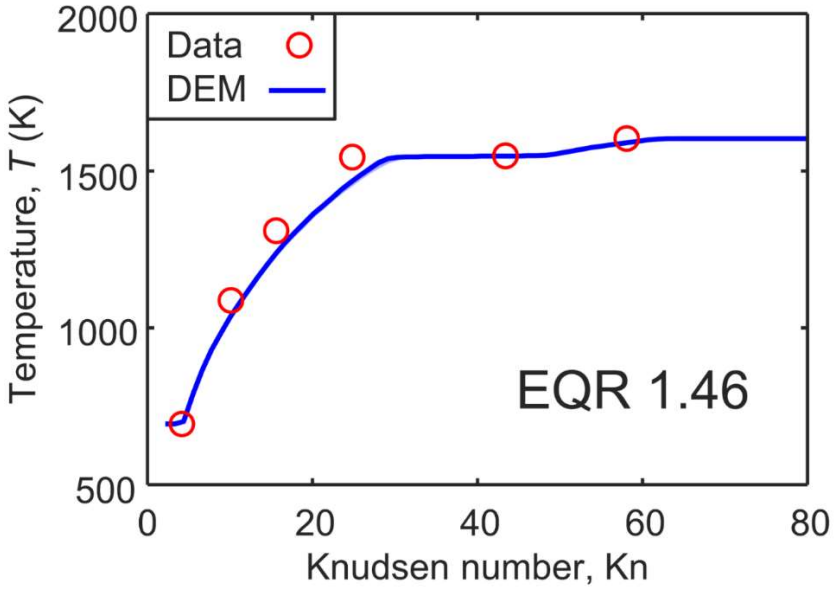

Figure D7: Temperature, T, as a function of Knudsen number, Kn, measured during enclosed spray combustion of jet fuel at EQR = 1.46 (symbols) and used as an input in DEM (line).

Figure D8 shows the evolution of *t* as a function of HAB at EQR = 1.59 (circles) and 1.46 (triangles) derived by DEM. At EQR = 1.46, *t* increases from about 12 ms at HAB = 5 cm up to about 400 ms at HAB = 63 cm. Increasing EQR to 1.59 enhances *t* by a factor of 3 on average. This can be attributed to the 25 % smaller dispersion O_2 flowrate used at EQR = 1.59 compared to that at EQR = 1.46. This reduces also the maximum flame *T* by about 60 K (Fig. 3.1). The *t* enhancement obtained here is consistent with measurements in premixed flames [15]. There, *t* was enhanced by a factor of 2.5 by reducing the gas velocity by 21 %.

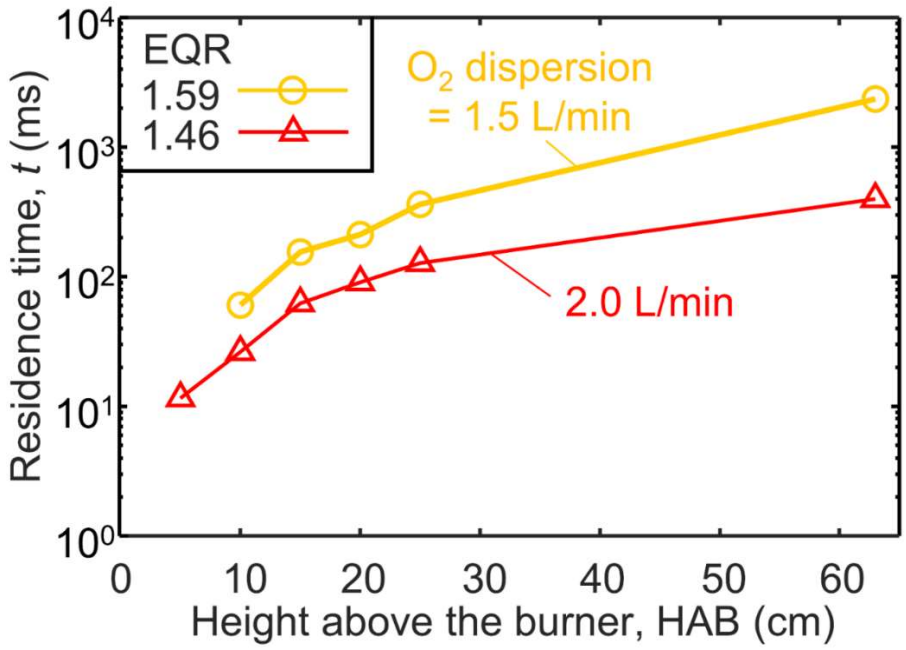

Figure D8: Evolution of *t* as a function of HAB at EQR 1.59 (circles) and 1.46 (triangles).

Figure D9 shows all of the experimental (symbols) and DEM derived (lines) mobility size distributions at EQR = 1.59 and 1.46 and at HAB = 5, 10, 15, 20, 25 and 63 cm.

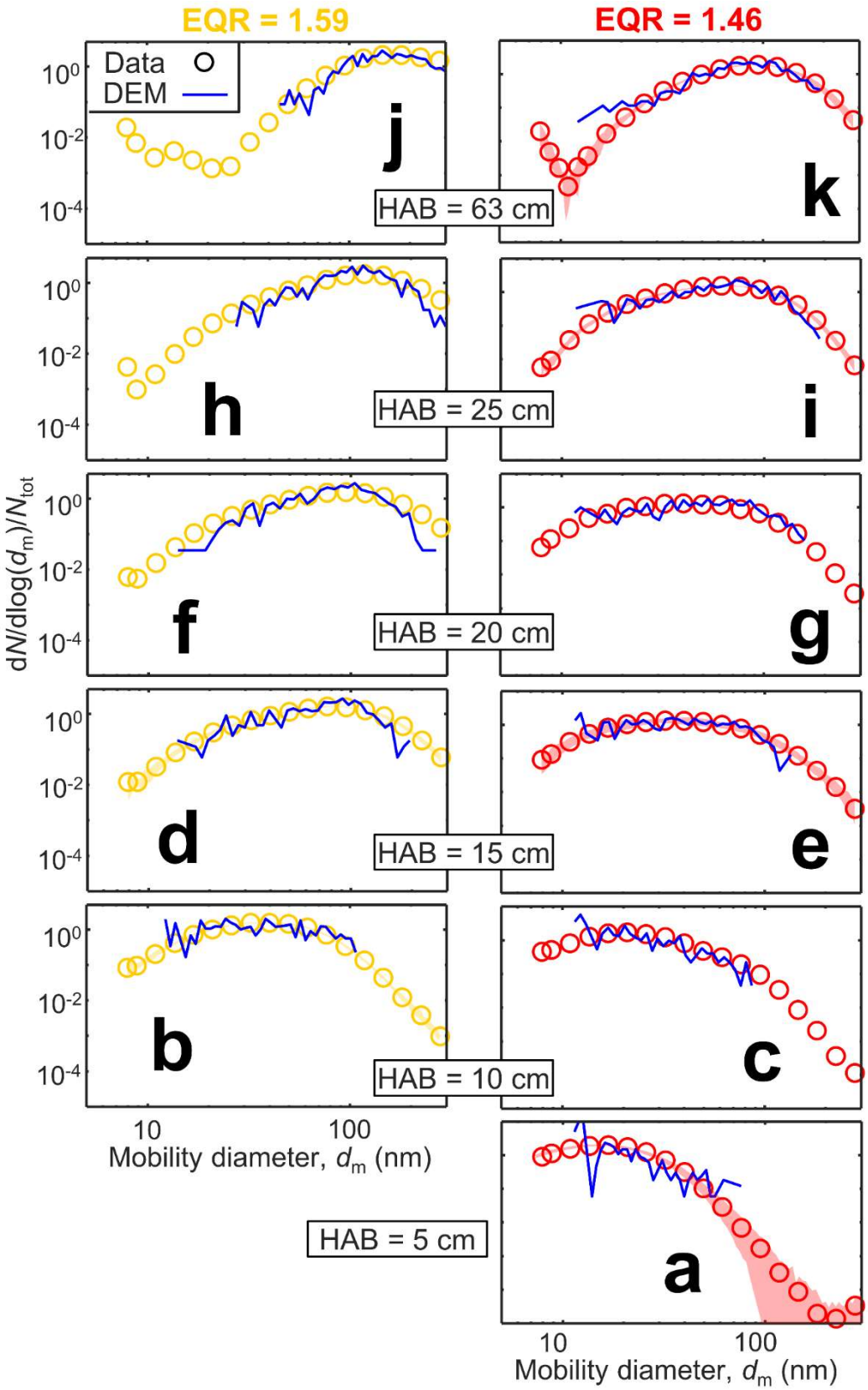

Figure D9: Experimental (symbols) and DEM-derived (lines) mobility size distributions at EQR = 1.59 (b, d, f, h, j) and 1.46 (a, c, e, g, i, k) at HAB = 5 – 63 cm.

Soot is composed of polydisperse PPs which are better represented by histograms. Their size distributions from TEM imaging are shown in Figure D10 for EQR = 1.46, 1.59, 1.73 and 1.88 at HAB = 5, 10, 15, 20, 25 and 63 cm.

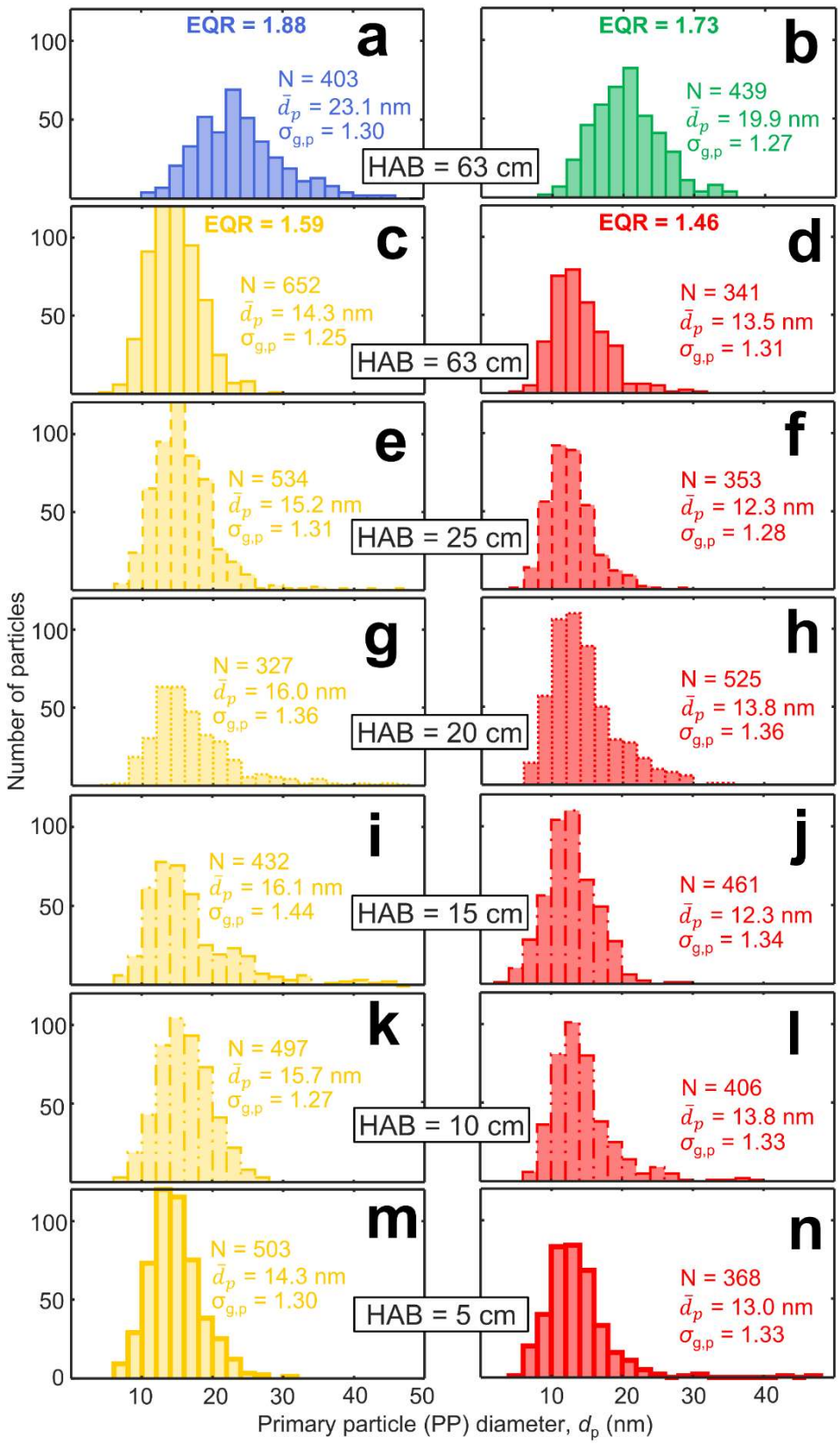

Figure D10: Histograms of the PP diameters measured by TEM at HAB = 63 cm and EQR = 1.88 (a), 1.73 (b), 1.59 (c) and 1.46 (d). Inside the flame, PP size distributions are shown at HAB = 25 (e, f), 20 (g, h), 15 (i, j), 10 (k, l) and 5 cm (a, b) at EQR = 1.59 (e, g, i, k, m) and 1.46 (f, h, j, l, n).

The full Raman spectra of soot made at EQR of a) 1.59 and b) 1.46 are shown in Fig. D11 at HAB = 5, 10, 15, 20, 25 and 63 cm.

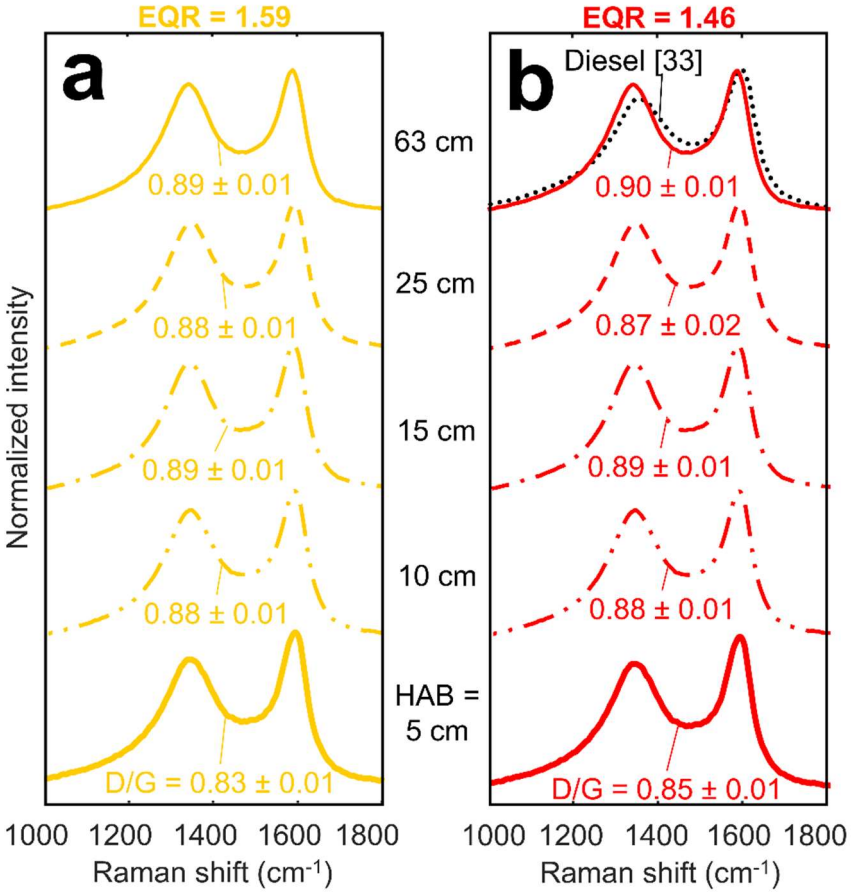

Figure D11: Raman spectra of soot at EQR = 1.59 (a) and 1.46 (b) at HAB = 5, 10, 15, 20, 25 and 63 cm and diesel soot [33] (dotted line).

The organic carbon (OC) to total carbon (TC) ratios of soot produced at each EQR are shown in Figure D12 using thermal gravimetric analysis (TGA) following the method of [16] with more detail given elsewhere [1]. The OC/TC ratio decreases from EQR = 1.88 to 1.59 then begins to increase more quickly from 1.59 to 1.46. At even lower EQR, the OC/TC ratio further increases when measured with TGA [1].

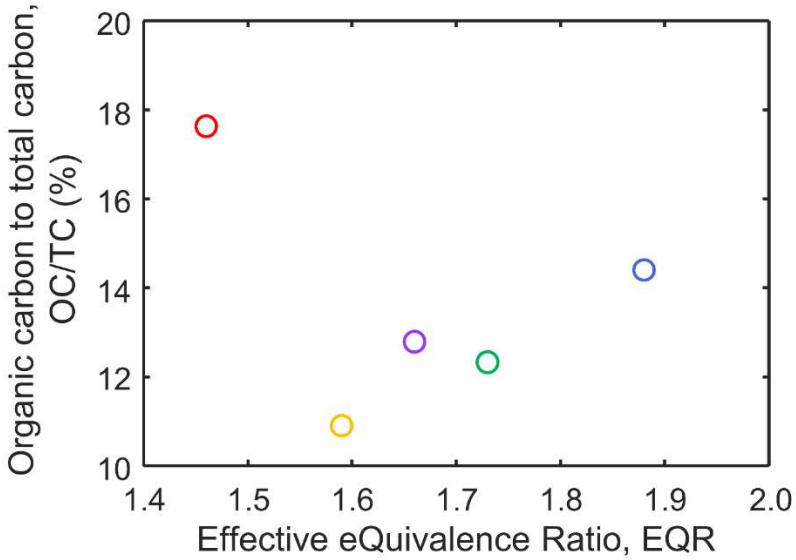

Figure D12: Organic carbon to total carbon (OC/TC) ratios at EQR = 1.46, 1.59, 1.66, 1.73, 1.88.

In order to further probe the graphitization of soot, high resolution TEM (HRTEM) was used to image the graphene layers making up the primary particles as shown in Figure C13.

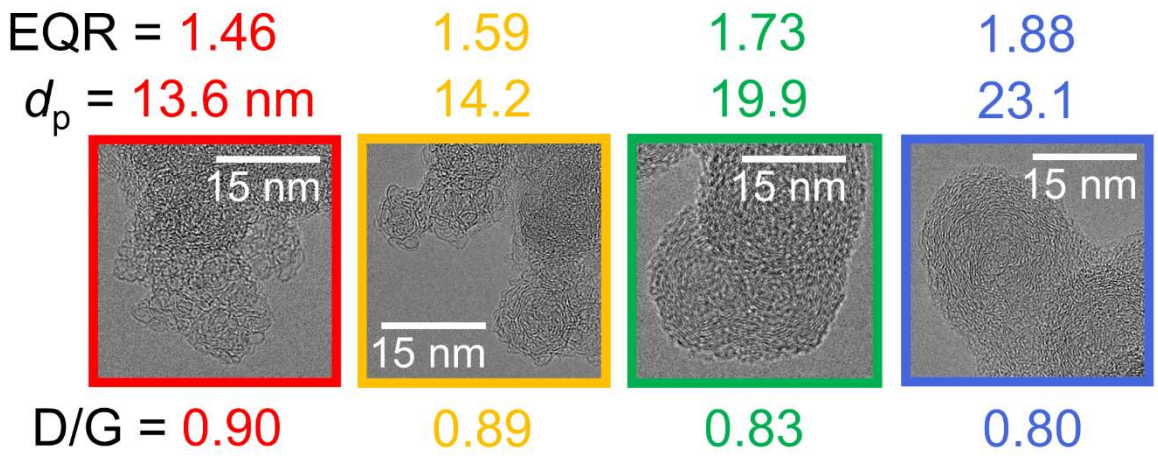

Figure D13: Exemplary HRTEM images of soot produced (from left to right) at EQR = 1.46, 1.59, 1.73 and 1.88 along with the respective median d_p and mean D/G ratio.

D1. References

[1] Trivanovic U, Kelesidis GA, Pratsinis SE. High-throughput generation of aircraft-like soot. *Aerosol Sci Technol* (2022) **56**, 732–43.

[2] Goudeli E, Gröhn AJ, Pratsinis SE. Sampling and dilution of nanoparticles at high temperature. *Aerosol Sci Technol* (2016) **50**, 591–604.

[3] Mädler L, Kammler HK, Mueller R, Pratsinis SE. Controlled synthesis of nanostructured particles by flame spray pyrolysis. *J Aerosol Sci* (2002) **33**, 369–89.

[4] Meierhofer F, Hodapp M, Achelis L, Buss L, Noriler D, Meier HF, Fritsching U. Investigation of atomization concepts for large-scale flame spray pyrolysis (FSP). *Materwiss Werksttech* (2014) **45**, 765–78.

[5] Hinds WC. Aerosol Technology: Properties, Behavior, and Measurement of Air Borne Particles. second ed. Hoboken, New Jersey: John Wiley & Sons; (1999).

[6] Kitano T, Nishio J, Kurose R, Komori S. Evaporation and combustion of multicomponent fuel droplets. *Fuel* (2014) **136**, 219–25.

[7] Willingham CB, Taylor WJ, Pignocco JM, Rossini FD. Vapor pressures and boiling points of some paraffin, alkylcyclopentane, alkylcyclohexane, and alkylbenzene hydrocarbons. *J Res Natl Bur Stand (1934)* (1945) **35**, 219–44.

[8] Lemmon EE, Bell IH, Huber ML, McLinden MO. Thermophysical properties of fluid systems. In: Linstrom PJ, Mallard WG, editors. NIST Chem. WebBook, NIST Stand. Ref. Database Number 69, Gaithersburg, MD, 20899: National Institute of Standards and Technology.

[9] Shaddix CR. A New Method To Compute the Radiant Correction of Bare-Wire Thermocouples. 33rd ASME Natl. Heat Transf. Conf. Mediterr. Combust. Symp., Naples, Italy: (2017).

[10] Kelesidis GA, Kholghy MR, Zuercher J, Robertz J, Allemann M, Duric A, Pratsinis SE. Light scattering from nanoparticle agglomerates. *Powder Technol* (2020) **365**, 52–9.

[11] Öktem B, Tolocka MP, Zhao B, Wang H, Johnston M V. Chemical species associated with the early stage of soot growth in a laminar premixed ethylene – oxygen – argon flame. *Combust Flame* (2005) **142**, 364–73.

[12] Nellis G, Klein S. Heat Transfer. New York, New York: Cambridge University Press; (2009).

[13] Scadron MD, Warshawsky I. Experimental determination of time constants and nusselt numbers for bare-wire thermocouples in high-velocity air streams and analytic approximation of condution and radiation errors. Clevland, Ohio: (1952).

[14] Lesieur M. Turbulence in Fluids. vol. 40. Dordrecht: Springer; (1997).

[15] Bonpua J, Yagües Y, Aleshin A, Dasappa S, Camacho J. Flame temperature effect on sp2 bonds on nascent carbon nanoparticles formed in premixed flames (Tf , max 2100 K): A Raman spectroscopy and particle mobility sizing study. *Proc Combust Inst* (2019) **37**, 943–51.

[16] Klingshirn CD, West ZJ, DeWitt MJ, Higgins A, Graham J, Corporan E. Quantification of elemental and total carbon in combustion particulate matter using thermal-oxidative analysis. *J Air Waste Manag Assoc* (2019) **69**, 1003–13.

Appendix E

Supplementary Information for Chapter 4: Trade-off between soot and NO emissions during enclosed spray combustion of jet fuel

Figure E1 shows the comparison between the number of soot primary particles counted and the median primary particle diameter obtained from Transmission Electron Microscopy (TEM) for Burner to Ring Distances, BRD = 50 (red line), 40 (purple line), 30 (blue line), 20 (green line) and 10 (yellow line) cm. In each case, an asymptote is approached by 200 particles counted as has been observed previously for soot [1] and TiO_2 [2]. Thus, more than 200 primary particles were sized for each condition.

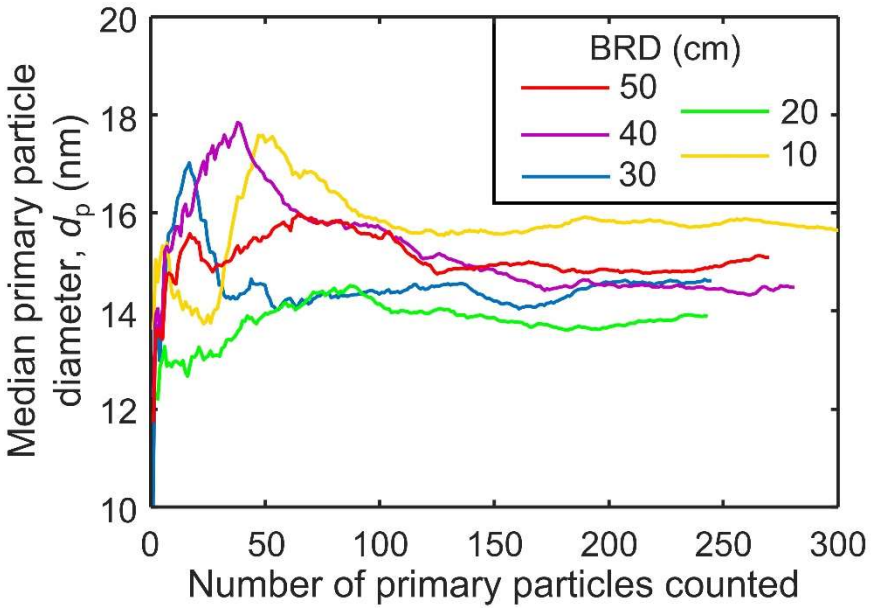

Figure E1: The median primary particle diameter, d_p, as a function of the number of primary particles counted. Variation in the median levels off when approximately 200 particles were counted.

Example images used to obtain the results in Figure E1 are shown in Figure E2 for soot produced with N_2 quenching at BRD = a) 10, b) 20, c) 30, d) 40 and e) 50 cm. Figure E2f shows soot produced with air quenching at BRD = 50 cm.

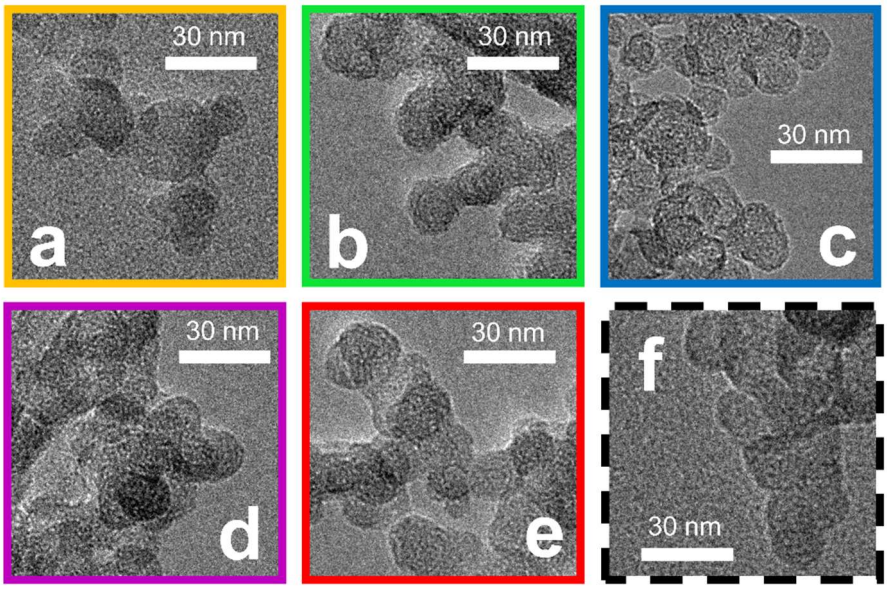

Figure E2: Exemplary TEM images of soot produced with pure N_2 quenching at a) BRD = 10, b) 20, c) 30, d) 40 and e) 50 cm. The particles in f) were produced with air quenching at BRD = 50 cm.

Figure E3 shows the centerline temperature profiles for Enclosed Spray Combustion (ESC) of jet A1 fuel with swirl-injection of air (open symbols) and pure N_2 (filled symbols) at BRD of a) 50 b) 40, c) 30, d) 20 and e) 10 cm.

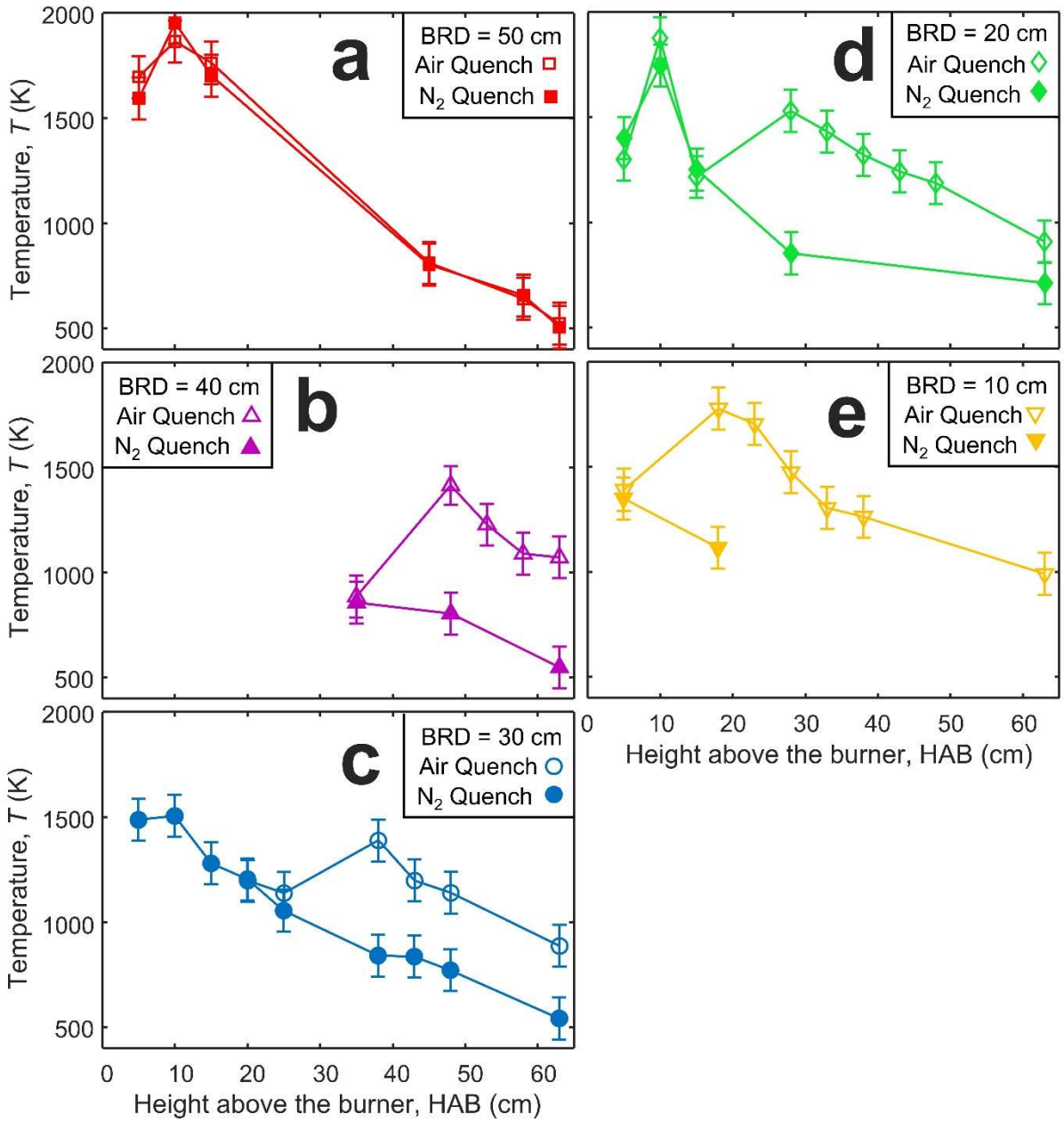

Figure E3: The centerline flame temperature from ESC of jet A1 fuel when pure N_2 (filled symbols) or air (open symbols) are swirl-injected through a torus ring at BRD = a) 50, b) 40, c) 30, d) 20 and e) 10 cm.

The mobility size distributions of soot produced at BRD = 50 (dot-dashed line), 40 (dashed line), 30 (solid line), 20 (dotted line) and 10 cm (double dot-dashed line) are shown in Figure E4 where the shaded area represents the standard deviation between repeated measurements. Fitting these data to log normal distributions results in median d_m = 196 ± 2.9, 170 ± 8.8, 142 ± 4.1, 133 ± 6.3 and 111 ± 2.9 nm at BRD = 50, 40, 30, 20 and 10 cm, respectively. The geometric standard deviation, GSD at these same BRD are 1.57 ± 0.01, 1.61 ± 0.01, 1.65 ± 0.01, 133 ± 0.01 and 1.71 ± 0.03.

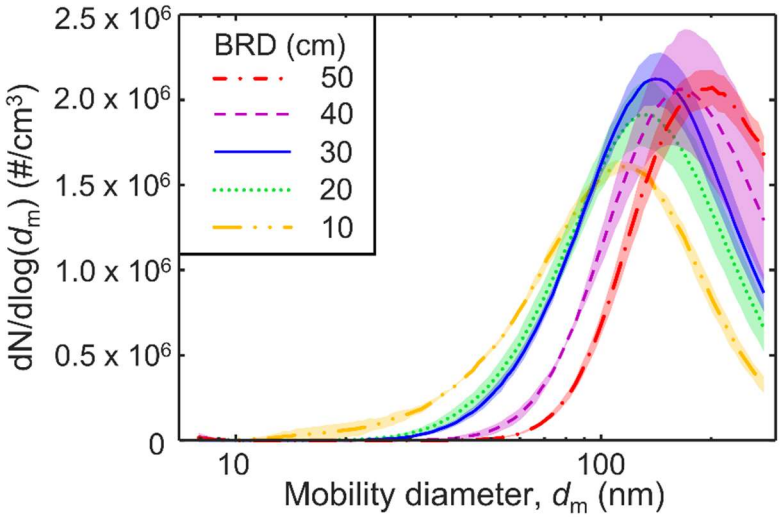

Figure E4: The mobility size distributions of soot produced from ESC of jet A1 fuel when N_2 was swirl injected through a torus ring at BRD = 50 (dot-dashed line), 40 (dashed line), 30 (solid line), 20 (dotted line) and 10 cm (double dot-dashed line).

A photo of the experimental set up is shown in Figure E5 with a BRD = 20 cm. The quartz glass tubes are clear but around HAB = 10 cm, soot begins to visibly accumulate on the walls of the enclosure. Air is injected through the torus ring oxidizing any remaining fuel and the soot produced earlier in the flame and therefore no soot is visibly accumulating on the enclosure walls downstream of the torus ring.

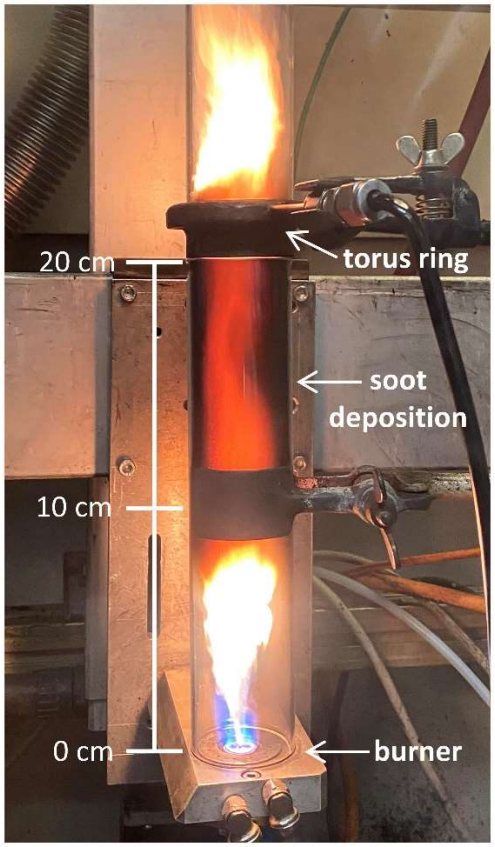

Figure E5: The experimental set up for ESC of jet A1 fuel with BRD = 20 cm and swirl injection of air. In the lower tube soot is formed and visibly deposits on the sides of the quartz glass tube. In the second tube the soot is oxidized and the tube is visually clean.

The primary particle size distributions of soot produced with 0% O_2 injected through the ring (N_2 only) are shown in Figure E6a at BRD = 50 (squares), 40 (triangles), 30 (circles), 20 (diamonds) and 10 cm (inverse triangles). There are no significant differences in primary particle size between soot produced at all BRD. For BRD ≤ 40 cm, the primary particle size after air injection could not be measured due to the extremely low concentrations. At BRD = 50 cm, a sufficient sample size of soot after air injection was obtained (Figure E6b, open squares). At this BRD, there was no significant difference between the primary particle sizes after pure N_2 or air injection.

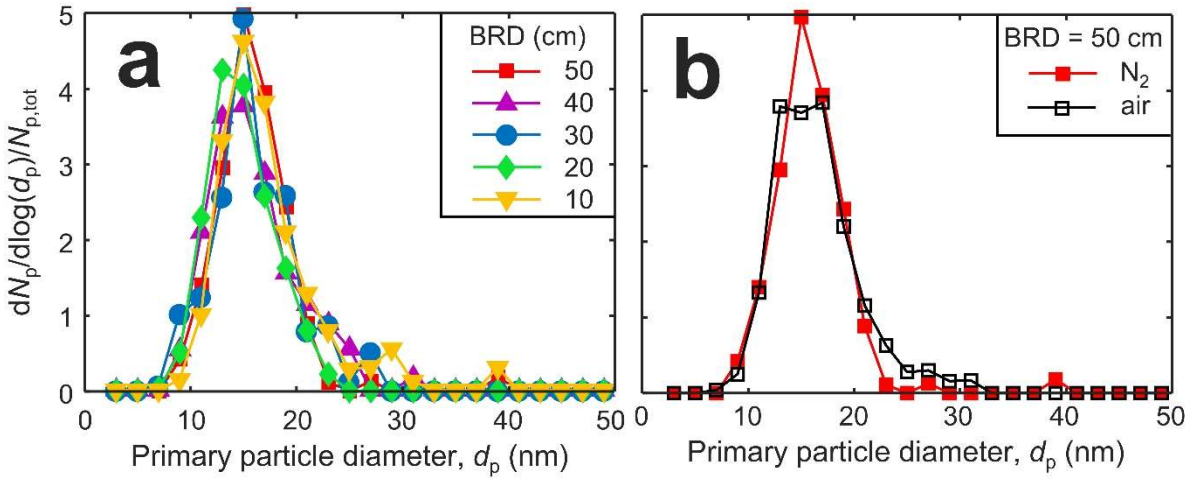

Figure E6: The primary particle size distributions obtained from TEM imaging with a) pure N_2 quench at BRD = 50 (squares), 40 (triangles), 30 (circles), 20 (diamonds) and 10 cm (inverse triangles) having median primary particle diameters of 15.1, 15.2, 14.6, 13.8 and 15.7 nm, respectively and b) at BRD = 50 cm with pure N_2 (red filled squares) and air (black open squares) which showed virtually no change compared to N_2 quenching with a median primary particle diameter of 14.9 nm.

The volume fraction, f_v, was estimated using the SMPS size distributions and primary particle sizes accounting for its agglomerated structure by [3]:

$$f_v = \frac{\pi}{6}\sum_{i=1}^{k} N_i d_{m,i}^{2.22} d_p^{-0.78} \qquad \text{(E.1)}$$

where N_i is the number concentration of soot with $d_{m,i}$ and mean d_p. The index k denotes the d_m bins measured with the SMPS and varies from 1 to 100. At BRD ≤ 40 cm with air quenching, soot quantities were too small to obtain a sufficient sample for analysis. So, the d_p was estimated by assuming that it was reduced by 17%, when compared to the d_p produced at the same BRD with N_2 quenching [4]. Figure E7a shows both the pure N_2 (filled symbols) and estimated air f_v (open symbols). At BRD = 50 cm, there is significant overlap which makes it impossible to distinguish between symbols for pure N_2 and air injection. Figure E7b zooms in on just the f_v after pure N_2 injection which does show a slight increase with BRD. This is because the mobility size distributions shifted to slightly larger sizes at larger BRD although the total number concentration stayed approximately constant at 4 x 10^7 #/cm^3 (Figure 4.3).

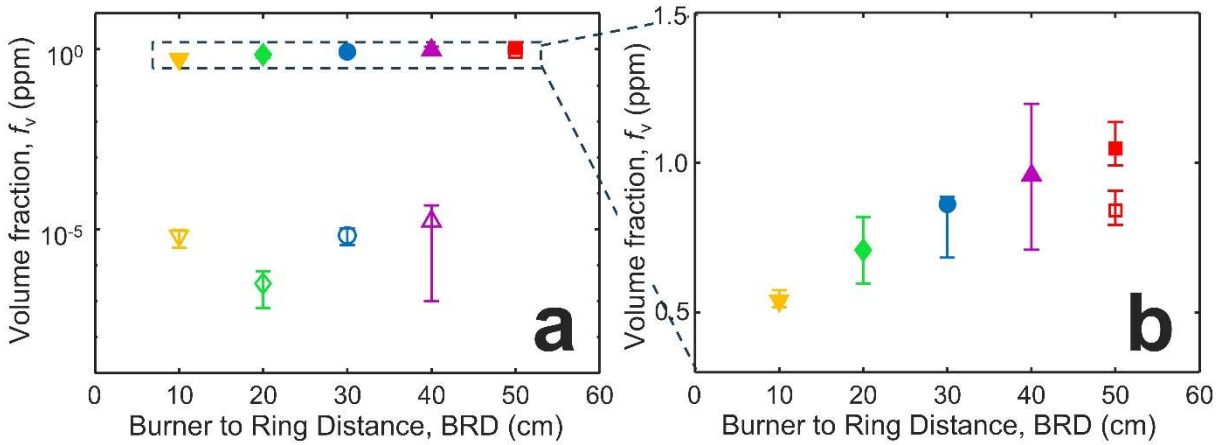

Figure E7: The estimated emitted volume fraction, f_v, of soot a) with air (open symbols) and pure N_2 (filled symbols) and b) a linear scale for the latter as a function of the BRD.

The NO emissions produced with various O_2 volume fractions injected through the torus ring at BRD = 30 cm from 0 to 20 vol% O_2 are shown in Figure E8. There is a steady increase in NO as the O_2 fraction increases as would be expected based on the simultaneously decreasing soot number concentration (Figure 4.3).

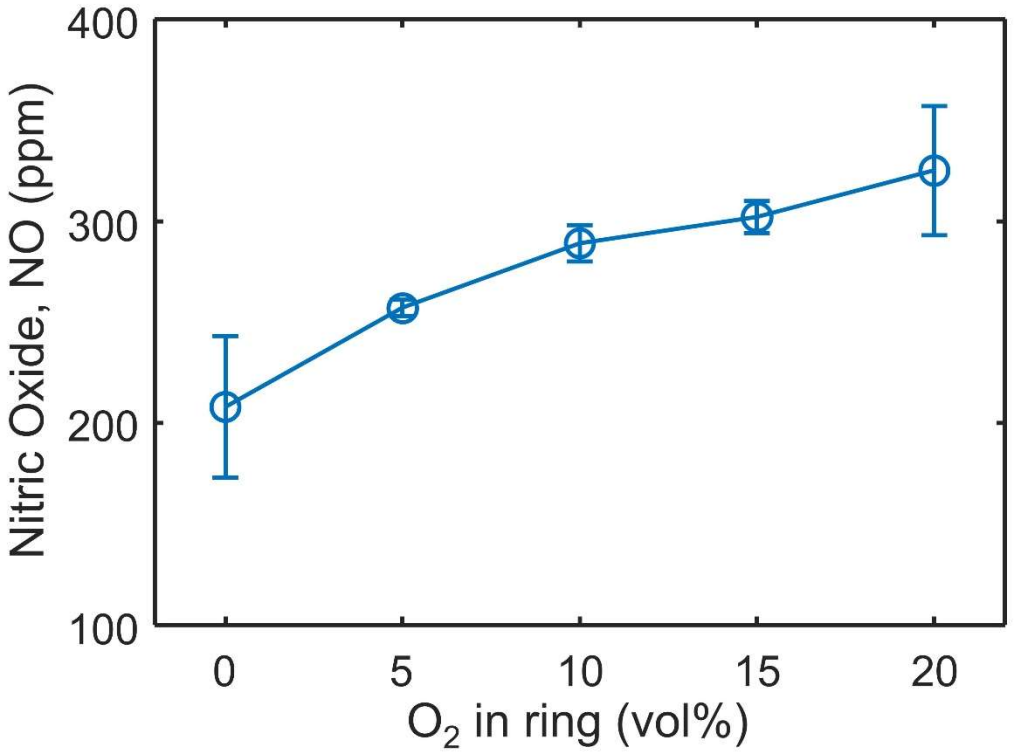

Figure E8: The NO concentration produced at BRD = 30 cm at O_2 at 0, 5, 10, 15 and 20 vol %.

In addition to the NO emissions produced after air quenching at BRD = 10 – 50 cm (Figure 4.5), the NO produced during pure N_2 quenching was also measured as shown in Figure E9.

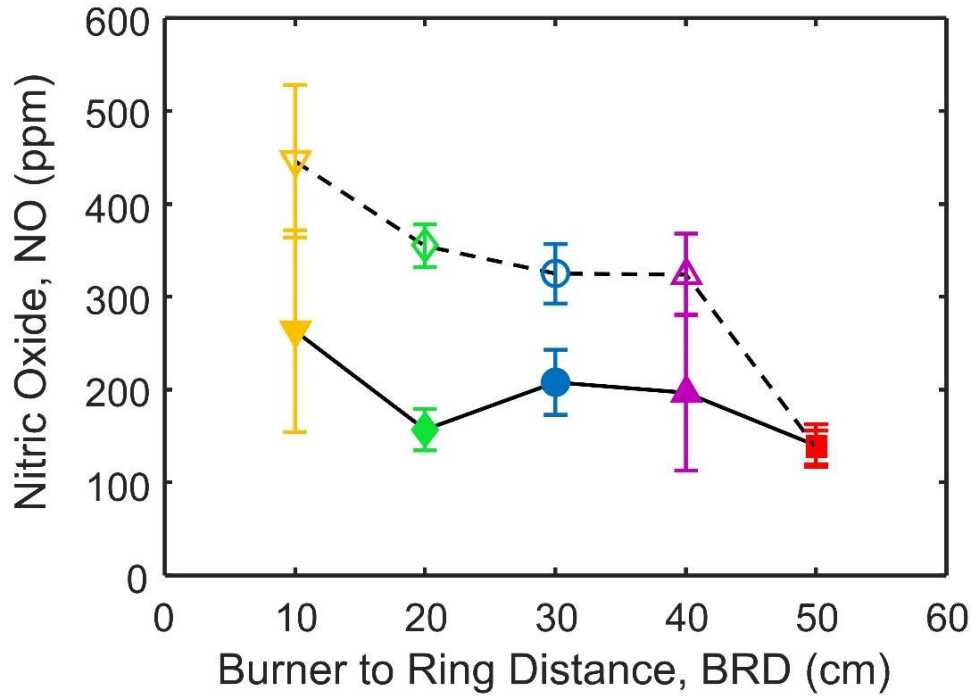

Figure E9: The NO concentration produced with air quenching (open symbols) and pure N_2 quenching (filled symbols).

The NO concentration emitted from ESC of jet fuel increased linearly with the temperature 5 cm after air injection through the torus ring (Figure 4.6 and Figure E10, open symbols). This linear relationship (Eq. 4.1) also held true when pure N_2 was injected into the system (filled symbols) as depicted in Figure E10 (dot-dashed line).

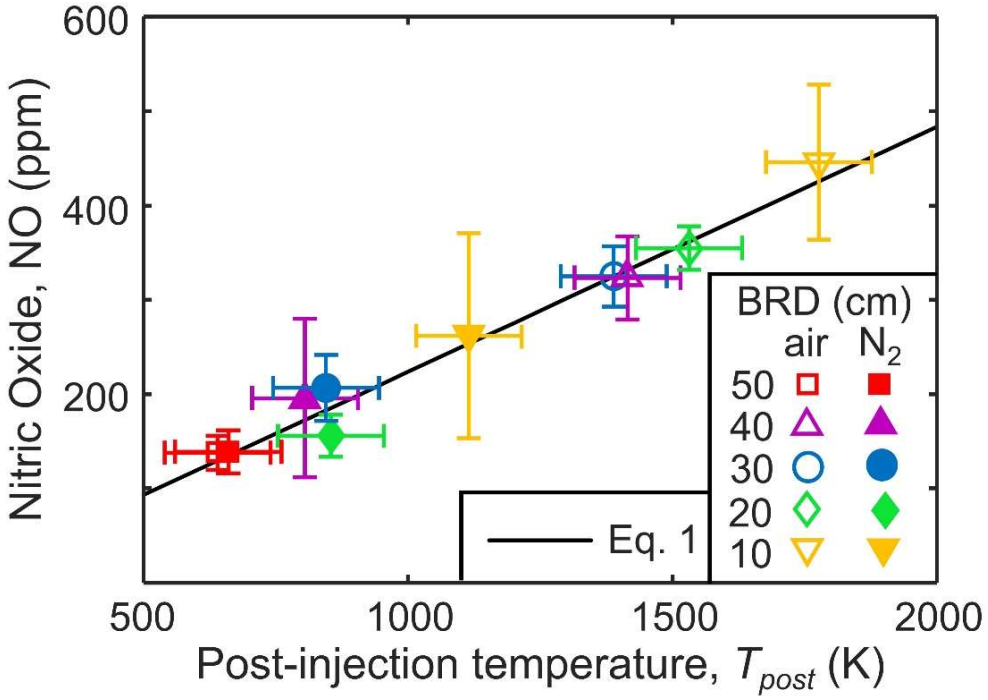

Figure E10: The correlation between post-injection temperature, T_{post}, and NO emissions with air (open symbols) and N_2 quenching (filled symbols) with the best fit (solid line).

E1. References

[1] Kelesidis GA, Kholghy MR, Zuercher J, Robertz J, Allemann M, Duric A, Pratsinis SE. Light scattering from nanoparticle agglomerates. *Powder Technol* (2020) **365**, 52–9.

[2] Tsantilis S, Kammler HK, Pratsinis SE. Population balance modeling of flame synthesis of titania nanoparticles. *Chem Eng Sci* (2002) **57**, 2139–56.

[3] Kelesidis GA, Pratsinis SE. Determination of the volume fraction of soot accounting for its composition and morphology. *Proc Combust Inst* (2021) **38**, 1189–96.

[4] Kelesidis GA, Nagarkar A, Trivanovic U, Pratsinis SE. Toward elimination of soot emissions from jet fuel combustion. *Environ Sci Technol* (2023) **57**, 10276–83.

Curriculum Vitae

Una Trivanovic

Education

2020 – 2024 Ph.D. in Mechanical and Process Engineering, ETH Zürich, Switzerland
Thesis: Synthesis and dynamics of carbonaceous nanoparticles during enclosed spray combustion, (Prof. Sotiris E. Pratsinis)

2017 – 19 M.A.Sc. in Mechanical Engineering, University of British Columbia, Canada
Thesis: Characterization of the effects of fuel and entrained salt on soot morphology, (Prof. Steven N. Rogak)

2011 – 16 B.S. in Mechanical Engineering, Montana State University

2011 – 16 B.A. in Modern Languages & Literature, Montana State University

2014 Semester abroad, Université Paul Valèry, Montpellier, France

Experience

2024 – now Scientist, Particles and Aerosols Laboratory, Swiss Federal Institute of Metrology (METAS)

2019 Visiting Researcher, Boies Research Group, University of Cambridge, UK,
Project: Image analysis of microscopy of carbon nanotubes (Prof. Boies)

2016 – 17 Condition Monitoring Specialist, SKF Canada, Ltd., Canada
Reliability of rotating equipment for oil & gas, paper, chemical and metal manufacturing

2015 – 16 Undergraduate Researcher, Montana State University, USA
Alignment of graphene-carboxymethyl cellulose nanocomposite (Prof. Sofie)

2015 Reliability Engineering Intern, SKF Canada, Ltd., Canada
Baseline vibration readings on rotating equipment and automated diagnostics

2014 Predictive Maintenance Co-op Student, Zellstoff Celgar Ltd., Canada
Automated diagnostics software for oil analysis databases and shape analysis.

Honours & Awards

2023 Best Poster Award, European Aerosol Conference, Sept. 3 – 8, 2023, Málaga, Spain

2023 Macroscopic Art Award, American Association for Aerosol Research 41st Annual Conference, Oct. 2 – 6, 2023, Portland, USA

2023 Fellow of the Global Young Scientists Summit, Jan. 16 – 20, 2023, Singapore

2022 *Environmental Science: Atmospheres* Poster Award, 11th International Aerosol Conference, Sept. 4 – 9, 2022, Athens, Greece

2022 Best Poster Award, 6th International Sooting Flame Workshop, July 22 – 23, 2022, Vancouver, Canada

2022 Best Poster Award, 25th ETH-Conference on Combustion Generated Nanoparticles (Virtual), June 21-23, 2022, Zürich, Switzerland

2022	Gesellschaft für Aerosolforschung (GAeF) Student Travel Support
2020	NSERC Canada Graduate Scholarship-Doctoral ($CAD 105 000)
2019	Mitacs Globalink Research Award
2019	UBC Go Global Self-Initiated Research Award
2017, 2018	UBC Faculty of Applied Science Masters Graduate Award

Teaching

Teaching Assistant:

- Micro- and Nanoparticle Technology (MSc-level) Fall 2021, 2022, ETH Zürich. 5 – 15 students
- Mass Transfer (BSc-level) Fall 2020, ETH Zürich. 80 – 120 students
- Brownian Motion Laboratory Practicum (BSc-level) Spring 2020, ETH Zürich. 5 – 20 students
- Materials for Mechanical Design (BSc-level) Fall 2018, University of British Columbia. 5 – 20 students
- Intro. to the Mechanical Design Process (BSc-level) Spring 2018, 2019, University of British Columbia. 5 – 20 students
- Applied Engineering Data Analysis (BSc-level) Fall 2015, Montana State University. 5 students (tutoring)

Pedagogical Training:

- MECH Teaching Assistant Best Practices Training, University of British Columbia, 09/2017
- MECH Classroom Orientation Training, University of British Columbia, 09/2017

Supervision of Student Research:

1. Alex Weber, “Impact of sustainable aviation fuels on soot from enclosed spray combustion”, MSC Semester Project, ETH Zürich, Spring 2024.
2. Alex Weber, “Morphology and nanostructure of aircraft-like soot”, student project in the class Micro- and Nanoparticle Technology, ETH Zürich, Fall 2023.
3. Giacomo Rizzo, “Exploring carbon-slurries for flame spray synthesis of nanoparticles”, student project in the class Micro- and Nanoparticle Technology, ETH Zürich, Fall 2022.
4. Yannik Meisterhans, “Hydrophobicity of carbonaceous nanoparticles after oxidation”, BSc Thesis, ETH Zürich, Spring 2022.
5. Michael Pereira Martins, “Evolution of soot primary particle size and nanostructure during spray combustion, MSc Semester Project, ETH Zürich, Spring 2022.
6. Matteo d’Andria, “Thermal gravimetric analysis of aircraft-like soot”, student project in the class Micro- and Nanoparticle Technology, ETH Zürich, Fall 2021.
7. Michael Pereira Martins, “Tuning the hydrophobicity of carbonaceous nanoparticles”, student project in the class Micro- and Nanoparticle Technology, ETH Zürich, Fall 2021.
8. Amogh Nagarkar, “The impact of oxidation on soot size distribution, morphology and nanostructure”, MSc Semester Project, ETH Zürich, Spring 2021. (Co-supervisor)
9. Michael Pereira Martins, “Monitoring soot dynamics during flame spray pyrolysis of jet fuel”, BSc Thesis, ETH Zürich, Spring 2021.

Service

Session Chair at Scientific Conferences:

American Association for Aerosol Research 41st Conference 2023, Portland, USA (2-6/10/2023)
Session Combustion I: "Soot Formation, Morphology, and emissions"

11th International Aerosol Conference 2022, Athens, Greece (4-9/9/2022)
Session BAP-5: "Aerosol transport properties and fluid dynamics"

European Aerosol Conference 2021 (Virtual), (30/8-3/9/2021).
Session AT-5: "High temperature aerosols"

Reviewer (in parenthesis # of articles):

Journal of Aerosol Science (6)
Scientific Reports (1)
Journal of Geophysical Research – Atmospheres (1)
African Journal of Environmental Science & Technology (1)
Carbon (1)

Laboratory Oversight Duties:

2022 – 24 Safety responsible person, Particle Technology Laboratory, ETH Zurich
2018 – 19 Radiation safety officer, Aerosol Laboratory, University of British Columbia

Educational Outreach:

2023 *AAAR Social Media Ambassador*
Served as a member of the team promoting the American Association of Aerosol Research (AAAR) annual conference on social media for the conference.

2023 *Pint of Science*
Pint of Science festival presenter making research accessible to the public

2022 – 23 *Fix the Leaky Pipeline Peer Mentoring*
This program brings together women from across Switzerland to provide peer mentoring for one another. Our group of 12 PhD students organizes monthly workshops to learn new skills and support each other through our PhDs

2022 *Kangaroo goes science*
Female 7th grade students (aged 13-14) were invited to learn about natural sciences and engineering. I contributed a video: Sind Nanopartikel schädlich oder nützlich?

2016 – now *EngineerGirl*
Contributor to the EngineerGirl website which highlights women in engineering and answers questions girls and young women have about engineering

2015 – 16 *Robotics outreach*
As part of the NASA robotic mining competition our team participated in community events designed to expose kids (aged 5 – 16 years old depending on the event) to science and technology. I acted as the team outreach coordinator organizing and participating in all events. Example event

2013 – 14 *Expanding Your Horizons group leader*
An annual event at Montana State University (now called MSU STEAM Day) to introduce middle school aged girls (11 – 14) to science, technology, engineering and math (STEM). As a group leader, I guided my group of girls through various hands-on STEM activities around campus and answered their questions

2013 *Girl Scouts Badge Day leader*
Helped Girl Scouts earn their engineering badge by guiding them through projects

Publications and Presentations

Refereed Publications

- Trivanovic, U., Pratsinis, S.E. (2024) Trade-off between soot and NO emissions during enclosed spray combustion of jet fuel, In preparation.
- Sipkens, T.A., Dastanpour, R., Trivanovic, U., Nikookar, H., Rogak, S.N. (2024) atems: Analysis tools for TEM images of soot, In preparation.

14. Trivanovic, U., Pratsinis, S.E. (2024) Opinion: Eliminating aircraft soot emissions, *Aerosol Research,* 2, 207–223.
13. Lizonova, D., Trivanovic, U., Demokritou, P., Kelesidis, G.A. (2024) Dispersion and dosimetric challenges of hydrophobic nanoparticles in in vitro cellular studies, *Nanomaterials*, 14, 589, doi: 10.3390/nano14070589
12. Trivanovic, U., Pereira Martins, M., Benz, S., Kelesidis, G.A., Pratsinis, S.E. (2023) Dynamics of soot surface growth and agglomeration by enclosed spray combustion of jet fuel, *Fuel*, 342, 127864, doi: 10.1016/j.fuel.2023.127864
11. Kelesidis, G.A., Nagarkar, A., Trivanovic, U., Pratsinis, S.E. (2023) Towards eliminating soot emissions from jet fuel combustion, *Environmental Science and Technology*, 57, 10276–10283, doi: 10.1021/acs.est.3c01048
10. Trivanovic, U., Kelesidis, G.A., Pratsinis, S.E. (2022) High-throughput generation of aircraft like soot, *Aerosol Science and Technology* 56, 732-743, doi: 10.1080/02786826.2022.2070055
9. Sipkens, T.A., Trivanovic, U., Naseri, A., Bello, O.W., Baldelli, A., Kazemimanesh, M., Bertram, A.K., Kostiuk, L., Corbin, J.C., Olfert, J.S., Rogak, S.N. (2021) Using two-dimensional distributions to inform the mixing state of soot and salt particles produced in gas flares, *Journal of Aerosol Science* 158, 105826, doi: 10.1016/j.jaerosci.2021.105826
8. Kazemimanesh, M., Baldelli, A., Trivanovic, U., Popovicheva, O., Timofeev, M., Shonija, N., Obvintsev, Y., Kuang, C., Jefferson, A.M., Corbin, J.C., Goss, G.G., Alessi, D.S., Johnson, M.R., Rogak, S.N., Olfert, J.S. (2021) Particulate emissions from turbulent diffusion flames with entrained droplets: A laboratory simulation of gas flaring emissions, *Journal of Aerosol Science* 157, 105807, doi: 10.1016/j.jaerosci.2021.105807
7. Peng, W., Yang, J., Corbin, J.C., Trivanovic, U., Lobo, P., Kirchen, P., Rogak, S.N., Gagné, S., Miller, J.W., Cocker, D. (2020) Comprehensive analysis of the air quality impacts of switching a marine vessel from diesel fuel to natural gas. *Environmental Pollution* 266, 115404, doi: 10.1016/j.envpol.2020.115404
6. Trivanovic, U., Sipkens, T.A., Kazemimanesh, M., Baldelli, A., Jefferson, A.M., Conrad, B.M., Johnson, M.R., Corbin, J.C., Olfert, J.S., Rogak, S.N. (2020) Morphology and size of soot from gas flares as a function of fuel and water addition, *Fuel* 279, 118478, doi: 10.1016/j.fuel.2020.118478
5. Baldelli, A., Trivanovic, U., Sipkens, T.A., Rogak, S.N. (2020) On determining soot maturity: A review of the role of microscopy-and spectroscopy-based techniques. *Chemosphere* 252, 126532, doi: 10.1016/j.chemosphere.2020.126532
4. Baldelli, A., Trivanovic, U., Corbin, J.C., Lobo, P., Gagné, S., Miller, J.W., Kirchen, P., Rogak, S.N. (2020) Typical and atypical morphology of non-volatile particles from a diesel and natural gas marine engine. *Aerosol and Air Quality Research* 20, 730-740, doi: 10.4209/aaqr.2020.01.0006

3. Corbin, J. C., Peng, W., Yang, J., Sommer, D.E., Trivanovic, U., Kirchen, P., Miller, J.W., Rogak, S.N., Cocker, D.R., Lobo, P., Gagné, S. (2019) Characterization of particulate matter emitted by a marine engine operated with liquefied natural gas and diesel fuels. *Atmospheric Environment* 220, 117030, doi: 10.1016/j.atmosenv.2019.117030
2. Trivanovic, U., Corbin, J.C., Peng, W., Yang, J., Kirchen, P., Miller, J.W., Lobo, P., Gagné, S., Rogak, S.N. (2019) Size and morphology of soot produced by a dual-fuel marine engine. *Journal of Aerosol Science* 138, 105448, doi: 10.1016/j.jaerosci.2019.105448
1. Baldelli, A., Trivanovic, U., Rogak, S.N. (2019) Electron tomography of soot for validation of 2D image processing and observation of new structural features, *Aerosol Science and Technology*, 53, 575-587. doi: 10.1080/02786826.2019.1578860

Invited Lectures

1. "High throughput generation of aircraft-like soot" AAAR AS&T Lectures (virtual) (19/04/2023) https://www.youtube.com/watch?v=rOormsGmB6w
2. "Enclosed spray combustion of jet fuel: a surrogate of aircraft soot emissions?" Global Young Scientists Summit, Singapore (17/1/2023) https://www.youtube.com/watch?v=gB58ep6In1Y

Presentations

Oral Presentations:

1. Kelesidis, G.A., Nagarkar, A., Trivanovic, U., Pratsinis, S.E., "Eliminating Soot Emissions from Jet Fuel Combustion." AIChE Annual Meeting 2023, Orlando, USA (5-10/11/2023)
2. Trivanovic, U., Kelesidis, G.A., Pratsinis, S.E., "Soot Size Distribution & Structure during Enclosed Spray Combustion of Jet Fuel" American Association for Aerosol Research 41st Annual Conference 2023, Portland, USA (2-6/10/2023)
3. Kelesidis, G.A., Nagarkar, A., Trivanovic, U., Pratsinis, S.E., "Eliminating Soot Emissions from Jet Fuel Combustion." American Association for Aerosol Research 41st Annual Conference 2023, Portland, USA (2-6/10/2023)
4. Trivanovic, U., Pereira Martins, M., Kelesidis, G.A., Pratsinis, S.E., "Carbon Black or Soot Surface Growth & Agglomeration during Enclosed Spray Combustion" European Aerosol Conference 2023, Malaga, Spain (3-8/9/2023)
5. Kelesidis, G.A., Nagarkar, A., Trivanovic, U., Pratsinis, S.E., "Eliminating Soot Emissions from Jet Fuel Combustion." European Aerosol Conference 2023, Malaga, Spain (3-8/9/2023)
6. Trivanovic, U., Kelesidis, G.A., Pratsinis, S.E., "High-throughput generation of aircraft-like soot: Dynamics of soot surface growth and agglomeration by enclosed spray combustion of jet fuel" 26th ETH Nanoparticles Conference, Zürich, Switzerland (20-22/6/2023, scheduled)
7. Kelesidis, G.K., Trivanovic, U., Pratsinis, S.E., "High-throughput generation of aircraft-like soot" 9th World Congress on Particle Technology, Madrid, Spain (18-22/9/2022)
8. Trivanovic, U., Kelesidis, G.K., Pratsinis, S.E., "High-throughput generation of aircraft-like soot" Cambridge Particle Meeting, Cambridge, UK (25/6/2022)
9. Trivanovic, U., Kelesidis, G.K., Pratsinis, S.E. "High-throughput soot generation by flame spray pyrolysis" European Aerosol Conference 2021, Virtual (30/8-3/9/2021)
10. Kazemimanesh, M., Baldelli, A., Trivanovic, U., Popovicheva, O., Timofeev, M., Shonija, N., Obvintsev, Y., Kuang, C., Jefferson, A.M., Corbin, J.C., Goss, G.G., Alessi, D.S.,

Johnson, M.R., Rogak, S.N., Olfert J.S., "Particulate emissions from laboratory gas flares with entrained droplets" European Aerosol Conference 2021, Virtual, (30/8-3/9/2021)

11. Naseri, A., Sipkens, T.A., Trivanovic, U., Kazemimanesh, M., Bello, O.W., Bertram, A., Corbin, J.C., Rogak, S.N., Olfert, J.S., "Comparison of inversion schemes for retrieving black carbon mixing state distributions using CPMA-SP2 measurements", 38th Annual American Association for Aerosol Research Conference, Virtual (5-9/10/2020)
12. Peng, W., Yang, J., Li, Q., Corbin, J.C., Trivanovic, U., Lobo, P., Rogak, S.N., Kirchen, P., Gagné, S., Cocker, D.R., Miller, J.W., "Air Quality Benefits of Switching a Freight Ferry from Diesel Fuel to Natural Gas", 8th International Urban Freight Conference, Long Beach, USA (16-18/10/2019)
13. Peng, W., Yang, J., Corbin, J.C., Li, Q., Trivanovic, U., Rogak, S.N., Lobo, P., Kirchen, P., Gagné, S., Cocker, D.R., Miller, J.W., "Impacts of switching from diesel to liquefied natural gas (LNG) for a marine vessel", 37th Annual American Association for Aerosol Research Conference, Portland, USA (14-18/10/2019)
14. Trivanovic, U., Baldelli, A., Spikens, T., Kazemimanesh, M., Conrad, B., Jefferson, A.M., Corbin, J., Johnson, M., Olfert, J., Rogak, S. "Effects of fuel mixture and inorganic salts on the morphological and optical properties of soot from gas flares", European Aerosol Conference 2019, Gothenburg, Sweden (25-30/8/2019)
15. Trivanovic, U., Corbin, J.C., Baldelli, A., Kazemimanesh, M., Conrad, B.M., Jefferson, A.M., Peng, J., Yang, J., Kirchen, P., Miller, J.W., Johnson, M.R., Olfert, J.S., Lobo, P., Gagné, S., Rogak, S.N., "Primary particle and aggregate size of soot relationships for soot from a marine engine and gas flares", UK Combustion Aerosol Conference and Cambridge Particle Meeting, Cambridge, UK (26-28/6/2019)
16. Trivanovic, U., Baldelli, A., Kazemimanesh, M., Conrad, B.M., Jefferson, A.M., Corbin, J.C., Johnson, M.R., Olfert, J.S., Rogak, S.N., "The effect of inorganic salts from flowback operations on the size, effective density, mixing State, and optical properties of soot from gas flares", 2019 Spring Technical Meeting of the Canadian Section of the Combustion Institute, Kelowna, Canada (13-16/5/2019)
17. Baldelli, A., Trivanovic, U., Rogak, S.N., "Use of electron tomography to analyze the actual primary particles distribution and agglomerate morphology of soot", 10th International Aerosol Conference, St. Louis, USA (2-7/9/2018)
18. Baldelli, A., Dastanpour, R., Trivanovic, U., Jefferson, A.M., Olfert, J.S., Moallemi, A., Thomson, K.A., Johnson, M.R., Popovicheva, O., Rogak, S.N., "Physio-chemical characterization of small scale gas flaring", 10th International Aerosol Conference, St Louis, USA, (2-7/9/2018)

Poster Presentations:

1. Trivanovic, U., Pratsinis, S.E., "Soot-free Emissions from Jet Fuel Combustion: Oxidation Dynamics of Aircraft-like Soot" American Association for Aerosol Research 41st Annual Conference 2023, Portland, USA (2-6/10/2023)
2. Trivanovic, U., Kelesidis, G.A., Pratsinis, S.E., "Evolution of soot size distribution & nanostructure during enclosed spray combustion of jet fuel" European Aerosol Conference 2023, Malaga, Spain (3-8/9/2023)
3. Trivanovic, U., Meisterhans, Y., Kelesidis, G.K., Pratsinis, S.E., "Carbon black surface chemistry and internal nanostructure during internal oxidation", 11th International Aerosol Conference, Athens, Greece (4-9/9/2022)

4. Nagarkar, A., Kelesidis, G.K., Trivanovic, U., Pratsinis, S.E. “Oxidation dynamics of soot produced by spray combustion of jet fuel”, 11th International Aerosol Conference, Athens, Greece (4-9/9/2022)
5. Trivanovic, U., Pereira Martins, M., Kelesidis, G.K., Pratsinis, S.E., “High-throughput generation of aircraft-like soot”, 11th International Aerosol Conference, Athens, Greece (4-9/9/2022)
6. Trivanovic, U., Pereira Martins, M., Kelesidis, G.K., Pratsinis, S.E., “Carbonaceous aerosol formation & growth by enclosed spray combustion of hydrocarbons”, 11th International Aerosol Conference, Athens, Greece (4-9/9/2022)
7. Trivanovic, U., Pereira Martins, M., Kelesidis, G.K., Pratsinis, S.E., “High-throughput generation of aircraft-like soot”, 11th International Aerosol Conference, Athens, Greece (4-9/9/2022)
8. Trivanovic, U., Pereira Martins, M., Kelesidis, G.K., Pratsinis, S.E., “Dynamics of soot nanoparticles during spray combustion of jet fuel”, 39th International Symposium on Combustion, Vancouver, Canada (24-29/7/2022)
9. Trivanovic, U., Kelesidis, G.K., Pratsinis, S.E., “High-throughput generation of aircraft-like soot” 6th International Sooting Flame Workshop, Vancouver, Canada (22-23/7/2022)
10. Trivanovic, U., Sipkens, T.A., Kazemimanesh, M., Baldelli, A., Jefferson, A.M., Conrad, B.M., Johnson, M.R., Corbin, J.C., Olfert, J.S., Rogak, S.N., “Effect of sodium chloride solutions on soot morphology and mixing state from a large-scale laboratory flare”, Fuels, Processes, and Combustion Physics in the Energy Transformation WE-Heraeus-Seminar, Bad Honnef, Germany (8-12/3/2020)
11. Bello, O.W., Sipkens, T.A., Kazemimanesh, M., Trivanovic, U., Naseri, A., Schmidt, S., Baldelli, A., Callahan, R., Bui, D., Bertram, A., Rogak, S.N., Harynuk, J.J., Kostiuk, L., Olfert, J.S., “Emission characterisation from a propane flame with entrained droplets of salt solutions”, Petroleum Technology Alliance Canada - 2019 Methane Emissions Reduction Forum, Banff, Canada, (26-27/11/2019)
12. Baldelli, A., Trivanovic, U., Kazemimanesh, M., Olfert, J., Rogak, S.N., “Effects of fuel mixture and flowback fluid on the effective density, mixing state, and nanostructure of soot emissions from a lab-scale flare”, 2018 Petroleum Technology Alliance Canada - 2018 Methane Emissions Forum, Banff, Canada (27-28/11/2018)
13. Baldelli, A., Trivanovic, U., Rogak, S.N., “Use of electron tomography to analyze the actual primary particles distribution and agglomerate morphology of soot”, 10th International Aerosol Conference, St. Louis, USA (2-7/9/2018)
14. Muretta, J., Trivanovic, U., “Second derivative Fourier transform infrared spectroscopy analysis of aligned graphene and graphene oxide in carboxymethyl cellulose films”, Materials Science & Technology Conference and Exhibition 2016, Salt Lake City, USA (23-27/10/2016)